universität wien

DISSERTATION / DOCTORAL THESIS

Titel der Dissertation /Title of the Doctoral Thesis

„Oriented acicular magnetite micro-inclusions in plagioclase from oceanic gabbro“

verfasst von / submitted by

Ge Bian

angestrebter akademischer Grad / in partial fulfilment of the requirements for the degree of

Doktorin der Naturwissenschaften (Dr. rer. nat.)

Wien, 2023 / Vienna 2023

Studienkennzahl lt. Studienblatt / degree programme code as it appears on the student record sheet:	A 796 605 426
Dissertationsgebiet lt. Studienblatt / field of study as it appears on the student record sheet:	Erdwissenschaften
Betreut von / Supervisor:	Univ.-Prof. Dr. Rainer Abart

Acknowledgement

First and foremost, I would like to express my heartfelt thanks to my supervisor Uni.-Prof. Dr. Rainer Abart for his continuous guidance of my doctoral studies. His attentive attitude, immense knowledge and deep insights have set an example for me in the practice of science. Moreover, his kindness and geniality have supported me throughout.

My endless thanks go to Dr. Olga Ageeva, for her elaborate groundwork and our inspiring discussions. I appreciate her patience and generosity during our time working together. Warmest thanks go to Dr. Thomas Griffiths, who always opens his door and offers a helping hand.

Sincere thanks to all colleagues and collaborators who helped build up the data for this project: to Dr. Olga Ageeva for the comprehensive documentation and careful selection of samples; to Dr. Gerlinde Habler from our group for the phenomenal FIB specimens; to Prof. Aleksander Rečnik from Jožef Stefan Institute for the wonderful TEM data; to Dr. Chen Li and Prof. Timothy Pennycook from University of Antwerp and to Dr. Vladimir Roddatis from GFZ Potsdam for their truly impressive STEM data; and to Dr. András Kovács and Dr. Qianqian Lan from Forschungszentrum Jülich for the beautiful electron holography and STEM data. Special thanks for all the insightful discussions with everyone. It has been an honour to learn from and work with you all!

I am more than grateful to have met all my brilliant fellows in this friendly and cheerful research group! Thanks so much for all the joyful moments we shared together! We've created wonderful memories that I will always cherish. Vienna is indeed a lovely city to live in! I can't express my gratitude enough for having spent my study time here! Also thanks to my friends around the world for your great company!

Last but not least, my deepest thanks and regrets to my loving parents! Thanks for all your support for my pursuit of research. The pandemic has made things difficult for both sides. I'm truly sorry that I couldn't stay by your side and fulfil my responsibilities when you needed me the most!

Ge Bian

Vienna, Jan 2023

Curriculum Vitae

Education

06/2019-present	Doctoral student in Department of Lithospheric Research, University of Vienna Thesis: Oriented acicular magnetite micro-inclusions in plagioclase from oceanic gabbro
08/2015-07/2018	University of Science and Technology of China (USTC) Institute of Metal Research, Chinese Academy of Sciences (IMR, CAS) Master of Engineering Major: Materials Science and Engineering GPA: 3.93/4 Academic Ranking: 6/124 Overall Ranking: 3/124
09/2011-07/2015	Dalian Jiaotong University (DJTU) Bachelor of Engineering Major: Material Processing and Control Engineering GPA: 91.13/100 Academic Ranking: 2/115 Overall Ranking: 1/115

Research skills

Experimental skills

- (S)TEM imaging, EDX and EELS measurements
- SEM imaging and EDX measurement
- FIB for (S)TEM specimen preparation
- XRD lattice constants measurement and residual strain analysis

Analysis skills

- (S)TEM image analysis, Digital Micrograph, ImageJ
- Crystallography analysis, Crystal Maker, Single Crystal, VESTA
- Crystallographic orientation analysis, Matlab toolbox MTEX
- Precipitation crystallography, PTCLab
- Data analysis and scientific graphing, OriginLab, CorelDRAW, Adobe Illustrator

Programming skills: Matlab, Python

Grant

European Union's Horizon 2020 research and innovation programme under grant agreement No 823717 – ESTEEM3:

Magnetic behavior of Fe-Ti oxides micro-inclusions as carriers of paleomagnetism in plagioclase, collaboration with Forschungszentrum Jülich

Interface crystallography of magnetite micro-inclusions in plagioclase, collaboration with EMAT University of Antwerp

Publication

Bian G., Ageeva O., Rečnik A., Habler G. & Abart R., Formation pathways of oriented magnetite micro-inclusions in plagioclase from oceanic gabbro, Contributions to Mineralogy and Petrology, 176(12), 2021. Doi: 10.1007/s00410-021-01864-8

Bian G., Ageeva, O., Roddatis, V., Li, C., Pennycook, T.J., Habler, G.& Abart, R. (2023) Crystal structure controls on oriented primary magnetite micro-inclusions in plagioclase from oceanic gabbro. Journal of Petrology, egad008. https://doi.org/10.1093/petrology/egad008

Ageeva O., Bian G., Habler G., Pertsev A. & Abart R., Crystallographic and shape orientations of magnetite micro-inclusions in plagioclase, Contributions to Mineralogy and Petrology, 175:95(6), 2020. Doi: 10.1007/s00410-020-01735-8

Ageeva O., Habler G., Gilder S., Schuster R., Pertsev A., Pilipenko O., Bian G. & Abart R., Oriented Magnetite Inclusions in Plagioclase: Implications for the Anisotropy of Magnetic Remanence, Geochemistry Geophysics Geosystems 23(2), 2022. Doi: 10.1029/2021GC010272

Conference

Bian G., Ageeva O., Rečnik A., Habler G. & Abart R., Plagioclase hosted magnetite micro-inclusions origin determination, 2021, Mineralogical Conference Abstract book. p. 65

Bian G., Ageeva O., Habler G., Roddatis V. & Abart R., Atomic scale structure of a plagioclase–magnetite interface, 2021, EGU General Assembly 2021. 1 p. EGU21-2432

Bian G., Roddatis V., Ageeva O., Habler G. & Abart R., Plagioclase-magnetite interface characterization at atomic scale, 2021, Microscopy Conference 2021 Proceedings. p. 199.

Bian G., Li C., Ageeva O., Habler G. & Abart R., Systematics of faceted interfaces between oriented magnetite micro-inclusions and plagioclase host, Sep 2021, In: Mitteilungen der Österreichischen Mineralogischen Gesellschaft. 167

Bian G., Roddatis V., Ageeva O., Habler G. & Abart R., Nanoscale observation of interface between magnetite micro-inclusions and plagioclase host, 2022, International Mineralogical Association (IMA) General meeting

Abstract

Magnetite is the most important carrier of natural remanent magnetization in rocks. Oriented needle- and lath shaped magnetite micro-inclusions are frequently observed in plagioclase from oceanic gabbro dredged at mid-Atlantic ridge. The formation pathways and temperatures of these inclusions are of interest for paleomagnetic reconstructions. Systematic shape and crystallographic orientation relationships (SORs, CORs) between the magnetite micro-inclusions and the plagioclase host have been discerned using optical microscopy including universal stage and scanning electron microscopy based electron backscattered diffraction. Two fundamental inclusion types are discerned: plane normal- and PL[001] type. Specific orientation distributions of needle- and lath shaped plagioclase hosted magnetite micro-inclusions cause bulk magnetic anisotropy of the magnetite bearing plagioclase and bias the NRM vector measured from plagioclase single grain. The factors controlling the SORs and CORs are thus important. Based on petrographic evidence and mass balance considerations, precipitation from Fe-bearing plagioclase under reducing conditions at above > 600°C is the most likely formation pathway of the plane normal type inclusions, which therefore carry thermoremanent magnetization. PL[001] type inclusions are of secondary nature and probably formed at lower temperature. To understand the mechanisms underlying the systematic SORs and CORs, atomic scale investigations of the magnetite-plagioclase interfaces were performed using (scanning) transmission electron microscopy. The elongation directions of needle- and lath shaped plane normal inclusions is controlled by the alignment of oxygen layers of both phases across the interface. Inclusion shapes are influenced by the oxygen sublattices in both crystal structures. The orientations and structures of magnetite-plagioclase interfaces were rationalized based on experimental observations and geometrical reconstructions, and several configurations were unraveled. The interfaces may follow oxygen layers of both phases or low index lattice plane of either phase or may ensure commensurate impingement lattice planes of both phases at the interface. Dislocations and stacking faults close to the interfaces have been inferred to release local stress caused by lack of lattice fit.

Zusammenfassung

Magnetit ist der wichtigste Träger der natürlichen remanenten Magnetisierung in Gesteinen. Orientierte nadel- und leistenförmige Magnetit-Mikroeinschlüsse werden häufig in Plagioklas aus ozeanischem Gabbro beobachtet, der am mittelatlantischen Rücken beprobt wurde. Die Bildungswege und Bildungstemperaturen dieser Einschlüsse sind für paläomagnetische Rekonstruktionen von Interesse. Systematische Form- und kristallografische Orientierungsbeziehungen (FOBs, KOBs) zwischen den Magnetit-Mikroeinschlüssen und dem Plagioklas-Wirtskristall wurden mit Hilfe optischer Mikroskopie, einschließlich Universaldrehtisch, und der auf der Rasterelektronenmikroskopie basierenden Beugung rückgestreuten Elektronen bestimmt. Es wurden zwei grundsätzliche Einschlusstypen unterschieden: der Flächennormal- und der PL[001]-Typ. Spezifische Orientierungsverteilungen von nadel- und leistenförmigen Magnetit-Mikroeinschlüssen in Plagioklas verursachen eine magnetische Anisotropie des magnetitführenden Plagioklases und beeinflussen den NRM-Vektor, der an Plagioklas-Einzelkörnern gemessen wird. Die Faktoren, welche die FOBs und KOBs kontrollieren, sind daher von Interesse. Ausgehend von petrographischen Evidenzen und Überlegungen zur Massenbilanz ist die Ausfällung aus Fe-haltigem Plagioklas unter reduzierenden Bedingungen bei über 600 °C der wahrscheinlichste Bildungsweg für die Einschlüsse vom Typ Flächennormal, diese weisen daher eine thermoremanente Magnetisierung auf. Einschlüsse vom Typ PL[001] sind sekundärer Natur und bilden sich wahrscheinlich bei niedrigeren Temperaturen. Um die Mechanismen zu verstehen, die den systematischen FOBs und KOBs zugrunde liegen, wurden Untersuchungen der Magnetit-Plagioklas-Grenzflächen auf atomarer Ebene mittels (Raster-)Transmissions-Elektronenmikroskopie durchgeführt. Die Längsrichtungen der nadel- und leistenförmigen Einschlüsse werden durch die Ausrichtung der Sauerstoffflagen beider Phasen an der Grenzfläche gesteuert. Die Formen der Einschlüsse werden von den Sauerstoffuntergittern in beiden Kristallstrukturen beeinflusst. Die Orientierungen und Strukturen der Magnetit-Plagioklas-Grenzflächen wurden auf der Grundlage experimenteller Beobachtungen und geometrischer Rekonstruktionen analysiert, und es wurden mehrere Konfigurationen entschlüsselt. Die Grenzflächen können den Sauerstofflagen beider Phasen oder Gitterebenen mit niedrigem Index einer der beiden Phasen folgen, oder sie können dafür sorgen, dass die Gitterebenen beider Phasen an der Grenzfläche exakt zusammenstoßen. Aus Versetzungen und Stapelfehlern in der Nähe der Grenzflächen wurde abgeleitet, dass sie lokale Spannungen freisetzen, die durch mangelnde Gitterpassung verursacht werden.

Preamble

This thesis focuses on magnetite micro-inclusions hosted by rock-forming plagioclase from oceanic gabbro dredged from the mid-Atlantic ridge. The thesis is structured in five chapters.

- Chapter 1 is an introduction setting the frame.
- Chapter 2 deals with the origin of magnetite micro-inclusions in rock-forming plagioclase from an oceanic gabbro that was dredged at the mid-Atlantic ridge. This chapter is taken from a published paper.
- Chapter 3 is focused on the factors controlling the shape orientation relationships (SORs) and crystallographic orientation relationships (CORs) of different types of primary magnetite micro–inclusions in plagioclase and possible evolution paths based on the microscopic configurations of the magnetite-plagioclase interfaces. This chapter is taken from a manuscript that is in press.
- Chapter 4 deals with the morphology, the spatial distribution, the CORs and SORs, as well as the factors controlling the CORs and SORs of secondary plagioclase hosted magnetite micro-inclusions based on petrographic evidence and atomic scale magnetite-plagioclase interface observations. This chapter is taken from a manuscript that is under review after revision.
- Chapter 5 summarizes the results from the three studies and puts them into a broader context.
- Finally, an appendix section gives supplementary data that could not be integrated in the three scientific papers.

Contents

Chapter 1

Introduction

1.1 The Earth's Magnetic Field

The Earth's magnetic field emanates from the interior of the Earth and extends to outer space. The shape of the Earth's magnetic field resembles the magnetic field of a gigantic bar magnet placed in the center of the Earth. The thought bar magnet has a dipolar configuration with a *geomagnetic south and north pole*. The axis of the bar magnet is slightly tilted relative to the rotation axis of the Earth, with the geomagnetic south pole located close to the geographic north pole and the geomagnetic north pole located close to the geographic south pole (Lanza and Meloni, 2006). The strength of the Earth's magnetic field at the Earth's surface generally increases from the equator to the poles and the value ranges from 25 to 65 μT, where T (tesla) is the unit describing the strength of the magnetic field, and is equal to $\mathrm{kg} \cdot \mathrm{s}^{-2} \cdot \mathrm{A}^{-1}$ in SI units (Finlay et al., 2010). For comparison, the strength of the magnetic field induced by a refrigerator magnet is approximately 10 mT. The positions on the Earth's surface where the geomagnetic field lines are vertical are called *magnetic (dip) poles*. The north and south magnetic poles are not exactly antipodal and do not coincide with geomagnetic poles as they have been wandering over geological times due to changes of the Earth's magnetic field (McElhinny and McFadden, 1999). The geomagnetic field extends several tens of thousands of kilometers into space and forms the Earth's *magnetosphere* (Ratcliffe, 1972). Without protection by the Earth's magnetosphere, solar wind would rip gasses out of the Earth's atmosphere and deplete the air we breathe (Blanc et al., 2005). Moreover, the Earth's magnetosphere also protects us from cosmic rays, which would damage our DNA and cause serious health problems, if the Earth were not shielded by the magnetosphere (Singh

et al., 2011). In addition, solar storms could damage Earth-orbiting satellites, power grids and electronic devices, which would impair our technologies (Baker et al., 2004). Furthermore, the Earth's magnetic field allows us to navigate using the compass, which usually aligns itself to the geomagnetic field. With the built-in biological compasses, the magnetoreceptors, many animals can navigate through the geomagnetic field (Wiltschko, 2012).

The Earth's magnetic field has protected Earth for at least 3.5 billion years (McElhinny and Senanayake, 1980; Usui et al., 2009). The occurrence of the geomagnetic field is due to a self-sustaining dynamo process in the Earth's core. During slow cooling and solidification of the Earth's core, heat is released and is transported to the mantle. This process causes convection of the mixture of molten iron and nickel in the outer core and thus produces flow and swirl and convection currents due to its conductive nature (Jordan, 1979). The motion of the convection currents in a magnetic field, which is induced by the rotation of the Earth, produces electric currents, which in turn produce a magnetic field. Thus, the generation of the Earth's magnetic field is a self-promoting loop (Buffett, 2000).

1.2 The Paleomagnetic Field

The Earth's magnetic field has varied over geological times (Glatzmaiers and Roberts, 1995; Irving, 1956). The study on the past Earth's magnetic field is referred to as *paleomagnetism*. The deviation of the magnetic north pole from the geographic north pole is defined as *declination*. At a certain location on the surface of the Earth, the angle between geomagnetic field line and the Earth surface is called *inclination*. The inclination is 0 at the magnetic equator and it is 90° at the magnetic dip poles. The strength of the geomagnetic field, the declination and the inclination altogether define the magnetic field at a point on the surface of the Earth. Based on the paleomagnetic records over the last 20 million years, the magnetic poles on Earth have been wandering and flipped in an aperiodic fashion (McElhinny and McFadden, 1999).

Specific minerals in specific rocks can record the direction and strength of the geomagnetic field at the time when they were formed and may maintain the geomagnetic records over billions of years (Dunlop and Özdemir, 2001). The permanent magnetization preserved in the minerals is referred to as the *natural remanent magnetization* (NRM). There are several types of NRMs according to the different recording mechanisms. Thermoremanent magnetization (TRM) is acquired

when the rocks cool through the Curie temperature T_c, which is the temperature at which the magnetic properties of magnetic materials change substantially. As the temperature decreases to the Curie temperature of a certain magnetic mineral, it will acquire a permanent magnetization. Conversely, if the temperature increases above the Curie temperature of the magnetic mineral, it will lose its permanent magnetization (Dunlop and Özdemir, 2001). TRM is regarded as the best source of paleomagnetism (Wohlfarth, 1958). Chemical remanent magnetization (CRM) is acquired during phase transformation or chemical reaction of magnetic minerals (Kobayashi, 1959). Detrital remanent magnetization (DRM) is acquired by the magnetic minerals in sediments during or soon after the deposition (Verosub, 1977). Isothermal remanent magnetization (IRM) is acquired when magnetic minerals are exposed to a strong magnetic field, such as during lightning strikes (Pinto and McWilliams, 1990; Verrier and Rochette, 2002). Viscous remanent magnetization (VRM) is the change in remanence of a magnetic mineral from initially acquired NRM to the equilibrium magnetization after a long period (Lowrie, 1973). Different types of NRMs can superimpose within one rock, and the remanence acquired during the formation of the rocks is the most important component of NRM, which is termed as *characteristic remanent magnetization* (ChRM). IRM and VRM are usually undesirable for interpreting the paleomagnetic record of a rock, and thus are usually removed by applying appropriate demagnetization techniques prior to experimental measurements (Dunlop and Özdemir, 2001).

Paleomagnetic studies have broad applications. Regional scale paleomagnetic records on the ocean floor have provided direct evidence of multiple reversals of the geomagnetic field as well as of plate tectonics (Heirtzler et al., 1968; McElhinny and McFadden, 1999). Ocean floor basalts show a series of stripes with reversed magnetic directions, which are symmetrical about the mid ocean ridge. As the ocean floor spreads, the newly formed ocean floor basalts record the geomagnetic field at the time when they solidify. When the Earth's

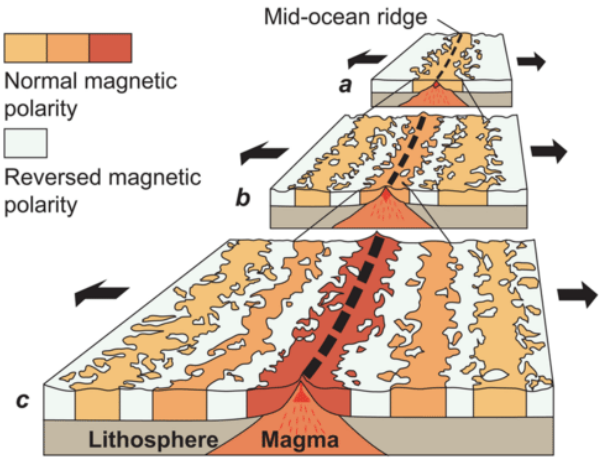

Figure 1.1: Magnetic stripes due to reversals of the Earth's field and seafloor spreading. The models show a ridge (a) about 5 million years ago (b) about 2 million years ago and (c) in the present. Courtesy of the US Geological Survey.

magnetic field reverses, the newly formed ocean floor basalts record the reversed magnetic field. Meanwhile, the newly formed ocean floor basalts are continuously pushed away from the mid ocean ridge on either side and the successive growth stages of the oceanic crust exhibit a stripe pattern of NRM with alternating polarity (Fig. 1.1) (Heirtzler and Le Pichon, 1965; Vine, 1966). Comparing the paleomagnetic records, in particular, the inclination and declination of the vector of NRM on a global scale, the past locations and movements of tectonic plates can be reconstructed, which was the first strong evidence for the hypothesis of global plate tectonics (Wegener, 1966). Paleomagnetism may also be used as a stratigraphic tool in addition to the traditional dating methods (McElhinny and McFadden, 1999).

1.3 Magnetic Properties

1.3.1 Magnetism

For paleomagnetism research, an understanding of how minerals in rocks record the Earth's magnetic field is necessary to develop and validate ancient magnetic field measurements. This field of study is called *rock magnetism*. Remanent magnetization is carried by magnetic minerals, such as iron oxides in the form of magnetite, maghemite and hematite or hydroxide, goethite or sulfide pyrrhotite (Dunlop and Özdemir, 2001). Different magnetic materials show different magnetic behavior.

Magnetization originates from the configurations of the electrons in the atoms of certain elements, whereas the nuclear contributions are usually insignificant (Jiles, 2015). Electrons carry negative charge and are in constant motion through the electron orbitals surrounding the atomic nucleus, which generates a magnetic field (Jones, 2013). The electron's magnetic moment describes the strength and direction of the magnetic field generated by a moving electron, which can be envisaged as a magnetic dipole. The magnetic moment of an electron is defined as Bohr magneton, and is expressed as μ_B (Breit, 1928). The direction of the electron magnetic dipole moment is determined by the spinning and orbiting of the electron (Jones, 2013). If in an atom, the magnetic moments contributed by all electrons are in opposite directions, such a configuration is called *electron pairing* (Coleman, 2000). The net magnetic moment of the atom with all paired up electrons is zero, and the overall magnetic field has zero strength. When the electrons

in the constituent atoms of a material are all paired up, the material is *diamagnetic* (Darwin, 1931; McClure, 1956). Exposing a diamagnetic material to an external magnetic field will change the orbital motion of the electrons, and hence an extremely small magnetic moment will be induced antiparallel to the direction of the externally imposed magnetic field, as shown in Fig. 1.2. This weak form of magnetism is called *diamagnetism*, which is found in all materials, but can only be observed in materials that are devoid of other forms of magnetism and only when an external magnetic field is present. In classical physics, the extent to which a material responds to an external magnetic field defines its magnetic susceptibility χ (Schenck, 1996). It is the ratio between magnetization of the material $\mathbf{M}$ and the strength of the external magnetic field $\mathbf{H}$, expressed as

$$\mathbf{M} = \chi \mathbf{H} \tag{1.1}$$

Magnetization $\mathbf{M}$ is the magnetic moment per unit volume, in SI units of amperes per meter. The strength of the external magnetic field $\mathbf{H}$ has the same unit. Therefore, magnetic susceptibility χ is a dimensionless material parameter. The repelling property of diamagnetic materials under an external magnetic field is described using a weak negative χ. The value falls in the order of -10^{-5} for common rock forming minerals (Tarling and Hrouda, 1993).

Paramagnetism arises when there are unpaired electrons in the atoms of the material (Parigi et al., 2019). Such atoms act as elementary electromagnets with dipolar magnetic moments. Paramagnetic materials typically contain randomly oriented magnetic dipoles under unmagnetized condition (Fig. 1.2). In the presence of an external magnetic field, the magnetic dipoles align and slightly promote the applied field, which exhibits little attraction to the external magnetic field, as shown in Fig. 1.2. Paramagnetic materials have a small positive χ. For common rock forming minerals, the magnetic susceptibility is in the range of 10^{-2} to 10^{-4} (Tarling and Hrouda, 1993).

Ferromagnetism derives from the spontaneous alignment of the magnetic moments of the atoms or ions in the material (Aharoni et al., 2000). A portion within the material, where all atomic or ionic magnetic moments are aligned, is called *magnetic domain* (Hubert and Schäfer, 2008). Under unmagnetized condition, the magnetic domains in a ferromagnetic material are randomly oriented, and the total magnetic field of the material is zero (Fig. 1.2). By placing a ferromagnetic material into an external magnetic field, the magnetic domains in the material

will align parallel to each other and produce a magnetic field (Fig. 1.2). The more magnetic domains are aligned, the stronger the magnetic field that is generated by the material. When all magnetic domains are aligned, the material is *magnetically saturated* (Hubert and Schäfer, 2008). Ferromagnetic materials possess high positive χ.

Antiferromagnetism forms when magnetic moments of the atoms or ions in a material are of equal magnitude and are spontaneously aligned in opposite directions, so that the total magnetic field of the material is zero, as shown in Fig. 1.2. Antiferromagnetism disappears when the material is heated above a certain temperature, referred to as the Néel temperature. Above the Néel temperature, the material will exhibit paramagnetism (Özdemir and Dunlop, 1996).

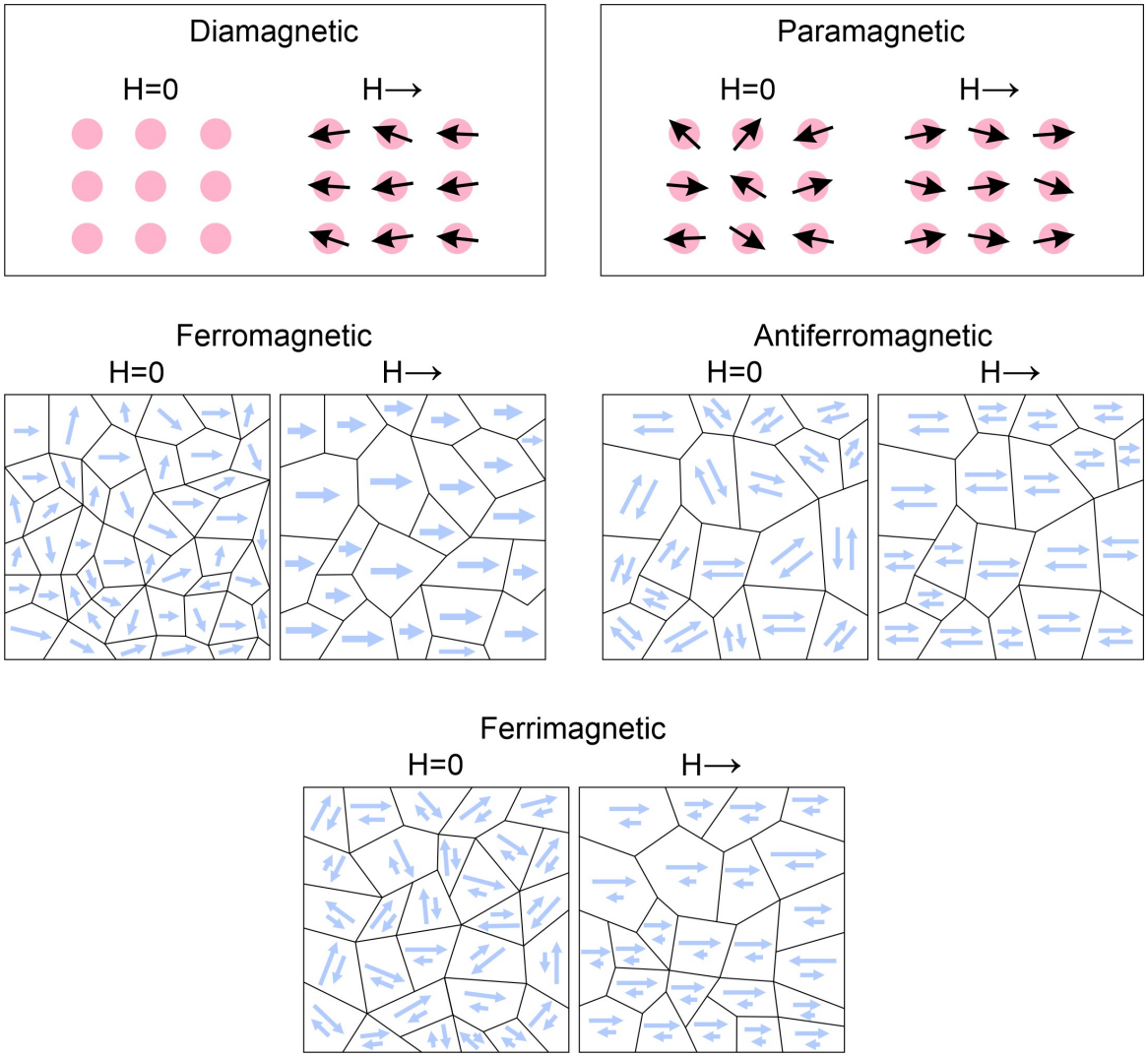

Figure 1.2: Sketches of magnetic moments in diamagnetic, paramagnetic, ferromagnetic, antiferromagnetic and ferrimagnetic materials under unmagnetized and magnetized conditions. Sketches after Kittel and Galt (1956).

Ferrimagnetism arises in a material where two species of magnetic ions are present (Néel, 1984). The two types of magnetic ions form sublattices in the material and the magnetic moments of the two sublattices are aligned in opposite directions. Because of the different types of the

magnetic ions, the magnetic moments of the two sublattices are different in magnitudes and do not cancel out (Smart, 1955). Thus, when placed in an external magnetic field, the magnetic domains of a ferrimagnetic material will align parallel to the external magnetic field and a finite total magnetic moment is preserved when the external field is removed (Fig. 1.2).

1.3.2 Magnetic hystersis

When placing a ferromagnetic material in a magnetic field, magnetism will be induced. This process is referred to as *magnetic induction*. The vector describing the strength and direction of the induced magnetic field is denoted as **B**, and the unit of **B** is the tesla (T). An alternative name for **B** is the *magnetic flux density*, which refers to the number of magnetic field lines passing through a unit area of the material. The relation between **B** and the external magnetic field **H** corresponds to what is referred to as *magnetic hysteresis* (Wasilewski, 1973). A schematic hysteresis loop of a ferromagnetic material is shown in Fig. 1.3. The hysteresis loop can be subdivided into the following stages:

1) When an external magnetic field is applied to a ferromagnetic material with zero initial magnetization, magnetism will be induced, and B will increase, as shown by the dashed line in Fig. 1.3. As H increases, B increases gradually until it reaches magnetic saturation, i.e. point *a* in Fig. 1.3. Magnetic saturation is reached when all of the magnetic domains in a ferromagnetic material are aligned; 2) When then the external magnetic field **H** is diminished, also B decreases, but the path the material takes in the B-H diagram is different than the path taken during the first magnetization run. When H becomes zero, some magnetic induction remains in the material, as shown by point *b* in Fig. 1.3. This point is referred to as *saturation residual magnetization*, also known as the *remanence*. In ferromagnetic material, some

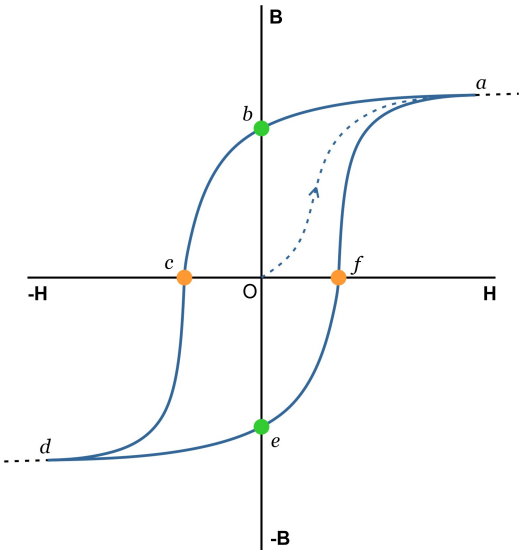

Figure 1.3: Schematic hysteresis loop of a ferromagnetic material showing the relationship between magnetic induction **B** and the external magnetic field **H**. Points *a* and *d* correspond to magnetic saturation. Points *b* and *e* correspond to magnetic remanence. Points *c* and *f* correspond to coercivity.

magnetic domains remain aligned while the alignment of other magnetic domains is disrupted (Hubert and Schäfer, 2008); 3) As the external magnetic field **H** reverses and the strength increases in the opposite direction, B continues to decrease. The strength of the external magnetic field H needed to make B become zero, which is point *c* in Fig. 1.3 is referred to as the *coercivity*. At this point, the external magnetic field has disrupted the alignment of the magnetic domains to the extent that the net magnetization of the ferromagnetic material is zero (Hubert and Schäfer, 2008); 4) Subsequently increasing the strength of the external magnetic field H in opposite direction, the ferromagnetic material reaches magnetic saturation, point *d*, which has the same magnitude of B as point *a* but in opposite direction; 5) Reducing the strength of the external field H to zero, magnetic induction reaches the remanence, point *e*, where B is of similar in magnitude as in point *b* but in opposite direction; 6) The magnetic induction of the material becomes zero when the strength of the external magnetic field reaches the coercivity in the opposite direction (point *f* in Fig. 1.3). The plot does not return to the origin where the hysteresis starts as coercivity force is required to remove the magnetic induction of the material; 7) The hysteresis loop is completed by reaching the magnetic saturation point *a* in 1) through a path centrosymmetric to the path described in 4). In the context of rock magnetism, minerals that respond strongly to a magnetic field and retain a remanence are of particular interest (Dunlop and Özdemir, 2001).

1.3.3 Magnetic anisotropy

Magnetic anisotropy describes the directional dependence of the magnetic moments in a magnetic material. Magnetic anisotropy usually results from a combination of contributions from different sources. *Magnetocrystalline anisotropy* describes the dependence of magnetic properties on crystallographic directions (Darby and Isaac, 1974). It is an intrinsic property of the magnetic material. *Shape anisotropy* arises from the influence of the shape of a magnetic particle on the directional dependence of its magnetic properties (Borradaile and Henry, 1997). For an elongated magnetic mineral, when shape anisotropy dominates, the preferred magnetization direction will be parallel to the elongation direction (Laval et al., 1965). Stress along a certain direction in the magnetic material may produce an easy axis for magnetization and thus introduce *stress anisotropy* if the impact of the stress is more significant than the other forms of anisotropy (Johnson et al., 1996).

1.3.4 Magnetic domains

Magnetic properties of a ferromagnetic material are largely controlled by its magnetic domain state. The formation of magnetic domains in a magnetized ferromagnetic material is driven by the minimization of the magnetostatic energy arising from the demagnetizing field (Stancil, 2012). *Demagnetizing field*, also known as the *stray field*, is generated inside of the magnetic material after magnetization. The direction of this field is the opposite to the direction of magnetization, which tends to minimize the total magnetic moments of the material, therefore it is called demagnetizing field. *Magnetostatic energy* arises from the generation of the demagnetizing field. The magnetostatic energy corresponds to the work required for magnetic poles to be present on the surface of the magnetic particle and act against magnetization (Aharoni, 1991). A ferromagnetic material can minimize the magnetostatic energy by accommodating the magnetization within itself and forming magnetic domains of differently oriented magnetic moments. The magnetic field lines form loops passing through each magnetic domain and thus reduce the demagnetizing field. Magnetic domains are separated by domain walls, which accommodate the transition of magnetization from two adjacent domains. As the nearby magnetic moments are forced to resist the tendency to align, domain walls introduce extra energy, which is referred to as the *domain wall energy* (Catalan et al., 2012). In addition, magnetic anisotropy can introduce further energy cost for formation of magnetic domains (Hubert and Schäfer, 2008). The equilibrium of magnetic domain structure in magnetic material is related to many factors and can be obtained by theoretical energy considerations and dedicated simulation (Garanin, 1997).

A general rule implies that the magnetic domain size for a certain ferromagnetic material is related to the grain size, shape of the grain and temperature (Atxitia et al., 2016). A grain that contains multiple magnetic domains is termed *multi-domain* grain. As the grain size decreases, it will reach a critical size where no domain walls can be accommodated in the grain. Below this value, the grain contains uniformly distributed magnetization and is referred to as a *single domain* grain (Butler and Banerjee, 1975). To change the magnetization of a single domain grain, the only method is to rotate the magnetization vector within the grain, which is extremely energetically expensive (Chen et al., 1992). Thus, for a single domain grain, it is difficult to change its magnetization. As a consequence, single domain grains possess high coercivity and remanence, and are said to be *magnetically hard*. These properties make them perfect carriers of

paleomagnetism (Dunlop, 1972).

As the grain size continues to decrease, it will reach the point when the thermal energy is sufficient to disturb the alignment of the magnetic moments of the atoms in the grain. As a result, the net magnetization of the grain will become zero under unmagnetized condition, and the coercivity and the remanence of the magnetic particle also become zero. In this magnetic state the magnetic grain will acquire magnetization in an applied magnetic field and behave paramagnetic, accordingly the particle is then said to be in a *superparamagnetic* state (Dunlop, 1972). The hysteresis loop of a superparamagnetic particle has a very thin shape reflecting the absence of coercivity and remanence.

Pseudo-single domain grains are transitional between single domain to multi-domain grains. A pseudo-single domain magnetic grain is expected to be comprised of several magnetic domains but it rather behaves as a single domain particle with high remanence. This type of domain state is of great interest in paleomagnetism as it covers the grain sizes of magnetic materials in nature (Dunlop and Özdemir, 2001; Reichel et al., 2017).

1.4 Magnetite and Titanomagnetite

1.4.1 Magnetite

Magnetite has the sum formula $Fe_2^{3+}Fe^{2+}O_4$, and is the first substance that was recognized to be magnetic. It pertains to the spinel group minerals. Magnetite has a cubic symmetry of space group *Fd3m*. A magnetite unit cell comprises 16 Fe^{3+}, 8 Fe^{2+} and 32 O^{2+}, where the oxygen anions form a close-packed face-centered cubic (FCC) lattice, and the cations occupy the interstices (Fig. 1.4). Among the cations, 8 Fe^{3+} and 8 Fe^{2+} occupy the octahedral sites and 8 Fe^{3+} occupy the tetrahedral sites (Fleet, 1981). Compared to the normal spinel structure, where divalent cations occupy the tetrahedral sites and trivalent cations occupy the octahedral sites, magnetite is classified as an *inverse spinel*. Magnetite shows ferrimagnetism with a Curie temperature of 580 °C (Banerjee and Moskowitz, 1985). Fig. 1.5 shows a sketch of the cation contributions to the magnetic moments in magnetite. The Fe^{3+} cations in the octahedral and tetrahedral sites couple up in an antiferromagnetic fashion via oxygen atoms and thus the ionic magnetic moments contributed by Fe^{3+} cancel out (Banerjee and Moskowitz, 1985). The magnetization of magnetite is contributed only

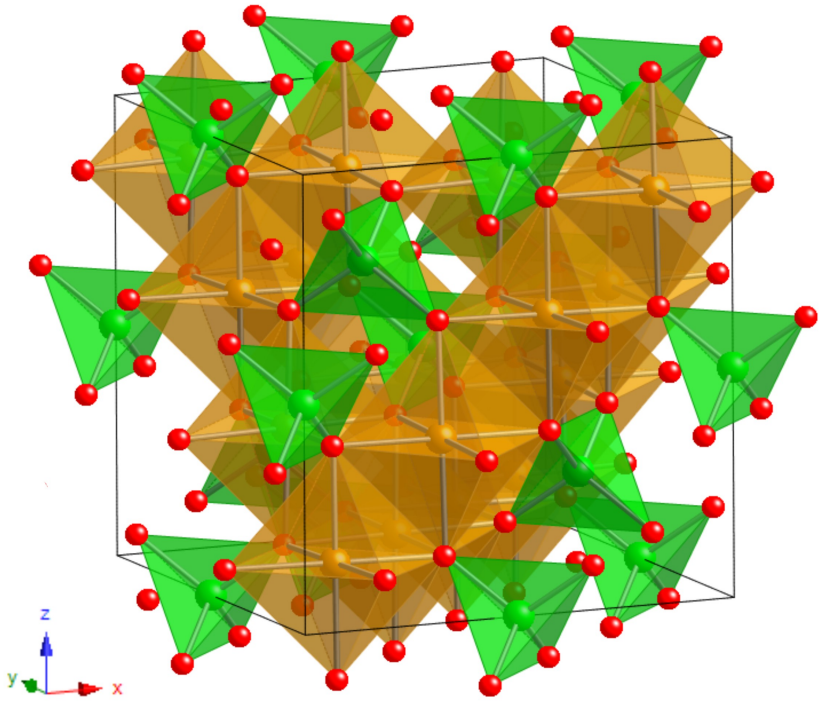

Figure 1.4: Polyhedral model of the crystal structure of magnetite. Red spheres represent oxygen anions. The octahedral and tetrahedral sites hosting Fe cations in their centers are shown in brown and green colors, respectively. The sizes of cations and anions are not drawn to scale.

by the Fe^{2+} cations in the tetrahedral sites (Zhang and Satpathy, 1991). Regarding the electron configuration in the electron shells of Fe^{2+}, which is expressed as $1s^2 2s^2 2p^6 3s^2 3p^6 3d^6$, there are four unpaired electrons in the 3d orbitals. Therefore, the magnetic moment of magnetite is 4 μ_B (Bohr magneton) per formula (Banerjee and Moskowitz, 1985).

The critical size for the transition between different magnetic domain states in magnetite particles strongly depends on shape. For equant magnetite grains, a grain size of 25-80 nm leads to single domain behavior at room temperature, while for elongated needle shaped magnetite grains, the critical size can reach several micrometers parallel to the elongation direction (Aharoni, 1988; Reichel et al., 2017). Magnetite grains in the size ranges between 0.1-20 μm are often considered as pseudo-single domain grains (Dunlop, 1972).

1.4.2 Titanomagnetite

Magnetite and ulvospinel are the two end members of the titanomagnetite solid solution series (Fig. 1.6). Ulvospinel has cubic crystal structure with the sum formula $Fe_2^{2+}TiO_4$ and belongs to the inverse spinel group of minerals as does magnetite (Price, 1981). Ulvospinel is paramagnetic

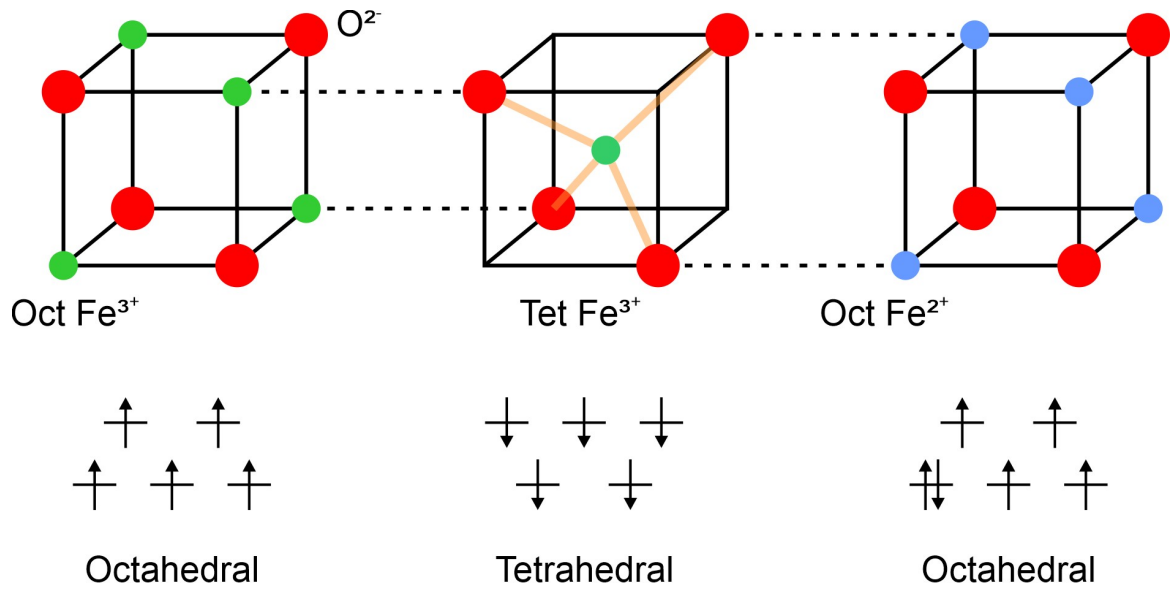

Figure 1.5: Sketch of ions in magnetite: Fe^{3+} on octahedral sites, Fe^{3+} on tetrahedral sites and Fe^{2+} on octahedral sites. The electron configurations in the different Fe cations are shown underneath. Fe^{3+} cations have 5 unpaired electrons and show opposite directions of magnetic moments in octahedral and tetrahedral sites, so that the net magnetic moments of the electrons associated with the Fe^{3+} cations cancel out. The octahedrally coordinated Fe^{2+} cations have 4 unpaired electrons, which contribute to the overall magnetic moments of magnetite. Image after Abedini et al. (2014)

at room temperature and antiferromagnetic at low temperature. The temperature of the paramagnetic — antiferromagnetic transition, i.e. the Néel temperature of ulvospinel is −153 °C (Readman, 1978). The titanomagnetite solid solution series shows complete miscibility at temperatures above 600 °C under reducing conditions. The compositional variation along the titanomagnetite solid-solution series may be expressed as

$$2\,Fe^{3+} \longleftrightarrow Fe^{2+} + Ti^{4+} \tag{1.2}$$

At elevated oxygen fugacity ulvospinel tends to be oxidized producing ilmenite ($FeTiO_3$) and magnetite. This process is indicated by the arrows in Fig. 1.6 from titanomagnetite series towards the titanohematite series and can be expressed as (Buddington and Lindsley, 1964):

$$6\,Fe_2TiO_4 + O_2 \longleftrightarrow 6\,FeTiO_3 + 2\,Fe_3O_4 \tag{1.3}$$

The transformation is known as *exsolution-oxidation* of ulvospinel (Tan et al., 2016). Pure ilmenite is paramagnetic at room temperature. The Néel temperature of ilmenite is between −218 and −205 °C (Connolly and Copenhaver, 2012). Low-temperature exsolution of ilmenite typically produces so-called *cloth-textures* of ultrafine lamellae in the magnetite host and typically aligned

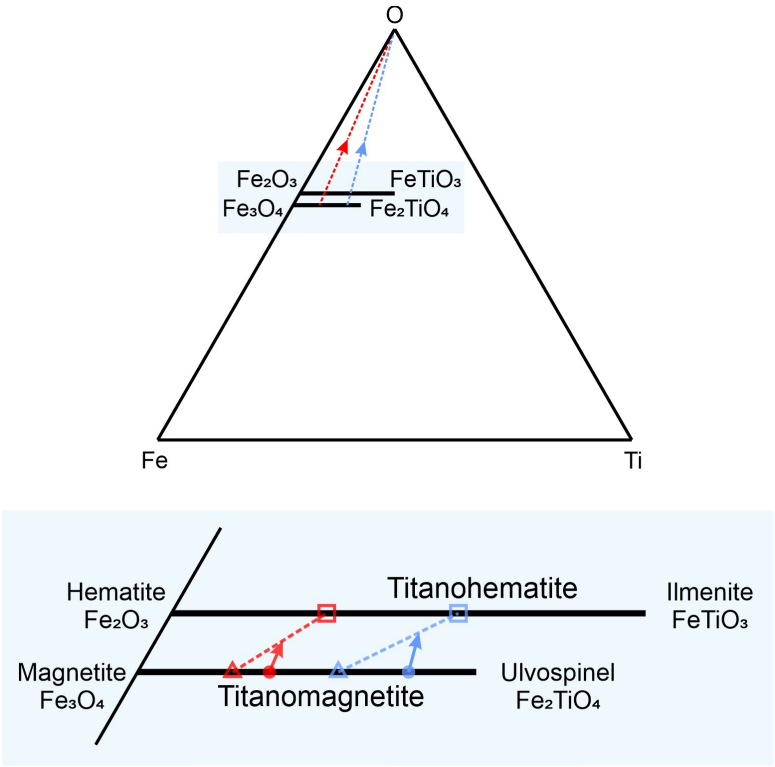

Figure 1.6: Fe- Ti-O ternary diagram with titanomagnetite and titanohematite series and related minerals indicated. Arrows show the directions of compositional changes associated with oxidation. An enlarged titanomagnetite and titanohematite series diagram is shown beneath the ternary diagram. Arrows indicate the directions of compositional shifts due to oxidation. Dashed lines represent tie lines for coexisting phases represented by triangles and squares as product phases from oxidation induced exsolution. (Personal communication Rainer Abart)

with MT{100} lattice planes, which follows the orientation relationship of magnetite and the preexisting ulvospinel (Buddington and Lindsley, 1964; Tan et al., 2016). Fig. 1.7 shows different morphologies of ulvospinel (Usp) and ilmenite (Ilm) exsolutions observed in plagioclase hosted magnetite (Mt) micro-inclusions from late-magmatic and hydrothermally altered gabbro. MT_1 and MT_2 denote the primary magnetite and the magnetite produced from exsolution-oxidation of ulvospinel (Eq. 1.3), respectively. Ulvospinel exsolutions show boxwork (honeycomb-like) and bulk textures in the magnetite host, and ilmenite exsolutions show fine lamellar textures.

Alternatively, the Fe_2TiO_4 component of titanomagnetite may be oxidized directly at high temperature producing ilmenite and magnetite, a process referred to as *oxy-exsolution* (Buddington and Lindsley, 1964). High-temperature exsolution of ilmenite shows trellis- and sandwich-type lamellar microstructure where the lamellae extend parallel to the ilmenite (0001) lattice plane which is aligned parallel to one set of the magnetite {111} lattice planes (Tan et al., 2016). This process is expected to happen above at least 600 °C, which is above the Curie temperature of magnetite, and is thus of interest in the context of TRM. Fig. 1.8 shows different morphologies of the ilmenite (ilm) exsolutions lamellae observed in plagioclase hosted magnetite (mt) micro-

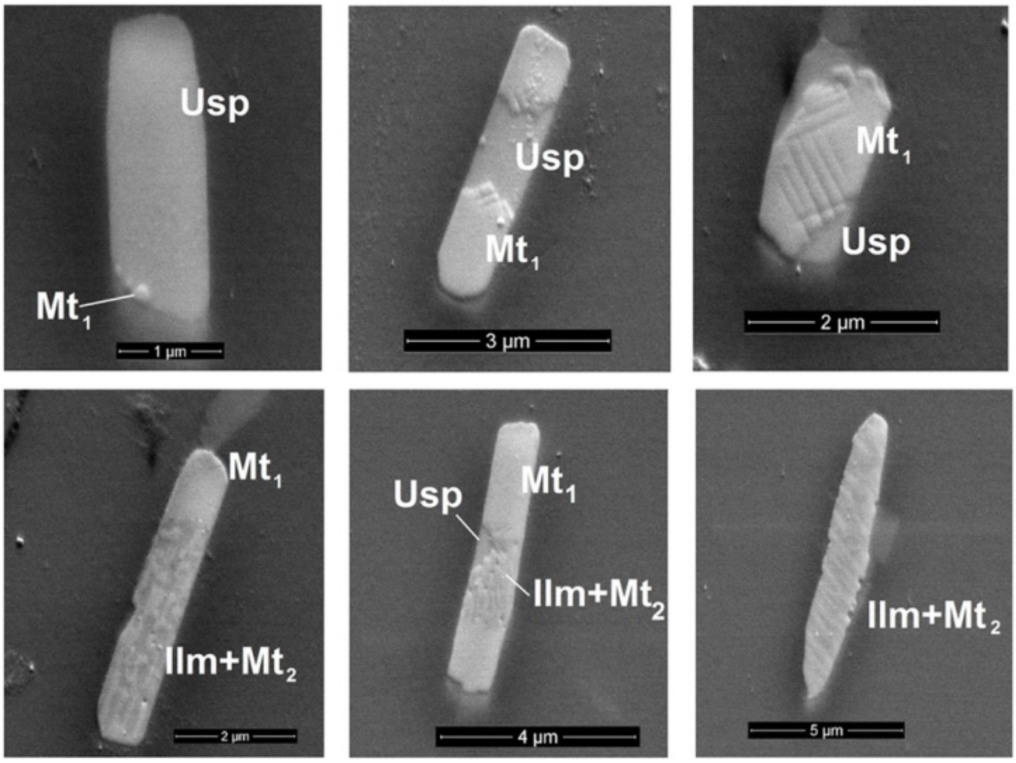

Figure 1.7: Secondary electron (SE) images showing exsolution microstructures in plagioclase hosted magnetite (Mt) micro-inclusions from oceanic gabbro. MT_1 and MT_2 denote primary magnetite and magnetite produced from exsolution-oxidation of ulvospinel (Eq. 1.3), respectively. Ulvospinel (Usp) shows boxwork and bulk textures and ilmenite (Ilm) shows ultrafine lamellar texture. (Images courtesy of Olga Ageeva)

inclusions from oceanic gabbro intruded by plagiogranite veins. Fig. 1.8A shows a transmitted light image of the magnetite micro-inclusions distributed in the plagioclase host. Fig. 1.8B-C show trellis- and sandwich-like textures of ilmenite in the magnetite host. Fig. 1.8D shows that the ilmenite exsolutions are disconnected from the magnetite micro-inclusion.

1.5 Oriented Magnetite Inclusions in Rock Forming Silicates

Magnetite is the most important carrier of NRM in rocks. Magnetite bearing olivine, pyroxene, plagioclase are a common phenomenon in mafic intrusive rocks (Ageeva et al., 2016; Divljan, 1960; Neumann and Christie, 1962; Poldervaart and Gilkey, 1954; Sobolev, 1990; Usui et al., 2015; Wenk et al., 2011). These inclusions are often observed in the form of needles and laths in the host minerals, with a grain size of several hundred nanometers in width and hundreds of micrometers in length. From chemical analysis and crystal symmetry obtained from scanning electron microscopy (SEM) based crystal orientation analysis by electron backscattered diffraction (EBSD) (Ageeva et al., 2020) and X-ray diffraction (Wenk et al., 2011) the inclusions were

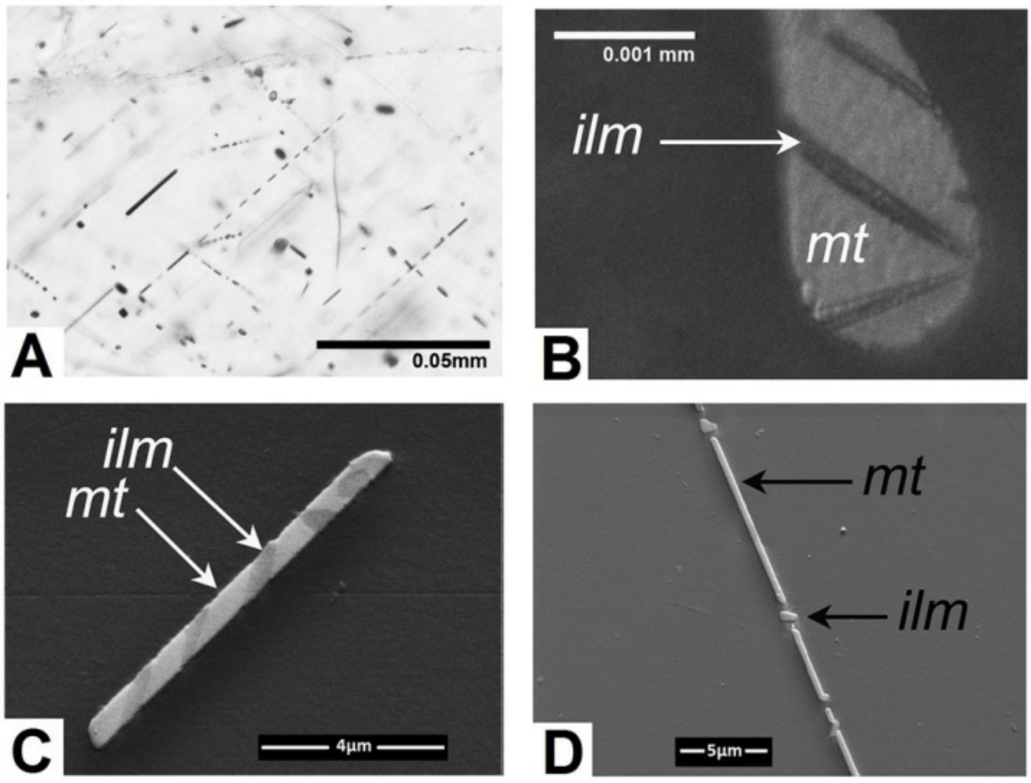

Figure 1.8: A. Transmitted light image of plagioclase hosted magnetite micro-inclusions from oceanic gabbro. B-C. Ilmenite (ilm) exsolutions in magnetite (mt) micro-inclusions of trellis- and sandwich-like textures. D. Ilmenite exsolutions disconnected from the magnetite micro-inclusion. Images taken from Ageeva et al. (2016).

identified as magnetite, which is sometimes associated with ilmenite and/or ulvospinel lamellae. Generally, magnetite is the volumetrically dominant phase in the Fe-Ti oxide micro-inclusions. Therefore, the inclusions are referred to as magnetite micro-inclusions. Due to their small size and high aspect ratio, the magnetite micro-inclusions behave as single domain or pseudo-single domain particles (Ageeva et al., 2022; Murthy et al., 1971; Renne et al., 2002). In addition, the magnetite micro-inclusions are enclosed by the stable silicate hosts that shelter them from externally imposed changes in the physical and chemical conditions. The inclusions are therefore ideal recorders of paleomagnetic signals (Dunlop and Özdemir, 2001).

The magnetite inclusions usually show systematic orientation relationships to the host minerals. In clinopyroxene, there are two classes of shape orientation relationships (SORs) and corresponding crystallographic orientation relationships (CORs) between needle-shaped magnetite micro-inclusions and the host, which are designated as “Z” and “X” types (Ageeva et al., 2017; Fleet et al., 1980; Renne et al., 2002). The elongation direction for “Z” type magnetite micro-inclusions is subparallel to clinopyroxene [001] crystallographic direction and for “X” type is subparallel to clinopyroxene [100] crystallographic direction. Both types of inclusions lie in the

clinopyroxene (010) lattice plane. Orthopyroxene has only one SOR type of magnetite micro-inclusions, the "Z" type, with the elongation direction subparallel to the crystallographic *c* axis of the orthopyroxene host (Fleet et al., 1980; Nikolaisen et al., 2022).

The distribution of magnetite micro-inclusions in plagioclase is more complicated. Five types of SOR between magnetite micro-inclusions and plagioclase have been described in intrusive rocks by Sobolev (1990) and one SOR type has been described in metamorphic rocks (Feinberg et al., 2004; Wenk et al., 2011). In plagioclase from oceanic gabbro dredged from the mid-Atlantic ridge, eight SOR classes and multiple CORs within each SOR class of needle- and lath shaped magnetite micro-inclusions have been discerned (Ageeva et al., 2020). As mentioned above, the elongation direction of a needle- or lath shaped magnetite grains corresponds to an easy axis for magnetization due to the effect of shape anisotropy. This anisotropy is also valid for the magnetic remanence of elongated magnetite. Thus, the distribution of populations of plagioclase hosted needle- and lath shaped magnetite micro-inclusions with different orientations contribute to an overall anisotropic susceptibility of remanence of plagioclase single grain containing oriented needle- and lath shaped magnetite micro-inclusions (Tarling and Hrouda, 1993). It has been reported that the different SORs and CORs can lead to bulk magnetic anisotropy of the inclusion-host assemblage and bias the NRM vectors measured from the silicate single grains (Ageeva et al., 2022; Fuller, 1963; Hargraves, 1959; Rochette et al., 1992; Rogers et al., 1979). Understanding the systematics of the distributions of the magnetite micro-inclusions in silicate host grains is thus essential for paleomagnetic reconstructions.

The primary task is to unravel the statistical distribution of inclusion populations pertaining to the different orientation classes of plagioclase hosted magnetite micro-inclusions. Such information is collected via correlated optical microscopy including measurements with the universal stage, and SEM based crystal orientation analysis by EBSD. The underlying reasons why the inclusions have certain orientation preferences are of great interest for rationalizing the observed distributions. Here the structural correspondences of magnetite and plagioclase to the SORs and CORs need to be considered in order to unravel the factors controlling the systematic SORs and CORs. In this context, the structural correspondences between the two phases under different SORs and CORs at the magnetite-plagioclase interface are of key interest. Thus, the microscopic configurations of magnetite-plagioclase interfaces need to be examined for different SORs and

CORs, and the habit planes of the interfaces need to be discussed based on experimental results and geometrical reconstructions.

State-of-the-art (scanning) transmission electron microscopy (STEM) is required for studying the complex magnetite-plagioclase interface structures. Correlated light optical microscopy, SEM based EBSD and STEM targeted at magnetite-plagioclase interfaces is the main focus of this doctoral study. Moreover, the magnetic properties of the individual magnetite micro-inclusions need to be studied as they are the fundamental contributors to the remanence, the magnetic behavior of which may be biased due to structural and/or chemical heterogeneities. Thus, the internal structures and chemical compositions of individual magnetite micro-inclusions need to be examined via (scanning) transmission electron microscopy. Preliminary chemical analyses performed on ChemiSTEM have shown that magnetite micro-inclusions contain different morphologies of ilmenite lamellae. In Fig. 1.9a, two ilmenite lamellae have rectangular shape with sharp vertical boundaries towards magnetite. In Fig. 1.9b, the ilmenite lamella on the left-hand side shows irregular shape with blurred boundaries to magnetite and the ilmenite lamella on the right-hand side shows oblique orientation with oblique blurred boundaries to magnetite. In Fig. 1.9c, the ilmenite lamella shows a hexagonal geometry with the boundaries inclined towards magnetite. The magnetic behaviors of needle shaped magnetite micro-inclusions need to be examined regarding the presence of the paramagnetic phases.

1.6 Geometrical Models for Rationalizing Interfaces in Crystalline Materials

Systematic SORs and CORs in the inclusion-host system result from many factors, including structural constraints, inclusion shapes, diffusion, the interfacial energy, etc. (Sutton and Balluffi, 1995). Among the aforementioned factors, minimization of the interfacial energy during nucleation and growth of the inclusions has been considered as the dominant factor (Putnis, 1992). Quantitative calculations of the interfacial energy for an inclusion-host system are rather challenging. Therefore, alternative methods to evaluate the structure and orientation of the crystalline interface have been widely developed to determine whether and why the recurrent CORs and SORs are preferred (Zhang and Weatherly, 2005). The method has been well-examined during

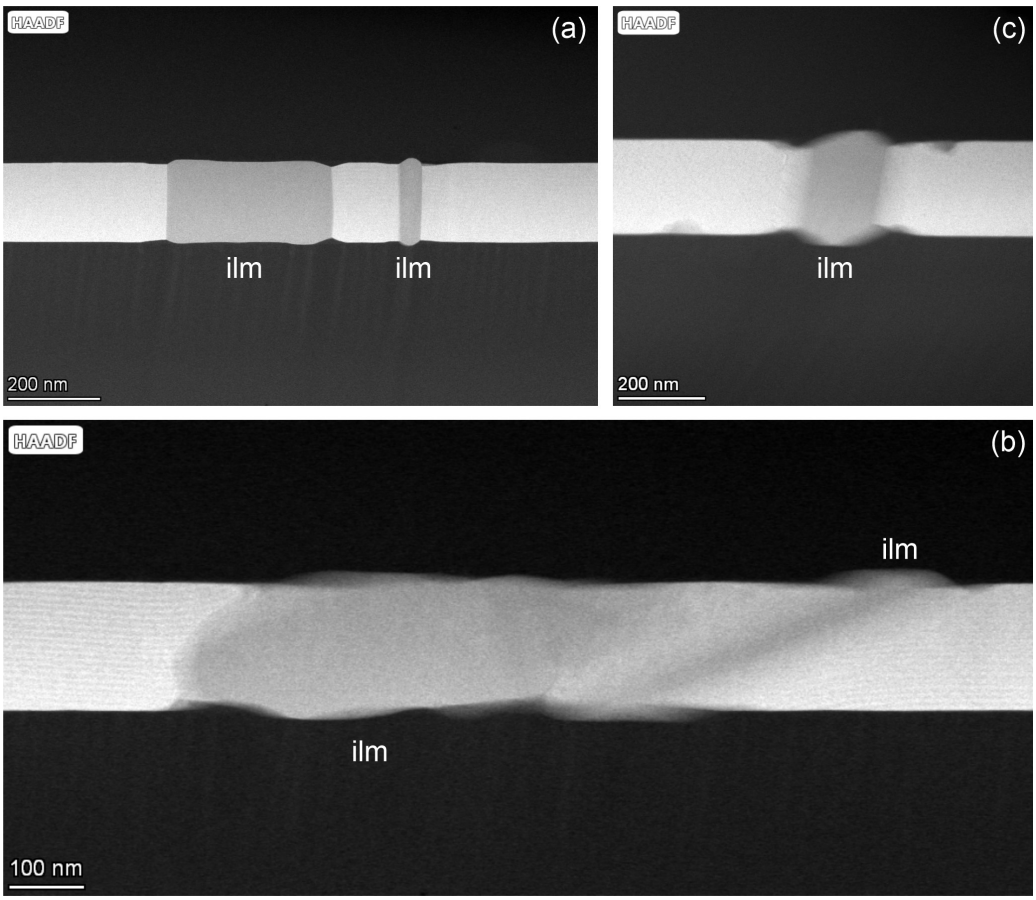

Figure 1.9: Scanning transmission electron microscopy (STEM) of magnetite micro-inclusions containing ilmenite (ilm) exsolutions. (a) and (b) were acquired from one single inclusion under the same viewing direction. The ilmenite lamellae show different morphologies. (a) Two ilmenite lamellae in magnetite have regular shapes with vertical sharp boundaries towards magnetite. (b) Ilmenite lamella on the left has irregular shape with blurred boundaries to magnetite. Ilmenite lamella on the right orients inclined with blurred oblique boundaries to magnetite. (c) Ilmenite lamella of a hexagonal geometry. The boundaries towards magnetite are inclined and blurred.

the past decades due to the burgeoning development of transmission electron microscopy, which provides direct observations of the atomic scale structures and orientations of interfaces in crystalline materials (Zhang, 2020). As the method involves the evaluations of match between the unit cells of the two phases sharing a common boundary and hence are referred to as geometrical models.

The most comprehensive geometrical method regarding the interpretation of the orientation and the structure of the interfaces in crystalline material is the *O-lattice theory* (Bollmann, 2012). Bollmann and Nissen (1968) have successfully applied the O-lattice theory to obtain the preferred orientation relationships of the exsolutions in monoclinic K-feldspar through a geometrical parameter evaluating the boundary energy of the calculated O-lattice. However, as the system gets more complicated, the calculations become strenuous and multiple parameters need to be introduced to evaluate the calculated O-lattice.

Orientations of the interface between exsolution lamellae in monoclinic augite and monoclinic pigeonite have been rationalized based on the *exact phase boundary* model (Robinson et al., 1971, 1977; Jaffe et al., 1975), where the interface preferred orientation and structure were directly obtained by comparing unit cells of the two phases. Fleet et al. (1980) have applied the exact phase boundary model to explain the preferred orientations of magnetite inclusions in pyroxene, a system between cubic and monoclinic crystal structures. Fig. 1.10 shows the construction of the exact phase boundary between cubic magnetite (mt) and monoclinic clinopyroxene (cpx). The dimension of each unit cell is indicated within Fig. 1.10. As the length of mt[110] and of cpx[010] are almost identical, the unit cell correspondence between magnetite and clinopyroxene can be simplified into a 2D problem, and so the unit cell match is performed on the plane projected along mt[110] and cpx[010]. A premise of applying the exact phase boundary model is that the unit cells for representing the crystal structures of the two phases need to be chosen so that they have similar dimension (Robinson et al., 1971, 1977). Figs. 1.10a-b show magnetite projected along mt[110] and multiplied clinopyroxene unit cells projected along cpx[010]. The cubic magnetite is represented by a general parallelogram, the red parallelogram shown in Fig. 1.10a, and is referred to as *alternative magnetite*, so that it is comparable with clinopyroxene (Fleet et al., 1980). Fig. 1.10c shows the multiplied unit cells of alternative magnetite (denoted as pmt) in the orientation of the *c* axis of alternative magnetite parallel to *c* axis of clinopyroxene in Fig. 1.10b. The exact phase boundary as well as the corresponding orientation relationship between the two unit cells can then be derived from straightforward calculations (Fleet et al., 1980). Superimposed parallelograms of alternative magnetite (red) and clinopyroxene (blue) are shown in Fig. 1.10d according to the calculated orientation relationship. The derived exact phase boundary between alternative magnetite and clinopyroxene intersects with all the coincident points between the two sets of parallelograms and is indicated as dashed line in Fig. 1.10d. The interface orientation and orientation relationship between the two phases derived from this geometrical model show good agreement with experimental observations, and has been applied as a geothermometer to estimate the formation temperature of magnetite inclusions in clinopyroxene (Fleet et al., 1980; Hwang et al., 2010).

In inclusion-host systems that contain phase with close packed oxygen sublattices in the crystal structures of the two phases, the preferred interface orientation and structure have been assigned

to the alignment of the oxygen layers across and parallel to the interface between the two phases, such as magnetite in olivine (Champness, 1970), magnetite in clinopyroxene (Hwang et al., 2010) and rutile in chrysoberyl (Drev et al., 2015). The morphologies of the inclusions in silicates can be exceedingly complex and not every interface between the inclusion and the host corresponds to the alignment of the oxygen layers between the two phases. A geometrical model, termed $\Delta \boldsymbol{g}$ *method*, which is based on the crystallographic correspondence between the two phases obtained in reciprocal space, has been applied to explain interface orientations of needle shaped magnetite in clinopyroxene and plate shaped hematite in rutile regardless of the oxygen sublattices correspondence (Hwang et al., 2010). In the current study, $\Delta \boldsymbol{g}$ method has been applied to explain interface orientations and structures of needle- and plate shaped magnetite inclusions in plagioclase, a system of cubic and triclinic crystal structures. Detailed calculation procedures regarding the interface preferences of plagioclase hosted plate- and needle shaped magnetite micro-inclusions using the $\Delta \boldsymbol{g}$ method are described in Chapter 3 and 4, respectively.

1.7 Experimental Methods

1.7.1 Transmission electron microscopy

Transmission electron microscopy (TEM) applies a highly accelerated electron beam as the illumination source to travel through sufficiently thin specimens and to interact with the sample material in order to obtain high-resolution nano-scale structural, crystallographic orientation and chemical information of the specimens. The specimens for TEM analyses are usually less than 100 nm thick and require dedicated sample preparation. Common preparation methods in material sciences include ion etching, Ar ion milling and focused ion beam (FIB) technique (Williams and Carter, 1996). In the current study, we applied TEM to observe the internal structure of the magnetite micro-inclusions and the magnetite-plagioclase interface structure for selected types of plagioclase hosted magnetite micro-inclusions, in order to understand the mechanisms underlying the observed systematic SORs and CORs between the two phases as well as the formation conditions of the inclusions. The TEM specimens investigated in this study were first selected according to the identifications via light optical microscopy including universal stage and SEM based EBSD analyses in order to determine the most suitable magnetite micro-inclusions for TEM stud-

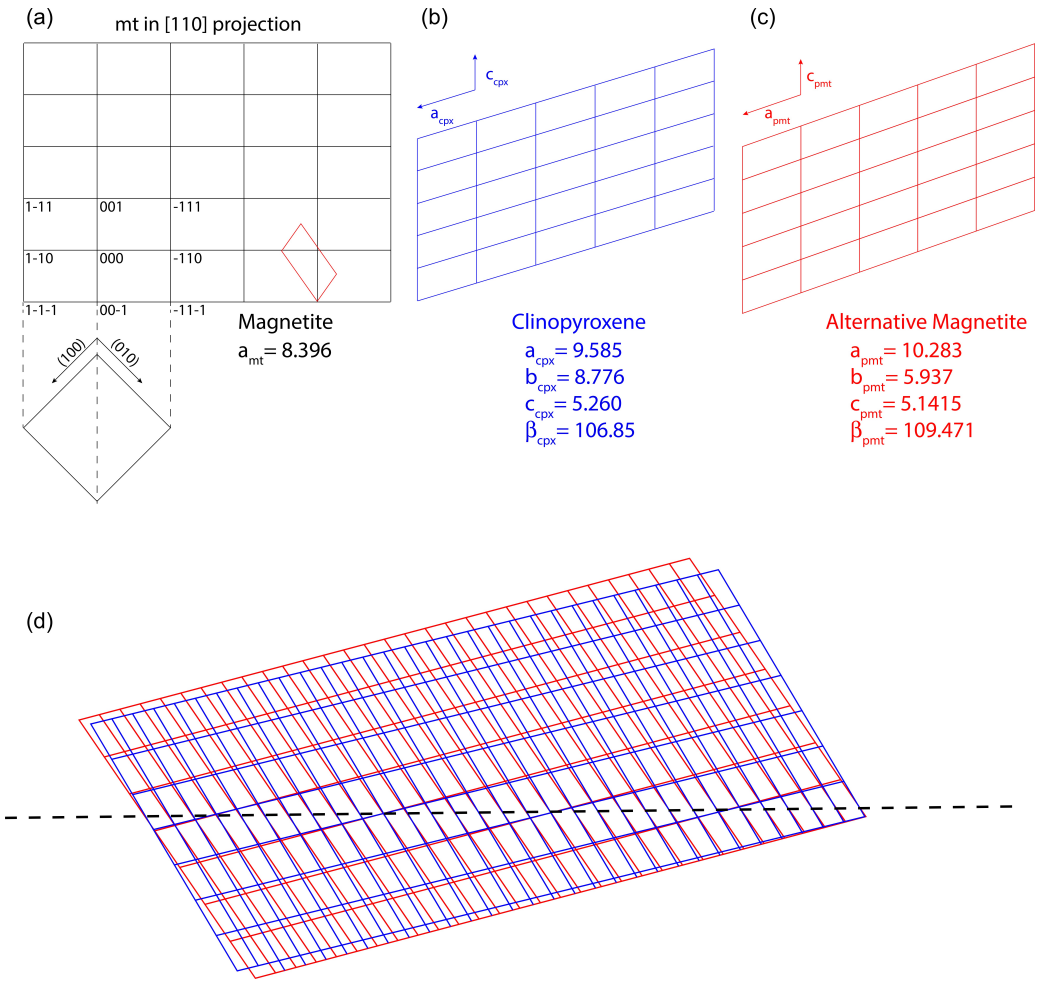

Figure 1.10: Sketch of construction of the exact phase boundary between magnetite (mt) and clinopyroxene (cpx). (a) Magnetite unit cell projected along mt[110]. Alternative magnetite unit cell is represented by the red parallelogram. (b) Multiplied clinopyroxene unit cells projected along cpx[010]. (c) Multiplied alternative magnetite unit cells obtained from (a). (d) Superimposed parallelograms of alternative magnetite (red) and clinopyroxene (blue) based on the orientation derived from the exact phase boundary model. The exact phase boundary intersects with all coincident points between the two sets of parallelograms and is indicated by the dashed line. Dimension of each unit cell is indicated therein. (Image courtesy of Rainer Abart)

ies. Then TEM specimens containing the selected inclusions were prepared using FIB technique in the Laboratory for scanning electron microscopy (SEM) and focused ion beam (FIB) applications, Faculty of Geosciences, Geography and Astronomy at the University of Vienna, Austria. Detailed descriptions of FIB operations can be found in each of the following chapters.

Two types of electrons are present after passing through the specimen, unscattered and scattered electrons. The unscattered electrons correspond to the central beam that carries morphological information, and the scattered electrons are diffracted due to interactions with the specimen material and carry detailed microstructural information (Williams and Carter, 1996). In the imaging mode, an objective aperture is applied to select only the central beam and to block the diffracted electrons in order to obtain a bright field (BF) image with enhanced contrast on the imaging plane. Another basic operation mode of TEM is the diffraction mode, where the imaging

plane is replaced by the back focal plane of the magnetic lens. With an inserted selected area aperture to constrain the area of interest on the specimen, a sharp diffraction pattern (DP) is generated for a crystalline specimen, which offers crystal symmetry and crystallographic orientation information. Both modes apply a parallel electron beam as the incident beam source to the specimen (Williams and Carter, 1996).

High-resolution (HR) TEM can provide atomic scale imaging. In conventional TEM, the amplitude contribution of the electron wave function is preserved during imaging while the phase contribution is lost. HR TEM enables a conversion of the phase contribution to the amplitude contribution in the exiting electron beam after passing through the specimen by tuning the aberrations of the electron optical system (Williams and Carter, 1996). As a result, the acquired HR TEM images are not directly interpretable due to the complex interactions between the electron wave and the sample material. In other words, the atomic columns observed in HR TEM images may not represent the precise locations of the actual atomic columns in the crystal structure. Thus, numerical simulations are required for comparison with experimental observations (Kirkland, 2011; Lopatin et al., 2020).

Conventional TEM imaging and selected area electron diffraction (SAED) analyses included in Chapter 2 were performed using a JOEL JEM-2100 TEM equipped with a LaB_6 electron source operated under 200 kV accelerating voltage. In addition, high-resolution (HR) TEM imaging was performed using a 200 kV FEG JOEL-2010F TEM with a point resolution of $\sim$ 0.19 nm, which provides atomic structure observations on selected magnetite micro-inclusions. A Si(Li) energy-dispersive X-ray spectrometer (TEM-EDS) integrated within JOEL-2010F was used for elemental analysis. Both TEM instruments were located at the Jožef Stefan Institute, Department of Nanostructured Materials in Ljubljana, Slovenia. (HR)TEM images post-processes were carried out by DigitalMicrograph^{TM} from Gatan Inc., USA.

1.7.2 Scanning transmission electron microscopy

In contrast to conventional TEM, which applies a parallel electron beam for imaging, scanning transmission electron microscopy (STEM) uses a convergent electron beam for scanning the specimen so that each point of the specimen interacts with the incident electron beam. STEM offers sub-Å resolutions imaging (Krivanek et al., 1999). Angular bright field (ABF) imaging allows for

imaging of light elements, such as oxygen (Okunishi et al., 2012). High angle annular dark field (HAADF) imaging can be directly interpreted because the contrast of the atomic columns in the image is directly proportional to the atomic number of the elements, i.e. a Z-contrast image (Nellist and Pennycook, 2000). The development of spherical aberration (Cs) corrector has improved the resolution of STEM drastically and enables single atom identifications, which is suitable for mineral crystal structure identifications, where unit cells are usually large with low symmetry and contain many atoms (Haider et al., 1998; Krivanek et al., 1999; Pennycook, 2017).

We have applied state-of-the-art STEM and investigated selected types of magnetite micro-inclusions hosted by plagioclase. In particular, we applied the relatively novel STEM technique, integrated differential phase contrast iDPC-STEM imaging. iDPC-STEM images are collected using a dedicated detector at the imaging plane, which records phase contributions in the electron wave function after interaction with sample material (Lazić et al., 2016). The images acquired from sufficiently thin specimens are directly interpretable as the projected electrostatic potential (Yücelen et al., 2018). iDPC-STEM can image light and heavy elements simultaneously at sub-Å resolution with low beam current, which is usually required for imaging of silicates, which are typically beam sensitive. The signal to noise ratio (SNR) of iDPC is superior to other phase contrast imaging techniques, such as annular dark field (ADF) imaging (Yücelen et al., 2018). HAADF and iDPC images are acquired simultaneously, which can be used as complementary information for determining crystal structures. Fig. 1.11 exemplarily shows the crystal structure of plagioclase captured by HAADF, ADF and iDPC-STEM detectors in our specimen. The plagioclase crystal structure model is superimposed at the top-left corner in each subfigure for comparison. The simulated images of plagioclase obtained using QSTEM software (Koch, 2002) are superimposed at the top-right corner of the corresponding experimental acquisitions. It can be seen that all images in Fig. 1.11 can be directly interpretable while the iDPC-STEM image contains more information than the other two images (Kirkland, 2011; Lopatin et al., 2020).

The STEM specimens investigated in this study were prepared using FIB technique. Standard STEM was performed on a Thermo Fisher Scientific Themis Z at University of Antwerp, in the frame of European Union's Horizon 2020 research and innovation programme under grant agreement No 823717 – ESTEEM3. The microscope is equipped with a X-FEG electron source and a monochromator. For imaging, the instrument was operated at 200 kV with a beam current of

5 pA for low-dose exposure. A convergence semi-angle of 20 mrad was used. The STEM results are presented in Chapter 3.

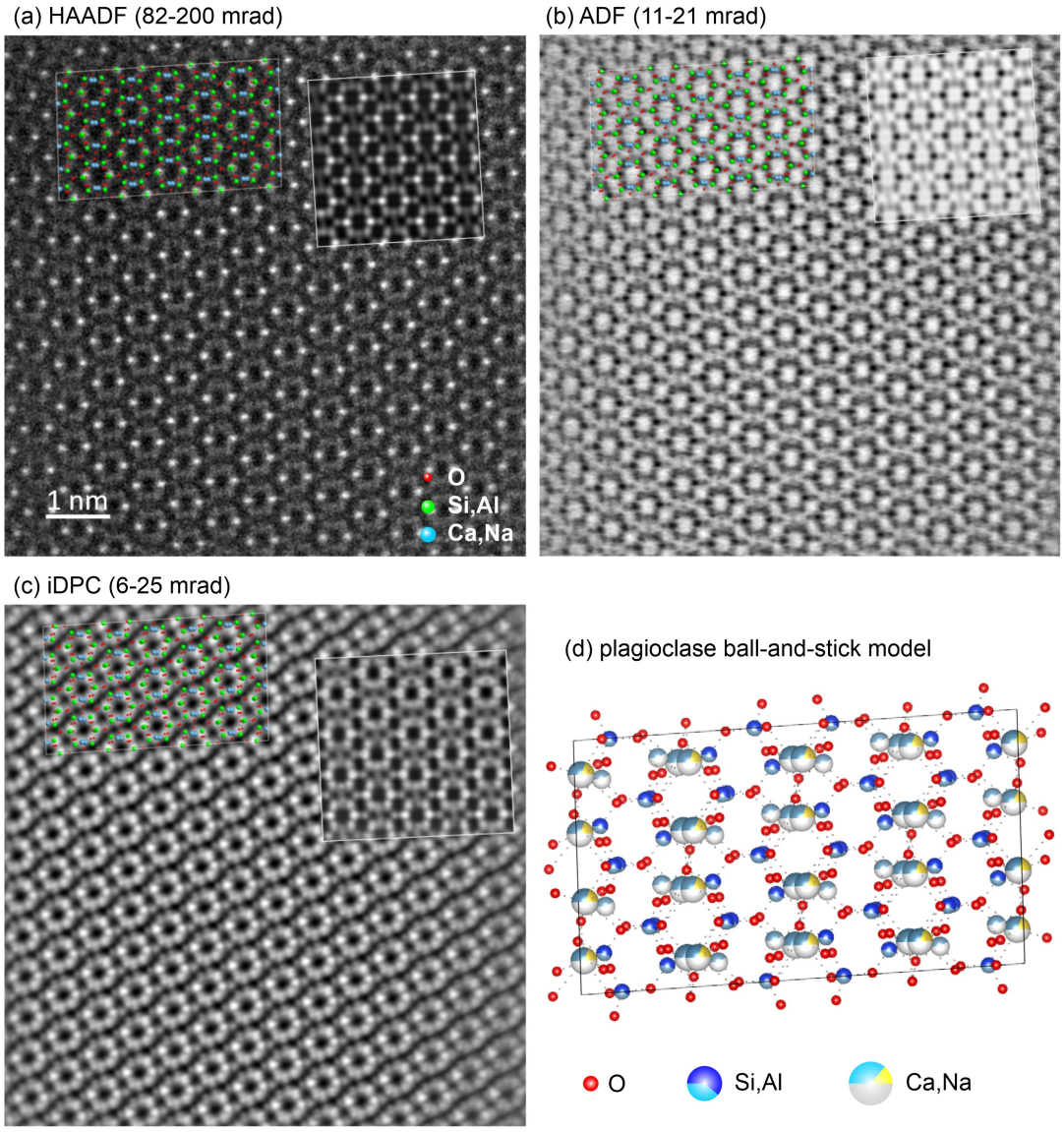

Figure 1.11: (a) High angle annular dark field (HAADF), (b) annular dark field (ADF) with collection angles 11-21 mrad, (c) integrated differential phase contrast (iDPC) with collection angles 6-25 mrad scanning electron transmission electron microscopy (STEM) of plagioclase along PL[001]. The crystal structure ball-and-stick model of plagioclase is superimposed at the top-left corner of each acquisition according to the atomic column correspondence. Elements and spheres correspondences in the ball-and-stick models are indicated at the bottom-right corner in (a). The corresponding simulated images are insets at the top-right corners. (d) Ball-and-stick model of plagioclase crystal structure oriented with respect to the orientation in (a-c). Elements and spheres correspondences in the ball-and-stick model are indicated underneath. Cations and anions are not shown in scale. Dashed lines represent bonds between atoms.

In order to obtain the best resolved crystal structures of plagioclase and magnetite, some of the specimens were further thinned using Ar ion milling at Deutsches GeoForschungsZentrum (GFZ), Potsdam Imaging and Spectral Analysis (PISA) facility. STEM imaging with an iDPC detector was performed at 300 kV with a 10 pA probe current on a Thermo Fisher Scientific Themis Z at the GFZ-

PISA facility. The microscope is equipped with a X-FEG electron source with a monochromator (energy resolution is < 0.3 eV) and a Cs S-CORR Probe Corrector (80-300 kV) that offers a space resolution < 0.06 nm at 300 kV. High resolution chemical analysis was performed with a SuperX energy dispersive X-ray spectroscopy (EDS) system installed on the Themis Z STEM in Potsdam. The iDPC-STEM imaging and chemical analyses are presented in Chapter 3 and 4.

1.8 Research Questions

In this doctoral study, we aim to answer the following research questions:

- What is the nature of oriented, needle- and lath shaped magnetite micro-inclusions in plagioclase from oceanic gabbro?

  The magnetite micro-inclusions in the plagioclase host are expected to have been titanomagnetite initially. As temperature decreased, the titanomagnetite exsolved into magnetite and ilmenite and/or ulvospinel and formed lamellar structures within the magnetite micro-inclusions. The microstructures and the CORs of the exsolved lamellae in the magnetite host bear information on the exsolution process and the conditions under which it occurred as well as on the conditions at which magnetite micro-inclusions precipitation from plagioclase. Therefore, the internal structures and chemical compositions of the magnetite micro-inclusions need to be examined. Due to their small sizes, (S)TEM and the integrated chemical analyses are the methods required for this purpose.

- What are the most likely formation pathways of the magnetite micro-inclusions in the plagioclase from oceanic gabbro?

  Since the needle- and lath shaped magnetite micro-inclusions hosted by silicates are excellent paleomagnetic recorders, it is essential to understand the origin of these inclusions including their formation conditions and formation processes. To answer this question, the morphology of the magnetite micro-inclusions needs to be examined. Chemical analyses are required on the plagioclase host. Moreover, one of the reasons why the magnetite micro-inclusions are of special interest for paleomagnetic studies is because they are protected by the silicate hosts from external alterations over geological times, which prevents them from recrystallization or alteration. However, external factors still show impacts on the

magnetite micro-inclusions. According to petrographic evidence, some magnetite micro-inclusions show potentially secondary features and therefore may represent different generations. The genesis of different generations of magnetite micro-inclusions is important in the context of the types of the NRM they record and for interpreting the NRM vectors they yield, i.e. if it is a primary or secondary paleomagnetic signal. Thus, examining the generations and clarifying the conditions when each generation of magnetite micro-inclusions was formed is necessary.

- What are the mechanisms underlying the systematic SORs and CORs between the magnetite micro-inclusions and the plagioclase host?

  In total, eight SORs and corresponding CORs between the magnetite micro-inclusions and the plagioclase host have been discerned from previous petrographic and crystallographic studies on samples from oceanic gabbro. The systematic orientation distributions of the needle- and lath shaped magnetite micro-inclusions contribute to the magnetic anisotropy of magnetite bearing plagioclase single grains. Such anisotropy may bias the NRM vectors obtained from single grain measurements and complicate the interpretation of the paleomagnetic signal. Thus, understanding the factors controlling the preferred elongation directions of magnetite micro-inclusions is essential for understanding and reconstructing the paleomagnetic record from magnetite bearing plagioclase single grains. This question relates to both the SORs and CORs between the two phases as the shape preference can be affected by the crystallographic correspondence and vice versa. In addition, when examining the SORs and the corresponding CORs of the magnetite micro-inclusions in the plagioclase host, each SOR class is found to have several CORs. Among these, some can be rationalized with lattice plane correspondences between the two phases, while others cannot be explained by the correspondence of rational indices of lattice planes from either phase. Potential COR transformations of the magnetite micro-inclusions are expected within one SOR class. Overall, the crystalline interfaces between the two phases are crucial for determining the controlling factors of the SORs and CORs, as well as for investigating potential transitions between CORs within a single SOR class. Therefore, the orientations and structures of the magnetite-plagioclase interfaces in different SOR and COR classes need to be studied via atomic scale STEM imaging.

- What are the magnetic properties of individual magnetite micro-inclusions in the plagioclase host?

  From optical microscopy, SEM, and STEM results, magnetite micro-inclusions are observed to contain ilmenite and/or ulvospinel lamellae with different morphologies. The compartmentalization of the volumetrically dominant magnetite induced by these paramagnetic phases may cause impact on the overall magnetic behavior of individual needle- and lath shaped magnetite inclusions. For instance, shape anisotropy arisen from the elongation of the magnetic inclusion may be affected by the effective length of a magnetite inclusion due to the presence of lamellae or inclusions of paramagnetic phases such as ilmenite and/or ulvospinel. Therefore, it is worth examining how strongly magnetic induction is affected by the presence of paramagnetic phases in the individual magnetite micro-inclusions. (This part of the study is still ongoing.)

1.9 Scientific Approach

In this study, we investigate the origin of magnetite micro-inclusions in rock forming plagioclase from oceanic gabbro that was dredged from mid-Atlantic ridge. The chemical compositions of the micro-inclusions and their internal microstructures that are related to the presence of ilmenite and /or ulvospinel within the magnetite micro-inclusions have been identified using STEM and conventional TEM.

Several generations of magnetite micro-inclusions in the plagioclase host have been discerned according to petrographic evidence. The formation pathways of the magnetite micro-inclusions in the plagioclase host have been discussed based on mass balance considerations. The formation temperatures of the magnetite micro-inclusions have been constrained according to petrographic evidence and the ilmenite and/or ulvospinel exsolutions in magnetite observed in (S)TEM.

The systematics of CORs and SORs of needle- and lath shaped magnetite micro-inclusions with respect to the plagioclase host have been determined from optical microscopy, universal stage and EBSD technique. The underlying mechanisms of the formation of the SORs and CORs have been discussed based on the combination of inclusions shape preferences, crystallographic orientation analysis, and atomic scale magnetite-plagioclase interface configurations.

Atomic scale magnetite-plagioclase interface structures have been investigated using state-of-the-art iDPC-STEM. Recurrent interface orientations have been rationalized using geometrical models based on experimental observations. The shape and crystallographic preferences of the magnetite micro-inclusions to the plagioclase host have been discussed in relation to the crystal structures of the two phases.

The reliability of the magnetic signals recorded by plagioclase hosted magnetite micro-inclusions has been justified according to the aforementioned aspects. Magnetic studies on individual magnetite micro-inclusions are ongoing. Electron holography has been applied to selected magnetite micro-inclusions to visualize magnetic induction maps of the remanence of the magnetite micro-inclusions after being exposed to external magnetic field. There we study the competition between shape and magnetocrystalline anisotropy within needle shaped magnetite micro-inclusions which are compartmentalized by the presence of ilmenite/ulvospinel lamellae. In addition, the response of magnetite micro-inclusions with and without ilmenite/ulvospinel lamellae to external fields in different directions is of interest.

Bibliography

A. Abedini, A. R. Daud, M. A. Abdul Hamid, and N. Kamil Othman. Radiolytic formation of fe3o4 nanoparticles: Influence of radiation dose on structure and magnetic properties. *PLOS ONE*, 9 (3):1–8, 03 2014. doi: 10.1371/journal.pone.0090055.

O. Ageeva, G. Habler, D. Topa, T. Waitz, C. Li, A. Pertsev, T. Griffiths, O. Zhilicheva, and R. Abart. Plagioclase hosted fe-ti-oxide micro-inclusions in an oceanic gabbro-plagiogranite association from the mid atlantic ridge at 13°34' n. *American Journal of Science*, 316(2):85–109, 2016. ISSN 0002-9599. doi: 10.2475/02.2016.01.

O. Ageeva, G. Habler, A. Pertsev, and R. Abart. Fe-Ti oxide micro-inclusions in clinopyroxene of oceanic gabbro: phase content, orientation relations and petrogenetic implication. *Lithos*, 290: 104–115, 2017. doi: 10.1016/j.lithos.2017.08.007.

O. Ageeva, G. Bian, G. Habler, A. Pertsev, and R. Abart. Crystallographic and shape orientations of magnetite micro-inclusions in plagioclase. *Contributions to Mineralogy and Petrology*, 175(10): 1–16, 2020. doi: 10.1007/s00410-020-01735-8.

O. Ageeva, G. Habler, S. A. Gilder, R. Schuster, A. Pertsev, O. Pilipenko, G. Bian, and R. Abart. Oriented magnetite inclusions in plagioclase: Implications for the anisotropy of magnetic remanence. *Geochemistry, Geophysics, Geosystems*, page e2021GC010272, 2022. doi: 10.1029/2021GC010272.

A. Aharoni. Elongated single-domain ferromagnetic particles. *Journal of Applied Physics*, 63(12): 5879–5882, 1988. doi: 10.1063/1.340280.

A. Aharoni. Magnetostatic energy calculations. *IEEE Transactions on Magnetics*, 27(4):3539–3547, 1991. doi: 10.1109/20.102925.

A. Aharoni et al. *Introduction to the Theory of Ferromagnetism*, volume 109. Clarendon Press, 2000.

U. Atxitia, D. Hinzke, and U. Nowak. Fundamentals and applications of the landau–lifshitz–bloch equation. *Journal of Physics D: Applied Physics*, 50(3):033003, dec 2016. doi: 10.1088/1361-6463/50/3/033003.

D. Baker, S. Kanekal, X. Li, S. Monk, J. Goldstein, and J. Burch. An extreme distortion of the van allen belt arising from the 'hallowe'en'solar storm in 2003. *Nature*, 432(7019):878–881, 2004. doi: 10.1038/nature03116.

S. K. Banerjee and B. M. Moskowitz. *Ferrimagnetic Properties of Magnetite*, pages 17–41. Springer US, Boston, MA, 1985. ISBN 978-1-4613-0313-8.

M. Blanc, R. Kallenbach, and N. Erkaev. Solar system magnetospheres. *Space Science Reviews*, 116 (1-2):227–298, 2005. doi: 10.1007/s11214-005-1958-y.

W. Bollmann. *Crystal defects and crystalline interfaces*. Springer Science & Business Media, 2012.

W. Bollmann and H.-U. Nissen. A study of optimal phase boundaries: the case of ex-solved alkali feldspars. *Acta Crystallographica Section A*, 24(5):546–557, Sep 1968. doi: 10.1107/S0567739468001178.

G. Borradaile and B. Henry. Tectonic applications of magnetic susceptibility and its anisotropy. *Earth-Science Reviews*, 42(1):49–93, 1997. ISSN 0012-8252. doi: https://doi.org/10.1016/S0012-8252(96)00044-X.

G. Breit. The magnetic moment of the electron. *Nature*, 122(3078):649–649, 1928. doi: 10.1038/122649a0.

A. F. Buddington and D. H. Lindsley. Iron-Titanium Oxide Minerals and Synthetic Equivalents. *Journal of Petrology*, 5(2):310–357, 06 1964. ISSN 0022-3530. doi: 10.1093/petrology/5.2.310.

B. A. Buffett. Earth's core and the geodynamo. *Science*, 288(5473):2007–2012, 2000. doi: 10.1126/science.288.5473.2007.

R. F. Butler and S. K. Banerjee. Theoretical single-domain grain size range in magnetite and titanomagnetite. *Journal of Geophysical Research (1896-1977)*, 80(29):4049–4058, 1975. doi: https://doi.org/10.1029/JB080i029p04049.

G. Catalan, J. Seidel, R. Ramesh, and J. F. Scott. Domain wall nanoelectronics. *Rev. Mod. Phys.*, 84:119–156, Feb 2012. doi: 10.1103/RevModPhys.84.119.

P. Champness. Nucleation and growth of iron oxides in olivines,(Mg, Fe) 2Sio4. *Mineralogical magazine*, 37(291):790–800, 1970. doi: 10.1180/minmag.1970.037.291.05.

W. Chen, S. Zhang, and H. N. Bertram. Energy barriers for thermal reversal of interacting single domain particles. *Journal of Applied Physics*, 71(11):5579–5584, 1992. doi: 10.1063/1.351376.

P. Coleman. On the verge of magnetism. *Nature*, 406(6796):580–581, 2000. doi: 10.1038/35020678.

T. F. Connolly and E. D. Copenhaver. *Bibliography of magnetic materials and tabulation of magnetic transition temperatures*, volume 180. Springer Science Business Media, 2012.

M. Darby and E. Isaac. Magnetocrystalline anisotropy of ferro- and ferrimagnetics. *IEEE Transactions on Magnetics*, 10(2):259–304, 1974. doi: 10.1109/TMAG.1974.1058331.

C. G. Darwin. The diamagnetism of the free electron. In *Mathematical Proceedings of the Cambridge Philosophical Society*, volume 27, pages 86–90. Cambridge University Press, 1931. doi: 10.1017/S0305004100009373.

S. Divljan. The results of field and laboratory studies of aventurine plagioclases from some norwegian pegmatites. In *In Proceedings of the 21st International Geological Congress, Norden*, pages 94–101, 1960.

S. Drev, M. Komelj, M. Mazaj, N. Daneu, and A. Rečnik. Structural investigation of (130) twins and rutile precipitates in chrysoberyl crystals from Rio das Pratinhas in Bahia (Brazil). *American Mineralogist*, 100(4):861–871, 04 2015. ISSN 0003-004X. doi: 10.2138/am-2015-5120.

D. J. Dunlop. Magnetite: Behavior near the single-domain threshold. *Science*, 176(4030):41–43, 1972. doi: 10.1126/science.176.4030.41.

D. J. Dunlop and Ö. Özdemir. *Rock magnetism: fundamentals and frontiers*. Number 3. Cambridge university press, 2001.

J. M. Feinberg, H.-R. Wenk, P. R. Renne, and G. R. Scott. Epitaxial relationships of clinopyroxene-hosted magnetite determined using electron backscatter diffraction (ebsd) technique. *American Mineralogist*, 89(2-3):462–466, 2004. doi: 10.2138/am-2004-2-328.

C. C. Finlay, S. Maus, C. Beggan, T. Bondar, A. Chambodut, T. Chernova, A. Chulliat, V. Golovkov, B. Hamilton, M. Hamoudi, et al. International geomagnetic reference field: the eleventh generation. *Geophysical Journal International*, 183(3):1216–1230, 2010.

M. Fleet, G. A. Bilcox, and R. L. Barnett. Oriented magnetite inclusions in pyroxenes from the Grenville Province. *The Canadian Mineralogist*, 18(1):89–99, 1980.

M. E. Fleet. The structure of magnetite. *Acta Crystallographica Section B*, 37(4):917–920, Apr 1981. doi: 10.1107/S0567740881004597.

M. D. Fuller. Magnetic anisotropy and paleomagnetism. *Journal of Geophysical Research (1896-1977)*, 68(1):293–309, 1963. doi: https://doi.org/10.1029/JZ068i001p00293.

D. A. Garanin. Fokker-planck and landau-lifshitz-bloch equations for classical ferromagnets. *Phys. Rev. B*, 55:3050–3057, Feb 1997. doi: 10.1103/PhysRevB.55.3050.

G. A. Glatzmaiers and P. H. Roberts. A three-dimensional self-consistent computer simulation of a geomagnetic field reversal. *Nature*, 377(6546):203–209, 1995. doi: 10.1038/377203a0.

M. Haider, H. Rose, S. Uhlemann, E. Schwan, B. Kabius, and K. Urban. A spherical-aberration-corrected 200kv transmission electron microscope. *Ultramicroscopy*, 75(1):53–60, 1998. ISSN 0304-3991. doi: https://doi.org/10.1016/S0304-3991(98)00048-5. URL `https://www.sciencedirect.com/science/article/pii/S0304399198000485`.

R. B. Hargraves. Magnetic anisotropy and remanent magnetism in hemo-ilmenite from ore deposits at allard lake, quebec. *Journal of Geophysical Research (1896-1977)*, 64(10):1565–1578, 1959. doi: https://doi.org/10.1029/JZ064i010p01565.

J. Heirtzler, G. Dickson, E. Herron, W. pitman III, and X. Le Pichon. Marine magnetic anomalies, geomagnetic field reversals, and motions of the ocean floor and continents. *Journal of Geophysical Research*, 73(6):2119–2136, 1968. doi: 10.1029/JB073i006p02119.

J. R. Heirtzler and X. Le Pichon. Crustal structure of the mid-ocean ridges: 3. magnetic anomalies over the mid-atlantic ridge. *Journal of Geophysical Research*, 70(16):4013–4033, 1965. doi: 10.1029/JZ070i016p04013.

A. Hubert and R. Schäfer. *Magnetic domains: the analysis of magnetic microstructures*. Springer Science & Business Media, 2008.

S.-L. Hwang, P. Shen, T.-F. Yui, and H.-T. Chu. On the coherency-controlled growth habit of precipitates in minerals. *Journal of Applied Crystallography*, 43(3):417–428, 2010. doi: 10.1107/S0021889810007454.

E. Irving. Palaeomagnetic and palaeoclimatological aspects of polar wandering. *Geofisica pura e applicata*, 33(1):23–41, 1956. doi: 10.1007/BF02629944.

H. W. Jaffe, P. Robinson, R. J. Tracy, and M. Ross. Orientation of Pigeonite Exsolution Lamellae in Metamorphic Augite: Correlation with Composition and Calculated Optimal Phase Boundaries. *American Mineralogist*, 60(1-2):9–28, 02 1975. ISSN 0003-004X.

D. Jiles. *Introduction to magnetism and magnetic materials*. CRC press, 2015.

M. T. Johnson, P. J. H. Bloemen, F. J. A. den Broeder, and J. J. de Vries. Magnetic anisotropy in metallic multilayers. *Reports on Progress in Physics*, 59(11):1409, nov 1996. doi: 10.1088/0034-4885/59/11/002.

D. S. Jones. *The theory of electromagnetism*. Elsevier, 2013.

T. H. Jordan. Structural geology of the earth's interior. *Proceedings of the National Academy of Sciences*, 76(9):4192–4200, 1979. doi: 10.1073/pnas.76.9.4192.

E. J. Kirkland. On the optimum probe in aberration corrected adf-stem. *Ultramicroscopy*, 111(11): 1523–1530, 2011. ISSN 0304-3991. doi: https://doi.org/10.1016/j.ultramic.2011.09.002.

C. Kittel and J. Galt. Ferromagnetic domain theory. volume 3 of *Solid State Physics*, pages 437–564. Academic Press, 1956. doi: https://doi.org/10.1016/S0081-1947(08)60136-8.

K. Kobayashi. Chemical remanent magnetization of ferromagnetic minerals and its application to rock magnetism. *Journal of geomagnetism and geoelectricity*, 10(3):99–117, 1959. doi: 10.5636/jgg.10.99.

C. T. Koch. *Determination of core structure periodicity and point defect density along dislocations*. Arizona State University, 2002.

O. Krivanek, N. Dellby, and A. Lupini. Towards sub-Å electron beams. *Ultramicroscopy*, 78(1): 1–11, 1999. ISSN 0304-3991. doi: https://doi.org/10.1016/S0304-3991(99)00013-3.

R. Lanza and A. Meloni. *The Earth's magnetism*, volume 280. Springer, 2006.

G. Laval, C. Mercier, and R. Pellat. Necessity of the energy principles for magnetostatic stability. *Nuclear Fusion*, 5(2):156, jun 1965. doi: 10.1088/0029-5515/5/2/007.

I. Lazić, E. G. Bosch, and S. Lazar. Phase contrast stem for thin samples: Integrated differential phase contrast. *Ultramicroscopy*, 160:265–280, 2016. ISSN 0304-3991. doi: https://doi.org/10.1016/j.ultramic.2015.10.011.

S. Lopatin, A. Aljarb, V. Roddatis, T. Meyer, Y. Wan, J.-H. Fu, M. Hedhili, Y. Han, L.-J. Li, and V. Tung. Aberration-corrected stem imaging of 2d materials: Artifacts and practical applications of threefold astigmatism. *Science Advances*, 6(37):eabb8431, 2020. doi: 10.1126/sciadv.abb8431.

W. Lowrie. Viscous remanent magnetization in oceanic basalts. *Nature*, 243(5401):27–29, 1973. doi: 10.1038/243027a0.

J. McClure. Diamagnetism of graphite. *Physical Review*, 104(3):666, 1956. doi: 10.1103/PhysRev.104.666.

M. McElhinny and W. Senanayake. Paleomagnetic evidence for the existence of the geomagnetic field 3.5 ga ago. *Journal of Geophysical Research: Solid Earth*, 85(B7):3523–3528, 1980. doi: 10.1029/JB085iB07p03523.

M. W. McElhinny and P. L. McFadden. *Paleomagnetism: continents and oceans*. Elsevier, 1999.

G. S. Murthy, M. E. Evans, and D. I. Gough. Evidence of single-domain magnetite in the michikamau anorthosite. *Canadian Journal of Earth Sciences*, 8(3):361–370, 1971. doi: 10.1139/e71-036.

L. Néel. Magnetic properties of ferrites: ferrimagnetism and antiferromagnetism. *Physical Chemical & Earth Sciences*, (31):18, 1984.

P. Nellist and S. Pennycook. The principles and interpretation of annular dark-field z-contrast imaging. volume 113 of *Advances in Imaging and Electron Physics*, pages 147–203. Elsevier, 2000. doi: https://doi.org/10.1016/S1076-5670(00)80013-0.

H. Neumann and O. Christie. Observations on plagioclase aventurines from southern norway. *Nor Geol Tidsskr*, 42:389–393, 1962.

E. S. Nikolaisen, R. Harrison, K. Fabian, N. Church, S. A. McEnroe, B. E. Sørensen, and C. Tegner. Hysteresis parameters and magnetic anisotropy of silicate-hosted magnetite exsolutions. *Geophysical Journal International*, 229(3):1695–1717, 2022. doi: 10.1093/gji/ggac007.

E. Okunishi, H. Sawada, and Y. Kondo. Experimental study of annular bright field (abf) imaging using aberration-corrected scanning transmission electron microscopy (stem). *Micron*, 43 (4):538–544, 2012. ISSN 0968-4328. doi: https://doi.org/10.1016/j.micron.2011.10.007. Advancing HR-TEM and HR-STEM.

G. Parigi, E. Ravera, and C. Luchinat. Magnetic susceptibility and paramagnetism-based nmr. *Progress in nuclear magnetic resonance spectroscopy*, 114:211–236, 2019. doi: 10.1016/j.pnmrs.2019.06.003.

S. J. Pennycook. The impact of stem aberration correction on materials science. *Ultramicroscopy*, 180:22–33, 2017. ISSN 0304-3991. doi: https://doi.org/10.1016/j.ultramic.2017.03.020. URL `https://www.sciencedirect.com/science/article/pii/S0304399117301213`. Ondrej Krivanek: A research life in EELS and aberration corrected STEM.

M. J. Pinto and M. McWilliams. Drilling-induced isothermal remanent magnetization. *Geophysics*, 55(1):111–115, 1990. doi: 10.1190/1.1442765.

A. Poldervaart and A. K. Gilkey. On clouded plagioclase. *American Mineralogist*, 39(1-2):75–91, 02 1954. ISSN 0003-004X.

G. D. Price. Subsolidus phase relations in the titanomagnetite solid solution series. *American Mineralogist*, 66(7-8):751–758, 08 1981. ISSN 0003-004X.

A. Putnis. *An introduction to mineral sciences*. Cambridge University Press, 1992.

J. A. Ratcliffe. *An introduction to ionosphere and magnetosphere*. CUP Archive, 1972.

R. Readman. Magnetic properties of ulvöspinel. *Physics of the Earth and Planetary Interiors*, 16 (3):196–199, 1978. ISSN 0031-9201. doi: https://doi.org/10.1016/0031-9201(78)90011-0.

V. Reichel, A. Kovács, M. Kumari, E. Bereczk-Tompa, E. Schneck, P. Diehle, M. Pósfai, A. Hirt, M. Duchamp, D.-B. R.E., and F. D. Single crystalline superstructured stable single domain magnetite nanoparticles. *Scientific Reports*, 7(45484), 2017. doi: 10.1038/srep45484.

P. R. Renne, G. R. Scott, J. M. Glen, and J. M. Feinberg. Oriented inclusions of magnetite in clinopyroxene: Source of stable remanent magnetization in gabbros of the Messum Complex, Namibia. *Geochemistry, Geophysics, Geosystems*, 3(12):1–11, 2002. doi: 10.1029/2002GC000319.

P. Robinson, H. W. Jaffe, M. Ross, and C. Klein Jr. Orientation of exsolution lamellae in clinopyroxenes and clinoamphiboles: consideration of optimal phase boundaries. *American Mineralogist: Journal of Earth and Planetary Materials*, 56(5-6):909–939, 1971.

P. Robinson, M. Ross, G. Nord, J. Smyth, and H. Jaffe. Exsolution lamellae in augite and pigeonite; fossil indicators of lattice parameters at high temperature and pressure. *American Mineralogist*, 62(9-10):857–873, 1977.

P. Rochette, M. Jackson, and C. Aubourg. Rock magnetism and the interpretation of anisotropy of magnetic susceptibility. *Reviews of Geophysics*, 30(3):209–226, 1992. doi: https://doi.org/10.1029/92RG00733.

J. Rogers, J. Fox, and M. Aitken. Magnetic anisotropy in ancient pottery. *Nature*, 277:644–646, 1979. doi: 10.1038/277644a0.

J. F. Schenck. The role of magnetic susceptibility in magnetic resonance imaging: Mri magnetic compatibility of the first and second kinds. *Medical physics*, 23(6):815–850, 1996. doi: 10.1118/1.597854.

A. Singh, D. Siingh, and R. Singh. Impact of galactic cosmic rays on earth's atmosphere and human health. *Atmospheric Environment*, 45(23):3806–3818, 2011. doi: 10.1016/j.atmosenv.2011.04.027.

J. S. Smart. The néel theory of ferrimagnetism. *American Journal of Physics*, 23(6):356–370, 1955. doi: 10.1119/1.1934006.

P. Sobolev. Orientation of acicular iron-ore mineral inclusions in plagioclase. *International Geology Review*, 32(6):616–628, 1990.

D. D. Stancil. *Theory of magnetostatic waves*. Springer Science Business Media, 2012.

A. Sutton and R. Balluffi. *Interfaces in Crystalline Materials*. Clarendon Press, Oxford, 1995.

W. Tan, P. Liu, H. He, C. Y. Wang, and X. Liang. Mineralogy and Origin of Exsolution in Ti-rich Magnetite from Different Magmatic Fe-ti Oxide-bearing Intrusions. *The Canadian Mineralogist*, 54(3):539–553, 05 2016. ISSN 0008-4476. doi: 10.3749/canmin.1400069.

D. Tarling and F. Hrouda. *Magnetic anisotropy of rocks*. Springer Science & Business Media, 1993.

Y. Usui, J. A. Tarduno, M. Watkeys, A. Hofmann, and R. D. Cottrell. Evidence for a 3.45-billion-year-old magnetic remanence: Hints of an ancient geodynamo from conglomerates of south africa. *Geochemistry, Geophysics, Geosystems*, 10(9), 2009. doi: 10.1029/2009GC002496.

Y. Usui, T. Shibuya, Y. Sawaki, and T. Komiya. Rock magnetism of tiny exsolved magnetite in plagioclase from a paleoarchean granitoid in the pilbara craton. *Geochemistry, Geophysics, Geosystems*, 16(1):112–125, 2015. doi: https://doi.org/10.1002/2014GC005508.

K. L. Verosub. Depositional and postdepositional processes in the magnetization of sediments. *Reviews of Geophysics*, 15(2):129–143, 1977. doi: 10.1029/RG015i002p00129.

V. Verrier and P. Rochette. Estimating peak currents at ground lightning impacts using remanent magnetization. *Geophysical Research Letters*, 29(18):14–1, 2002. doi: 10.1029/2002GL015207.

F. J. Vine. Spreading of the ocean floor: New evidence: Magnetic anomalies may record histories of the ocean basins and earth's magnetic field for 2×10^8 years. *Science*, 154(3755):1405–1415, 1966. doi: 10.1126/science.154.3755.1405.

P. J. Wasilewski. Magnetic hysteresis in natural materials. *Earth and Planetary Science Letters*, 20 (1):67–72, 1973. ISSN 0012-821X. doi: https://doi.org/10.1016/0012-821X(73)90140-4.

A. Wegener. *The origin of continents and oceans*. Courier Corporation, 1966.

H.-R. Wenk, K. Chen, and R. Smith. Morphology and microstructure of magnetite and ilmenite inclusions in plagioclase from Adirondack anorthositic gneiss. *American Mineralogist*, 96(8-9): 1316–1324, 08 2011. ISSN 0003-004X. doi: 10.2138/am.2011.3760.

D. B. Williams and C. B. Carter. *The transmission electron microscope*. Springer, Boston, MA., 1996. doi: 10.1007/978-1-4757-2519-3.

R. Wiltschko. *Magnetic orientation in animals*, volume 33. Springer Science & Business Media, 2012.

E. P. Wohlfarth. Relations between different modes of acquisition of the remanent magnetization of ferromagnetic particles. *Journal of Applied Physics*, 29(3):595–596, 1958. doi: 10.1063/1.1723232.

E. Yücelen, I. Lazić, and E. Bosch. Phase contrast scanning transmission electron microscopy imaging of light and heavy atoms at the limit of contrast and resolution. *Scientific Report*, 8: 2676, 2018. doi: https://doi.org/10.1038/s41598-018-20377-2.

W.-Z. Zhang. Reproducible orientation relationships developed from phase transformations—role of interfaces. *Crystals*, 10(11):1042, 2020. doi: 10.3390/cryst10111042.

W.-Z. Zhang and G. Weatherly. On the crystallography of precipitation. *Progress in materials science*, 50(2):181–292, 2005. doi: 10.1016/j.pmatsci.2004.04.002.

Z. Zhang and S. Satpathy. Electron states, magnetism, and the verwey transition in magnetite. *Phys. Rev. B*, 44:13319–13331, Dec 1991. doi: 10.1103/PhysRevB.44.13319.

Özdemir and D. Dunlop. Thermoremanence and néel temperature of goethite. *Geophysical Research Letters*, 23(9):921–924, 1996. doi: 10.1029/96GL00904.

Chapter 2

Formation pathways of oriented magnetite micro-inclusions in plagioclase from oceanic gabbro

Ge Bian[1,*], Olga Ageeva[1,2], Aleksander Rečnik[3], Gerlinde Habler[1], Rainer Abart[1]
* Corresponding author

1. Department of Lithospheric Research, University of Vienna
2. Institute of Geology of Ore Deposit, Petrography, Mineralogy, and Geochemistry, Russian Academy of Sciences (IGEM, RAS)
3. Department of Nanostructured Materials, Jožef Stefan Institute

Manuscript status: released publication

Contributions to Mineralogy and Petrology 2021, 176:104 https://doi.org/10.1007/s00410-021-01864-8

Received: 12 July 2021 / Accepted: 4 November 2021 / Published online: 22 November 2021

Submitter's own contribution:

In this study, I have performed TEM data collections, achieved TEM results analyses and interpretations, carried out electron probe microanalysis (EPMA) results analyses and applied crystallographic orientation analyses and mass balance considerations for inclusion genesis discussions. I have prepared the first draft of this manuscript.

Abstract

Plagioclase hosted needle- and lath-shaped magnetite micro-inclusions from oceanic gabbro dredged at the mid-Atlantic ridge at 13° 01–02' N, 44° 52' W were investigated to constrain their formation pathway. Their genesis is discussed in the light of petrography, mineral chemistry, and new data from transmission electron microscopy (TEM). The magnetite micro-inclusions show systematic crystallographic and shape orientation relationships with the plagioclase host. Direct TEM observation and selected area electron diffraction (SAED) confirm that the systematic orientation relations are due to the alignment of important oxygen layers between the magnetite micro-inclusions and the plagioclase host, a hypothesis made earlier based on electron backscatter diffraction data. Precipitation from Fe-bearing plagioclase, which became supersaturated with respect to magnetite due to interaction with a reducing fluid, is inferred to be the most likely formation pathway. This process probably occurred without the supply of Fe from an external source but required the out-diffusion of oxygen from the plagioclase to facilitate partial reduction of the ferric iron originally contained in the plagioclase. The magnetite micro-inclusions contain oriented lamellae of ilmenite, the abundance, shape and size of which indicate high-temperature exsolution from Ti-rich magnetite constraining the precipitation of the magnetite micro-inclusions to temperatures in excess of $\sim$ 600 °C. This is above the Curie temperature of magnetite, and the magnetic signature of the magnetite-bearing plagioclase grains must, therefore, be considered as the thermoremanent magnetization.

Keywords

Oriented plagioclase-hosted magnetite micro-inclusions · Correlated optical and electron microscopy · Crystallographic and shape orientation relationships · Exsolution

2.1 Introduction

Magnetite (MT) is the most important carrier of the natural remanent magnetization (NRM) of rocks. In igneous and metamorphic rocks, magnetite may be present as individual grains in the rock matrix, or, alternatively, it may occur in the form of μm to sub-μm sized usually oriented inclusions hosted by rock-forming silicate phases such as olivine, pyroxene, amphibole and feldspar (Fleet et al., 1980; Davis, 1981; Dunlop and Özdemir, 2001; Renne et al., 2002; Lappe et al., 2011; Usui et al., 2015; Knafelc et al., 2019). Oriented needle- and lath-shaped magnetite micro-inclusions are common in plagioclase (PL) and pyroxene (PX) from mafic intrusions and were described from the Skaergaard intrusion (Wager and Mitchell, 1951),

the Stillwater Igneous Complex (Montana, USA) (Selkin et al., 2014), the Jurassic Dufek (Cheadle and Gee, 2017), Bushveld layered intrusion (Feinberg et al., 2006) and from oceanic gabbro (Kent et al., 1978; Davis, 1981). Due to their peculiar magnetic properties, silicate-hosted magnetite micro-inclusions are of particular interest in paleomagnetic research (Chang et al., 2016; Biedermann et al., 2020). Their small size typically leads to single domain or pseudo-single domain magnetic behavior, which results in extraordinarily stable magnetization (Dunlop, 1981; Feinberg et al., 2005; Tarduno et al., 2006, 2020).

The crystallographic orientation relationships (CORs) and shape orientation relationships (SORs) between magnetite micro-inclusions and plagioclase host crystals have been rationalized earlier. Six frequently observed as well as two less common orientation classes of magnetite microinclusions in plagioclase host have been discerned (Sobolev, 1990; Wenk et al., 2011; Ageeva et al., 2016, 2020). While the CORs and SORs between the magnetite micro-inclusions and the plagioclase host are well documented (Ageeva et al., 2020), the formation pathways of plagioclase-hosted magnetite micro-inclusions have not been fully revealed yet. Knowing the formation conditions of these inclusions is of pivotal importance for paleomagnetic reconstructions. In particular, the temperature at which they were formed decides on whether their magnetic memory is based on thermal or chemical remanence and whether they record the magnetic field during the high-temperature stage of the rocks or during an intermediate or low-temperature hydrothermal stage.

In this communication, we explore the origin of magnetite micro-inclusions in rock-forming plagioclase from an oceanic gabbro that was dredged at the mid-Atlantic ridge. We employed correlated optical microscopy including universal stage, scanning electron microscopy (SEM), electron probe microanalysis (EPMA), and transmission electron microscopy (TEM). In particular, high-resolution TEM imaging and selected area electron diffraction (SAED) were used to test the hypothesis on the CORs and the SORs between the magnetite micro-inclusions and the plagioclase host that have previously been put forward based on electron backscatter diffraction crystal orientation data (Ageeva et al., 2016, 2020). The combined evidence is used to construct a genetic model for the plagioclase-hosted magnetite microinclusions, and the implications for paleomagnetic reconstructions are discussed.

2.2 Samples and geological background

The material under study is taken from an oceanic gabbro dredged at the mid-Atlantic ridge. In this gabbro, the rock forming plagioclase shows abundant needle- or lath-shaped magnetite micro-inclusions. This feature is observed in all plagioclase grains of the gabbro and it is also common in plagioclase from gabbroic rocks from other sampling localities along the mid-Atlantic ridge at 11° N, 43° W to 17° N, 45° W (Ageeva

et al., 2016). Out of a series of gabbro specimen showing similar petrographic characteristics, specimen L30-277-7 from dredge line 30L 277 at the western flank of the rift valley at 13° 01-02' N, 43° 53' W in the course of the 30-th cruise of R/V "Professor Logachev" (2007) was selected as a representative sample. The gabbro pertains to a gabbro-peridotite association comprising peridotite-hosted gabbroic intrusions, which crop out in the footwall of a lowangle large-offset detachment fault, a structure that is typical for slow-spreading ridges (Smith et al., 2008; Silantyev et al., 2011; Ondréas et al., 2012; Peirce et al., 2019, 2020). The studied rock is a medium-grained gabbronorite consisting of plagioclase ($\sim$ 60 vol%), ortho- and clinopyroxene ($\sim$ 30 vol%), amphibole ($\sim$ 10 vol%) and minor Fe, Ti oxides ($\leq$ 0.5 vol%). The bulk rock compositions of gabbro specimen from the mid-Atlantic ridge at 13° N to 13.5° N, 45° W are given in Table S2.1 of the supplementary material. The plagioclase has labradorite composition (mineral chemical analyses of plagioclase, orthopyroxene and clinopyroxene are presented in the supplementary material). It is hypidiomorphic and forms tabular and rarely subhedral 0.5–5-mm-sized grains. Based on its microstructural relations to pyroxene (see supplementary material, Fig. S2.1), plagioclase is inferred to have crystallized relatively early in the crystallization sequence, which is in line with the expected crystallization sequence of tholeiitic melt at the low pressures prevailing in a mid-ocean ridge environment (Grove and Baker, 1984; Grove et al., 1992; Ariskin and Barmina, 2004; Villiger et al., 2007; Suhr et al., 2008). The rocks analyzed by these latter authors compare well with the rocks under study, corroborating that plagioclase was the earliest phase to crystallize from the melt. Orthopyroxenes (En62-63Wo3-5, X_{Mg} = 65–66) and clinopyroxenes (En39-42Wo41-48, X_{Mg} = 73–76) occur as prismatic and subhedral grains 3–5 mm in size with a dense cleavage network and with clinopyroxene lamellae in orthopyroxene and vice versa. Clinopyroxene contains needle-shaped magnetite micro-inclusions and ilmenite plates (≤ 5 μm thick). Rare magnesiohornblende ($X_{Mg} = 74$) locally replaces clinopyroxene. Fe–Ti oxides are present as up to 1-mm-sized grains of magnetite, ilmenite, and exsolved titanomagnetite, that typically occupy interstitial positions in the rock matrix. Locally, pyroxene is replaced by actinolite indicating hydrothermal alteration at a relatively low temperature.

2.3 Analytical methods

2.3.1 Optical microscopy

A Leica DM4500 P optical microscope equipped with a Zeiss Axiocam 208 Colour camera was applied for polarization microscopy. The plagioclase-hosted magnetite micro-inclusions including their shape orientation relationships to the plagioclase host were observed under plane-polarized light. In cross-polarized

light, plagioclase twinning and the respective twin boundaries could be identified and related to the distribution of the magnetite micro-inclusions.

2.3.2 Electron probe microanalysis

A Cameca SXFiveFe electron probe micro-analyzer (FEG-EPMA), located at the Department of Lithospheric Research, University of Vienna (Austria), was used for mineral chemical analysis. The instrument is equipped with a FEG Schottky type field-emission gun electron source and with five crystal spectrometers for wavelength dispersive elemental analysis. The instrument was operated with an accelerating voltage of 20 kV and a probe current of 8 nA. For routine point analyses of plagioclase, the beam was defocused to 5 μm to minimize Na-loss. For the analysis of line profiles, a 20 μm defocused beam was used to integrate over plagioclase and magnetite micro-inclusions. For quantitative analysis, the instrument was calibrated against well-characterized mineral standards, and the Phi-Rho-Z routine was employed for matrix correction.

2.3.3 Scanning electron microscopy and focused ion beam application

An FEI Quanta 3D FEG-SEM at the Faculty of Earth Sciences, Geography and Astronomy, University of Vienna (Austria) was used for secondary electron (SE) imaging and focused ion beam (FIB) preparation of specimens for investigation by TEM. The FIB-SEM is equipped with a Schottky type field-emission gun electron source, a liquid metal Gaion source gas injection system for Pt- and C deposition, and an Omniprobe 100.7 micromanipulator for in situ lift-out. SE imaging and TEM specimen extraction were applied to a chemo-mechanically polished carbon-coated thin section. SE images were collected at 15 kV accelerating voltage and 4 nA probe current. During imaging, the sample was at 14.5 mm working distance at the image center of the tilted sample.

Applying the FIB technique, two site- and orientation specific, about 50 nm thin 5 μm by 10-μm-sized lamellae were extracted. The foils contain needle-shaped PL(112)n-MT and PL(150)n-MT micro-inclusions located near Albite twin boundaries of the plagioclase host, where PL(*hkl*)n-MT denotes a magnetite micro-inclusion with its elongation direction parallel to the PL(*hkl*) plane normal. The FIB sections were oriented so that the elongation direction of the magnetite micro-inclusion is sub-parallel to the plane of the TEM foil, and the magnetite–plagioclase interfaces are perpendicular to the latter. During FIB preparation, the sputtering or deposition progress was monitored using electron beam (EB) induced SE imaging. The electron beam conditions were set to 10 kV accelerating voltage and 0.13 nA probe current, and FIB induced SE imaging was done at FIB settings of 30 kV accelerating voltage and 10 pA to 1 nA probe current.

Platinum-deposition was applied to generate a protecting and supporting layer before specimen extraction, and to attach the TEM specimen first to the tungsten micromanipulator needle tip and finally to a Cu lift-out grid. During the Pt deposition steps, the FIB settings were at 30 kV accelerating voltage and 0.1–0.3 nA, whereas during foil extraction the FIB probe current was successively lowered from 50 to 3 nA or 1 nA. The about 2-μm-thick lamellae were transferred to the Cu grid by in situ lift-out.

Subsequently, final thinning was performed at FIB settings of 30 kV accelerating voltage and successively decreasing ion probe current of 1 nA to 0.01 nA. Finally, a FIB cleaning step was applied to the surface planes of the finally thinned TEM specimen using a FIB accelerating voltage of 5 kV and a FIB probe current of 48 pA. For both TEM specimen, the final foil thickness close to the Pt layer was at 50–60 nm, whereas local parts of the foil adjacent to a perforation were thinner.

2.3.4 Transmission electron microscopy and energy-dispersive X-ray spectroscopy

A JOEL JEM-2100 TEM equipped with a LaB_6 electron source operated under 200 kV accelerating voltage was used for conventional TEM imaging and for selected area electron diffraction (SAED) experiments. High-resolution (HR) TEM imaging was done using a 200 kV FEG JOEL-2010F TEM with a point resolution of $\sim$ 0.19 nm, which allows for atomic structure observations. Both TEM instruments are located at the Jožef Stefan Institute, Department of Nanostructured Materials in Ljubljana, Slovenia. An analytical double-tilt sample holder with a tilt range of $\pm$ 15° in both α and β axes was used for precise alignments into specific zone axes. Since plagioclase has a rather complex crystal structure, the strategy for finding the desired zone axes was to refer to the zone axes of the embedded magnetite micro-inclusions. To obtain the proper CORs among individual phases, SAED patterns were recorded in two projections. SAED patterns from plagioclase were acquired with low excitation of condenser C1 lens separately from magnetite and the other phases due to the severe sensitivity to electron irradiation and consequent bending of the FIB foil. During HRTEM imaging, plagioclase became amorphous under high electron currents due to its extreme beam sensitivity. A Si(Li) energy-dispersive X-ray spectrometer (TEM-EDS) integrated within JOEL-2010F was used for elemental analysis. (HR)TEM images were processed and analyzed using DigitalMicrograph^{TM} from Gatan Inc., USA.

2.4 Results

2.4.1 Chemical composition of plagioclase

The anorthite content of the plagioclase varies from An58-51 in big, ≥ 4-mm-sized grains to An53-50 in medium-sized grains to An52-48 in small, ≤ 0.5-mm-sized grains. The lowest anorthite contents are An46, which are observed along healed cracks. Large, several mm-sized plagioclase grains are characterized by cloudy domains with grey stain in the grain interiors and by several hundred microns wide clear rims (Fig. 2.1a). The optical zoning is accompanied by chemical zoning with a continuous decrease of the anorthite content from An58 in the core to An51 in the rim. A profile of EPMA point analyses taken with a 20 μm

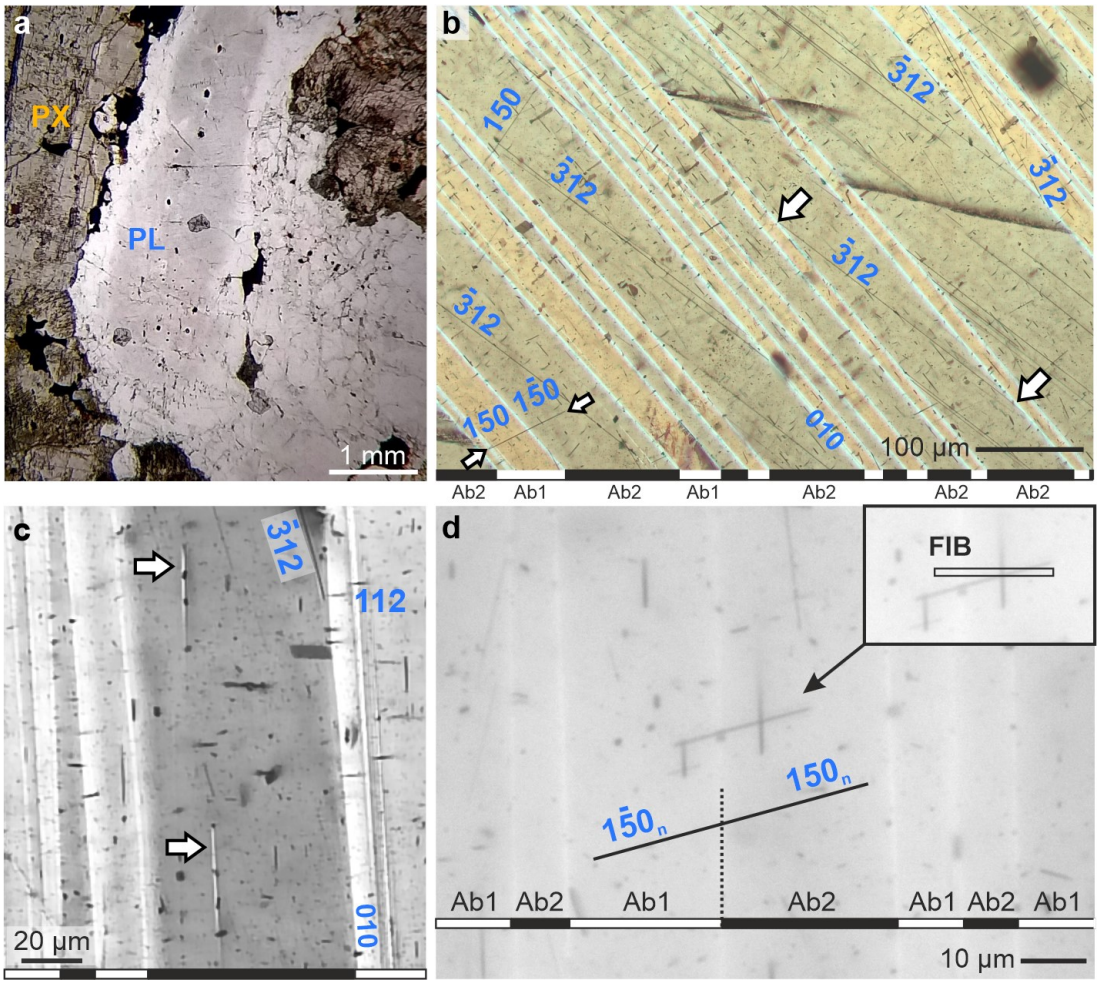

Figure 2.1: Transmitted light images, **a**, **d** plane-polarized light, **b**, **c** crossed polarizers, of plagioclase. **a** Several mm-sized plagioclase grain with clouded core region and 100–200-μm-wide clear rim. **b** Albite twinned plagioclase grain with magnetite micro-inclusions; arrows on the right show a PL($\bar{3}$12)n-MT inclusion ending at Albite twin boundaries; arrows on the lower left show a PL(150)n-MT inclusion traversing an Albite twin boundary. **c** Domain of plagioclase with typical PL(112)n-MT inclusions, which appear short because they are oriented sub-perpendicular to the specimen surface, as well as PL($\bar{3}$12)n-MT which are sub-parallel to the specimen surface. The white arrows show small, lens-shaped Albite twin individuals with abundant isometric magnetite micro-inclusions. The magnetite needles that are oriented parallel to the twin boundaries are PL[001]-MT and PL(100)n-MT type needles (not labeled). **d** PL(150)n-MT inclusion traversing a twin boundary before extraction of a TEM foil (see Fig. 2.7). The trace of the TEM foil on the specimen surface is shown in the insert. The magnetite needle crossing the PL(150)n-MT inclusion shown in the insert is of PL[001]-MT type.

defocused beam and a step size of 15 μm from the cloudy core into the clear rim is shown in Fig. 2.2. With the chosen analytical setting, each analysis averages over the plagioclase host and the abundant magnetite inclusions, and a nearly continuous coverage of the locally integrated compositions along the profile is obtained. It is seen that the total Fe content is more variable and generally higher in the cloudy core region, where it varies between 0.3 and 0.7 wt% FeO_T, than in the clear rim, where FeO_T is in the range of 0.25–0.3 wt%. The comparatively high variability of the FeO_T content in the core region is probably due to the effect of individual magnetite inclusions, which could not be eliminated completely through application of the defocused beam. On average, the FeO_T in the cloudy core region is estimated to be about 0.45 wt%, whereas it is only about 0.25 wt% in the clear rims. Measurements with a beam focused to 5 μm produced more variable iron contents but the concentrations of FeO_T were never below 0.25 wt%. This value is also valid in the inclusion-free domains and is thus considered as the FeO_T background concentration.

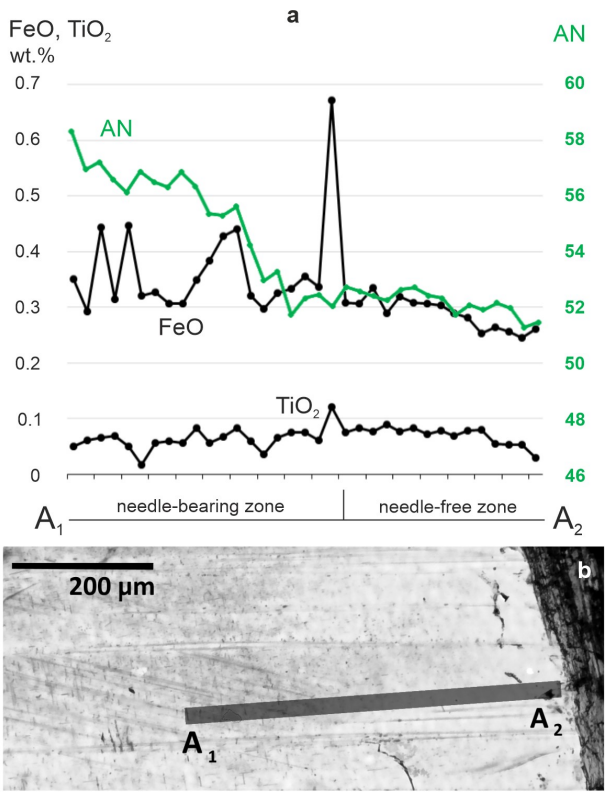

Figure 2.2: Compositional variation along the core-to-rim profile A_1-A_2 traversing a needle-bearing and a needle-free zone of a plagioclase grain. **a** FeO_T and TiO_2 contents in wt% indicated by black and anorthite content (AN) by green lines. The spikes in the FeO_T and TiO_2 profiles are probably caused by magnetite inclusions. **b** Optical image (transmitted light) with profile line; the width of the line corresponds to the 20 μm defocused beam used for microprobe analysis.

2.4.2 Distribution and morphology of the micro-inclusions

Under cross-polarized light, plagioclase twinning after the Manebach, Carlsbad, Albite and Pericline twin laws can be observed, where the latter two form polysynthetic twins (Fig. 2.1). If the cloudy domains in the grain interiors are viewed at high magnification under transmitted light, abundant lath- and needle-shaped μm and sub-μm sized magnetite grains appear. These magnetite micro-inclusions are present at up to $\sim$ 1 vol% and are responsible for the grey stain that is seen in the internal regions of the plagioclase grains. The clear rims are devoid of optically discernible magnetite micro-inclusions.

The magnetite micro-inclusions show specific shape orientations, where four to five different shape orientation groups can usually be discerned in a given plagioclase domain (Fig. 2.1, also see the sup-

plementary material, Figs. S2.2, S2.3)). It has been shown by Ageeva et al. (2020) that the elongation directions of the so-called *plane-normal* type inclusions follow the normal directions of specific plagioclase lattice planes including the PL(112)n, PL($1\bar{5}0$)n, PL($\bar{3}12$)n, PL(150)n and PL(100)n directions, where PL(*hkl*)n designates the direction that is normal to the PL(*hkl*) plane. One additional inclusion type has its elongation direction parallel to the PL[001] direction. An overview image of a plagioclase domain showing magnetite micro-inclusions with five well discernible SORs with respect to the plagioclase host is shown in the supplementary material (Fig. S2.2). The magnetite micro-inclusions investigated in detail in this study pertain to two of the *plane-normal* orientation classes, namely PL(112)n and PL(150)n.

The magnetite micro-inclusions are often bounded by plagioclase twin boundaries and change their shape orientations across twin boundaries. An overview image showing a plagioclase with magnetite micro-inclusions with shape orientations changing across Carlsbad and Albite twin boundaries is shown in the supplementary material (Fig. S2.3). In Fig. 2.1b, a plagioclase grain with polysynthetic Albite twins labeled Ab1 and Ab2 is shown. PL($\bar{3}12$)n-MT micro-inclusions are visible in the Ab2-oriented twin individuals. These micro-inclusions typically extend all across the Ab2-oriented twin individuals and are bounded by the twin boundaries on both sides. In the upper right of Fig. 2.1b, PL($\bar{3}12$)n-MT micro-inclusions can be seen in both, Ab1 and Ab2 twin individuals, where they appear mirrored about the twin boundary. Out of the magnetite micro-inclusions of the different orientation classes, only those that are elongated parallel to PL(150)n or PL($1\bar{5}0$)n transverse the Albite twin boundaries, apparently without any change in the orientation of their elongation direction and shape. This is due to the invariance of these two directions with respect to the Albite twin operation. Another interesting feature is shown in Fig. 2.1c, where small, about 50 μm long and 1–2 μm wide, lens-shaped Albite twin domains are accompanied by small, 1–2-μm-sized magnetite micro-inclusions of isometric shape aligned along the twin individuals. In the studied material, the spatial association of the small magnetite micro-inclusions and twin boundaries is typical and suggests a relation between Albite twinning and the formation of the magnetite micro-inclusions.

2.4.3 Magnetite-ilmenite intergrowth

Several oriented sandwich-like lamellae of ilmenite (ILM) can be seen within the magnetite micro-inclusions (Figs. 2.3, 2.4a). The ilmenite lamellae are about 100–200 nm wide and mostly are oriented perpendicular to the elongation direction of the hosting magnetite needle. The total amount of the ilmenite lamellae in magnetite is estimated to be less than 15 vol% of the opaque inclusion in all ilmenite-bearing inclusions. TEM observations show that the interface between ilmenite lamellae and magnetite host are sharp and that they are parallel to the ILM(0001) and one of the MT{111} lattice planes (Fig. 2.3c). In addition to

the relatively coarse lamellae, tiny, several nm-sized ilmenite domains are dispersed in the magnetite host (see highlighted domain in Fig. 2.3d).

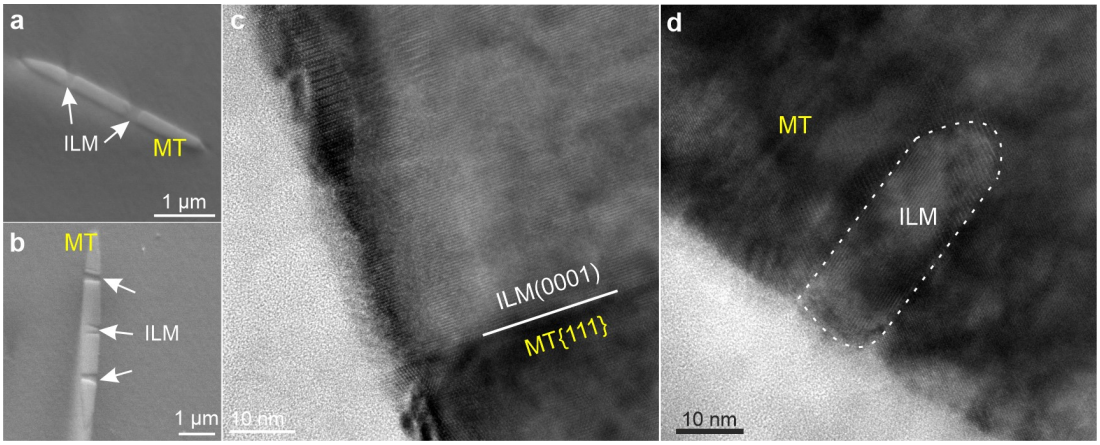

Figure 2.3: **a, b** Tilt corrected secondary electron (SE) images obtained at 70° tilt, showing magnetite micro-inclusions hosting sandwich-like ilmenite lamellae. **c** High-resolution TEM (HRTEM) image showing a sharp contact between an ilmenite lamella and the magnetite host. The phase boundary is ILM(0001) || MT{111}. **d** HRTEM image showing an ultra-fine ilmenite highlighted with white dashed line in a magnetite host.

2.4.4 Composite micro-inclusions

Sometimes the magnetite micro-inclusions are accompanied by orthopyroxene (OPX), clinopyroxene (CPX), amphibole, and mica so that composite multiphase inclusions arise. Orthopyroxene is the most abundant accompanying phase. Its volume fraction is in the range of 1–5% of the magnetite it accompanies. It can be seen in Fig. 2.4a that the smooth interface between magnetite and plagioclase is interrupted, where magnetite is in contact with orthopyroxene. In contrast, when present, amphibole and mica do not seem to interrupt the needle shape of the magnetite inclusion, they rather seem to have grown on top of the magnetite needle only replacing plagioclase (Fig. 2.4a).

2.4.5 Crystallographic and shape orientation relationships between the magnetite micro-inclusions and the plagioclase host

The CORs between the magnetite micro-inclusions and the plagioclase host were investigated using SAED and HRTEM. No direct image of both phases could be acquired at the same time, because of the extreme beam sensitivity of plagioclase. As the FIB foils are considerably bent, the SAED patterns at different positions within one crystal had to be acquired at slightly different tilting conditions to maintain a certain projection. (HR)TEM images and the corresponding SAED patterns of two PL(112)n-MT micro-inclusions and the plagioclase host are shown in Figs. 2.4, 2.5. Originally, the two inclusions probably pertained to a single inclusion, which split into two separate inclusions in the course of recrystallization. The elongation

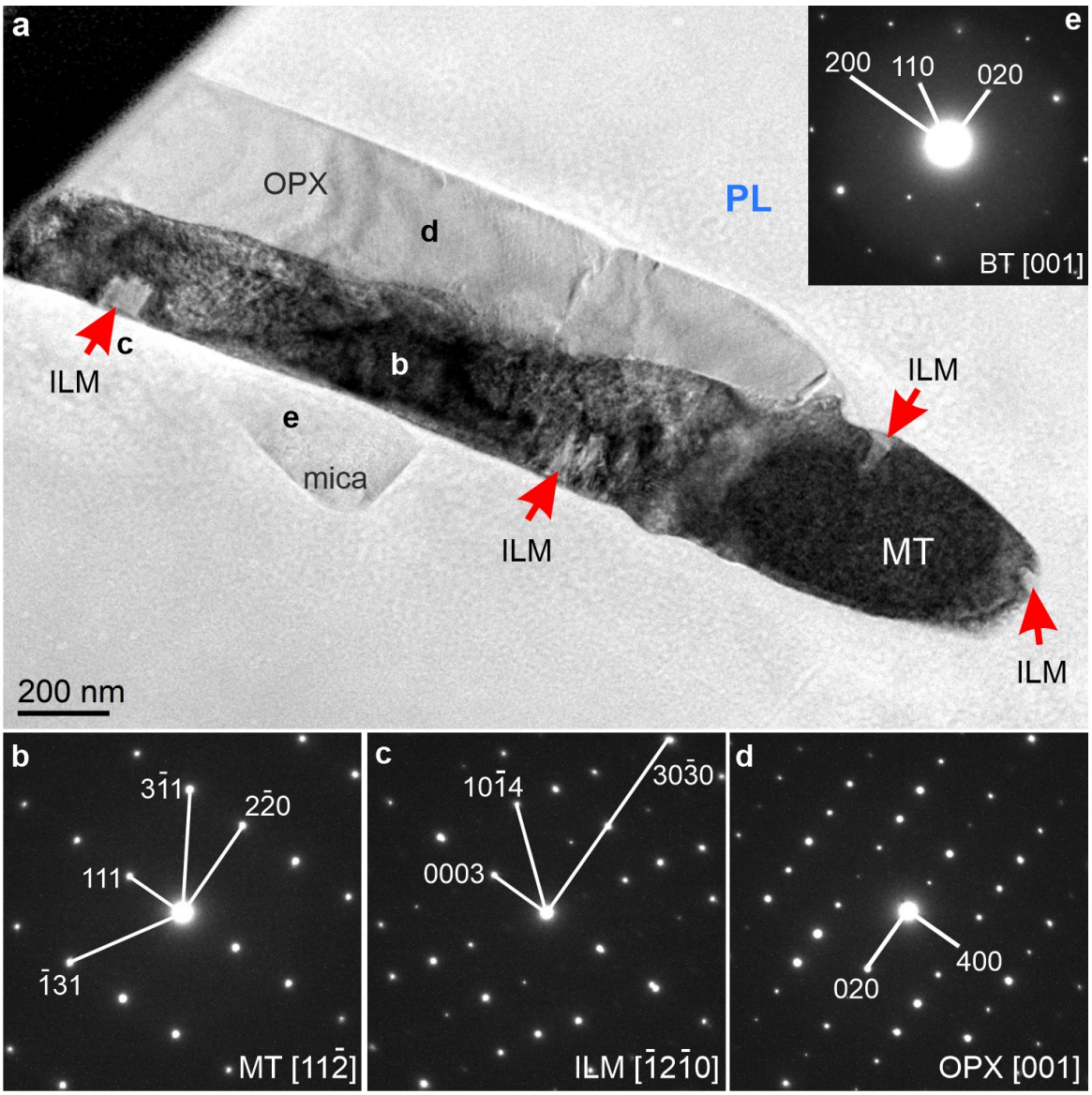

Figure 2.4: **a** Bright-field TEM image of the left part of the split PL(112)n-MT needle shown in Fig. 2.5a; this is a composite micro-inclusion comprising PL(112)n-MT with ilmenite lamellae and accompanying orthopyroxene and mica locally growing between the plagioclase host and the magnetite. **b–e** SAED patterns of magnetite, ilmenite, orthopyroxene and mica; the locations where SAED patterns were taken are indicated by lower case alphabetical labels in **a**. Systematic CORs exist among all four inclusion phases, namely MT{111} || ILM(0001) || OPX(100) || BT(100), MT{110} || ILM(1010) || OPX(010) || BT(010), and as a consequence, MT ⟨112⟩ || ILM[1210] || OPX[001] || BT[001].

directions are slightly different for the two related inclusions (Fig. 2.5a) indicating that the SORs and probably also the CORs were slightly modified during recrystallization and do not exactly represent the supposed original orientation relationships. The left inclusion in Fig. Fig. 2.5a is of polyphase nature while the right one is only comprised of a single magnetite needle. Small amounts of ilmenite are present at the tips of both segments of the split PL(112)n-MT micro-inclusion.

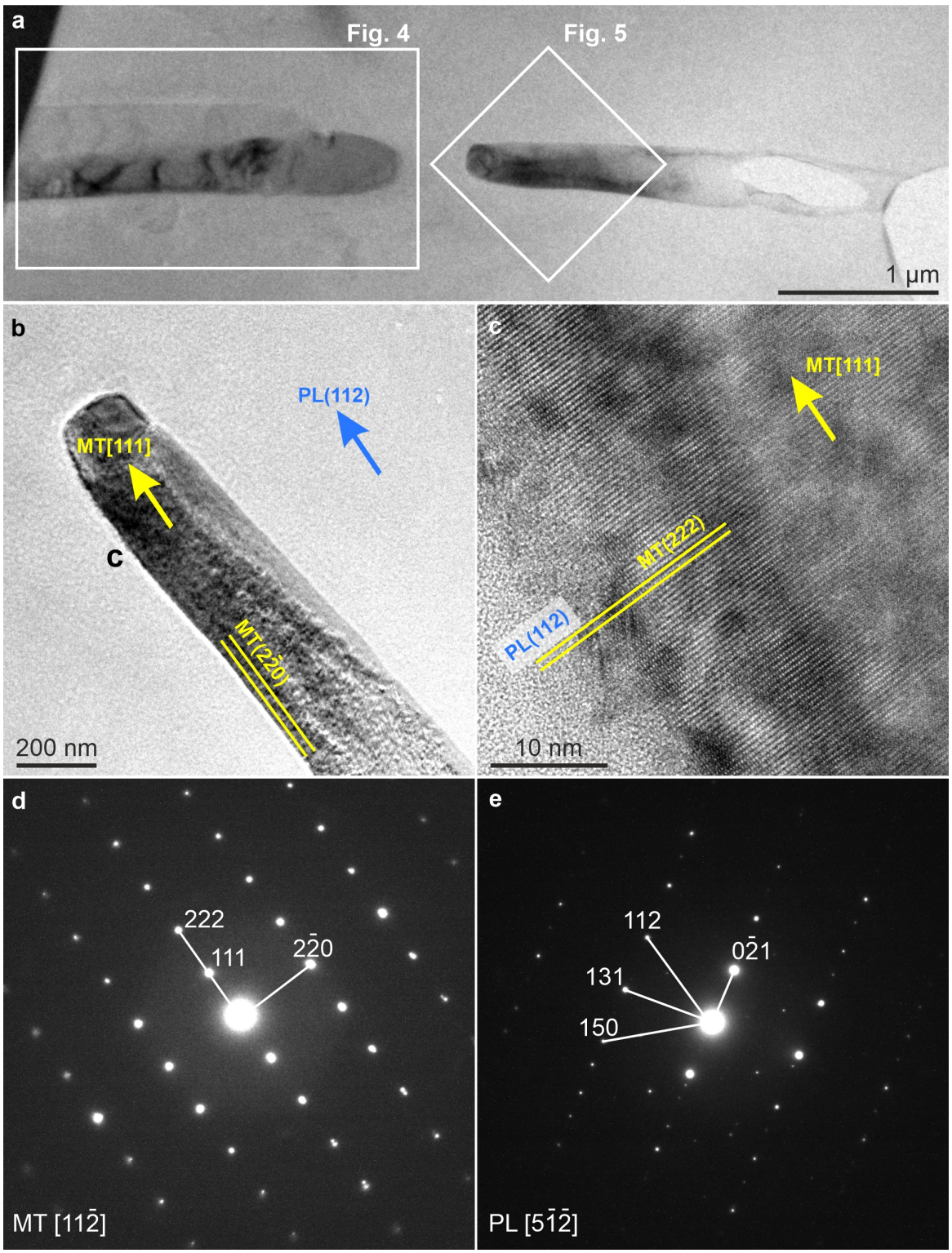

Figure 2.5: **a** Low-magnification bright-field TEM image of a split PL(112)n-MT micro-inclusion and surrounding plagioclase. **b–e** Refer to the right part of the split needle shown in **a**. **b, c** HRTEM image of the magnetite (upper right) plagioclase (lower left) interface; yellow arrow indicates the inclusion elongation direction; yellow line duplets show the traces of the MT(222) and MT(2$\bar{2}$0) lattice planes. The lattice fringes of MT(222) are clearly visible, the associated MT[111] corresponds to the inclusion elongation direction. The plagioclase has been amorphized due to beam damage. **d** SAED pattern of magnetite viewing direction MT[11$\bar{2}$]. **e** SAED pattern of plagioclase viewing direction PL[5$\bar{1}\bar{2}$]. From comparing **d** and **e**, it becomes obvious that the length and orientations of $\vec{g}_{\mathrm{MT222}}$ and $\vec{g}_{\mathrm{PL112}}$ are nearly identical.

Single-phase PL(112)n-MT micro-inclusion

The elongation direction of the single-phase PL(112)n-MT micro-inclusion, that is the right inclusion in Fig. 2.5a, closely corresponds to $\vec{g}_{\mathrm{MT222}}$ (Fig. 2.5b), which is aligned parallel to $\vec{g}_{\mathrm{PL112}}$ (Fig. 2.5c), where $\vec{g}_{hkl}$ is the primitive lattice plane vector in reciprocal space, and the length of $\vec{g}_{hkl}$ is proportional to the reciprocal of the corresponding d-spacing in the direct lattice. The long magnetite–plagioclase interfaces defining the elongation direction of the inclusion are nearly perpendicular to the plane of the foil, so that they appear sharp under the chosen projection. The traces of these interfaces are sub-parallel to one of the MT{110} lattice planes, but in detail they are slightly curved and show an angular deviation of up to about 5 ° from the trace of the MT{110} plane. The nearly identical values of $\vec{g}_{\mathrm{MT222}}$ and $\vec{g}_{\mathrm{PL112}}$, with respect to both, orientation and length (Fig. 2.5d,e), imply that the MT{222} and the PL(112) lattice planes are well aligned across the magnetite–plagioclase interface, with only minute lattice mismatch. Defining the relative lattice misfit as $|d_{\mathrm{PL112}} - d_{\mathrm{MT222}}|/d_{\mathrm{MT222}}$ a numerical value of 0.014 is obtained using 1 bar 298 K crystallographic data from Wenk et al. (2011) for plagioclase and from O'Neill and Dollase (1994) for magnetite. The MT{222} lattice planes are clearly visible on the HRTEM image of the magnetite–plagioclase interface (Fig. 2.5c). No fringes of the corresponding PL(112) lattice plane can, however, be observed because of the extremely quick amorphization of the plagioclase under the electron beam.

Composite PL(112)n-MT micro-inclusion

A bright-field TEM image and SAED patterns of the part of the split PL(112)n-MT needle that forms the composite inclusion, that is the left inclusion in Fig. 2.5a, are shown in Fig. 2.4. The inclusion comprises magnetite, ilmenite, orthopyroxene and mica. The crystallographic orientation relationships of the two parts of the split PL(112)n-MT needle to the plagioclase host and with respect to the accompanying phases are shown in Fig. 2.6. According to its elongation direction and the COR to the plagioclase host, the magnetite inclusion is still classified as a PL(112)n-MT micro-inclusion, albeit with an about 10° deviation from the elongation of the single-phase PL(112)n-MT micro-inclusion. The magnetite contains irregularly distributed lamellae of ilmenite, which show a SOR parallel to the MT{111} lattice plane that is perpendicular to the needle elongation direction. The ilmenite shows a specific COR with the magnetite with MT{111} || ILM(0001) and MT{110} || ILM($10\bar{1}0$), which also implies MT⟨112⟩ || ILM[$\bar{1}2\bar{1}0$]. This crystallographic orientation relationship has been reported from several cases of magnetite–ilmenite intergrowth in the literature (Feinberg et al., 2005; Wenk et al., 2011) and is ascribed to the parallel alignment of close-packed oxygen layers parallel to MT{111} in the cubic close-packed (ccp) oxygen sublattice of magnetite and parallel to ILM(0001) in the hexagonal close-packed (hcp) oxygen sublattice of ilmenite. In addition,

the observed COR ensures parallel alignment of close-packed directions within these layers.

Orthopyroxene and mica are locally present along the long interfaces bounding the magnetite needle parallel to its elongation direction. In the domain shown in Figs. 2.4a and 2.5a, the orthopyroxene forms an elongated grain parallel to the elongation direction of the magnetite needle. The SAED patterns in Fig. 2.4 reveal a specific COR between magnetite and orthopyroxene with MT{111} || OPX(100) and MT{110} || OPX(010), which also implies MT⟨112⟩ || OPX [001]. The COR between magnetite and orthopyroxene is very precise indicating a direct contact between magnetite and orthopyroxene during growth of orthopyroxene on pre-existing magnetite or, vice versa, growth of magnetite in contact with pre-existing orthopyroxene. The orthopyroxene has a relatively smooth interface towards the plagioclase but a wavy, somewhat irregularly shaped interface to the magnetite. The shapes of magnetite and orthopyroxene, and especially the geometry of the magnetite–orthopyroxene interface suggest that a pre-existing magnetite was partially replaced by orthopyroxene. Similar inferences were made by Gao et al. (2019), who observed scalloped magnetite–amphibole interfaces, where magnetite was partially replaced by amphibole.

Based on chemical composition and SAED patterns, the phase on the other side of the magnetite inclusion in Fig. 2.4a is most likely biotite (BT). The SAED patterns in Fig. 2.4 reveal a specific COR between magnetite and biotite with MT{111} || BT(100) and MT{110} || BT(010), which also implies MT⟨112⟩ || BT[001]. In contrast to the interface segment where magnetite is in contact with orthopyroxene, the segment of the magnetite perimeter that is in contact with mica appears to have remained unaffected by the mica.

In summary, specific CORs with MT{111} || ILM(0001) || OPX(100) || BT(100) and MT{110} || ILM($10\bar{1}0$) || OPX(010) || BT(010), which also imply MT⟨112⟩ || ILM[$\bar{1}2\bar{1}0$] || OPX[001] || BT[001], exist among all phases of the composite inclusion. In addition, the COR of the magnetite from the composite inclusion deviates by about 10° from the COR of a single-phase PL(112)n-MT micro-inclusion with the plagioclase host. The *d*-spacings of the PL(112), MT{111} and OPX(100) lattice planes are related by close to integer multiples with $4 \times d_{\mathrm{MT111}} = 4 \times 4.85 \approx d_{\mathrm{OPX100}} = 18.36 \approx 8 \times d_{\mathrm{PL112}} = 8 \times 2.46$, so that a fair lattice match is ensured across magnetite–orthopyroxene (0.053 rel. misfit), magnetite–plagioclase (0.014 rel. misfit), orthopyroxene–plagioclase (0.066 rel. misfit) interfaces extending approximately parallel to the needle elongation direction.

PL(150)n-MT micro-inclusion

Figure 2.7a shows a low-magnification TEM image of a PL(150)n-MT micro-inclusion. The elongation direction of the magnetite needle is sub-parallel to one of the MT⟨111⟩ directions. In addition, the needle

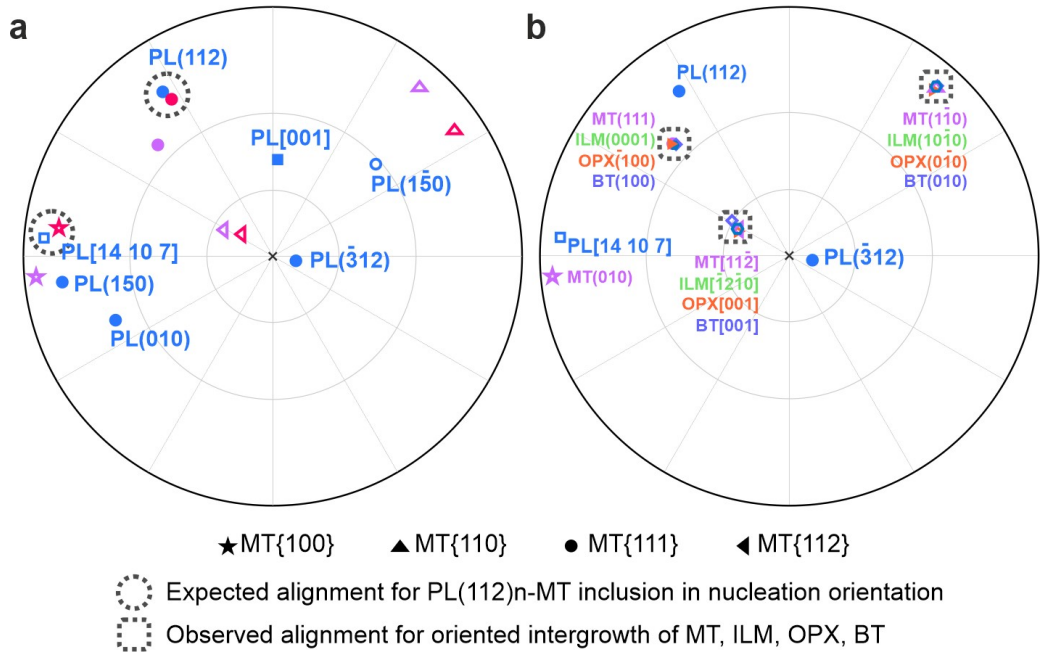

Figure 2.6: **a** Stereographic projections showing the crystallographic orientations of the single-phase PL(112)n-MT magnetite inclusion (red) and of the composite micro-inclusion with magnetite (purple) to the plagioclase host (blue). The plane poles and directions that are expected to coincide for a PL(112)n-MT magnetite inclusion (Ageeva et al., 2020) are indicated with the dashed circles. **b** CORs of the phases pertaining to the composite micro-inclusion. The coincidence of the plane poles and directions among the different phases (Fig. 2.4) are indicated with the dashed squares. The orientation of the PL(112) n-MT single-phase inclusion (red) coincides almost perfectly with the expected nucleation COR, while the orientation of the composite PL(112)n-MT micro-inclusion (purple) deviates by about 10° from the ideal COR.

elongation direction and thus also the corresponding MT⟨111⟩ direction closely coincide with the normal direction to the PL(150) lattice plane of the plagioclase host. The magnetite–plagioclase interfaces bounding the inclusion parallel to its elongation direction on both sides closely correspond to a MT{110} facet (Fig. 2.7c, d). In Fig. 2.7c, this interface appears to be sharp, while in Fig. 2.7d, it has a somewhat wavy appearance on the nm-scale. The lattice fringes of the corresponding lattice planes in the plagioclase host cannot be seen due to the rapid amorphization of the plagioclase under the electron beam. As a consequence, the exact degree of alignment of the magnetite–plagioclase interfaces with the lattice planes of the plagioclase host cannot be directly observed. The SAED patterns shown in Fig. 2.7e, f reveal that $\vec{g}_{\mathrm{MT222}}$ is nearly identical to $\vec{g}_{\mathrm{PL150}}$, implying that the MT{222} planes that are oriented perpendicular to the needle elongation direction are very well aligned with the PL(150) lattice planes with only a minute relative misfit of $|d_{\mathrm{PL150}} - d_{\mathrm{MT222}}|/d_{\mathrm{MT222}} = 0.012$ across the magnetite–plagioclase interface bounding the inclusion parallel to its elongation direction. When the inclusion passes through an Albite twin boundary, the PL(150)n-Mt inclusion becomes a PL(1$\bar{5}$0)n-Mt inclusion. This transformation will be further addressed in the “Discussion”.

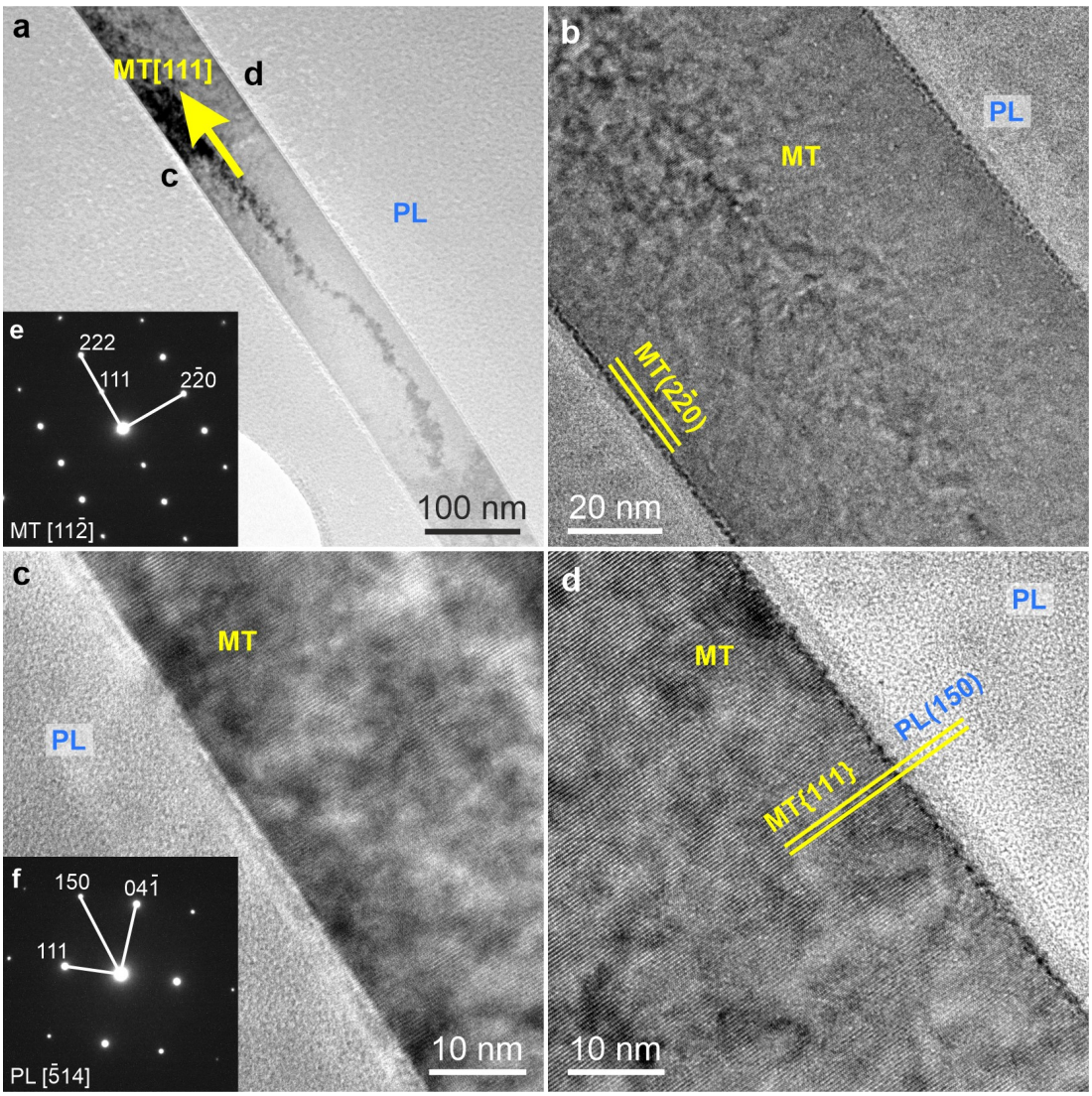

Figure 2.7: **a** Bright-field TEM images of a PL(150)n-MT inclusion under low-magnification. **b** HRTEM image showing the magnetite–plagioclase interface on both sides of the magnetite micro-inclusion. **c** HRTEM image showing the sharp boundary from the lower part of **b**. **d** HRTEM image showing the wavier boundary from the upper part of **b**. **e, f** SAED patterns of magnetite under the MT[11$\bar{2}$] zone axis and plagioclase under zone axis PL[$\bar{5}$14]. Comparing **e** and **f**, $\vec{g}_{\mathrm{MT222}}$ is nearly identical to $\vec{g}_{\mathrm{PL150}}$ with regard to length and orientation.

2.5 Discussion

The foremost interest in this study is to unravel the potential formation pathway(s) of the plagioclase-hosted magnetite micro-inclusions and to constrain their formation temperatures. This is of crucial importance for the interpretation of the remanent magnetization of the magnetite-bearing plagioclase grains.

One may consider that magnetite and the potentially accompanying phases crystallized from the melt first. The observed shape orientation relationships (SORs) and crystallographic orientation relationships (CORs) could then be generated in the course of attachment of the magnetite and accompanying phases to the surface of the growing plagioclase according to the best geometrical fit of their macroscopic shape, a process referred to as *synneusis* (Vance, 1969). For the case at hand, this hypothesis can be rejected, because given a MORB type chemistry of the bulk rock, plagioclase crystallizes before orthopyroxene and magnetite

at the conditions expected for crystallization in a mid-ocean ridge environment (Grove and Baker, 1984; Grove et al., 1992; Ariskin and Barmina, 2004; Villiger et al., 2007; Suhr et al., 2008).

Based on the combined petrographic, mineral chemical and microstructural evidence, we discuss two hypotheses for their genesis:

Hypothesis 1: Nucleation and growth of magnetite and potentially associated phases on the surface of plagioclase growing from the melt and engulfment during further plagioclase growth.

Hypothesis 2: Precipitation of magnetite and potentially associated phases from Fe-bearing plagioclase in a solid-state reaction or in a sequence of solid-state reactions.

The first hypothesis implies that magnetite and the potentially accompanying phases nucleated on the surface of the growing plagioclase. The newly forming magnetite and potentially accompanying phases thus would grow in contact with the plagioclase, at least along parts of their surfaces, allowing for the evolution of systematic CORs by topotaxy (Griffiths et al., 2020).

The second hypothesis implies that the magnetite and the accompanying phases precipitated from an Fe-bearing plagioclase, which became supersaturated with respect to magnetite (Wenk et al., 2011; Biedermann et al., 2016; Nikolaisen et al., 2020). In this case, the magnetite and the accompanying phases were in contact with the crystal structure of the host plagioclase during their entire nucleation and growth history. Thus, systematic SORs and CORs are expected to form so that the elastic strain energy due to macroscopic misfit and the interfacial energy arising from lattice mismatch at the newly generated phase boundaries are minimized.

With respect to the chemical mass balance, the first hypothesis implies that the Mg, Fe^{2+} and Fe^{3+} needed for the formation of magnetite and associated phases were never present in the crystal structure of plagioclase. In contrast, according to the second hypothesis, the Mg, Fe^{2+} and Fe^{3+} needed for the formation of magnetite and associated phases were derived from or delivered through the plagioclase, and local chemical mass balance needs to be taken into consideration. Two end-member scenarios are conceivable for precipitation of magnetite from supersaturated plagioclase. The plagioclase host crystal may have behaved as a closed system. This would require that the Mg, Fe^{2+} and Fe^{3+} needed were originally present in the lattice of plagioclase. In this case, supersaturation with respect to magnetite could only arise from changes in temperature and/or pressure, where cooling is the most likely scenario. Alternatively, the plagioclase crystal may have been open with respect to chemical mass transfer allowing for the exchange of chemical components between the interior of the plagioclase grain and the surrounding matrix and/or melt. In this case, changes in the chemical potentials of components such as O_2, FeO and MgO may have caused supersaturation of Fe-bearing plagioclase with respect to magnetite. The resulting crystallization of

magnetite would then be referred to as *open system precipitation* (Proyer et al., 2013). In the following, we discuss the possible formation pathways in the light of the observed crystallographic and shape orientation relationships, microstructural and chemical evidence.

2.5.1 Implication of the observed crystallographic and shape orientation relationships

Single-phase PL(112)n-MT micro-inclusion

According to the classification scheme of Ageeva et al. (2020), the main orientation of the PL(112)n-MT inclusions is defined as MT{111} ‖ PL(112) and MT{110} ‖ PL(150). In the case at hand, MT{111} ‖ PL(112) is fulfilled within the accuracy of the orientation determination, but the lattice of the magnetite inclusion is rotated away from the main orientation by about 29° around its elongation direction. This rotation preserves the alignment of oxygen layers that are parallel to one of the MT{111} and to the PL(112) lattice planes. It may be a primary feature, or it may be due to recrystallization. According to Ageeva et al. (2020), the nucleation orientation of the PL(112)n-MT inclusions is defined as MT⟨001⟩ ‖ PL[14 10 7] and MT{111} ‖ PL(112), which is rather close to the observed COR (Fig. 2.5b-e, 2.6a). Accordingly, the single-phase PL(112) n-MT inclusion is classified as “near nucleation orientation”.

The coincidence of the $\vec{g}_{\mathrm{MT222}}$ and $\vec{g}_{\mathrm{PL112}}$ in reciprocal space reveals that these two lattice planes are well aligned with only a minute mismatch of about 0.014 between the corresponding *d*-spacings across the magnetite–plagioclase interfaces bounding the magnetite needle parallel to its elongation direction. The SAED data thus corroborate the supposition expressed earlier by Ageeva et al. (2020) that the alignment of important oxygen layers from both crystal structures is the mechanism underlying the systematic SOR and COR between the magnetite micro-inclusions and the plagioclase host and also explain the high aspect ratios of the magnetite micro-inclusions.

Composite PL(112)n-MT micro-inclusion

The part of the split PL(112)n-MT needle that forms the composite inclusion (Fig. 2.4, 2.6) is characterized by excellent alignment of MT{111} with OPX(100) and ILM(0001) but an about 10° misorientation of these lattice planes with respect to PL(112). Like MT{111}, the OPX(100) and the ILM(0001) lattice plane correspond to close-packed oxygen layers. The *d*-spacings of these lattice planes are related by nearly integer factors, so that a good match across the magnetite–orthopyroxene and the magnetite–ilmenite phase boundaries is ensured. The orientation of the single-phase PL(112)n-MT microinclusion corresponds

to the expected COR more closely than the orientation of the magnetite from the composite inclusion (Fig. 2.6). This suggests that the deviation from the expected COR for a PL(112)n-MT micro-inclusion may arise from strain associated with the growth of orthopyroxene and the other accompanying phases. In any case, the strong CORs among magnetite, orthopyroxene and ilmenite indicate that orthopyroxene and ilmenite grew together with or on the pre-existing magnetite.

PL(150)n-MT micro-inclusion

According to Ageeva et al. (2020), the main orientation of PL(1$\bar{5}$0)n-MT inclusions is defined as MT{111} || PL(1$\bar{5}$0) and MT{110} || PL(112). The SAED of the investigated PL(150)n-MT inclusion reveals that MT{111} || PL(150) and MT{112} || PL($\bar{3}$12) (Fig. 2.7). This COR can be explained as an effect of plagioclase twinning after the Albite law. The PL(1$\bar{5}$0) and PL(150) lattice planes are perfectly parallel in two plagioclase domains that are related by the Albite twin law. As a consequence, the plane-normal directions have identical orientation and a PL(1$\bar{5}$0)n-Mt inclusion becomes a PL(150)n-Mt inclusion, when it passes through an Albite twin boundary (Fig. 2.1d, 2.8). At the same time, the second alignment of lattice planes that defines the specific COR between magnetite micro-inclusion and plagioclase host changes from MT{110} || PL(112) to MT{112} || PL($\bar{3}$12) (Fig. 2.8). Thus, when passing through an Albite twin boundary, the PL(1$\bar{5}$0)n-MT inclusions preserve their elongation direction, but the descriptions of the COR are different in the two twin domains of the plagioclase host. Again, the coincidence of the $\vec{g}_{\mathrm{MT222}}$ and $\vec{g}_{\mathrm{PL150}}$ in reciprocal space indicates a good match between these two lattice planes across the magnetite–plagioclase interface of PL(150)n-MT inclusions, and further corroborates that the elongation direction of the plane-normal type inclusions is determined by the alignment of important oxygen layers from both crystal structures.

Despite of the angular deviation of the composite inclusion from ideal topotaxy, which is ascribed to recrystallization, all three inclusions investigated in this study correlate with the plane-normal orientation classes that were identified earlier from large electron backscatter diffraction data sets (Ageeva et al., 2020). The HRTEM imaging and the SAED results confirm the alignment of the lattice planes corresponding to close-packed oxygen lattice planes of magnetite with important oxygen layers of the host plagioclase. These results suggest oriented nucleation and growth of magnetite in contact with a pre-existing plagioclase lattice. The fact that the SORs and CORs are fixed to the lattice of plagioclase in the different twin individuals indicates that the twinning, including Albite twinning, already existed, when the magnetite inclusions formed or at least when they attained their final orientation relationships to the plagioclase host. The fact that the orthopyroxene and mica grains accompanying the magnetite in the composite inclusion

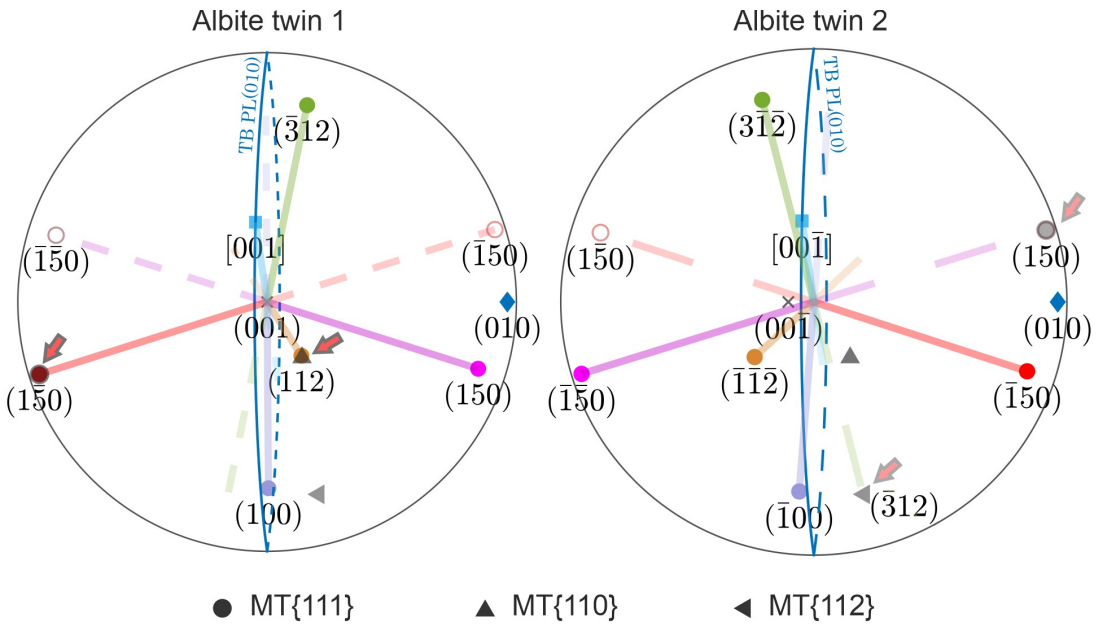

Figure 2.8: Stereographic projections showing the elongation directions of the magnetite inclusions in the plagioclase host and their relations to the Albite twin law. All elongation directions change orientation when subjected to the Albite twin operation, except for the PL(1$\bar{5}$0) n and the PL(150)n type inclusions. A PL(1$\bar{5}$0)n-MT inclusion in an Albite twin 1 has exactly the same orientation of its elongation direction as a PL(150)n-MT type inclusion in Albite twin 2. The blue large circle labeled (010) represents the Albite twin boundary. The black symbols indicate lattice plane poles of the magnetite inclusion. The magnetite lattice planes that are aligned parallel to important oxygen layers in plagioclase for PL(1$\bar{5}$0)n and the PL(150)n needles in the two different Albite twins are highlighted with the orange arrows.

strictly adhere to specific CORs indicates that they grew either together with or after the formation of magnetite.

The observed SORs and CORs are still compatible with oriented nucleation of magnetite and potentially accompanying phases on the surface of growing plagioclase (hypothesis 1) as well as with the precipitation from supersaturated plagioclase (hypothesis 2). It has been shown recently that specific SORs tend to be selected depending on the orientation of the growth facet, if needle-shaped micro-inclusions are formed by oriented nucleation on the surface of a growing crystal (Griffiths et al., 2020). In the plagioclase under consideration, the SORs of the magnetite micro-inclusions always follow specific crystallographic directions, and differences in SOR between different domains in a plagioclase grain are only due to the effect of twinning. There is no evidence for selection of subsets of SORs in different domains that could have arisen from the effect of oriented nucleation on different growth facets. This is why hypothesis 1 is rejected, and precipitation of magnetite and possibly of magnetite and accompanying pyroxene from a supersaturated plagioclase host is considered as the most likely formation pathway. In addition to the microstructural and textural analyses, mass balance considerations may provide important constraints on the formation pathways of the magnetite inclusions in the plagioclase host. Possible mass balance scenarios are discussed in the following section.

2.5.2 Mass balance considerations for precipitation from the plagioclase host

If the magnetite inclusions formed by precipitation from a supersaturated Fe-bearing plagioclase, the question arises, whether this is stoichiometrically possible in a closed system setting, or whether open system precipitation needs to be invoked. The former case would imply that all components needed for the formation of magnetite were derived from the plagioclase host crystal exclusively, while in the latter case, chemical mass transfer through the plagioclase host would need to be allowed, and any chemical change within the plagioclase host could be achieved by exchange with the surrounding melt or rock matrix.

From petrographic evidence, the volume fraction of the magnetite inclusions in the investigated plagioclase crystals is estimated to be $\leq 1\%$. Together with the measured background concentration of about 0.25 wt% FeO_T in inclusion-free domains of plagioclase, this amounts to an overall Fe content of about 0.6 wt% in the plagioclase host. This is well within the range of typical Fe contents of plagioclase from gabbroic rocks, where plagioclase usually has FeO_T contents of 0.2–1.0 wt% (Smith and Brown, 1988; Bernstein et al., 1992; Tegner, 1997; Brandriss and Bird, 1999).

The sum formula of plagioclase may be expressed as MT_4O_8 with the M site occupied by the large low-valence cations Na^+, Ca^{2+} and K^+ and the T site occupied by the small high-valence cations Si^{4+} and Al^{3+}. Ferric iron may substitute for Al^{3+} on the T site giving rise to the $CaFe^{3+}AlSi_2O_8$, $NaFe^{3+}Si_3O_8$, and $KFe^{3+}Si_3O_8$ end-member components. Ferrous iron and magnesium may enter the T site, where they substitute for Al^{3+} implying the coupled substitution of Al^{3+} by Si^{4+}, also on the T site. This gives rise to the $CaFe^{2+}Si_3O_8$ and the $CaMgSi_3O_8$ end-member components. Alternatively, Fe^{2+} and Mg^{2+} may substitute for Ca^{2+} on the M site, which produces the $Fe^{2+}Al_2Si_2O_8$ and $MgAl_2Si_2O_8$ end-member components. It was argued that Fe^{2+} and Mg^{2+} preferentially occupy the T site (Wenk and Wilde, 1973; Longhi et al., 1976), but substitution of Fe^{2+} for Ca^{2+} on the M site has also been demonstrated by optical spectroscopy and electron paramagnetic resonance analysis (Bell and Mao, 1973; Hofmeister and Rossman, 1984). Experiments on basic magma revealed that the partitioning of FeO_T into plagioclase is enhanced by high anorthite content of the plagioclase, by high oxygen fugacity, and by high silica content of the melt (Longhi et al., 1976; Phinney, 1992). The enhancement of Fe incorporation with increasing anorthite content is ascribed to the increased availability of Ca^{2+} on the M site for substitution by Fe^{2+} and Mg^{2+} (Bell and Mao, 1973; Hofmeister and Rossman, 1984) and to the increased availability of Al^{3+} on the T site for substitution by Fe^{3+} (Lundgaard and Tegner, 2004). The enhancement of Fe uptake with increasing SiO_2 content of the melt has been ascribed to an increase of the activity of Fe-bearing species in the melt with increasing polymerization of the melt (Lundgaard and Tegner, 2004). Finally, the enhancement of Fe uptake with

increasing fO_2 reflects the Fe^{3+}/FeO_T ratio in the melt coupled with the preferential substitution of Fe^{3+} for Al^{3+} on the T site (Lundgaard and Tegner, 2004). Plagioclase from gabbroic rocks usually contains both ferric and ferrous iron, and the Fe^{3+}/FeO_T ratio is typically in the range of 0.4–0.7 (Nakada et al., 2019).

In a closed system setting, the Fe needed for precipitation of magnetite within the plagioclase host may thus well have been derived from the plagioclase host exclusively. The segregation of only Fe_3O_4 from plagioclase is, however, unlikely, as there is no phase component in plagioclase with this stoichiometry. Precipitation of magnetite from plagioclase in a closed system setting should be accompanied by the co-precipitation of additional phases. Composite inclusions containing orthopyroxene, clinopyroxene, amphibole or biotite in addition to magnetite are indeed observed. Out of these phases, amphibole and biotite appear to be related to late stage hydrothermal activity that postdates formation of the magnetite precipitates. This is why only mass balance scenarios for the precipitation of magnetite and of magnetite with accompanying pyroxene are discussed in the following paragraphs.

For analyzing chemical mass balance during the precipitation of magnetite and potentially accompanying pyroxene, we choose a set of 7 chemical components including SiO_2, Al_2O_3, FeO, MgO, CaO, Na_2O and O_2, and we allow for 13 phases or phase components including $CaAl_2Si_2O_8$, $CaFe^{3+}AlSi_2O_8$, $CaFe^{2+}Si_3O_8$, $CaMgSi_3O_8$, $Fe^{2+}Al_2Si_2O_8$, $NaAlSi_3O_8$, $NaFe^{3+}Si_3O_8$, $MgSiO_3$, $FeSiO_3$, $MgFe^{3+}_2O_4$, Fe_3O_4, $CaSiO_3$ and O_2. For the chosen system, a stoichiometric reaction equation for the precipitation of magnetite and pyroxene from Fe- and/or Mg-bearing plagioclase accompanied by a reduction of the Fe and/or Mg content of the plagioclase can be written (for details of the analysis see Appendix):

$$\begin{aligned}&(2+4x)\,CaFe^{3+}AlSi_2O_8 + (4x-1)\,Fe^{2+}Al_2Si_2O_8 = \\ &1\,Fe_3O_4 + (2-2x)\,CaFe^{2+}Si_3O_8 + 6x\,CaAl_2Si_2O_8 + (10x-4)\,FeSiO_3 + x\,O_2\end{aligned} \tag{2.1}$$

For $x > 0.4$, both, magnetite and pyroxene are produced from Fe^{2+}- and Fe^{3+}-bearing plagioclase, for $x = 0.4$, only magnetite is formed. If $x < 0.4$, pyroxene would be on the reactant side. In many cases, magnetite forms single-phase inclusions. In the composite inclusions, the accompanying pyroxene is volumetrically subordinate as compared to magnetite. Taking the oxygen equivalent as proxy for the proportions among the molar volume, the volumetric proportion of magnetite and pyroxene produced by the reaction according to Eq. 2.1 is 4:3, if $x = 0.5$. This overrates the volume proportion of pyroxene as compared to what is observed in the composite inclusions, thus $0.4 \leq x \leq 0.5$ may be inferred, where x is closer to 0.4 than to 0.5.

For the given choice of phases and phase components, the formation of magnetite or of magnetite and pyroxene from Fe-bearing plagioclase liberates oxygen. Thus, such a reaction requires that the host

plagioclase behaves as an open system with respect to oxygen but the cations can be balanced locally. From petrographic evidence, it may be inferred that the magnetite precipitates formed during or after development of the polysynthetic Albite twins. In addition, small precipitates of magnetite are concentrated along Albite twin boundaries, indicating that precipitation of magnetite was enhanced in the vicinity of the twin boundaries. The tendency of magnetite inclusions to form concentrations parallel to the Albite and Pericline twin planes was also reported from Whitney (1972) and by Sobolev (1990) corroborating links between the precipitation of magnetite and twinning in plagioclase. It may thus be hypothesized that the twin boundaries may have served as passageways for the exchange of oxygen between the interior of the plagioclase grain and the rock matrix.

We recall that the plagioclase grains are optically zoned with cloudy, inclusion-rich internal regions mantled by clear, inclusion-free regions at the rims, and, based on petrographic evidence, plagioclase is inferred to have been the first phase to crystallize from the melt. Mineral chemical analysis revealed that the early plagioclase growth zones incorporated Fe at FeO_T levels of 0.5-1.0 wt% during primary magmatic crystallization from a tholeiitic melt. In a later stage, when pyroxene and Fe–Ti oxides started to crystallize, less Fe was available in the melt. This caused relatively low Fe contents in the late growth increments of the plagioclase, which now form the relatively Fe poor rims that are devoid of magnetite inclusions.

The precipitation of magnetite within the Fe-rich portions of the plagioclase was probably driven by a decrease of the fO_2 in the rock matrix. The serpentinization of the associated ultramafic rocks, which may be represented by the simplified reaction:

$$6\,Mg_{1.5}Fe_{0.5}SiO_4 + 7\,H_2O = 3\,Mg_3[Si_2O_5](OH)_4 + Fe_3O_4 + H_2 \tag{2.2}$$

where $Mg_{1.5}Fe_{0.5}SiO_4$ is olivine, and $Mg_3[Si_2O_5](OH)_4$ is a simplified formula for a serpentine mineral, is an effective source for reducing fluids in a mid-ocean ridge environment (Klein et al., 2020). Thus, it is well conceivable that interaction of the gabbro with reducing fluids from serpentinization provided a driving force for the out-diffusion of oxygen from the plagioclase. This, in turn, leads to the partial reduction of the ferric iron originally contained in the plagioclase and precipitation of magnetite. According to Eq. 2.1, the precipitation of magnetite may, but need not necessarily be accompanied by the formation of orthopyroxene.

If chemical mass transfer into and out of the plagioclase host were possible not only for oxygen but also for the cations, any mass balance scenarios can be envisaged, and any association of inclusion phases, be it isolated magnetite, magnetite–orthopyroxene assemblages or more complex multiphase inclusions, could be formed by open system precipitation. The chemical mass transfer between the interior of the host

plagioclase and the matrix cannot be explained by volume diffusion of trivalent cations through the lattice of plagioclase, because this process is exceedingly slow (Cherniak, 2010). Fast diffusion pathways along one- or two-dimensional defects such as edge dislocations or twin boundaries would have to be invoked instead. If the magnetite inclusions indeed formed by introduction of FeO and MgO components from the rock matrix, the overall zoning of the plagioclase grains with the clouded, inclusion-rich core regions and the clear rims would require the rims to be of secondary nature. The regular optical zoning of the plagioclase grains, however, rather suggests a primary origin. Moreover, if Fe and Mg were supplied by their in-diffusion, also the rims of the plagioclase should have been affected. The rims are, however, less Fe rich than the core regions and free of magnetite micro-inclusions. Thus, precipitation of magnetite from Fe-bearing plagioclase that became supersaturated with respect to magnetite due to interaction with a reducing fluid from serpentinization of associated ultramafic rocks is considered the most likely formation pathway. The strong crystallographic orientation relationships between magnetite and orthopyroxene and the irregular shape of the magnetite–orthopyroxene interface suggests that during the reaction corresponding to Eq. 2.1, magnetite nucleated and grew first in contact with the plagioclase host, and orthopyroxene nucleated on the magnetite and partially replaced it somewhat later. The temperature at which this precipitation took place can be further constrained from the internal microstructures of the magnetite micro-inclusions. In this context, the ilmenite lamellae within the magnetite needles are of particular interest.

2.5.3 Implication of magnetite–ilmenite intergrowth

As shown in Figs. 2.3 and 2.4, ilmenite is present in the magnetite inclusions in two microstructural variants. It may be present as single, relatively coarse, lath-shaped lamellae parallel to one of the MT{111} lattice planes of the magnetite host crystal. Typically, only a few of these coarse ilmenite lamellae are present within a single magnetite micro-inclusion, and they usually occupy less than 15 vol% of the inclusions. The ilmenite shows a strong COR to the magnetite host with MT{111} ‖ ILM(0001) and MT{110} ‖ ILM($10\bar{1}0$). In addition, small, several nm-sized ilmenite grains are present dispersed in the hosting magnetite needle.

The microstructures and textures of magnetite–ilmenite intergrowth depend on the formation mechanisms (McConnell, 1975; Speczik et al., 1988). At temperatures below $\sim$ 600 °C, Ti-rich magnetite tends to exsolve ulvospinel. Magnetite–ulvospinel assemblages obtained from exsolution of Ti-rich magnetite have been described from oceanic gabbro before (Feinberg et al., 2004; Ageeva et al., 2017), but are not typical in the sample under study. Ulvospinel is stable only at low oxygen fugacity and tends to be oxidized otherwise. The tendency for ulvospinel to become oxidized increases with decreasing temperature. This

usually leads to low-temperature oxidation of ulvospinel that has exsolved from Ti-rich magnetite below $\sim$ 600 °C, which characteristically produces fine ilmenite lamellae forming cloth microstructures, where the individual ilmenite lamellae are oriented parallel to the MT{100} planes (Tan et al., 2016). This is not what is observed in the magnetite micro-inclusions under study. At higher fO_2, the Fe_2TiO_4 component in Ti-rich magnetite usually becomes oxidized at temperatures above the magnetite–ulvospinel solvus by a reaction of the type

$$6\,Fe_2TiO_4 + O_2 = 6\,FeTiO_3 + 2\,Fe_3O_4 \tag{2.3}$$

This process is referred to as *oxidation-exsolution* and usually produces coarse, sandwich-like ilmenite lamellae in nearly pure magnetite. Ilmenite lamellae from oxidation-exsolution are typically oriented parallel to the MT{111} lattice planes with ILM(0001) || MT{111}, which is compatible with our observations. Oxidation-exsolution is considered the most important pathway for the exsolution of ilmenite lamellae from Ti-rich magnetite (Tan et al., 2016). Oxidation-exsolution of ilmenite from Ti-rich magnetite occurs at temperatures above the crest of the magnetite–ulvospinel solvus, that is at temperatures in excess of $\sim$ 600 °C. Cooling at constant oxygen fugacity shifts the equilibrium represented by Eq. 2.3 to the right side. As a consequence, cooling at constant fO_2 is sufficient to drive exsolution of ilmenite or of an ilmenite-hematite solid-solution from Ti-rich magnetite.

At even higher temperatures, crystals of the magnetite–ulvospinel solid-solution series may incorporate appreciable amounts of $FeTiO_3$ component, so that a non-stoichiometric, cation-deficient Ti-rich magnetite is produced. Such a non-stoichiometric, Ti-rich magnetite may be envisaged as a solid solution between an $\square\,Fe^{2+}_4Ti^{4+}_4O_{12}$ and an $Fe^{2+}_3Fe^{3+}_6O_{12}$ end-member component, where $\square$ denotes a cation vacancy (Lattard, 1995; Lattard et al., 2005). It has been shown experimentally that cation-deficient Ti-rich magnetite becomes stoichiometric by exsolving ilmenite, when it is cooled below about 900 °C (Lattard, 1995; Lattard et al., 2005; Tan et al., 2016), a process that is referred to as *direct exsolution*. Due to the limited incorporation of the $FeTiO_3$ component into cation-deficient Ti-rich magnetite, the maximum amount of ilmenite that may be produced by direct exsolution is estimated to be less than about 15 vol% (Taylor, 1964).

The ilmenite lamellae observed in the magnetite micro-inclusions in the sample under study are compatible with both oxidation-exsolution and with direct exsolution from a non-stoichiometric Ti-rich magnetite. Both processes occur at temperatures above $\sim$ 600 °C. The generally small volume fraction of the ilmenite lamellae in the magnetite micro-inclusions may be taken as an indication for direct exsolution at $\geq$ 900 °C. In any case, the observed magnetite–ilmenite intergrowth reflects processes that were operative at temperatures in excess of about 600 °C and testify to a high-temperature origin of the plagioclase-hosted

magnetite micro-inclusions.

2.5.4 Relation between magnetite formation and Albite twinning

Most of the magnetite micro-inclusions are bounded by twin boundaries related to the polysynthetic Albite twins in the plagioclase host as shown in Fig. 2.1. Only inclusions with special CORs can actually pass through the twin boundaries. This phenomenon indicates that the inclusions most likely formed at the same time or after twinning had occurred. Albite twinning may occur during growth of plagioclase at low temperature, during cooling-induced monoclinic to triclinic symmetry change, or by deformation (Smith and Brown, 1988). Growth twinning produced during low-temperature crystallization can be excluded for the magmatic plagioclases under study. Due to the lack of any associated deformation features, deformation twinning is regarded as unlikely. The morphology of the polysynthetic Albite twins and the frequently associated Pericline twins rather point to an origin as transformation twins. This view is corroborated by the presence of Carlsbad and Manebach twins, which are typically formed during the growth of monoclinic feldspar (Nespolo and Souvignier, 2017). The presence of Carlsbad and Manebach twins indicates that the plagioclase originally grew with monoclinic symmetry and that the polysynthetic Albite twins formed as a result of cooling-induced high-low inversion (Seifert, 1964). In albite, the transition from analbite to monalbite occurs at around 930 °C (Okamura and Ghose, 1975). This puts an upper temperature limit on inclusion formation.

A schematic sketch illustrating the preferred genetic model for the formation of the oriented magnetite and composite micro-inclusions in plagioclase from oceanic gabbro is shown in Fig. 2.9. In the magmatic stage, the plagioclase crystallized from the melt forming growth twins after the Carlsbad and Manebach twin laws (Fig. 2.9a). In a second, supposedly late magmatic stage, polysynthetic twins after the Albite and Pericline twin laws were formed in plagioclase a process that was probably related to the monoclinic–triclinic transformation (Fig. 2.9b). Synchronously or after the Albite and Pericline twinning, Ti-rich magnetite started to precipitate from the plagioclase grain (Fig. 2.9c). Figure 2.9d shows a sketch of an individual titanomagnetite inclusion. The titanomagnetite inclusions may be accompanied by orthopyroxene and/or clinopyroxene (Fig. 2.9e). Figure 2.9f shows the specific case described in Fig. 2.4a, where titanomagnetite exsolved lamellae ilmenite. In addition, mica formed during a late hydrothermal stage.

Plagioclase hosted, oriented needle-shaped magnetite micro-inclusions are a common phenomenon in igneous mafic rocks. Precipitation of the magnetite micro-inclusions from Fe-bearing plagioclase appears to be a viable formation pathway. Primary magmatic plagioclase from mafic igneous rocks has sufficiently

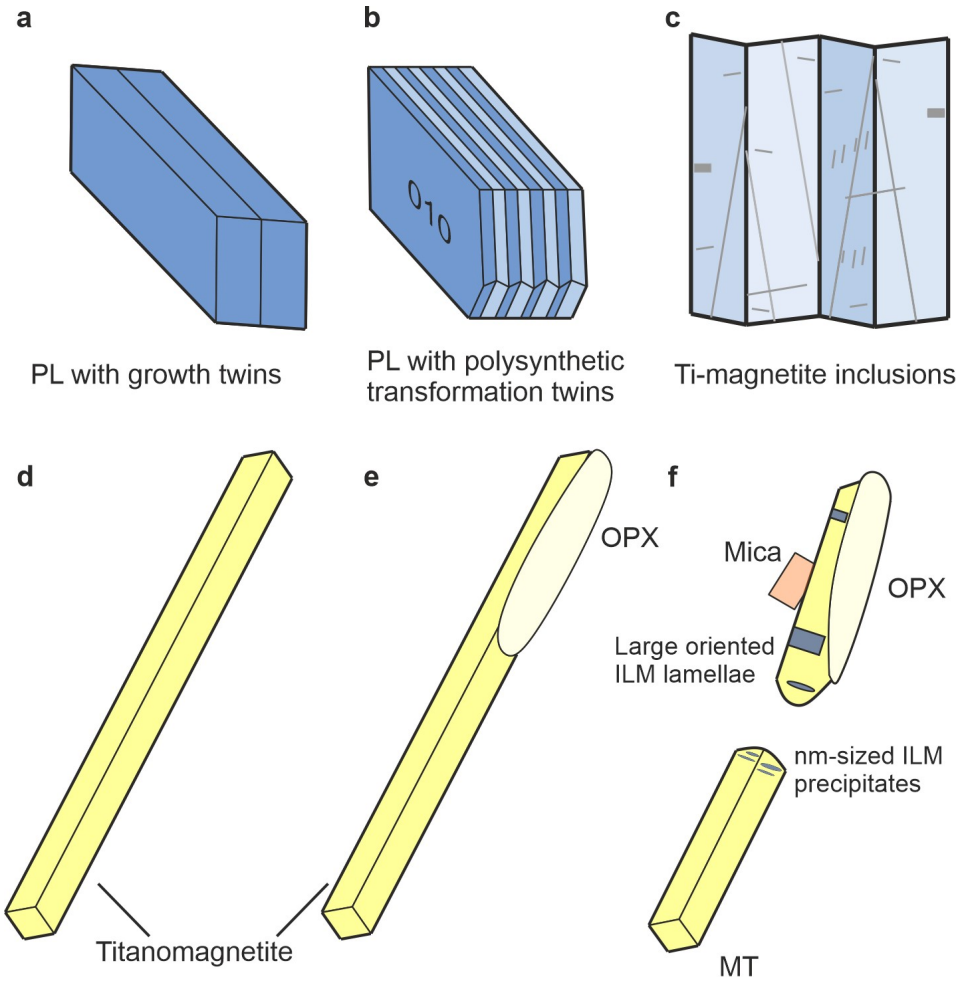

Figure 2.9: Schematic illustration of inclusion genesis. **a** Plagioclase with growth twinning after the Manebach or Carlsbad twin laws. **b** Plagioclase with polysynthetic twins due to twinning after the Albite twin law. **c** Oriented needle-shaped micro-inclusions of Ti-magnetite appear synchronous to or after Albite twinning. **d** Homogeneous Ti-magnetite micro-inclusions with prismatic shape and high aspect ratio in the plagioclase host. **e** Orthopyroxene grown on the magnetite simultaneously to or shortly after its precipitation from the plagioclase host. **f** Specific case with decomposition of Ti-magnetite into magnetite and ilmenite lamellae and mica that supposedly formed at a late hydrothermal stage as shown in Fig. 2.4.

high FeO_T contents so that the Fe needed for the precipitation of magnetite can be derived from the plagioclase host exclusively. The mechanism by which an Fe-bearing plagioclase becomes supersaturated with respect to magnetite may differ between different environments. For the case at hand, interaction with a reducing fluid derived from the serpentinization of mantle peridotite is the most likely reason. Understanding the formation pathways and, in particular, constraining the crystallization temperature of the plagioclase-hosted magnetite micro-inclusion is highly relevant for paleomagnetic reconstructions. Moreover, the systematic SORs and CORs of the magnetite micro-inclusion with respect to the plagioclase host may potentially cause magnetic anisotropy, which is of particular importance in the context of single grain paleomagnetic techniques (Tarduno et al., 2006) and the analysis of rock magnetic fabric (Higgins, 2006; Selkin et al., 2014). A systematic study trying to relate the statistical distribution of magnetite micro-inclusion orientations to the anisotropy of magnetic susceptibility and remanence is underway.

2.6 Conclusions

Oriented needle- and lath-shaped magnetite micro-inclusions in rock-forming plagioclase from oceanic gabbro dredged at the mid-Atlantic ridge at 13° 01–02' N, 44° 52' W were investigated. The micro-inclusions show systematic shape and crystallographic orientation relationships with the plagioclase host. The magnetite needles are elongated along one of their MT⟨111⟩ directions and the needle elongation directions are aligned with one of the PL(112)n, PL($1\bar{5}0$)n, PL($\bar{3}12$)n, PL(150)n or PL(100)n directions, where PL(*hkl*)n denotes the direction normal to the PL(*hkl*) lattice plane. One additional inclusion type has its elongation direction parallel to one of the MT⟨110⟩ directions and the PL[001] direction. The orientation relationships are due to the good fit between oxygen layers in the crystal structures of both phases. The magnetite grains may be accompanied by subordinate ortho- and/or clinopyroxene giving raise to composite inclusions. Both the single-phase magnetite as well as the composite magnetite–pyroxene micro-inclusions probably formed by exsolution from an Fe-bearing plagioclase. This process requires partial reduction of the ferric iron originally contained in the plagioclase and thus necessitates extraction of oxygen from the plagioclase. This probably occurred during interaction with reducing fluids from the serpentinization of associated ultramafic rocks, which drove out-diffusion of oxygen from the plagioclase grains. The shape and crystallographic orientation relationships between the magnetite micro-inclusions and the plagioclase host follow the plagioclase lattice orientations in different plagioclase twin domains indicating that the inclusions were formed synchronous to or after twinning. The presence of up to about 15 vol% of oriented, relatively coarse ilmenite lamellae within the magnetite crystals indicates oxidation-exsolution or direct exsolution from Ti-rich magnetite at temperatures $\geq$ 600 °C. This is above the Curie temperature of magnetite implying that the magnetic signatures of the magnetite-bearing plagioclase grains represent thermoremanent magnetization.

Appendix

For analyzing possible mass balance scenarios for the precipitation of magnetite and potentially accompanying pyroxene from Fe- and Mg-bearing plagioclase, we select a set of 7 components, including SiO_2, Al_2O_3, FeO, MgO, CaO, Na_2O and O_2, and we allow for 12 mineral phases or phase components including $CaAl_2Si_2O_8$, $CaFe^{3+}AlSi_2O_8$, $CaFe^{2+}Si_3O_8$, $CaMgSi_3O_8$, $Fe^{2+}Al_2Si_2O_8$, $NaAlSi_3O_8$, $NaFe^{3+}Si_3O_8$, $MgSiO_3$, $FeSiO_3$, $MgFe^{3+}_2O_4$, Fe_3O_4, $CaSiO_3$ and oxygen. The sum formulae, abbreviations of the phase or phase component and the molar amounts of the oxide components contained in one formula unit of phase or phase component are given in Table 2.1. We define the composition vector of phase component j as

Table 2.1: Sum formulae and molar contents of the chosen system components per mole of formula unit of the phases and phase components selected for describing mass balance scenarios for the precipitation of magnetite and potentially accompanying pyroxene from Fe- and Mg-bearing plagioclase.

Sum formula	SiO_2	Al_2O_3	FeO	MgO	CaO	Na_2O	O_2
$CaAl_2Si_2O_8$	2	1	0	0	1	0	0
$CaFe^{3+}AlSi_2O_8$	2	0.5	1	0	1	0	0.25
$CaFe^{2+}Si_3O_8$	3	0	1	0	1	0	0
$CaMgSi_3O_8$	3	0	0	1	1	0	0
$Fe^{2+}Al_2Si_2O_8$	2	1	1	0	0	0	0
$NaAlSi_3O_8$	3	0.5	0	0	0	0.5	0
$NaFe^{3+}Si_3O_8$	3	0	1	0	0	0.5	0.25
$FeSiO_3$	1	0	1	0	0	0	0
$MgSiO_3$	1	0	0	1	0	0	0
$CaSiO_3$	1	0	0	0	1	0	0
Fe_3O_4	0	0	3	0	0	0	0.5
$MgFe_2^{3+}O_4$	0	0	2	1	0	0	0.5
O_2	0	0	0	0	0	0	1

$$n_j = \begin{pmatrix} n_1^j \\ n_2^j \\ \vdots \\ n_c^j \end{pmatrix} \tag{2.4}$$

where n_i^j gives the number of moles of component i contained per formula unit of phase or phase component j, and c is the number of components. We now build a matrix **A** using the composition vectors of the twelve phases or phase components and of oxygen as the columns of **A** and calculate the orthonormal basis of the zero space of **A**. This delivers a set of six linearly independent equations, which correspond to all linearly independent stoichiometric reaction equations that may be written among the phases and

phase components:

$$CaFe^{3+}AlSi_2O_8 + NaAlSi_3O_8 = CaAl_2Si_2O_8 + NaFe^{3+}Si_3O_8 \quad (2.5)$$

$$CaMgSi_3O_8 + FeSiO_3 = CaFe^{2+}Si_3O_8 + MgSiO_3 \quad (2.6)$$

$$CaAl_2Si_2O_8 + FeSiO_3 = Fe^{2+}Al_2Si_2O_8 + CaSiO_3 \quad (2.7)$$

$$2\,CaFe^{3+}AlSi_2O_8 + 4\,FeSiO_3 = 2\,CaFe^{2+}Si_3O_8 + Fe^{2+}Al_2Si_2O_8 + Fe_3O_4 \quad (2.8)$$

$$2\,CaFe^{3+}AlSi_2O_8 + CaMgSi_3O_8 + 4\,FeSiO_3 = 3\,CaFe^{2+}Si_3O_8 + Fe^{2+}Al_2Si_2O_8 + MgFe_2^{3+}O_4 \quad (2.9)$$

$$4\,CaFe^{3+}AlSi_2O_8 + 2\,CaFe^{2+}Si_3O_8 + 4\,Fe^{2+}Al_2Si_2O_8 = 6\,CaAl_2Si_2O_8 + 10\,FeSiO_3 + O_2 \quad (2.10)$$

The stoichiometric equations of all possible reactions can be written as linear combinations of Eqs. 2.5-2.10. The first three equations correspond to cation exchange reactions. Equation 2.5 represents the exchange of Al and Fe^{3+} between Ca and Na plagioclase. Equation 2.6 represents the exchange of Fe^{2+} and Mg between Ca plagioclase and pyroxene. Equation 2.7 represents the exchange of Fe^{2+} and Ca between plagioclase and pyroxene. Equations 2.8 –2.10 correspond to net-transfer reactions. Equation 2.8 represents a reaction producing magnetite from Fe^{3+}-bearing plagioclase and Fe^{2+}-bearing pyroxene. Equation 2.9 represents a reaction producing magnesioferrite from Fe- and Mg-bearing Ca plagioclase and Fe pyroxene. Finally, Eq. 2.10 represents a reaction producing Fe pyroxene and oxygen from Fe-bearing plagioclase.

From combining Eqs. 2.8 and 2.10, a reaction equation for the formation of magnetite or magnetite and pyroxene on the expense of Fe-bearing Ca plagioclase is obtained. Taking Eq. 2.8 $+x$ Eq. 2.10, we have

$$\begin{aligned}&(2+4x)\,CaFe^{3+}AlSi_2O_8 + (4x-1)\,Fe^{2+}Al_2Si_2O_8 = \\ &1\,Fe_3O_4 + (2-2x)\,CaFe^{2+}Si_3O_8 + 6x\,CaAl_2Si_2O_8 + (10x-4)\,FeSiO_3 + x\,O_2\end{aligned} \quad (2.11)$$

For $0.4 < x$, both magnetite and pyroxene are produced from Fe-bearing plagioclase; for $x = 0.4$, only magnetite is formed. Equation 2.11 is written in the Mg- and Na-free subsystem. Both components and the corresponding phase components may be involved by adding in Eqs. 2.5, 2.6, 2.7, and 2.9, so that Mg pyroxene, Ca pyroxene and magnesioferrite phase components would appear on the product side in addition.

Acknowledgements

The dredge samples were provided by courtesy of Alexey Pertsev. We gratefully acknowledge the constructive and helpful comments by three anonymous reviewers. Editorial hangling is gratefully acknowledged.

Funding

Open access funding provided by University of Vienna. This research was funded by the Austrian Science Foundation (FWF) Grant Nr. I 3998-N29 and by the Russian Foundation for Basic Research (RFBR) Grant Nr. 18-55-14003. Support by Slovene Research Agency (ARRS) N1-0115 Grant is gratefully acknowledged.

Author Contributions

All the authors contributed to the study conception and design. Material preparation, data collection, and analysis were performed by GB, OA, GH, AR and RA. The first draft of the manuscript was written by GB, and all the authors commented on previous versions of the manuscript. All the authors read and approved the final manuscript.

Bibliography

O. Ageeva, G. Habler, D. Topa, T. Waitz, C. Li, A. Pertsev, T. Griffiths, O. Zhilicheva, and R. Abart. Plagioclase hosted fe-ti-oxide micro-inclusions in an oceanic gabbro-plagiogranite association from the mid atlantic ridge at 13°34' n. *American Journal of Science*, 316(2):85–109, 2016. ISSN 0002-9599. doi: 10.2475/02.2016.01.

O. Ageeva, G. Habler, A. Pertsev, and R. Abart. Fe-Ti oxide micro-inclusions in clinopyroxene of oceanic gabbro: phase content, orientation relations and petrogenetic implication. *Lithos*, 290:104–115, 2017. doi: 10.1016/j.lithos.2017.08.007.

O. Ageeva, G. Bian, G. Habler, A. Pertsev, and R. Abart. Crystallographic and shape orientations of magnetite micro-inclusions in plagioclase. *Contributions to Mineralogy and Petrology*, 175(10):1–16, 2020. doi: 10.1007/s00410-020-01735-8.

A. A. Ariskin and G. S. Barmina. Comagmat: development of a magma crystallization model and its petrological applications. 2004.

P. Bell and H. Mao. Measurements of the polarized crystal field spectra of ferrous and ferric iron in seven terrestrial plagioclases. *Carnegie Institution of Washington Year Book*, 72:574–576, 1973.

S. Bernstein, M. T. Rosing, C. K. Brooks, and D. K. Bird. An ocean-ridge type magma chamber at a passive volcanic, continental margin: the kap edvard holm layered gabbro complex, east greenland. *Geological Magazine*, 129(4):437–456, 1992. doi: 10.1017/S001675680001952X.

A. R. Biedermann, T. Pettke, R. J. Angel, and A. M. Hirt. Anisotropy of magnetic susceptibility in alkali feldspar and plagioclase. *Geophysical Supplements to the Monthly Notices of the Royal Astronomical Society*, 205(1):479–489, 2016. doi: 10.1093/gji/ggw042.

A. R. Biedermann, M. Jackson, M. Chadima, A. M. Hirt, and J. M. Feinberg. Beyond the second-order magnetic anisotropy tensor: higher-order components due to oriented magnetite exsolutions in pyroxenes, and implications for palaeomagnetic and structural interpretations. *Geophysical journal international*, 223(2):915–933, 2020. doi: 10.1093/gji/ggaa355.

M. E. Brandriss and D. K. Bird. Effects of h2o on phase relations during crystallization of gabbros in the kap edvard holm complex, east greenland. *Journal of Petrology*, 40(6):1037–1064, 1999. doi: 10.1093/petroj/40.6.1037.

L. Chang, A. P. Roberts, D. Heslop, A. Hayashida, J. Li, X. Zhao, W. Tian, and Q. Huang. Widespread occurrence of silicate-hosted magnetic mineral inclusions in marine sediments and their contribution to paleomagnetic recording. *Journal of Geophysical Research: Solid Earth*, 121(12):8415–8431, 2016. doi: 10.1002/2016JB013109.

M. J. Cheadle and J. S. Gee. Quantitative textural insights into the formation of gabbro in mafic intrusions. *Elements: An International Magazine of Mineralogy, Geochemistry, and Petrology*, 13(6):409–414, 2017. doi: 10.2138/gselements.13.6.409.

D. Cherniak. Cation diffusion in feldspars. *Reviews in Mineralogy and Geochemistry*, 72(1):691–733, 2010. doi: 10.2138/rmg.2010.72.15.

K. E. Davis. Magnetite rods in plagioclase as the primary carrier of stable nrm in ocean floor gabbros. *Earth and Planetary Science Letters*, 55(1):190–198, 1981.

D. J. Dunlop. The rock magnetism of fine particles. *Physics of the Earth and Planetary Interiors*, 26(1-2): 1–26, 1981. doi: 10.1016/0031-9201(81)90093-5.

D. J. Dunlop and Ö. Özdemir. *Rock magnetism: fundamentals and frontiers*. Number 3. Cambridge university press, 2001.

J. M. Feinberg, H.-R. Wenk, P. R. Renne, and G. R. Scott. Epitaxial relationships of clinopyroxene-hosted magnetite determined using electron backscatter diffraction (ebsd) technique. *American Mineralogist*, 89(2-3):462–466, 2004. doi: 10.2138/am-2004-2-328.

J. M. Feinberg, G. R. Scott, P. R. Renne, and H.-R. Wenk. Exsolved magnetite inclusions in silicates: Features determining their remanence behavior. *Geology*, 33(6):513–516, 2005. doi: 10.1130/G21290.1.

J. M. Feinberg, R. J. Harrison, T. Kasama, R. E. Dunin-Borkowski, G. R. Scott, and P. R. Renne. Effects of internal mineral structures on the magnetic remanence of silicate-hosted titanomagnetite inclusions: An electron holography study. *Journal of Geophysical Research: Solid Earth*, 111(B12), 2006. doi: 10.1029/2006JB004498.

M. Fleet, G. A. Bilcox, and R. L. Barnett. Oriented magnetite inclusions in pyroxenes from the Grenville Province. *The Canadian Mineralogist*, 18(1):89–99, 1980.

W. Gao, C. L. Ciobanu, N. J. Cook, A. Slattery, F. Huang, and D. Wang. Nanoscale study of lamellar exsolutions in clinopyroxene from olivine gabbro: Recording crystallization sequences in iron-rich layered intrusions. *American Mineralogist: Journal of Earth and Planetary Materials*, 104(2):244–261, 2019. doi: 10.2138/am-2019-6764.

T. A. Griffiths, G. Habler, and R. Abart. Determining the origin of inclusions in garnet: challenges and new diagnostic criteria. *American Journal of Science*, 320(9):753–789, 2020. doi: 10.2475/11.2020.01.

T. L. Grove and M. B. Baker. Phase equilibrium controls on the tholeiitic versus calc-alkaline differentiation trends. *Journal of Geophysical Research: Solid Earth*, 89(B5):3253–3274, 1984. doi: 10.1029/JB089iB05p03253.

T. L. Grove, R. J. Kinzler, and W. B. Bryan. Fractionation of mid-ocean ridge basalt (morb). *Washington DC American Geophysical Union Geophysical Monograph Series*, 71:281–310, 1992. doi: 10.1029/GM071p0281.

M. D. Higgins. *Quantitative textural measurements in igneous and metamorphic petrology*. Cambridge university press, 2006.

A. M. Hofmeister and G. R. Rossman. Determination of fe3+ and fe2+ concentrations in feldspar by optical absorption and epr spectroscopy. *Physics and Chemistry of Minerals*, 11(5):213–224, 1984. doi: 10.1007/BF00308136.

D. V. Kent, B. Honnorez, N. D. Opdyke, and P. J. Fox. Magnetic properties of dredged oceanic gabbros and the source of marine magnetic anomalies. *Geophysical Journal International*, 55(3):513–537, 1978. doi: 10.1111/j.1365-246X.1978.tb05925.x.

F. Klein, J. D. Tarnas, and W. Bach. Abiotic sources of molecular hydrogen on earth. *Elements: An International Magazine of Mineralogy, Geochemistry, and Petrology*, 16(1):19–24, 2020. doi: 10.2138/gselements.16.1.19.

J. Knafelc, J. Filiberto, E. C. Ferré, J. A. Conder, L. Costello, J. R. Crandall, M. D. Dyar, S. A. Friedman, D. R. Hummer, and S. P. Schwenzer. The effect of oxidation on the mineralogy and magnetic properties of olivine. *American Mineralogist: Journal of Earth and Planetary Materials*, 104(5):694–702, 2019. doi: 10.2138/am-2019-6829.

S.-C. L. Lappe, N. S. Church, T. Kasama, A. B. da Silva Fanta, G. Bromiley, R. E. Dunin-Borkowski, J. M. Feinberg, S. Russell, and R. J. Harrison. Mineral magnetism of dusty olivine: a credible recorder of pre-accretionary remanence. *Geochemistry, Geophysics, Geosystems*, 12(12), 2011. doi: 10.1029/2011GC003811.

D. Lattard. Experimental evidence for the exsolution of ilmenite from titaniferous spinel. *American Mineralogist*, 80(9-10):968–981, 1995. doi: 10.2138/am-1995-9-1013.

D. Lattard, U. Sauerzapf, and M. Käsemann. New calibration data for the fe–ti oxide thermo-oxybarometers from experiments in the fe–ti–o system at 1 bar, 1,000–1,300 c and a large range of oxygen fugacities. *Contributions to Mineralogy and Petrology*, 149:735–754, 2005. doi: 10.1007/s00410-005-0679-2.

J. Longhi, D. Walker, and J. F. Hays. Fe and mg in plagioclase. In *Lunar and planetary science conference proceedings*, volume 7, pages 1281–1300, 1976.

K. L. Lundgaard and C. Tegner. Partitioning of ferric and ferrous iron between plagioclase and silicate melt. *Contributions to Mineralogy and Petrology*, 147:470–483, 2004. doi: 10.1007/s00410-004-0568-0.

J. McConnell. Microstructures of minerals as petrogenetic indicators. *Annual Review of Earth and Planetary Sciences*, 3(1):129–155, 1975.

R. Nakada, M. Sato, M. Ushioda, Y. Tamura, and S. Yamamoto. Variation of iron species in plagioclase crystals by x-ray absorption fine structure analysis. *Geochemistry, Geophysics, Geosystems*, 20(11):5319–5333, 2019. doi: 10.1029/2018GC008131.

M. Nespolo and B. Souvignier. Structural analysis of twins in feldspars. i. carlsbad twinning. *European Journal of Mineralogy*, 29(6):939–947, 2017. doi: 10.1127/ejm/2017/0029-2678.

E. S. Nikolaisen, R. J. Harrison, K. Fabian, and S. A. McEnroe. Hysteresis of natural magnetite ensembles: Micromagnetics of silicate-hosted magnetite inclusions based on focused-ion-beam nanotomography. *Geochemistry, Geophysics, Geosystems*, 21(11):e2020GC009389, 2020. doi: 10.1029/2020GC009389.

F. P. Okamura and S. Ghose. Analbite→ monalbite transition in a heat treated twinned amelia albite. *Contributions to Mineralogy and Petrology*, 50(3):211–216, 1975. doi: 10.1007/BF00371041.

H. Ondréas, M. Cannat, Y. Fouquet, and A. Normand. Geological context and vents morphology of the ultramafic-hosted Ashadze hydrothermal areas (Mid-Atlantic Ridge 13° N). *Geochemistry, Geophysics, Geosystems*, 13(11), 2012. doi: 10.1029/2012GC004433.

H. S. C. O'Neill and W. Dollase. Crystal structures and cation distributions in simple spinels from powder xrd structural refinements: MgCr2o4, ZnCr2o4, Fe3O4 and the temperature dependence of the cation distribution in ZnAl2O4. *Physics and Chemistry of Minerals*, 20(8):541–555, 1994. doi: 10.1007/BF00211850.

C. Peirce, G. Reveley, A. Robinson, M. Funnell, R. Searle, N. Simão, C. MacLeod, and T. Reston. Constraints on crustal structure of adjacent occs and segment boundaries at 13° n on the mid-atlantic ridge. *Geophysical Journal International*, 217(2):988–1010, 2019. doi: 10.1093/gji/ggz074.

C. Peirce, A. Robinson, M. Funnell, R. Searle, C. MacLeod, and T. Reston. Magmatism versus serpentinization—crustal structure along the 13° n segment at the mid-atlantic ridge. *Geophysical journal international*, 221(2):981–1001, 2020. doi: 10.1093/gji/ggaa052.

W. Phinney. Partition coefficients for iron between plagioclase and basalt as a function of oxygen fugacity: Implications for archean and lunar anorthosites. *Geochimica et Cosmochimica Acta*, 56(5):1885–1895, 1992. doi: 10.1016/0016-7037(92)90318-D.

A. Proyer, G. Habler, R. Abart, R. Wirth, K. Krenn, and G. Hoinkes. Tio 2 exsolution from garnet by open-system precipitation: evidence from crystallographic and shape preferred orientation of rutile inclusions. *Contributions to Mineralogy and Petrology*, 166:211–234, 2013. doi: 10.1007/s00410-013-0872-7.

P. R. Renne, G. R. Scott, J. M. Glen, and J. M. Feinberg. Oriented inclusions of magnetite in clinopyroxene: Source of stable remanent magnetization in gabbros of the Messum Complex, Namibia. *Geochemistry, Geophysics, Geosystems*, 3(12):1–11, 2002. doi: 10.1029/2002GC000319.

K. E. Seifert. The genesis of plagioclase twinning in the nonewaug granite. *American Mineralogist: Journal of Earth and Planetary Materials*, 49(3-4):297–320, 1964.

P. A. Selkin, J. S. Gee, and W. P. Meurer. Magnetic anisotropy as a tracer of crystal accumulation and transport, middle banded series, stillwater complex, montana. *Tectonophysics*, 629:123–137, 2014. doi: /10.1016/j.tecto.2014.03.028.

S. Silantyev, E. Krasnova, M. Cannat, N. Bortnikov, N. Kononkova, and V. Beltenev. Peridotite-gabbro-trondhjemite association of the mid-atlantic ridge between 12° 58 and 14° 45 n: Ashadze and logachev hydrothermal vent fields. *Geochemistry International*, 49:323–354, 2011. doi: 10.1134/S0016702911040070.

D. K. Smith, J. Escartín, H. Schouten, and J. R. Cann. Fault rotation and core complex formation: Significant processes in seafloor formation at slow-spreading mid-ocean ridges (mid-atlantic ridge, 13–15 n). *Geochemistry, Geophysics, Geosystems*, 9(3), 2008. doi: 10.1029/2007GC001699.

J. V. Smith and W. L. Brown. *Feldspar minerals*. Springer Science & Business Media, 1988.

P. Sobolev. Orientation of acicular iron-ore mineral inclusions in plagioclase. *International Geology Review*, 32(6):616–628, 1990.

S. Speczik, J. Wiszniewska, and R. Diedel. Minerals, exsolution features and geochemistry of fe-ti ores of the suwałki district (north-east poland). *Mineralium Deposita*, 23:200–210, 1988. doi: 10.1007/BF00204302.

G. Suhr, E. Hellebrand, K. Johnson, and D. Brunelli. Stacked gabbro units and intervening mantle: A detailed look at a section of iodp leg 305, hole u1309d. *Geochemistry, Geophysics, Geosystems*, 9(10), 2008. doi: 10.1029/2008GC002012.

W. Tan, P. Liu, H. He, C. Y. Wang, and X. Liang. Mineralogy and Origin of Exsolution in Ti-rich Magnetite from Different Magmatic Fe-ti Oxide-bearing Intrusions. *The Canadian Mineralogist*, 54(3):539–553, 05 2016. ISSN 0008-4476. doi: 10.3749/canmin.1400069.

J. Tarduno, R. Cottrell, and A. Smirnov. The paleomagnetism of single silicate crystals: Recording geomagnetic field strength during mixed polarity intervals, superchrons, and inner core growth. *Reviews of Geophysics*, 44(1), 2006. doi: 10.1029/2005RG000189.

J. A. Tarduno, R. D. Cottrell, R. K. Bono, H. Oda, W. J. Davis, M. Fayek, O. v. Erve, F. Nimmo, W. Huang, E. R. Thern, et al. Paleomagnetism indicates that primary magnetite in zircon records a strong hadean geodynamo. *Proceedings of the National Academy of Sciences*, 117(5):2309–2318, 2020. doi: 10.1073/pnas.191655311.

R. W. Taylor. Phase equilibria in the system feo-fe2o3-tio2 at 1300° c. *American Mineralogist: Journal of Earth and Planetary Materials*, 49(7-8):1016–1030, 1964.

C. Tegner. Iron in plagioclase as a monitor of the differentiation of the skaergaard intrusion. *Contributions to Mineralogy and Petrology*, 128(1):45–51, 1997. doi: 10.1007/s004100050292.

Y. Usui, T. Shibuya, Y. Sawaki, and T. Komiya. Rock magnetism of tiny exsolved magnetite in plagioclase from a paleoarchean granitoid in the pilbara craton. *Geochemistry, Geophysics, Geosystems*, 16(1):112–125, 2015. doi: https://doi.org/10.1002/2014GC005508.

J. Vance. On synneusis. *Contribution to Mineralogy and Petrology*, 24:7–29, 1969. doi: 10.1007/BF00398750.

S. Villiger, P. Ulmer, and O. Müntener. Equilibrium and fractional crystallization experiments at 0· 7 gpa; the effect of pressure on phase relations and liquid compositions of tholeiitic magmas. *Journal of Petrology*, 48(1):159–184, 2007. doi: 10.1093/petrology/egl058.

L. R. Wager and R. Mitchell. The distribution of trace elements during strong fractionation of basic magma—a further study of the skaergaard intrusion, east greenland. *Geochimica et Cosmochimica Acta*, 1(3):129–208, 1951. doi: 10.1016/0016-7037(51)90016-6.

H.-R. Wenk and W. Wilde. Chemical anomalies of lunar plagioclase, described by substitution vectors and their relation to optical and structural properties. *Contributions to Mineralogy and Petrology*, 41(2): 89–104, 1973. doi: 10.1007/BF00375035.

H.-R. Wenk, K. Chen, and R. Smith. Morphology and microstructure of magnetite and ilmenite inclusions in plagioclase from Adirondack anorthositic gneiss. *American Mineralogist*, 96(8-9):1316–1324, 08 2011. ISSN 0003-004X. doi: 10.2138/am.2011.3760.

P. R. Whitney. Spinel inclusions in plagioclase of metagabbros from the adirondack highlands. *American Mineralogist: Journal of Earth and Planetary Materials*, 57(9-10):1429–1436, 1972.

Supplementary Information

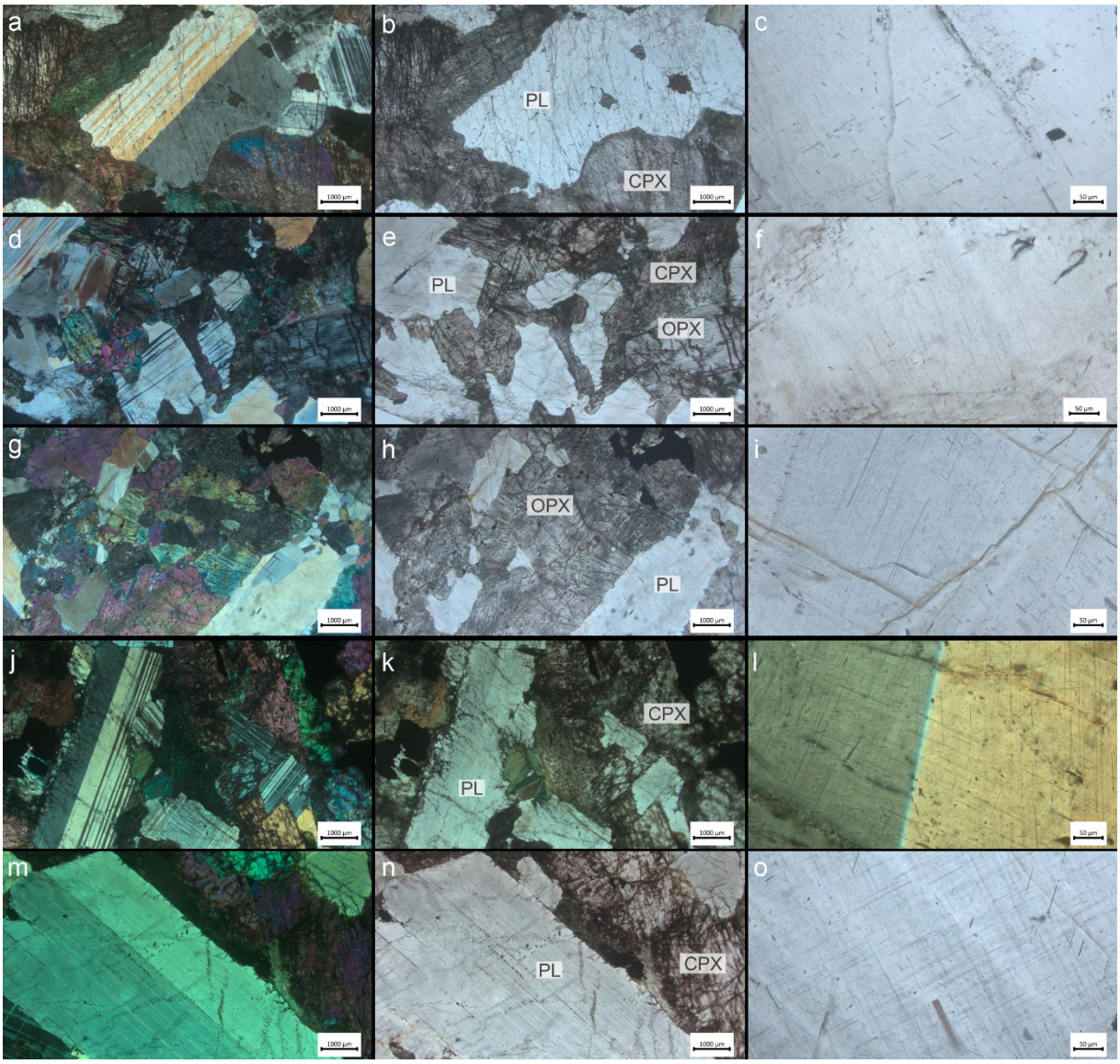

Figure S2.1: Transmitted light optical images; left and central columns show microstructure overview under crossed polarizers (left column) and plane polarized light (central column) and details of plagioclase grains with magnetite micro-inclusions (right column). Samples are from the mid-Atlantic ridge. Sample L32-101-1 (a-c): coarse-grained gabbronorite injected by fine-grained felsic stringers from Oceanic Core Complex 13°34.179'N, 44°54.990'W; Sample L30-277-7 (d-f) and sample L30-277-10 (g-i): gabbro-norites from the western flank of the rift valley at Oceanic Core Complex 13°30.883'N, 44°57.727'W; Sample 1514-17 (j-o): oxide gabbro from the Ashadze complex (peridotites and evolved oxide gabbros) 12°59.330'N, 44°51.466'W (compare bulk rock composition given in Table S2.1); CPX – clinopyroxene, OPX – orthopyroxene, PL – plagioclase

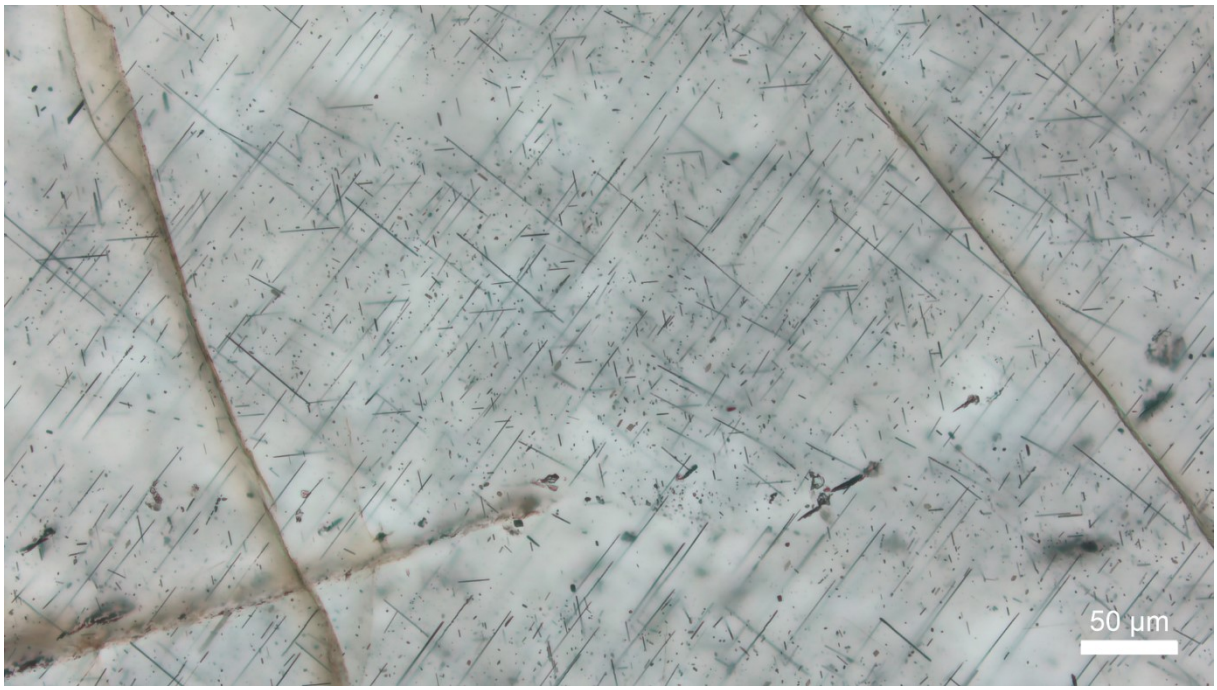

Figure S2.2: Light optical microphotograph (plane polarized light) showing a domain in plagioclase with needle-shaped magnetite micro-inclusions with at least five well discernible shape orientation relationships to the plagioclase host; sample L30-277-7

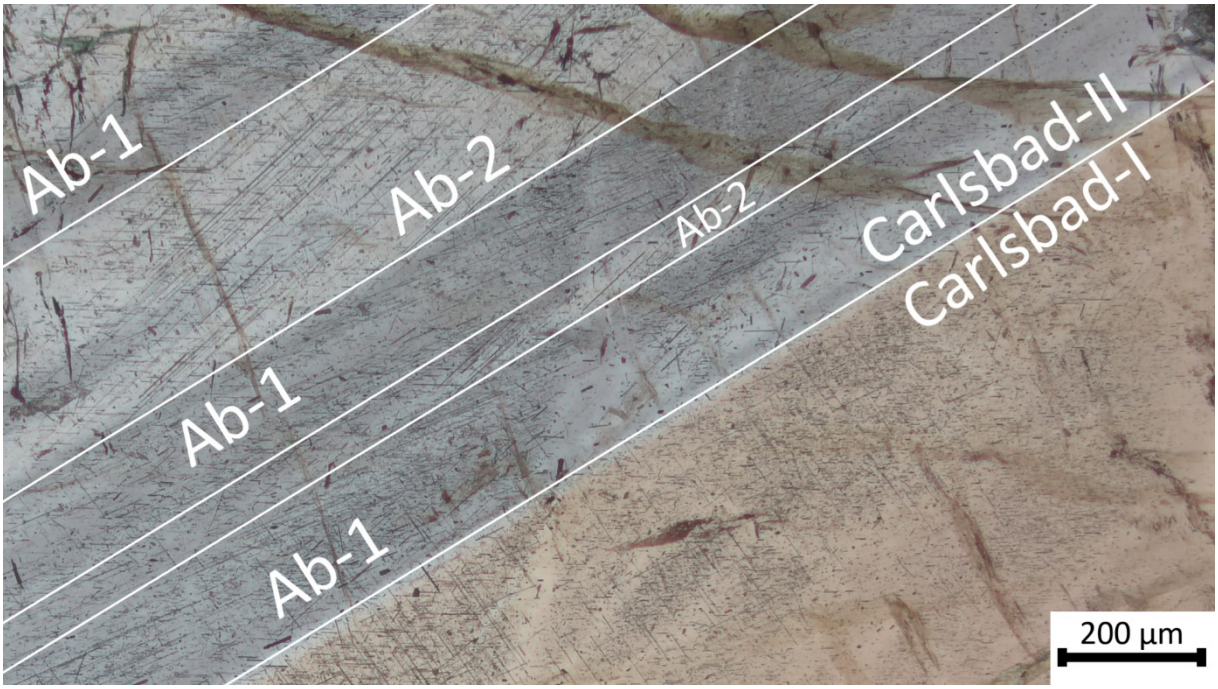

Figure S2.3: Light optical microphotograph (crossed polarizers) showing a domain in plagioclase with needle-shaped magnetite micro-inclusions with shape orientations following the Carlsbad and Albite twins of the plagioclase host; sample L30-277-7

Table S2.1: XRF whole rock analyses of gabbro with plagioclase-hosted magnetite micro-inclusions; sample 1514-25 most closely resembles sample L30-277-7, which was studied in detail.

N	Loc*	SiO_2	Al_2O_3	TiO_2	Fe_2O_3	MnO	MgO	CaO	Na_2O	K_2O	P_2O_5	LOI	Sum	Description
1480-9	1	50.40	19.00	0.40	6.58	0.18	7.40	11.90	2.73	0.10	<.05	1.24	100.00	gabbro
1480-10	1	50.60	15.60	0.36	8.27	0.37	11.80	7.51	2.18	0.14	<.05	3.21	100.00	gabbro
1514-17	2	44.00	13.00	3.57	19.30	0.20	8.09	8.70	2.37	0.21	0.09	0.21	99.70	oxide gabbro
1514-39	2	49.00	15.10	1.58	12.70	0.22	7.23	11.00	2.59	0.15	<.05	0.38	99.90	fine-grained gabbro
1514-25	2	50.20	16.90	1.15	10.90	0.19	5.99	9.74	3.50	0.17	<.05	1.07	99.90	coarse-grained gabbro
L32-101-1	3	54.6	17.8	0.64	6.1	0.1	10.3	6.47	3.42	0.41	0.057	0.3	100	coarse-grained gabbro with plagiogranite veins
L32-262-4	4	50.7	19.3	0.28	6.01	0.1	9.64	9.04	2.6	0.17	<.05	2.17	100	gabbro

* Location (dredge lines start points): 1 Ashadze complex (peridotites and evolved oxide gabbros) 12° 59.330'N, 44° 51.466' W; 2 Ashadze complex 12° 59.324' N, 44° 51.634' W; 3 Oceanic Core Complex 13°34.179' N, 44° 54.990' W; 4 Oceanic Core Complex 13° 31.116' N, 44°56.964' W

Reference

Dredge stations 1480 and 1514

Beltenev, V.E., Ivanov, V.N., Krotov, A.G. et al., 2006. Geological structure of the site 13°N of the Mid-Atlantic Ridge (Ashadze ore cluster): Report on Cruise 26 of the R/V 'Professor Logatchev' (in Russian). Polar Marine Geosurvay Expedition, Saint Petersburg – Lomonosov.

Dredge stations L32-101 and L32-262

Beltenev, V.E., Ivanov, V.N., Antipov, G.V. et al., 2010. Geological and Geophysical studies in order to identify areas promising for deep-sea polymetallic sulfides in the MAR axial zone (within 11°-12°30' N) and search work on the site 13°31' N (in Russian). Report of the Polar Marine Geosurvay Expedition, Saint Petersburg – Lomonosov.

Table S2.2: Representative major element compositions of plagioclase from inclusion-bearing zone (Domain 1-3) to inclusion-free zone (Domain 4-6)

Domain	1		2		3		4		5		6	
Sample	277-7		277-7		277-7		277-7		277-7		277-7	
Beam size / μm	5×4	20×15	5×4	20×15	5×4	20×15	5×4	20×15	5×4	20×15	5×4	20×15
Na_2O	4.740	4.817	4.788	4.852	5.111	5.160	5.346	5.302	5.214	5.365	5.376	5.285
FeO	0.284	0.314	0.299	0.307	0.403	0.325	0.282	0.306	0.300	0.282	0.264	0.254
SiO_2	53.670	53.757	53.886	53.793	54.365	54.643	54.415	54.428	54.859	54.984	54.671	54.734
CaO	11.848	11.577	11.735	11.53	10.937	10.868	10.880	10.869	10.635	10.788	10.556	10.579
K_2O	0.133	0.139	0.161	0.136	0.146	0.155	0.145	0.173	0.148	0.176	0.157	0.191
TiO_2	0.051	0.07	0.065	0.06	0.078	0.066	0.070	0.083	0.071	0.078	0.062	0.081
MgO	0.042	0.044	0.043	0.029	0.045	0.013	0.031	0.037	0.022	0.017	0.035	0.02
Al_2O_3	29.301	29.569	29.144	29.058	28.605	28.65	28.312	28.535	28.499	28.419	28.646	28.393
Total	100.07	100.29	100.12	99.77	99.69	99.88	99.483	99.734	99.748	100.108	99.767	99.537
Si	2.428	2.425	2.436	2.439	2.464	2.469	2.471	2.466	2.480	2.479	2.472	2.480
Al	1.562	1.572	1.553	1.553	1.528	1.526	1.515	1.524	1.518	1.511	1.527	1.516
Fe	0.011	0.012	0.011	0.012	0.015	0.012	0.011	0.012	0.011	0.011	0.010	0.010
Ca	0.574	0.560	0.568	0.560	0.531	0.526	0.529	0.528	0.515	0.521	0.511	0.513
Na	0.416	0.421	0.420	0.426	0.449	0.452	0.471	0.466	0.457	0.469	0.471	0.464
K	0.008	0.008	0.009	0.008	0.008	0.009	0.008	0.010	0.009	0.010	0.009	0.011
Sum	5.001	5.001	5.000	5.000	4.998	4.996	5.008	5.007	4.992	5.003	5.003	4.997
An	57.559	56.585	56.991	56.320	53.719	53.300	52.492	52.585	52.527	52.100	51.565	51.934
Ab	41.671	42.606	42.079	42.889	45.426	45.795	46.675	46.419	46.602	46.887	47.522	46.950
Or	0.769	0.809	0.931	0.791	0.854	0.905	0.833	0.997	0.870	1.012	0.913	1.116

Oxides in wt%; cations per eight oxygen atoms; An = 100 × Ca / (Ca+Na+K); Ab = 100 × Na / (Ca+Na+K); Or = 100 × K / (Ca+Na+K)

Table S2.3: Representative major element compositions of orthopyroxene from core zone (Domain 1-3) to rim zone (Domain 4-6)

Domain	1	2	3	4	5	6
Sample	277-7-ar2	277-7-ar2	277-7-ar2	277-7-ar2	277-7-ar2	277-7-ar2
SiO_2	53.358	53.083	53.489	53.66	53.247	53.470
TiO_2	0.424	0.452	0.360	0.337	0.397	0.455
Cr_2O_3	N.A.	N.A.	N.A.	N.A.	N.A.	N.A.
Al_2O_3	1.248	1.069	1.208	1.221	1.150	1.160
FeO	20.258	20.66	19.678	19.604	20.18	21.156
MnO	N.A.	N.A.	N.A.	N.A.	N.A.	N.A.
MgO	21.859	22.102	22.597	22.282	22.447	21.789
CaO	2.366	1.988	2.347	2.378	2.098	1.703
Na_2O	0.045	0.034	0.031	0.048	0.030	0.013
Total	99.56	99.39	99.71	99.53	99.55	99.75
Si	1.99	1.98	1.98	1.99	1.98	2.00
Ti	0.01	0.01	0.01	0.01	0.01	0.01
Cr	0.00	0.00	0.00	0.00	0.00	0.00
Al	0.05	0.05	0.05	0.05	0.05	0.05
Fe	0.63	0.65	0.61	0.61	0.63	0.66
Mn	0.00	0.00	0.00	0.00	0.00	0.00
Mg	1.21	1.23	1.25	1.23	1.24	1.21
Ca	0.09	0.08	0.09	0.09	0.08	0.07
Na	0.00	0.00	0.00	0.00	0.00	0.00
Sum	4.00	4.00	4.00	4.00	4.00	4.00
Mg#	65.8	65.6	67.2	66.9	66.5	64.7
Wo	4.870	4.069	4.777	4.886	4.276	3.510
En	62.583	62.924	63.965	63.675	63.626	62.459
Fs	32.547	33.007	31.258	31.438	32.099	34.032

Oxides in wt%; cations per six oxygen atoms; Wo = 100 × Ca / (Ca+Mg+Fe); En = 100 ×× Mg / (Ca+Mg+Fe); Fs = 100 × Fe / (Ca+Mg+Fe)

Table S2.4: Representative major element compositions of clinopyroxene from core zone to rim zone (Domain 1-3)

Domain	1	2	3
Sample	277-7-ar2	277-7-ar2	277-7-ar2
SiO_2	53.420	52.523	53.742
TiO_2	0.087	0.206	0.037
Cr_2O_3	N.A.	N.A.	N.A.
Al_2O_3	0.528	1.412	0.219
FeO	7.967	9.594	7.625
MnO	N.A.	N.A.	N.A.
MgO	14.148	14.592	13.958
CaO	22.884	19.708	24.044
Na_2O	0.118	0.259	0.069
K_2O	0.028	0.063	< 0.001
Total	100.31	100.31	100.31
Si	2.00	1.99	2.01
Ti	0.00	0.01	0.00
Cr	0.00	0.00	0.00
Al	0.02	0.06	0.01
Fe	0.25	0.30	0.24
Mn	0.00	0.00	0.00
Mg	0.79	0.82	0.78
Ca	0.92	0.80	0.96
Na	0.01	0.02	0.00
Sum	4.00	4.00	4.00
Mg#	76.0	73.0	76.5
Wo	46.91	41.50	48.66
En	40.34	42.73	39.29
Fs	12.75	15.77	12.05

Oxides in wt%; cations per six oxygen atoms; Wo = 100 × Ca / (Ca+Mg+Fe); En = 100 × Mg / (Ca+Mg+Fe); Fs = 100 × Fe / (Ca+Mg+Fe)

Chapter 3

Crystal structure controls on oriented primary magnetite micro-inclusions in plagioclase from oceanic gabbro

Ge Bian[1,*], Olga Ageeva[1,2], Vladimir Roddatis[3], Chen Li[4,†], Timothy J Pennycook[4], Gerlinde Habler[1], Rainer Abart[1]
* Corresponding author † New affiliation: Thermo Fisher Scientific

1. Department of Lithospheric Research, University of Vienna
2. Institute of Geology of Ore Deposit, Petrography, Mineralogy, and Geochemistry, Russian Academy of Sciences (IGEM, RAS)
3. Helmholtz Centre Potsdam, GFZ German Research Centre for Geosciences
4. Electron microscopy for materials science (EMAT), University of Antwerp

Manuscript status: manuscript accepted for publication

Journal of Petrology, egad008, https://doi.org/10.1093/petrology/egad008

Received: 29 July 2022 / Published online: 27 January 2023

Submitter's own contribution:

In this study, I have performed STEM specimens preparation using FIB technique, carried out STEM results analyses and interpretations, achieved crystallographic orientation analyses, and applied $\Delta\mathbf{g}$ method for a plate-shaped magnetite micro-inclusion basal plane structure and orientation reconstructions. In addition, I have prepared the first draft of this manuscript.

Abstract

Oriented needle-, lath- and plate-shaped magnetite micro-inclusions in rock forming plagioclase from mafic intrusive rocks, were investigated using correlated optical microscopy and scanning transmission electron microscopy. The magnetite micro-inclusions were analysed on cuts parallel and perpendicular to the inclusion–elongation directions. The crystal structures of the two phases are in direct contact along the interfaces. The shape, shape orientation and crystallographic orientation relationships between the magnetite micro-inclusions and the plagioclase host appear to be controlled by the tendency of the system to optimise lattice match along the interfaces. The elongation direction of the inclusions ensures good match between prominent oxygen layers in the magnetite and plagioclase crystal structures across the interfaces bounding the inclusions parallel to their elongation direction. In cross-section, additional modes of lattice match, such as the commensurate impingement of magnetite and plagioclase lattice planes along the interfaces, the parallel alignment of the interfaces to low-index lattice planes of magnetite or plagioclase, or the parallel alignment to low index lattice planes of both phases are observed, which appear to control the selection of interface facets, as well as the shape and crystallographic orientation relationships between magnetite micro-inclusions and plagioclase host. The systematics of the inclusion cross-sectional shapes and crystallographic orientation relationships indicate recrystallisation of magnetite with potential implications for natural remanent magnetisation of magnetite-bearing plagioclase grains.

Keywords

Scanning transmission electron microscopy · Plagioclase hosted magnetite microinclusions · Interface facets · Crystallographic and shape orientation relationships

3.1 Introduction

Oriented magnetite micro-inclusions in rock forming silicate minerals are a common phenomenon in magmatic and metamorphic rocks. Such inclusions often take the form of needles, laths or plates and have been described from olivine (Champness, 1970; Zhang et al., 1999), pyroxene (Fleet et al., 1980; Feinberg et al., 2004; Ageeva et al., 2017) and feldspar (Ageeva et al., 2016; Wenk et al., 2011). In terms of volume, plagioclase is the most abundant mineral in the Earth's crust. Plagioclase from mafic intrusions and their metamorphic derivatives often contains abundant needle-, lath- or plate-shaped magnetite micro-inclusions showing systematic shape orientation relationships (SORs) and crystallographic orienta-

tion relationships (CORs) to the plagioclase host (Ageeva et al., 2016, 2020; Sobolev, 1990; Wenk et al., 2011). Based on their elongation directions, two types of magnetite micro-inclusions have been discerned: the first inclusion type has its elongation direction parallel to one of the MT⟨111⟩ directions, which, in turn, is aligned (sub)parallel to the normal direction of one of seven specific plagioclase lattice planes, including PL(112), PL($\bar{3}$12), PL(150), PL(1$\bar{5}$0), PL(100), PL($\bar{3}\bar{1}$2) and PL(1$\bar{1}$2). According to the classification scheme of Ageeva et al. (2020), magnetite inclusions pertaining to this type are referred to as *plane-normal inclusions*. The PL(112), PL($\bar{3}$12), PL(150), PL(1$\bar{5}$0) lattice planes correspond to oxygen layers in the plagioclase crystal structure with nearly identical *d*-spacing as MT{222}, which corresponds to close-packed oxygen layers in the crystal structure of magnetite. Accordingly, the SORs and CORs of the plane-normal type inclusions have been ascribed to the nearly coherent alignment of the close-packed oxygen planes parallel to MT{222} and the corresponding oxygen layers in plagioclase (Ageeva et al., 2020; Bian et al., 2021). This parallel alignment leaves one degree of freedom for rotation about the inclusion elongation direction, giving rise to several CORs within each orientation class. When, apart from the alignment of MT{222} with one of the abovementioned specific PL(*hkl*) lattice planes, no additional rational crystallographic correspondence is found between magnetite and plagioclase, the inclusion is said to have *general orientation* within the respective orientation class. When, apart from the parallel alignment of MT{222} and a specific PL(*hkl*) lattice plane, a second crystallographic alignment between the lattices of magnetite and plagioclase exists, the inclusion is said to have a *specific orientation* within the respective PL(*hkl*)-n orientation class (Ageeva et al., 2020). Two specific orientations have been discerned within the respective orientation class. When one of the MT⟨001⟩ directions is aligned parallel to either PL[14, 10, 7] or the PL[-14, 10, -7] direction, the inclusion is classified as being in *nucleation orientation*. This crystallographic correspondence ensures that FeO_6 octahedra, a building block of crystal structure of magnetite can be accommodated in the channels, formed by six-member rings of AlO_4-SiO_4 tetrahedra and running parallel to PL[001] in the crystal structure of plagioclase. When, instead, one of the MT{220} lattice planes is aligned parallel to a second of the specific lattice planes of plagioclase, the inclusion is classified as being in *main orientation* (Ageeva et al., 2020).

The second basic type of magnetite micro-inclusions has its elongation direction parallel to MT⟨110⟩ ∥ PL[001] and is referred to as *PL[001] inclusions*. Several orientation variants related by rotations about the inclusion elongation direction exist also for this inclusion type. Apart from the needle-, lath- and plate-shaped magnetite micro-inclusions, small magnetite micro-inclusions with equant shapes may be present. These inclusions are referred to as *dust-like inclusions*, which also show systematic CORs to the plagioclase host. The plane–normal inclusions supposedly formed by precipitation from primary magmatic Fe-bearing

plagioclase, which became supersaturated with respect to magnetite due to cooling or due to changes in oxygen fugacity (Bian et al., 2021). In contrast, most of the PL[001] inclusions appear to have formed during late magmatic, hydrothermal or metamorphic stages.

Magnetite is the most important carrier of the natural remanent magnetisation of rocks, and magnetite-bearing grains of silicate minerals have been investigated intensively due to their significance for paleomagnetic reconstructions (Dunlop and Özdemir, 2001; Nikolaisen et al., 2020, 2022). Ageeva et al. (2022) showed that the shape preferred orientation of needle- and lath-shaped magnetite micro-inclusions in plagioclase leads to pronounced anisotropy of the magnetic remanence of magnetite bearing plagioclase grains. As a consequence, the magnetic memory of magnetite bearing plagioclase may be biased, and the direction of the vector of remanent magnetisation may deviate from the direction of the magnetic field at the time, when the rock cooled through the Curie temperature. Understanding the factors controlling the SORs and CORs of needle-, lath- and plate-shaped magnetite micro-inclusions in plagioclase is thus of key importance for paleomagnetic reconstructions, in particular, when single grain methods are applied (Tarduno et al., 2006).

In this paper, we report on high-resolution scanning transmission electron microscopy (HR STEM), as well as on integrated differential phase contrast scanning transmission electron microscopy (iDPC-STEM) of magnetite–plagioclase interfaces from representative inclusions of the plane-normal type. Magnetite–plagioclase interfaces were cut both along and perpendicular to the inclusion elongation directions. The magnetite–plagioclase interfaces are more complex than previously thought. The factors controlling the SORs and CORs of different types of plane-normal inclusions and possible evolution paths are discussed based on the microscopic configuration of the magnetite–plagioclase interfaces. Our findings bear potentially important implications for paleomagnetic reconstructions.

3.2 Sample material and analytical methods

3.2.1 Sample material

Gabbro samples dredged from the mid-Atlantic ridge (MAR) during the 30th cruise of the Research Vessel Professor Logachev (Beltenev et al., 2007, 2009; Cipriani et al., 2009) were studied. The dredge sites were within oceanic core complexes at 13°N in the footwalls of a low-angle, large-offset extensional fault, a structural feature, which is typical for slow-spreading ridges (Karson et al., 1997; MacLeod et al., 2009). More information on the geology of the oceanic core complexes at 13°N can be found in (MacLeod et al., 2009; Ondréas et al., 2012; Pertsev et al., 2012; Escartin et al., 2017). The studied specimens are from

gabbroic intrusions in peridotite.

Representative plagioclase hosted magnetite micro-inclusions selected based on magnetite–plagioclase CORs obtained in an earlier electron backscattered diffraction (EBSD) study by Ageeva et al. (2020) were investigated. For detailed information on the EBSD method, the reader is referred to these latter authors. The SORs between the magnetite micro-inclusions and the plagioclase host were obtained by combining scanning electron microscopy (SEM) with light-optical polarisation microscopy. The orientations of the facets bounding the magnetite micro-inclusions were reconstructed from known inclusion elongation directions as determined by universal stage measurements under the polarisation microscope combined with the lattice orientations of plagioclase and magnetite as obtained from EBSD (Ageeva et al., 2020).

3.2.2 Focused Ion Beam-SEM and Ar ion-milling

Four specimens were prepared for transmission electron microscopy (TEM) analyses using the focused ion beam (FIB) technique. An FEI Quanta 3D FEG-SEM with integrated FIB device, located at the faculty of Earth Sciences, Geography and Astronomy, University of Vienna, Austria was used. The instrument is equipped with a Schottky field-emission electron gun and a liquid Ga-ion source, a gas injection system for Pt- and C deposition, and an Omniprobe 100.7 micromanipulator for in situ specimen lift-out. The inclusions for TEM studies were selected from chemo-mechanically polished carbon-coated thin sections based on shape orientation obtained from optical microscopy and crystallographic orientation obtained from EBSD analysis, using the same instrument as that for FIB preparation. The first TEM foil contains two needle-shaped PL($\bar{3}$12)n-MT micro-inclusions, one in nucleation and the other in main orientation. The FIB foil was cut perpendicular to the elongation directions of the inclusions and, hence, the cross-sections of the two inclusions were captured in the plane of the FIB foil. The second TEM foil contains a plate-shaped PL($\bar{3}$12)n-MT micro-inclusion in main orientation. The specimen was extracted so that the PL($\bar{3}$12) plane normal lies in the plane of the foil and the plate surface is perpendicular to the plane of the foil. The third TEM foil contains a needle-shaped PL(112)n-MT micro-inclusion in main orientation. The specimen was extracted so that the PL(112) plane normal lies in the plane of the foil. The fourth TEM foil contains the cross-section of the same PL(112)n-MT micro-inclusion as the third foil, and the needle elongation direction is perpendicular to the plane of the foil. Secondary electron (SE) imaging was employed during FIB extraction for monitoring the milling progress. The electron beam was set to 15 kV accelerating voltage and 50 pA probe current. Platinum deposition was used to protect and support the TEM foils during milling, as well as to mount the foil temporarily to the tip of the tungsten micromanipulator needle and finally to the molybdenum grid. The foils were extracted using an ion beam accelerating voltage of 30 kV, and a

probe current that was successively decreased from 65 to 5 nA. The foils for lift-out were about 20 × 20 microns in area and about 2 to 2.5 microns in thickness. After extraction, the foils were attached to individual Mo grids. For the first three TEM foils, final thinning was done using an accelerating voltage 30 kV, and the probe current was gradually decreased from 1 to 0.03 nA. Finally, FIB low-kV cleaning steps were performed at 5 kV/48 nA and 2 kV/27 pA. The first three TEM foils have a thickness of 30 to 50 nm.

The second, third and fourth TEM specimens were further thinned with a Gatan DuoMill 600 ion mill using argon ions (Ar^+) accelerated through 1 kV and with an incident angle of 15°. Milling was done for about 1 hour from each side. The final thickness of the samples is $\sim$ 50 nm.

3.2.3 Scanning transmission electron microscopy

STEM was performed on a Thermo Fisher Scientific Themis Z at University of Antwerp. The microscope is equipped with a X-FEG electron source and a monochromator. For imaging, the instrument was operated at 200 kV with a beam current of 5 pA for low-dose exposure. A convergence semi-angle of 20 mrad was used. Bright field (BF) and high-angle annular dark field (HAADF) STEM imaging was done on a needle-shaped PL($\bar{3}$12)n-MT micro-inclusion in nucleation and in main orientation perpendicular to their elongation directions, respectively.

STEM imaging with an integrated differential phase contrast (iDPC) detector was performed at 300 kV with a 10 pA probe current on a Thermo Fisher Scientific Themis Z at the Helmholtz Centre Potsdam, German Research Centre for Geosciences (GFZ-PISA) facility, Potsdam. The microscope is equipped with a X-FEG electron source with a monochromator (energy resolution is <0.3 eV) and with a Cs S-CORR Probe Corrector (80–300 kV). The spatial resolution is <0.06 nm at 300 kV. iDPC-STEM is a relatively novel electron microscopy technique, which allows for imaging light and heavy elements simultaneously at sub-Å resolution with a low-dose incident beam. This is an annular dark field (ADF) technique where a detector consisting of four segments is used, and the iDPC-STEM image contrast is approximately proportional to the atomic number Z in contrast to a power of 1.7 for the HAADF or ADF images collected with a single detector (Bosch and Lazić, 2015; Lazić et al., 2016; Yücelen et al., 2018). High resolution chemical analysis was performed with a SuperX energy dispersive X-ray spectroscopy (EDS) system installed on the Themis Z STEM in Potsdam. HAADF- and iDPC-STEM imaging, as well as chemical analyses were performed on a plate-shaped PL($\bar{3}$12)n-MT micro-inclusion along its elongation direction, and a needle-shaped PL(112)n-MT micro-inclusion along and perpendicular to its elongation direction, respectively.

3.3 Results

3.3.1 Mineralogy and petrography

The investigated samples are from gabbro intrusions in peridotites from a mid ocean ridge environment. Plagioclase with anorthite contents of 40 to 60 mol% makes up about 50% by volume of the rock. Apart from plagioclase, clinopyroxene, orthopyroxene and amphibole are present as the main rock forming minerals. The chemical composition of plagioclase in the studied grains has been reported in Ageeva et al. (2020, 2022) and is included in the supplementary material. The investigated plagioclase has labradorite composition with an overall compositional variability of about 10 mol%. Labradorite has a triclinic crystal symmetry [C-1]. In the following, the crystal structure of labradorite (An62-An66) given by Wenk et al. (2011) with lattice constants $a = 8.1736$ Å, $b = 12.8736$ Å, $c = 7.1022$ Å, $\alpha = 93.462°$, $\beta = 116.054°$, $\gamma = 90.475°$ was used. The variation of d-spacings and angular relations is minute over the observed 10 mol% compositional variation. The chemical composition of the plagioclase reported in Wenk et al. (1980) and the plagioclase in our study are shown in Table 3.1.

In the petrographic thin section, oriented needle-, lath- and plate-shaped opaque inclusions can be discerned in plagioclase. Based on chemical composition and cubic symmetry, these inclusions were identified as magnetite containing lamellar or irregularly shaped domains of ilmenite and/or ulvospinel. These inclusions likely first formed as titanomagnetite within the plagioclase host, and exsolved into magnetite matrix with ilmenite and/or ulvospinel precipitates (Tan et al., 2016; Gao et al., 2019) in a second phase. A transmitted light plane polarised optical image of a plagioclase grain with oriented magnetite micro-inclusions is shown in Fig. 3.1.

Table 3.1: Chemical compositions of the plagioclase reported in Wenk et al. (1980) from Surtsey, and the plagioclase in the current study

	Wenk et al. (1980)	Plagioclase in the current study
Weight percent oxides		
SiO_2	53.29	54.29
Al_2O_3	30.90	28.58
CaO	13.11	10.93
Na_2O	3.51	5.13
K_2O	0.11	0.16
Fe_2O_3	0.36	0.39
Atoms per formula unit based on 8 oxygens		
Si	2.38	2.46
Al	1.63	1.53
Ca	0.63	0.53
Na	0.304	0.45
K	0.006	0.01
Fe	0.014	0.01

The plagioclase grain is twinned after the pericline twin law. The crystallographic orientation of twin domain 1 is shown in the inserted stereographic projection. Several of the plagioclase plane normal directions and the PL[001] direction, which all correspond to magnetite needle elongation directions, are shown. Based on their shape orientation parallel to the specific plagioclase plane normal directions, abundant needle-shaped PL(112)n-MT, PL($\bar{3}$12)n-MT, PL(100)n-MT and rare PL(150)n-MT micro-inclusions can be discerned in Fig. 3.1. In addition, PL[001] inclusions and a few plate-shaped magnetite inclusions are present. The edges of the plate-shaped magnetite inclusions follow specific crystallographic directions. For example, the edges trending from upper right to lower left are parallel to the PL($\bar{3}$12)-n direction, the nearly horizontal edges are parallel to one of the MT⟨111⟩ directions.

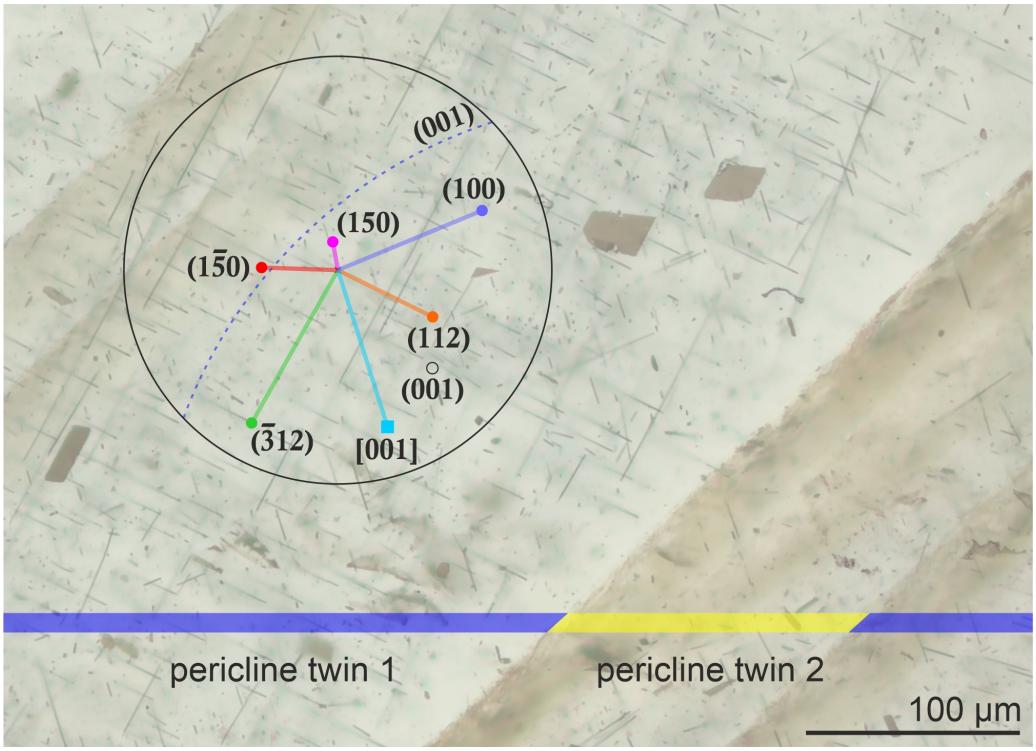

Figure 3.1: Transmitted light plane polarised optical photomicrograph of pericline twinned plagioclase with needle-, lath- and plate-shaped magnetite micro-inclusions. The stereographic projection (upper hemisphere) refers to the crystallographic orientation of twin domain 1 and shows the PL(112)n, PL(150)n, PL($\bar{3}$12)n, PL(1$\bar{5}$0)n, PL(100)n as well as the PL[001] direction as colored lines. The plane normal directions correspond to the elongation directions of the needle-shaped magnetite micro-inclusions. The dashed circle indicates the trace of the PL(001) lattice plane, which is the twin plane.

3.3.2 Needle-shaped PL($\bar{3}$12)n-MT micro-inclusions

PL($\bar{3}$12)n-MT micro-inclusions have one of their MT⟨111⟩ directions, the one that is parallel to the inclusion elongation direction, aligned parallel to the normal direction of the PL($\bar{3}$12) plane. As with all plane-normal inclusion types, general and specific orientation variants are discerned. Among the specific orientation variants, the nucleation orientation, defined by PL($\bar{3}$12)n ‖ MT[111], PL[14,-10,7] ‖ MT[100]

Table 3.2: Conventions for assigning specific Miller indices for the four studied magnetite micro-inclusions and the plagioclase host

No.	1st alignment	2nd alignment	Category
1	PL($3\bar{1}\bar{2}$) ‖ MT(222)	PL[14,-10,7] ‖ MT[100]	Needle-shaped PL($\bar{3}12$)n-MT inclusion in nucleation orientation
2	PL[$5\bar{1}\bar{2}$] ‖ MT[111]	PL(150) ‖ MT($\bar{1}01$)	Needle-shaped PL($\bar{3}12$)n-MT inclusion in main orientation
3	PL($\bar{3}12$) ‖ MT($22\bar{2}$)	PL(150) ‖ MT($2\bar{2}0$)	Plate-shaped PL($\bar{3}12$)n-MT inclusion in main orientation
4	PL(112) ‖ MT(222)	PL($1\bar{5}0$) ‖ MT($2\bar{2}0$)	Needle-shaped PL(112)n-MT inclusion in main orientation

and the main orientation, defined by PL($\bar{3}12$)n ∼ ‖ MT[111] and PL(150) ‖ MT($\bar{2}02$), are the most common (Ageeva et al., 2020). Needle-shaped PL($\bar{3}12$)n-MT micro-inclusions often exhibit about equal proportions of the two orientation variants within one plagioclase grain. Cross-sections of PL($\bar{3}12$)n-MT needles pertaining to either one of the two orientation variants were extracted using FIB. Standard HAADF STEM images of the two cross-sections are shown in Fig. 3.2a and d. The cross-section of the inclusion in nucleation orientation has a nearly hexagonal shape and is outwards convex all along its perimeter (Fig. 3.2a). By contrast, the inclusion in main orientation has a nearly rectangular cross-section with a re-entrant section along its perimeter (Fig. 3.2d). Specific Miller indices are applied for describing the CORs of the different plane-normal inclusion types. The conventions used for assigning specific Miller indices are listed in Table 3.2. The magnetite micro-inclusion in nucleation orientation has its elongation direction parallel to PL($\bar{3}12$)-n ‖ MT[111]. In addition, the COR is characterised by PL[14,-10,7] ‖ MT[100]. In contrast, the PL($\bar{3}12$)-n magnetite micro-inclusion in main orientation has its elongation direction parallel to PL[$\bar{5}12$] ‖ MT[111], which deviates by about 5° from the PL($\bar{3}12$)-normal direction. In addition, a second parallel alignment of low-index lattice planes, namely PL(150) ‖ MT($\bar{2}02$), holds. The CORs for PL($\bar{3}12$)n-MT micro-inclusions in nucleation orientation and in main orientation are illustrated in Fig. 3.2b-c and e-f, respectively. The stereographic projections follow the same orientation references as in Fig. 3.2a and d. Electron diffraction patterns for both cases can be found in the supplementary material Fig. S3.1-S3.2. The nucleation and main orientations are related by a two-step rotation of the lattice of magnetite relative to the lattice of plagioclase: (i) starting from a PL($\bar{3}12$)n-MT micro-inclusions in main orientation a ∼5° rotation of PL about PL(150)n makes PL($\bar{3}12$)n parallel to MT[111] (compare Fig. 3.2e and b), and (ii) a ∼20° rotation about the MT[111] direction, which is parallel to the needle elongation direction, leads to the COR corresponding to a PL($\bar{3}12$)n-MT micro-inclusions in nucleation orientation (compare Fig. 3.2f and c).

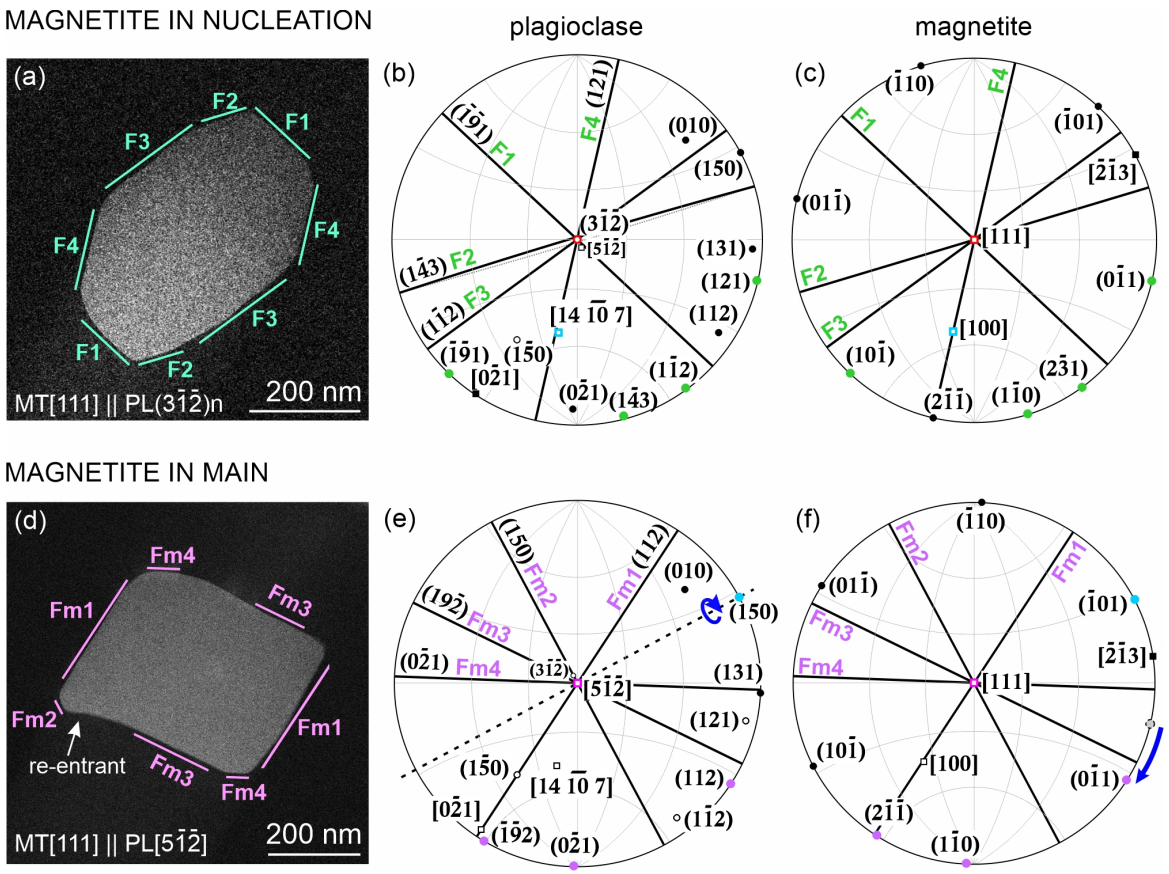

Figure 3.2: (a) Standard HAADF STEM image of needle-shaped PL($\bar{3}$12)n-MT micro-inclusions in nucleation orientation viewed in cross-section along MT[111] || PL(3$\bar{1}\bar{2}$)n and with interface facets F*i* (i = 1–4) indicated. (b,c) Stereographic projections of plagioclase and magnetite showing the COR of PL($\bar{3}$12)n-MT micro-inclusion in nucleation orientation. (d) HAADF cross-section view along MT[111] || PL[5$\bar{1}\bar{2}$] of needle-shaped PL($\bar{3}$12)n-MT micro-inclusions in main orientation. Interface facets are labelled as Fm*i* (i = 1–4). White arrow points to re-entrant section of the inclusion perimeter. (e,f) Corresponding stereographic projections of plagioclase and magnetite. The orientation of the stereographic projections (b-c) and (e-f) follow the reference frame in (a) and (d), respectively. Solid and hollow symbols represent upper and lower hemisphere poles. Crystallographic alignments between magnetite and plagioclase are indicated with the same colour code. Grey circle in (f) represents the MT(0$\bar{1}$1) pole in (c). The facets highlighted in (a) and (d) are (sub)parallel to low index lattice planes in plagioclase and in magnetite, respectively. They are indicated by large circles and labelled with Miller indices in (b-c) and (e-f), representing the lattice planes in plagioclase and in magnetite with the same colour codes. The two rotations relating the nucleation and main orientations are indicated with blue arrows in (e) and (f).

Interface configuration in nucleation orientation

The sides of the hexagonal cross-section of the PL($\bar{3}$12)n-MT inclusion in nucleation orientation are labelled F1 to F4 in Fig. 3.2a. The traces of these facets are connected by comparatively short segments with outwards convex curvature forming the rounded corners of the hexagonal cross-section. Standard high-resolution bright-field STEM images of the F1, F3 and F4 facets and the transitional area between F1 and F4 are shown in Fig. 3.3a-e. While the MT($\bar{2}$20), MT($\bar{2}$02) and MT(0$\bar{2}$2) lattice planes are resolved as lattice fringes in Fig. 3.3a-e, lattice fringes of PL(131), PL(04$\bar{1}$) and PL(1$\bar{1}$2) lattice planes are clearly resolved only in Fig. 3.3e. This is due to the fact that small rotations and/or tilts exist between the three HR-STEM images, as can be inferred from a comparison with the MT{220} lattice fringes. In Fig. 3.3e,

the traces of the MT($\bar{2}20$) lattice planes (solid lines) are 2.5° inclined relative to the yellow dashed line, which represents the orientation of the MT($\bar{2}20$) in Fig. 3.3d. While the PL(131) lattice planes are edge-on in Fig. 3.3e, where the direction of the electron beam is parallel to PL[6.5, -1, -3.5] and deviates by 2° from PL($3\bar{1}\bar{2}$)n, they are slightly inclined and are off the diffraction condition, thus only poorly resolved in Fig. 3.3a–d, where the electron beam is parallel to MT[111] and slightly deviates from PL($\bar{3}12$)n. The configurations of the magnetite–plagioclase interfaces differ between the different facets. Each facet is (sub)parallel to the lattice fringes of at least one of the phases. For example, facet F1 is approximately parallel to MT($\bar{2}02$), facet F3 is approximately parallel to PL($1\bar{1}2$) and facet F4 is approximately parallel to MT($0\bar{2}2$). At the transitional area between facets F1 and F4 shown in Fig. 3.3b, the magnetite–plagioclase interface shows a step-like configuration with the step terraces parallel to facet F1, which is approximately parallel to MT($\bar{2}02$).

Sketches of the geometrical correspondence of the resolved lattice fringes in magnetite and plagioclase across the F1, F3 and F4 facets shown in Fig. 3.3c–e are presented in Fig. 3.3g–i. The *d*-spacings of the lattice planes were calculated using the crystallographic data from Wenk et al. (1980) for plagioclase and from Fleet (1981) for magnetite, which yield, $d_{\mathrm{PL131}} = 2.83$ Å, $d_{\mathrm{PL041}} = 2.95$ Å, $d_{\mathrm{PL1\bar{1}2}} = 2.52$ Å and $d_{\mathrm{MT220}} = 2.97$ Å. Along facet F1, the MT($2\bar{2}0$) lattice planes and the PL($1\bar{1}2$) lattice planes impinge on the magnetite–plagioclase interface with a frequency of 4:5, while the MT($0\bar{2}2$) and the PL($04\bar{1}$) lattice planes impinge with a frequency of 6:3 (Fig. 3.3h). Furthermore, facet F1 is approximately parallel to MT($\bar{2}02$). Similarly, the MT($0\bar{2}2$) and the PL($04\bar{1}$) lattice planes impinge on interface segment F3 with a frequency of 6:7, while the MT($\bar{2}20$) and the PL(131) lattice planes impinge with a frequency of 4:9 (Fig. 3.3i). Facet F3 is (sub)parallel to MT($2\bar{3}1$) and PL($1\bar{1}2$). Apart from this correspondence of lattice planes, additional lattice planes also meet at facet F3 with only small mismatch (indicated with black circles at the interface segment). Along facet F4, the MT($\bar{2}20$) and PL($04\bar{1}$) lattice planes impinge on the interface with a frequency of 8:9 (Fig. 3.3g), and the F4 facet is close to parallel to MT($0\bar{2}2$) and PL(121).

The magnetite–plagioclase interfaces along facets F1, F3 and F4 may thus be considered as commensurate with respect to the MT($\bar{2}20$), MT($0\bar{2}2$), MT($\bar{2}02$) and PL($1\bar{1}2$), PL($04\bar{1}$), PL(131) lattice planes, which are resolved by STEM imaging (Howe et al., 2002). Each facet may contain additional pairs of magnetite and plagioclase lattice planes, which are commensurate along the interfaces, but here we only refer to those lattice planes that are resolved as lattice fringes on the BF STEM images. Despite the lack of a STEM image, facet F2 can be inferred to be close to parallel to MT($2\bar{2}0$) and PL($1\bar{4}3$) by comparing the facet trace with the stereographic projections in Fig. 3.2b, c.

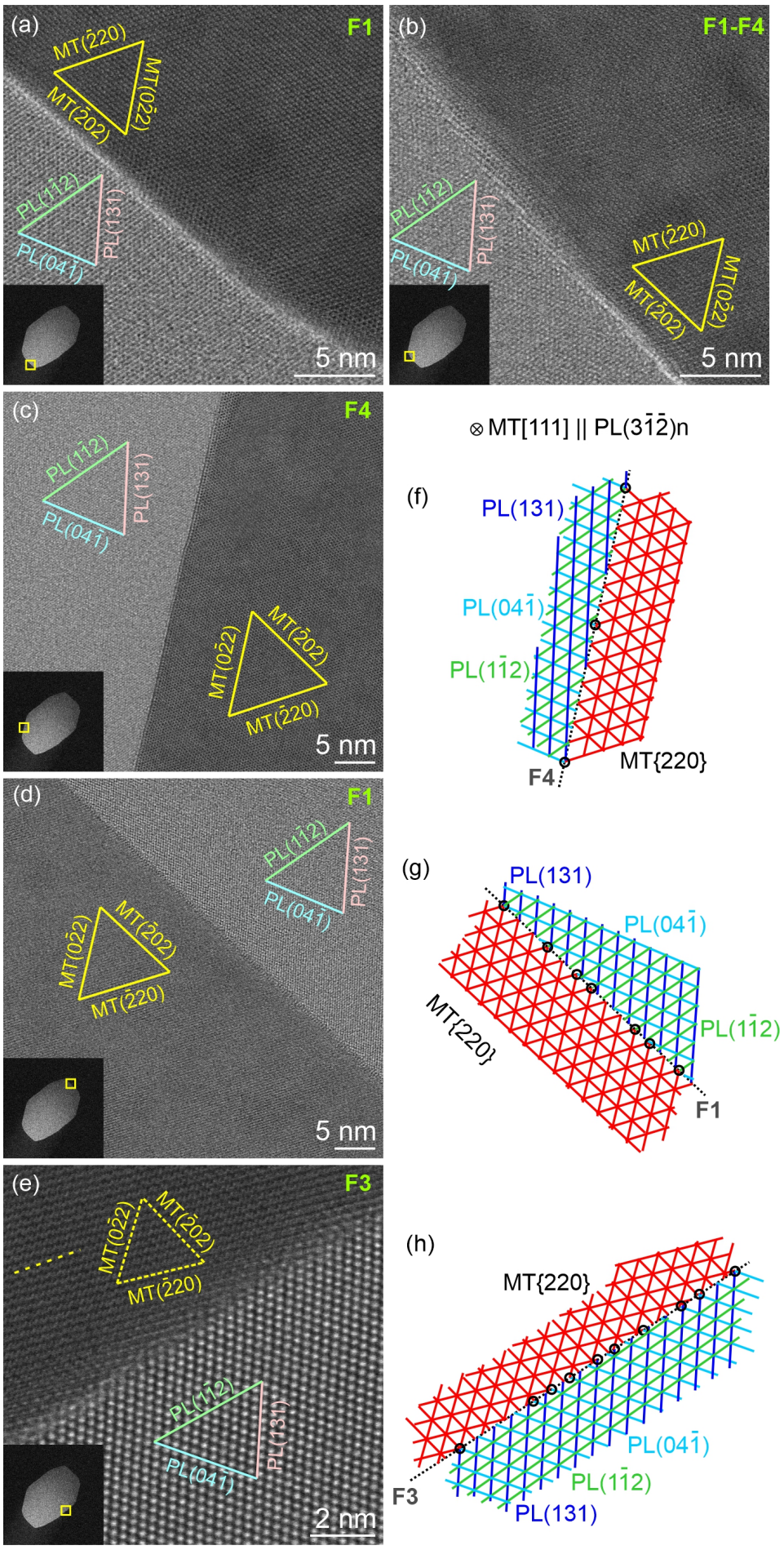

Figure 3.3: Standard high-resolution BF STEM images of magnetite–plagioclase interfaces of a PL($\bar{3}$12)n-MT inclusion in nucleation orientation. (a) Facet F1 at the lower part of the hexagonal perimeter, (b) F1-F4 transition, (c) F4, (d) F1 at the upper part of the hexagonal perimeter and (e) F3. An overview of the inclusion cross-section is inserted at the lower-left corner with the locations of the detail images highlighted by yellow squares. Well-resolved magnetite and plagioclase lattice fringes are indicated by solid lines labelled with the respective Miller indices. The yellow dashed line in (e) represent the orientation of the MT($\bar{2}$20) lattice planes in (d). Sketches of the lattice plane correspondence at the magnetite–plagioclase interfaces of facets (g) F4, (h) F1 and (i) F3. Points of (nearly) precise match between magnetite and plagioclase lattice planes are indicated with black circles.

Interface configuration in main orientation

The cross-section of the inclusion in main orientation (Fig. 3.2d) has an approximately rectangular shape, which is bounded by straight interface segments referred to as facets Fm1 and Fm3, which are connected by curved segments Fm2 and Fm4. Standard high-resolution BF STEM images of the different interface segments are shown in Fig. 3.4a-j. In all STEM images, at least one set of MT{220} lattice planes can be resolved as lattice fringes. Due to the beam sensitivity and the complex crystal structure of plagioclase, PL(131) lattice planes are resolved only in Fig. 3.4c,d,e,g. The magnetite–plagioclase interface along facet Fm1 on the left side of the rectangle (Fig. 3.4a) is edge-on, while it appears diffuse and seems to be inclined relative to the incident beam on the right side of the rectangle (Fig. 3.4d). Along facet Fm1 on the left side of the rectangle, the magnetite–plagioclase interface is nearly parallel to the MT($0\bar{2}2$) and PL(112) lattice fringes. Facets Fm2 are closely parallel to MT($\bar{2}02$) || PL(150) and represent only a small fraction of the magnetite–plagioclase interfaces. Facet Fm3 appears curved in the overview image shown in Fig. 3.2d, whereas it has relatively sharp straight segments on the nanometre scale as shown in Fig. 3.4b and diffuse segments as shown in Fig. 3.4f and h. The straight segments are close to parallel to the MT($\bar{2}11$) || PL($19\bar{2}$) lattice planes (Fig. 3.4b,g). Fig. 3.4c shows the transition between Fm3 and Fm1, which appears diffuse and contains two relatively sharp interface segments: one segment is parallel to Fm3, which is parallel to MT($\bar{2}11$), and the second is close to parallel to PL(131). Fig. 4e shows facet Fm4 and the connection to Fm1 at the lower-right corner of the rectangular cross-section. The straight segment of Fm4 is parallel to MT($\bar{2}20$) || PL($02\bar{1}$). Fig. 3.4i shows the transition between Fm1 and Fm2, which is curved with changing interface configurations on the nanometer scale. Fig. 3.4j shows a sketch of the lattice plane correspondence between magnetite and plagioclase. The contrast seen in the magnetite inclusion in Fig. 3.4f is ascribed to a defect. The type of the defect can, however, not be determined.

3.3.3 Plate-shaped PL($\bar{3}12$)n-MT micro-inclusion in main orientation

As stated above, needle-shaped PL($\bar{3}12$)n-MT micro-inclusions in main orientation follow the COR, where one of the MT$\langle 111\rangle$ $\sim$ || PL($\bar{3}12$)n, one set of the MT{220} || PL(150) and another set of the MT{220} $\sim$ || PL(112). While the alignment of MT$\langle 111\rangle$ (close) to PL($\bar{3}12$)n gives rise to the preferred elongation direction of the PL($\bar{3}12$)n-MT micro-inclusions, the second alignment of MT{220} || PL(150) may lead to preferred extension in a second direction leading to platy morphology of the micro-inclusion parallel to MT{220} || PL(150). A TEM foil of a plate-shaped PL($\bar{3}12$)n-MT micro-inclusion in main orientation was extracted perpendicular to the MT{220} || PL(150) basal plane of the plate and parallel to the MT[$11\bar{1}$] || PL($\bar{3}12$)n direction (Fig. 3.5). The incident electron beam is parallel to MT[112] || PL[$5\bar{1}8$]. The MT[$11\bar{1}$]

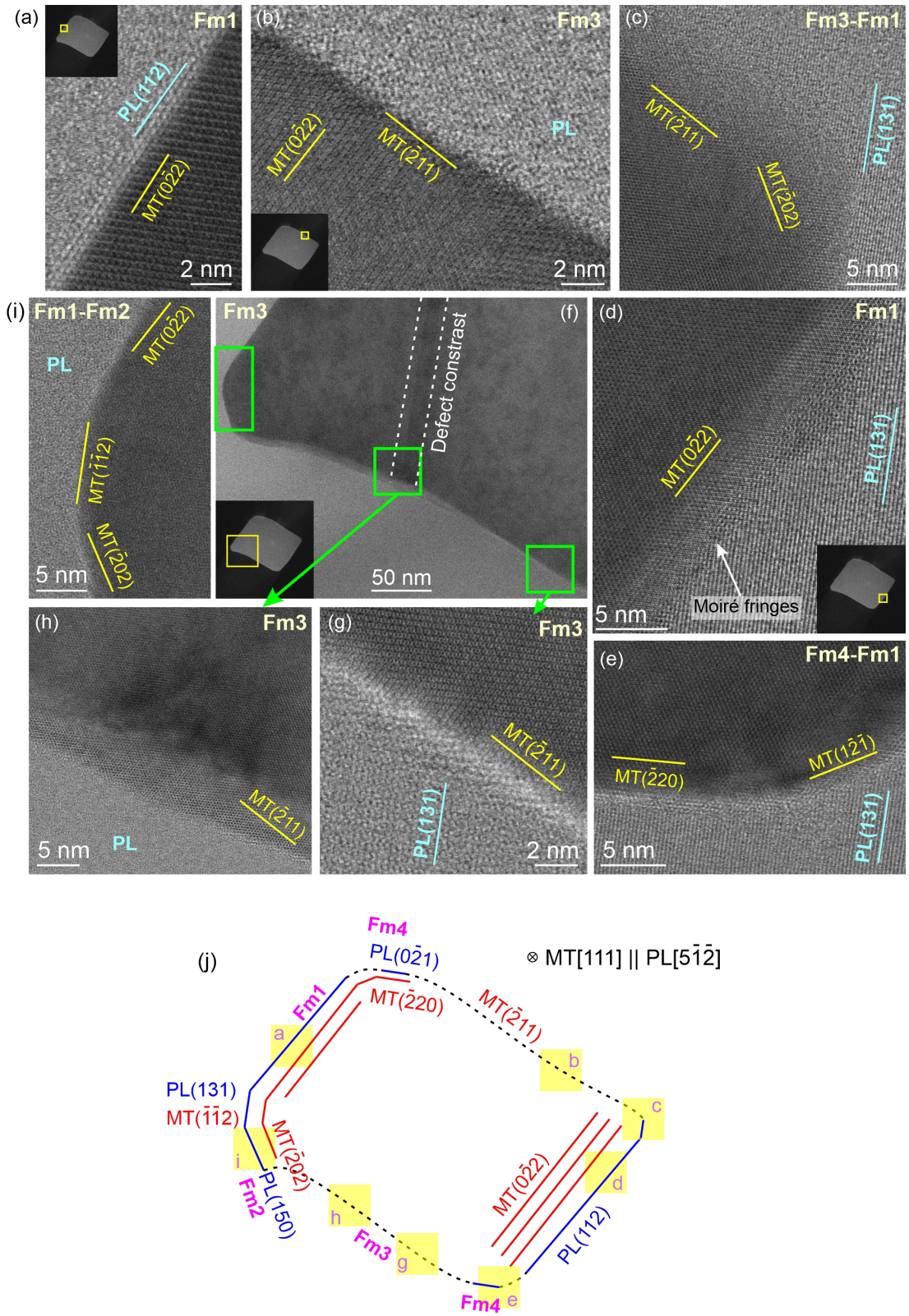

Figure 3.4: Standard high-resolution BF STEM images of magnetite–plagioclase interface facets (a) Fm1, (b) Fm3, (c) Fm3-Fm1, (d) Fm1, (e) Fm4-Fm1, (f, g, h) Fm3 and (i) Fm1-Fm2. An overview of the cross-section with the locations of the STEM images is inserted in (a, b, d, f). Lattice planes from both phases and moiré fringes are indicated when observed. (j) Sketch of lattice planes of the two phases alignment at each facet at the magnetite–plagioclase interface. Alphabetically labelled yellow squares represent the acquisition locations of the detailed STEM images. Viewing direction is parallel to MT[111] || PL[$5\bar{1}\bar{2}$] in all images.

and PL($\bar{3}12$)n directions lie in the plane of the foil, and the magnetite–plagioclase interfaces on either side of the plate, which are parallel to the MT($2\bar{2}0$) and PL(150) lattice planes, are edge-on (Fig. 3.5a). Standard HAADF STEM images of the two plane surfaces are shown in Fig. 3.5b and c.

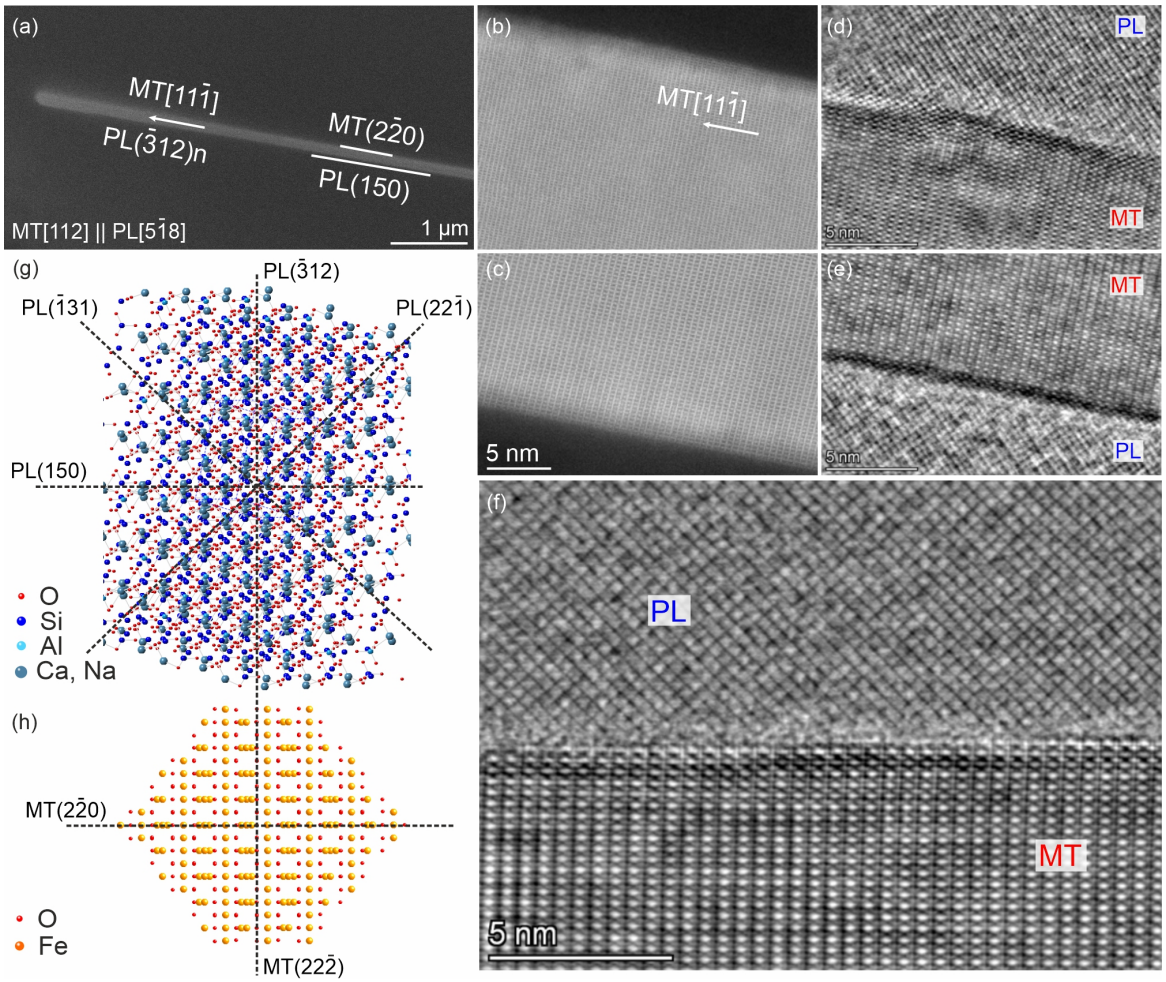

Figure 3.5: (a) SE image of a plate-shaped PL($\bar{3}$12)n-MT micro-inclusion after FIB extraction. The inclusion elongation direction (white arrow) lies in the plane of the foil, and the plate surface (white lines) is edge on. (b, c) Standard HAADF STEM imaging of magnetite–plagioclase interface: showing magnetite–plagioclase interfaces corresponding to the MT($2\bar{2}0$) || PL(150) plate surface bounding a plate-shaped PL($\bar{3}$12)n-MT micro-inclusion in main orientation on either side. The intersection of the foil and the plate is parallel to MT[11$\bar{1}$] – white arrow. (d, e) iDPC-STEM images of the magnetite–plagioclase interface from area (b) and (c), respectively. (f) Close-up iDPC-STEM image of the interface segment shows in (d), rotated. MT($22\bar{2}$) and MT($2\bar{2}0$), PL($\bar{1}$31) and PL($22\bar{1}$) lattice planes are resolved. (g, h) Crystal structure models of plagioclase and magnetite according to the orientation in f with lattice planes observed in iDPC-STEM images indicated. Viewing direction is parallel to MT[112] || PL[5$\bar{1}$8] in all images. Cations and anions are not shown to scale. In reality, the oxygen atoms are bigger and the cations are smaller. To stress the distribution of the cations and anions, the oxygen atoms are drawn at 1/6 of the real size proportion.

The lattice fringes corresponding to the MT($22\bar{2}$) and MT($2\bar{2}0$) lattice planes can be well discerned. The inclusion elongation direction is nearly parallel to MT[11$\bar{1}$] as indicated by the white arrow. Detailed iDPC-STEM images of the same interface segments as shown in Fig. 3.5b and c are presented in Fig. 3.5d and e. Fig. 3.5f shows the same interface segment as Fig. 3.5d after counter clockwise rotation about the viewing direction so that the magnetite–plagioclase interface is horizontal. Lattice fringes in magnetite and in plagioclase are well resolved. Fast Fourier transformation patterns of plagioclase and magnetite

obtained from Fig. 3.5f are shown in supplementary material Fig. S3.3. In plagioclase, the lattice fringes corresponding to PL($\bar{1}31$) and PL($22\bar{1}$) can be seen. Crystal structure models of plagioclase and magnetite oriented corresponding to the crystal orientation in Fig. 3.5f are shown in Fig. 3.5g, h. The PL($\bar{1}31$) and PL($22\bar{1}$) lattice fringes observed in Fig. 3.5f correspond to cation layers in the crystal structure model. In contrast, no lattice fringes corresponding to the PL($\bar{3}12$) and PL(150) lattice planes can be discerned. The MT($22\bar{2}$) lattice planes correspond to close-packed oxygen layers in the crystal structure of magnetite (Fig. 3.5h), and the MT($22\bar{2}$) ∥ PL($\bar{3}12$) lattice planes are in direct contact across the magnetite-plagioclase interfaces parallel to the inclusion elongation direction. The interface is sharp and fully crystalline, and in the observed domain, there is possibly a step in the interface (Fig. 3.5f). Nearly identical *d*-spacing of the corresponding oxygen layers in magnetite and plagioclase ensures semi-coherent alignment of the MT($22\bar{2}$) and the PL($\bar{3}12$) lattice planes across the magnetite–plagioclase interface bounding the inclusion along the elongation direction. Based on crystallographic data for room temperature and 1 bar pressure reported by Wenk et al. (1980) for plagioclase and by Fleet (1981) for magnetite, the lattice misfit along the MT$[11\bar{1}]$ ∥ PL($\bar{3}12$)n direction is $\delta = |d_{\mathrm{PL}\bar{3}12} - d_{\mathrm{MT}222}|/d_{\mathrm{PL}\bar{3}12} = 0.032$, which is likely accommodated by edge dislocation every about 31st MT($22\bar{2}$) plane at the magnetite-plagioclase interface. This supposition is corroborated by the analysis of Fig. 3.5f. The interface area in Fig. 3.5f is rather obscure and potentially occurring edge dislocations and associated half-planes in magnetite cannot be unambiguously identified. Counting the lattice planes further away from the interface yields 66 PL($\bar{3}12$) lattice planes and 68 MT($22\bar{2}$) lattice planes over the viewing area, indicating that two edge-dislocations and associated half-planes of MT($22\bar{2}$) exist that accommodate the misfit over the interface segment shown in Fig. 3.5f. The counting of lattice planes was done on an inverse fast Fourier transformation (iFFT) image obtained from Fig. 3.5f, which is shown in supplementary material Fig. S3.3.

3.3.4 Needle-shaped PL(112)n-MT micro-inclusion in main orientation

A needle-shaped PL(112)n-MT micro-inclusion was selected for dedicated atomic scale investigations of the magnetite–plagioclase interface. It is known from prior EBSD analyses that the inclusion is in main orientation according to the classification scheme of Ageeva et al. (2020), implying that MT$[111]$ ∥ PL(112)n, MT($2\bar{2}0$) ∥ PL($1\bar{5}0$). The inclusion elongation direction is MT$[111]$, which is aligned with the normal direction of the PL(112) plane to within 1.5° as determined by universal stage measurements. Two TEM foils were extracted from this inclusion using SEM-FIB technique, where one foil was cut parallel and the other one was cut perpendicular to the inclusion elongation direction. PL(112)n-MT micro-inclusions are rarely seen in nucleation orientation and therefore results are only shown for a PL(112)n-MT micro-inclusion in

main orientation.

Interface configuration along the needle elongation direction

Fig. 3.6 shows an overview image and details of a PL(112)n-MT micro-inclusion with its elongation direction in the plane of the foil. The viewing direction is parallel to MT$[11\bar{2}]$ || PL$[51\bar{3}]$ in all images. In the standard HAADF STEM image (Fig. 3.6a) the inclusion shows wedge shape tapering out to the left. The different grey scales are probably contributed by the non-uniform thickness of the inclusion. In some segments, the magnetite–plagioclase interface appears sharp, in other segments, it is more blurred. At the blurred segments, the interface is accompanied by a zone of reduced brightness in the magnetite indicating that in these domains the magnetite–plagioclase interface is inclined with respect to the incident electron beam so that the beam penetrates both magnetite and plagioclase in a narrow zone along the magnetite–plagioclase interface. The fact that the zones of reduced brightness only extend along parts of the magnetite–plagioclase interface indicates that the magnetite needle is partly bound by facets, which are inclined relative to the MT$[111]$ direction. Interface segments that appear sharp pertain to facets sharing the MT$[111]$ direction as a common zone axis and also contain the MT$[11\bar{2}]$ direction, which is parallel to the viewing direction. The overall 3D geometry of the magnetite needle thus deviates from a plain prism shape. The irregularly shaped domain with different grey shade highlighted by the green rectangle in Fig. 3.6a was identified as ilmenite based on its comparatively low Fe and high Ti content as seen in the element distribution maps shown in Fig. 3.6e.

In the iDPC-STEM images shown in Fig. 3.6b, the lattice fringes of both magnetite and plagioclase are in direct contact along the interface with no amorphous layers or gaps in between. Lattice fringes are resolved in magnetite and in plagioclase. Fast Fourier transformation patterns of magnetite and plagioclase obtained from Fig. 3.6b are shown in supplementary material Fig. S3.4. In the iDPC-STEM image the MT(222) lattice fringes are vertical and the MT$(2\bar{2}0)$ lattice fringes are horizontal. The lattice fringes observed in plagioclase are PL$(1\bar{2}1)$ and PL(031), and the fringes of the PL(112) planes can be seen only vaguely. The crystal structure models in Fig. 3.6c–d are oriented according to the observed COR and show that in plagioclase and in magnetite cation clusters are responsible for the detectable lattice fringes under iDPC-STEM imaging, while the MT(222) lattice planes correspond to close-packed oxygen layers in magnetite. Rugged planes parallel to PL(112) dominated by oxygen alternating with layers dominated by cations are visible in the crystal structure model of plagioclase, when viewed along the PL$[51\bar{3}]$ direction. The *d*-spacings of MT(222) and PL(112) are very similar, and the two lattice planes are aligned nearly parallel across the magnetite–plagioclase interface. A slight misalignment of about 1° between the two lattice

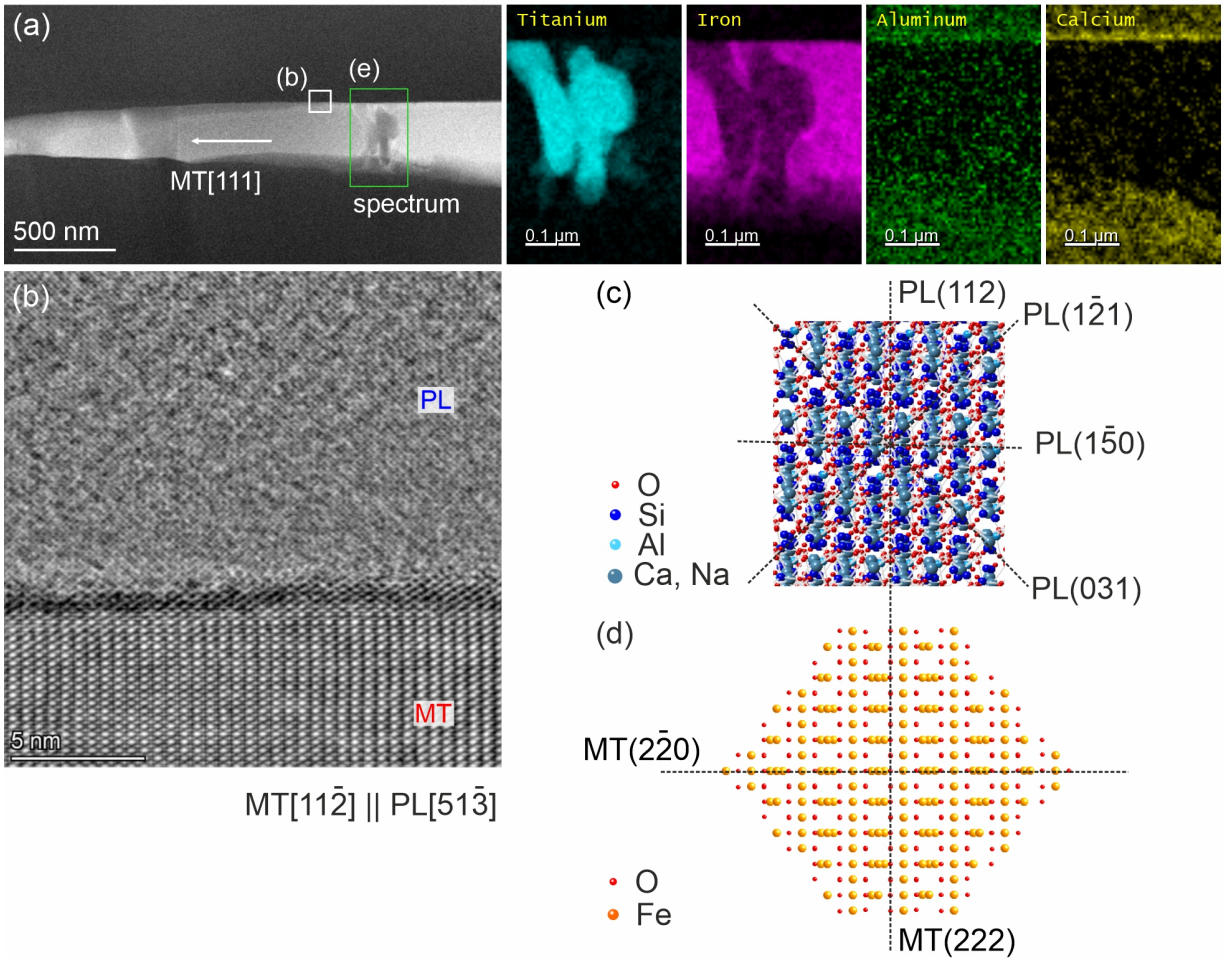

Figure 3.6: (a) Standard HAADF STEM image showing an overview of a needle-shaped PL(112)n- MT micro-inclusion in main orientation with its elongation direction oriented horizontally in the plane of the foil. The white rectangle with alphabetic label indicates the scanning area covered by the atomic scale iDPC-STEM image shown in (b). The green rectangle indicates the area covered by the element distribution maps shown in (e). (b) iDPC-STEM image of a magnetite–plagioclase interface segment that is edge on. The MT(222) and MT(2$\bar{2}$0) lattice planes are resolved in magnetite, and the PL(1$\bar{2}$1) and PL(031) lattice planes are resolved in plagioclase. (c, d) Crystal structure models for plagioclase and magnetite according to the orientation in (b) with the lattice planes observed in the iDPC-STEM images indicated: oxygen layers parallel to PL(112) and PL(1$\bar{5}$0), close-packed oxygen plane MT(222) and less densely packed oxygen plane MT(2$\bar{2}$0). (e) STEM-EDS element distribution maps of the area indicated by the green rectangle in (a). Segregation of Ca and Al at the upper magnetite–plagioclase interface. Viewing direction is parallel to MT[11$\bar{2}$] || PL[51$\bar{3}$] in all images. Cations and anions are not shown to scale. In reality, the oxygen atoms are bigger and the cations are smaller. To stress the distribution of the cations and anions, the oxygen atoms are drawn at 1/6 of the real size proportion.

planes is noticeable in Fig. 3.6b, suggesting a small tilt component may exist across the interface. Based on the lattice constants reported by Fleet (1981) and Wenk et al. (1980), the lattice misfit between MT(222) and PL(112) is calculated as $\delta = |d_{\mathrm{PL112}} - d_{\mathrm{MT222}}|/d_{\mathrm{PL112}} = 0.016$. Thus, edge dislocations are expected to be present at every $\sim$ 63rd MT(222) plane at the magnetite–plagioclase interface to accommodate the 1.6% lattice misfit. The presence of a misfit dislocation can indeed be inferred from an analysis of the iFFT image obtained from Fig. 3.6b, where 69 PL(112) lattice planes on one side of the magnetite–plagioclase interface correspond to 70 MT(222) lattice planes on the other side of the interface, indicating that one MT(222) half-plane exists at the magnetite–plagioclase interface in this area. The iFFT results are included

in supplementary material Fig. S3.4. The interface segment covered by scan area b in Fig. 3.6 is perpendicular to the plane of the foil and is thus viewed edge on. The interface is parallel to the MT($2\bar{2}0$) and the PL($1\bar{5}0$) lattice planes. It is seen in the crystal structure models that densely packed oxygen planes extend parallel to the MT($2\bar{2}0$) lattice plane and less well defined but still well-discernible oxygen layers extend parallel to the PL($1\bar{5}0$) lattice planes in plagioclase. Both these oxygen layers are aligned parallel to the magnetite–plagioclase interface. Locally elevated Ca and Al concentrations are observed within a few nm wide zone in the plagioclase along the upper magnetite–plagioclase interface in the area labelled e, indicating segregation of these elements at the interface (Fig. 3.6e). The Ca and Al enrichment at the magnetite–plagioclase interface implies an elevated anorthite content adjacent to the magnetite micro-inclusions as compared to the plagioclase matrix. The observed segregation was likely acquired in the course of dissolution and recrystallisation of the plagioclase during magnetite growth. The local enrichment is less pronounced along the lower magnetite–plagioclase interface, which is probably due to the fact that the upper interface is edge-on, while the lower interface is inclined relative to the incident beam. The inclination of the lower interface is also manifest from the gradually decreasing intensities of the Fe and Ti signals along a transect from the magnetite to the plagioclase (Fig. 3.6e).

Interface configuration of the needle cross-section

In Fig. 3.7a, a standard HAADF image of a cross-section of the PL(112)n-MT micro-inclusion shown in Fig. 3.6 is presented. The viewing direction is parallel to the inclusion elongation direction, and thus coincides with MT[111] || PL(112)n. The variation of the greyscale in the magnetite domain is due to curtaining effect induced during FIB preparation. STEM-EDS element distribution maps of the sample are shown in supplementary material Fig. S3.5. The inclusion cross-section has a nearly centro-symmetrical shape and is bounded by a number of differently oriented straight or slightly curved interface segments. Interestingly, the individual interface segments are connected by both outwards convex and outwards concave segments. Specific lattice planes in magnetite and plagioclase that are close to parallel to different interface segments are indicated by coloured lines in Fig. 3.7a. The facet orientations are derived from the iDPC-STEM image in Fig. 3.7b. Most facets appear in pairs bounding the inclusion on opposing sides. The facet pair highlighted with the straight yellow lines in Fig. 3.7a is special in that it is parallel to both MT($2\bar{2}0$) and PL($1\bar{5}0$). This also corresponds to the interface trace presented in Fig. 3.7b. The other interface segments are close to parallel to low-index lattice planes in magnetite, the indices are indicated in Fig. 3.7a, but no parallel alignment to low-index lattice planes in plagioclase can be identified. Fig. 3.7b shows an iDPC-STEM image of the magnetite–plagioclase interface at a segment with outwards convex curvature.

In magnetite, individual atomic columns are resolved and the lattice fringes corresponding to the MT($2\bar{2}0$) can be inferred (Fig. 3.7c). In plagioclase, the lattice fringes of the PL($13\bar{1}$) and PL($\bar{2}21$) lattice planes can be discerned even though they are slightly off zone axis. As can be seen in the crystal structure model shown in Fig. 3.7d, they correspond to linearly distributed clusters of cations in the plagioclase crystal structure.

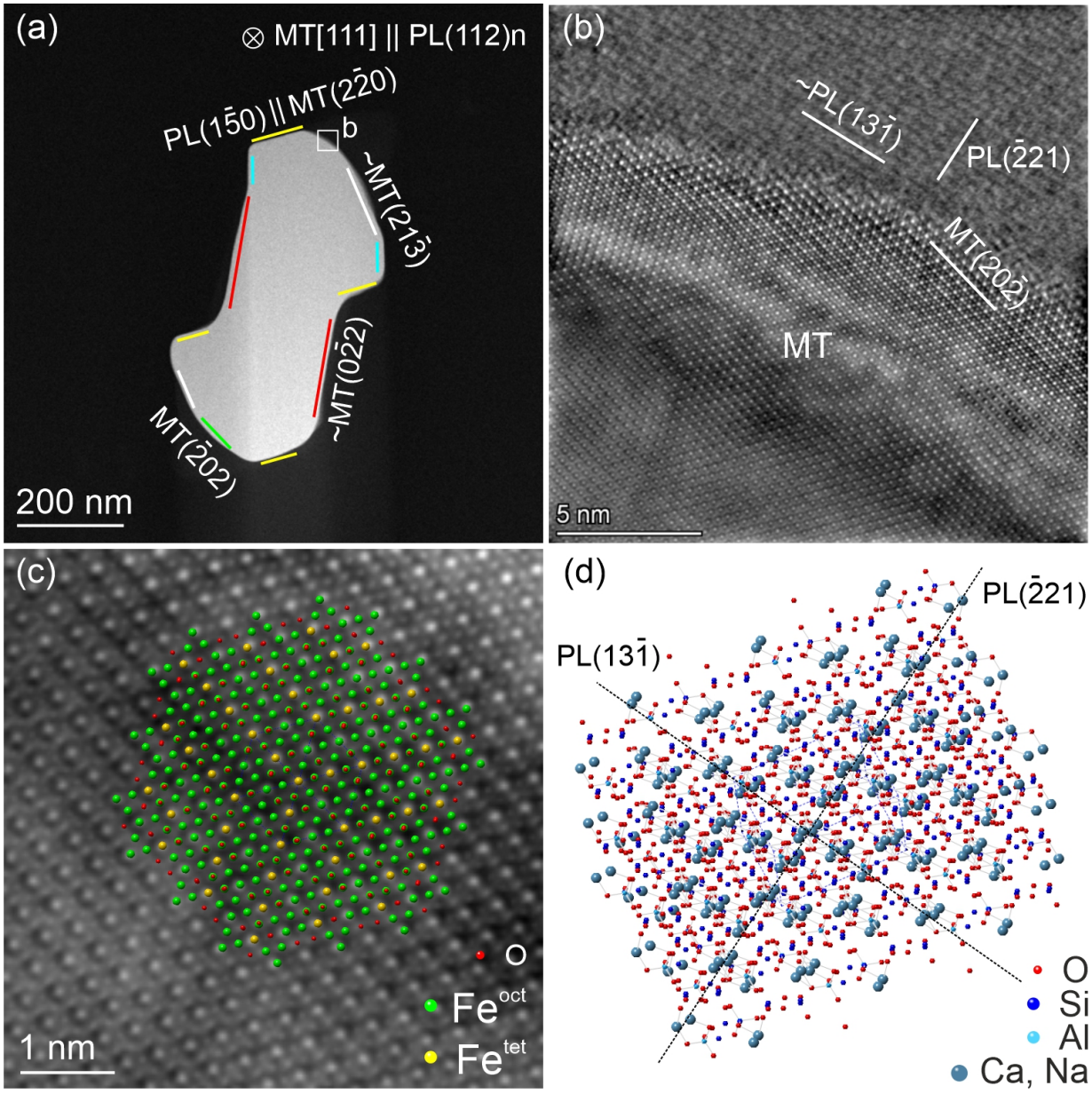

Figure 3.7: (a) Standard HAADF STEM overview image showing the cross-section of the PL(112)n-MT micro-inclusion shown in Fig. 3.6, viewing direction is MT[111] || PL(112)n. The traces of specific lattice planes in magnetite and in plagioclase are indicated with coloured lines. The white rectangle corresponds to the scan area covered by the iDPC-STEM image in (b). (b) iDPC-STEM image of a curved magnetite–plagioclase interface segment with three sets of lattice planes sharing the viewing direction as their common zone axis indicated. (c) Crystal structure model of magnetite overlain on a close up of the iDPC-STEM image shown in (b). Fe^{tet} and Fe^{oct} represent tetrahedrally and octahedrally coordinated Fe atoms, respectively. (d) Crystal structure model of plagioclase oriented according to the plagioclase orientation in (b). Discernible lattice fringes in (b) are indicated and correspond to distributed cation clusters. Cations and anions are not shown to scale. In reality, the oxygen atoms are bigger and the cations are smaller. To stress the distribution of the cations and anions, the oxygen atoms are drawn at 1/6 of the real size proportion.

3.4 Discussion

3.4.1 Plane-normal magnetite micro-inclusions

From petrographic evidence abundant needle-shaped PL(112)n-MT, PL($\bar{3}$12)n-MT, PL(100)n-MT and rare PL(150)n-MT micro-inclusions as well as abundant PL[001] inclusions and a few plate-shaped magnetite inclusions were identified in the investigated plagioclase grain (Fig. 3.1). Whereas the first four inclusion types pertain to the plane-normal inclusions according to Ageeva et al. (2020), the PL[001] inclusions pertain to a fundamentally different inclusion type. Bian et al. (2021) inferred that the magnetite micro-inclusions of the plane-normal type represent the first generation of plagioclase-hosted oriented magnetite micro-inclusions that formed by precipitation from Fe-bearing plagioclase in the course of a solid-state reaction or a sequence of solid-state reactions. In contrast, even though in the investigated plagioclase domain, the PL[001] inclusions occur together with the plane-normal inclusions and may be coeval, the PL[001] inclusions are generally ascribed to later hydrothermal processing and recrystallisation (Bian et al., 2021; Ageeva et al., 2022). The following discussion is restricted to the plane-normal type inclusions.

The elongated shape of plane-normal type magnetite micro-inclusions was ascribed to the good match of lattice planes corresponding to oxygen layers in both magnetite and plagioclase across the interfaces that contain the needle elongation direction (Ageeva et al., 2020). The associated CORs were ascribed either to configurations that facilitate nucleation (Ageeva et al., 2020), fast growth (Wenk et al., 2011), or to configurations that minimise interfacial energy (Ageeva et al., 2020), and elastic strain energy (Wenk et al., 2011). The CORs corresponding to the nucleation orientation have been related to the favourable orientation of FeO_6 octahedra, which are important building units of magnetite, in channels running parallel to the PL[001] direction in the crystal structure of plagioclase (Wenk et al., 2011; Ageeva et al., 2020). Accommodation of the FeO_6 octahedra in the channels of the plagioclase crystal structure most likely decreases the nucleation barrier for magnetite (Wenk et al., 2011). The nucleation barrier is mainly due to the generation of interfaces between the nucleus and the host (Sutton and Balluffi, 1995; Christian, 2002). Therefore, the nuclei tend to form coherent interfaces. Generally, a certain lattice misfit exists between the precipitate and the host, and such coherency will become exceedingly difficult to maintain, when the precipitate grows. This also applies to magnetite plagioclase pairs and, thus, the CORs between magnetite precipitates and the plagioclase host may change during precipitate growth. In the following, the preference of elongation directions, the associated CORs and interface configurations are discussed for the plane-normal type magnetite micro-inclusions in plagioclase.

3.4.2 Nucleation orientation and main orientation

Among the plane normal magnetite micro-inclusions, the PL($\bar{3}$12)-n MT inclusions are special in that they show approximately equal abundances of the orientation variants corresponding to nucleation and main orientation. Typically, as compared to needle-shaped plane normal magnetite micro-inclusions in main orientation, needle-shaped plane normal magnetite micro-inclusions in nucleation orientation show several features that are considered as primary. For example, their elongation direction is usually strictly aligned with the respective PL(*hkl*) plane-normal direction (Fig. 3.2b, c). In addition, the inclusions in nucleation orientation typically show regularly shaped faceted cross-sections, which are outwards convex all along the cross-section perimeter (Fig. 3.2a). The interface facet orientations are mostly related to MT{220} lattice planes, whereas plagioclase lattice planes appear to influence the selection of interface facets less strongly (Fig. 3.3a, c, d). The relation to the crystal lattice of the plagioclase host is reflected by the commensurate impingement of plagioclase and magnetite lattice planes along the magnetite–plagioclase interfaces (Fig. 3.3g, h, i).

In contrast, the elongation direction of magnetite micro-inclusions in main orientation typically deviates by a few degrees from the respective PL(*hkl*) plane-normal direction (Fig. 3.2e, f). In addition, magnetite micro-inclusions in main orientation usually show more complex shapes in cross-section with only a few faceted interface segments connected by curved interface segments, which may be outwards concave leading to locally re-entrant sections of the magnetite–plagioclase interface (Fig. 3.2d). Moreover, the faceted interface segments typically are aligned parallel to low index lattice planes of both magnetite and plagioclase. For example, the PL($\bar{3}$12)-n MT inclusion in main orientation shows nearly perfect parallel alignment of the prominent interface facet Fm1 with MT(0$\bar{2}$2) || PL(112) and of the less common facet Fm2 with MT($\bar{2}$02) ||PL(150). Based on the plagioclase crystal structure of Wenk et al. (1980), the angle between PL($\bar{3}$12) and PL(150) is 91.23°, and between PL($\bar{3}$12) and PL(112), it is 85.06°. The strong parallel alignments of MT(0$\bar{2}$2) with PL(112) and of MT($\bar{2}$02) with PL(150), while keeping the tilt of MT(111) relative to PL($\bar{3}$12) at a minimum, can thus well explain the about 5° deviation of the inclusion elongation direction from the PL($\bar{3}$12)-n direction (Fig. 3.2e, f). Also, the COR of the plate-shaped PL($\bar{3}$12)-n MT inclusion corresponds to the main orientation. The basal plane of the plate is parallel to the MT(2$\bar{2}$0) || PL(150) lattice planes, which correspond to oxygen layers in both phases. Finally, for the needle-shaped PL(112)n magnetite micro-inclusion, the inclusion elongation direction is aligned parallel to the PL(112)n direction to within about 1.5°, and the most prominent interface segment is aligned parallel with MT(2$\bar{2}$0) || PL(1$\bar{5}$0). The angle between PL(112) and PL(1$\bar{5}$0) is 91.12°. Strictly parallel alignment of MT(2$\bar{2}$0) parallel to PL(1$\bar{5}$0), while keeping the tilt of MT(111) relative to PL(112) at a minimum, thus leads to a 1.12°

deviation of the needle elongation direction from the PL(112)-n direction, which is well compatible with our observations. The observed CORs and SORs ensure continuity of the oxygen sub-lattices of magnetite and plagioclase across their interfaces. This is probably due to the fact that oxygen is rather immobile and the inclusion–host orientation relationships as well as the interface orientations organise themselves into configurations that minimise the extent of the re-arrangement of oxygen during growth of magnetite from plagioclase (Hwang et al., 2010; Tan et al., 2022).

3.4.3 Inclusion elongation direction

The elongation direction of needle- and lath-shaped precipitates is usually parallel to the interfaces with the best lattice match between the precipitate and the host crystal (Dahmen et al., 1984; Zhang, 2020). This rationale applies to all plagioclase hosted plane-normal type magnetite micro-inclusions. All these inclusions are elongated parallel to one of the MT⟨111⟩ directions, which, in turn, is aligned (sub)parallel to the normal direction of one of seven specific plagioclase lattice planes, including PL(112), PL($\bar{3}$12), PL(150), PL(1$\bar{5}$0), PL(100), PL($\bar{3}\bar{1}$2) and PL(1$\bar{1}$2). In the crystal structure of plagioclase, an alternation of oxygen-rich and cation-rich layers exists parallel to these specific lattice planes, and in the crystal structure of magnetite, densely packed oxygen layers are present parallel to MT{222}. The *d*-spacing of MT{222} is nearly identical to the *d*-spacing of the specific lattice planes in plagioclase. Thus, the densely packed oxygen layers in magnetite and the oxygen rich layers in plagioclase match very well. In particular, they are nearly coherent across the interface containing the corresponding MT⟨111⟩ direction and the plane normal to either one of the PL(112), PL($\bar{3}$12), PL(150), PL(1$\bar{5}$0), PL(100), PL($\bar{3}\bar{1}$2) and PL(1$\bar{1}$2) lattice planes as the common zone axis. Even though this ensures good lattice match at the interface in only one dimension (Howe et al., 2002), it is regarded as the crystallographic base for the preferred elongation directions of the different plane normal inclusion types (Ageeva et al., 2020). In detail, some lattice mismatch occurs even along the direction of good match, which can be accommodated either by elastic strain or by the introduction of misfit dislocations. Along the direction of good match, the following condition must hold (Howe, 1997):

$$|d_{\mathrm{PL}hkl}| = N \times |d_{\mathrm{MT222}}| \times (1 + \delta) \tag{3.1}$$

where N is a positive integer, $d_{\mathrm{PL}hkl}$ is the *d*-spacing of the PL(*hkl*) lattice plane corresponding to oxygen-rich layers in the crystal structure of plagioclase, d_{MT222} is the *d*-spacing of MT(222) and δ is the lattice misfit. If $\delta = 0$, every MT(222) lattice plane will coincide precisely with every N'th PL(*hkl*) lattice plane. The smaller N, the higher the fraction of lattice planes that are coherent across the interface. The preferred elongation direction with respect to the plagioclase lattice planes and the corresponding N and δ values are

Table 3.3: *d*-spacing of specific plagioclase lattice planes relevant for plane-normal inclusions and misfit δ calculated based on Fleet (1981); crystallographic data for plagioclase were taken from Wenk et al. (1980)

PL(*hkl*)	*d*-spacing / Å	Oxygen layers in plagioclase	N	$\lvert\delta\rvert$
112	2.46	Dense	1	0.016
$\bar{3}12$	2.50	Dense	1	0.032
150	2.40	Dense	1	0.012
$1\bar{5}0$	2.45	Dense	1	0.012
100	7.34	-	3	0.009
$\bar{3}\bar{1}2$	2.52	-	1	0.039
$1\bar{1}2$	2.53	-	1	0.042

listed in Table 3.3. The lattice constants of magnetite and plagioclase were taken from Fleet (1981) and Wenk et al. (1980), respectively. According to Weatherly and Nicholson (1968), misfit values of $|\delta| \leq 0.05$ allow formation of partially coherent precipitates. All seven orientation classes of the plane-normal needles fall into this range.

3.4.4 Effect of temperature

The plane-normal type magnetite micro-inclusions probably formed at high temperature above ∼600 °C (Bian et al., 2021), and thermal expansion needs to be taken into account when testing for geometrical match between the lattices of magnetite and plagioclase. The lattice parameters of magnetite are available from neutron diffraction at temperatures from 25°C to 800°C (Levy et al., 2012). The lattice parameters of plagioclase with compositions Ab_{100}, $An_{27}Ab_{73}$, $An_{35}Ab_{65}$, $An_{46}Ab_{54}$, $An_{60}Ab_{40}$, $An_{78}Ab_{22}$, $An_{89}Ab_{11}$, $An_{96}Ab_4$ and An_{100} are available from high resolution synchrotron X-ray powder diffraction for temperatures ranging from 25 °C to 620 °C, where Ab and An are the mole fractions of the albite ($NaAlSi_3O_8$) and anorthite ($CaAl_2Si_2O_8$) components (Tribaudino et al., 2010). The thermal expansion of plagioclase shows substantial anisotropy, where the direction with maximum thermal expansion accounts for over 70% of the total volume change, and it is close to parallel to the plane normal to the PL(100) lattice plane. This is close to the direction of the characteristic crankshaft-like chains of SiO_4 and AlO_4 tetrahedra in the crystal structure of plagioclase (Brown et al., 1984; Tribaudino et al., 2010). In Fig. 3.8 the *d*-spacing of the MT(222) lattice planes is compared with the *d*-spacing of plagioclase $An_{60}Ab_{40}$ lattice planes that are parallel to the basal planes of the different plane normal inclusion types.

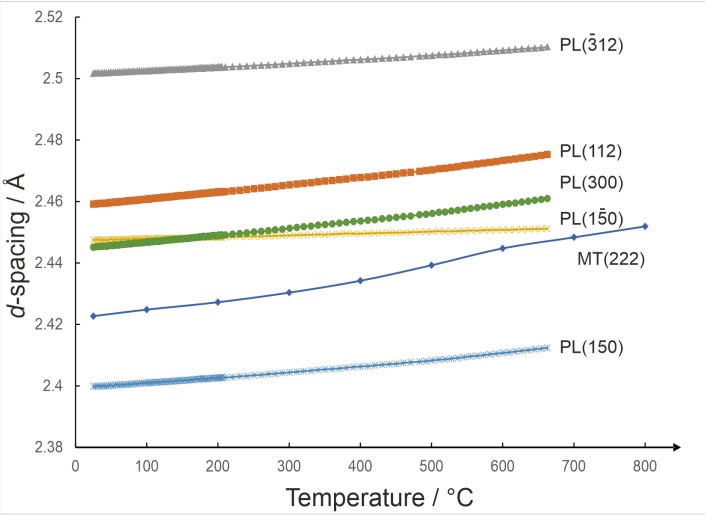

Figure 3.8: *d*-spacings of MT(222) and selected plagioclase lattice planes as a function of temperature; crystallographic data were taken from Tribaudino et al. (2010) for $An_{60}Ab_{40}$ (labradorite) and from Levy et al. (2012) for magnetite.

It is seen that the temperature dependence is highest for d_{MT222}. At temperatures above about 600°C, the *d*-spacing of PL(1$\bar{5}$0), PL(300) and PL(112) are closest to d_{MT222}, the *d*-spacing of PL($\bar{3}$12) is substantially higher and the *d*-spacing of PL(150) is substantially lower. The *d*-spacing difference between MT(222) and the different PL lattice planes does not appear to control the relative abundances of the different inclusion orientation classes. For example, although the *d*-spacing of PL(112) is never the closest to the d-spacing of MT(222), the PL(112)n inclusions are the most frequently observed inclusion type. This is why we infer that the lattice misfit across magnetite–plagioclase interfaces parallel to the needle elongation direction is important for defining the SOR, but it does not explain the relative abundances of the needles pertaining to the different orientation classes. The relatively high abundance of PL(112)n magnetite micro-inclusions may rather be due to the fact that plagioclase is relatively soft parallel to the PL(112)n direction as may be inferred from its relatively high coefficient of thermal expansion in this direction.

3.4.5 Selection of interface facets

Generally, it may be hypothesised that in microstructural equilibrium the interfaces bounding a crystalline precipitate in a host crystal will assume a configuration that minimises the free energy of the precipitate–host system (Sutton and Balluffi, 1995; Howe, 1997). The existence of faceted magnetite–plagioclase interfaces suggests that interface orientations are controlled by crystal structure. From our observations, we infer that in detail the selection of specific interface facets may be guided by different factors. For example, the interface segments F1 and F3 of the needle-shaped PL($\bar{3}$12)n-MT inclusion in nucleation orientation shown in Fig. 3.3 were probably selected, because of the lattice match with lattice planes of magnetite and plagioclase meeting at the interface in a commensurate manner. In contrast, interface segment F4 was probably selected, because of its parallel alignment with low-index lattice planes of both magnetite and plagioclase.

Apart from minimising interfacial energy in microstructural equilibrium, the shape of a precipitate and its interface configuration may also be controlled by kinetic factors. For example, the interface configuration may be selected that minimises the nucleation barrier and/or allows for fastest growth. Some heterogeneous phase transformations follow a path that minimises atomic movements (Christian, 2002). The COR of the PL(112)n-MT micro-inclusion in main orientation can be expressed as the parallel alignment of the PL(112) and the MT(222) lattice planes combined with a directional match within these planes, namely the parallel alignment of the PL$[\bar{1}\bar{1}1]$ and MT$[\bar{1}01]$ lattice directions, which are close-packed directions in the crystal structure of magnetite. According to the lattice parameters given by Wenk et al. (1980) for plagioclase and by Fleet (1981) for magnetite, the spacing between two lattice points along PL$[\bar{1}\bar{1}1]$ 1.8528 nm, and between two lattice points along MT$[\bar{1}01]$ is 0.5926 nm. Therefore, every third lattice point in magnetite along MT$[\bar{1}01]$ has a close match with a lattice point in plagioclase along PL$[\bar{1}\bar{1}1]$. The parallel alignment of two densely packed oxygen layers and of two directions within the oxygen layers minimises the extent of rearrangement of oxygen atoms during the transformation of plagioclase to magnetite, which probably eases nucleation and growth of magnetite in plagioclase (Dahmen, 1982; Wayman, 1994). The PL(112)n-MT micro-inclusion may thus nucleate directly in main orientation. The slight lattice mismatch along MT$[\bar{1}01]$ and PL$[\bar{1}\bar{1}1]$ may lead to the small deviation from parallel alignment between PL(112) and MT(222), which is usually less than 2° (Zhang, 2020).

3.4.6 Crystal structure control on plate-shaped magnetite microinclusion

In Fig. 3.9a simulated diffraction patterns of magnetite (red spots) and plagioclase (blue spots) viewed along MT$[112]$ ∥ PL$[5\bar{1}8]$ are superimposed according to the COR of the plate-shaped PL$(\bar{3}12)$n-MT micro-inclusion shown in Fig. 3.5f. In reciprocal space, a set of (*hkl*) lattice planes is represented by the so-called $\mathbf{g}_{hkl}$ vector, a vector emanating from the origin and pointing to the corresponding *hkl* diffraction spot. The $\mathbf{g}_{hkl}$ vector is perpendicular to the respective set of (*hkl*) lattice planes in real space, and its length is $1/d$, where d is the d-spacing of the (*hkl*) lattice planes. A vector $\Delta\mathbf{g}$ can be defined as the difference vector between a $\mathbf{g}_{hkl}$ vector of one phase and a $\mathbf{g}_{hkl}$ vector of the other phase (Zhang and Purdy, 1993). Some $\Delta\mathbf{g}$ vectors connecting pairs of closely spaced diffraction spots, where one pertains to magnetite and the other one pertains to plagioclase, are shown as black lines in Fig. 3.9a. It can be demonstrated by geometrical construction that the two sets of lattice planes, the diffraction spots of which are related by the vector $\Delta\mathbf{g}$, are perfectly coherent across a planar interface between the two phases that is perpendicular to the $\Delta\mathbf{g}$ vector. If in the superposed diffraction patterns of two phases, two or more non-equivalent $\Delta\mathbf{g}$ vectors are parallel to each other, all lattice planes containing the viewing direction as the common

Table 3.4: Lattice constants of magnetite (MT) (Fleet, 1981), of constrained magnetite (MT^c) when magnetite–plagioclase interface of PL($\bar{3}12$)n-MT plate inclusion is coherent

Phase	a / Å	b / Å	c / Å	α / °	β / °	γ / °
MT	8.3970	8.3970	8.3970	90	90	90
MT^c	8.5730	8.4216	8.3785	91.4792	92.4834	89.6406

zone axis are coherent across a planar interface that is perpendicular to the respective $\Delta\mathbf{g}$ vector. The $\Delta\mathbf{g}$ vectors connecting closely spaced diffraction spots of magnetite and plagioclase shown in Fig. 3.9a have all different directions, so that an exact phase boundary configuration cannot be identified. The situation can, however, be changed by applying a strain to either one or both of the lattices. In Fig. 3.9a two pairs of nearly coinciding $\mathbf{g}$ vectors one pertaining to magnetite and the other pertaining to plagioclase have been identified. One pair is represented by $\mathbf{g}_{PL1} = PL(\bar{3}12)$ and $\mathbf{g}_{MT1} = MT(22\bar{2})$ and the other by $\mathbf{g}_{PL2} = PL(2, 10, 0)$ and $\mathbf{g}_{MT2} = MT(5\bar{5}0)$. The two pairs of nearly coinciding $\mathbf{g}$ vectors can be made perfectly coincident by applying a constraint on one or both of the two lattices. The resulting relationship between the two lattices is referred to as the *constrained coincidence site lattice* (CCSL) (Ye and Zhang, 2002). The choice of which diffraction spots are made coincident by application of a constraint is arbitrary, but usually two criteria are employed to guide the selection: (i) the diffraction spots that are closest in reciprocal space should be selected to minimise the necessary strain; (ii) the unit cell of the resulting CCSL should be as small as possible, so that the density of CCSL points in direct space is high (Zhang et al., 2000; Ye and Zhang, 2002; Shi et al., 2013). The aforementioned two pairs of $\mathbf{g}$ vectors meet both criteria. However, they define the correspondence between the lattices of magnetite and plagioclase only in the plane perpendicular to the viewing direction. An additional constraint is needed in the third dimension to fully fix the correspondence between the two lattices. We chose the viewing direction MT[112] || PL[$5\bar{1}8$], where the length of vector MT[112] is 2.0561 Å and the length of vector PL[$5\bar{1}8$] is 5.5870 Å. To keep the constraint in the third dimension small, we chose PL[$5\bar{1}8$]/5 and MT[112]/2 as the reference vectors. The two pairs of selected diffraction spots and the selected lattice vectors in viewing direction are made coincident by applying a constraint on the lattice of magnetite. The procedure is described in the appendix. The resultant lattice parameters of the constrained magnetite MT^c are given in Table 3.4.

In Fig. 3.9b the superposition of the simulated diffraction patterns of constrained magnetite (red spots) and of plagioclase (blue spots) are shown for the same orientation relation and viewing direction as in Fig. 3.9a. Now the pairs of originally nearly coinciding $\mathbf{g}$ vectors, namely $\mathbf{g}_{PL1} = PL(\bar{3}12)$ and $\mathbf{g}^c_{MT1} = MT(22\bar{2})$ and the other by $\mathbf{g}_{PL2} = PL(2, 10, 0)$ and $\mathbf{g}^c_{MT2} = MT(5\bar{5}0)$, where superscript '*c*' refers to constrained magnetite, have become coincident.

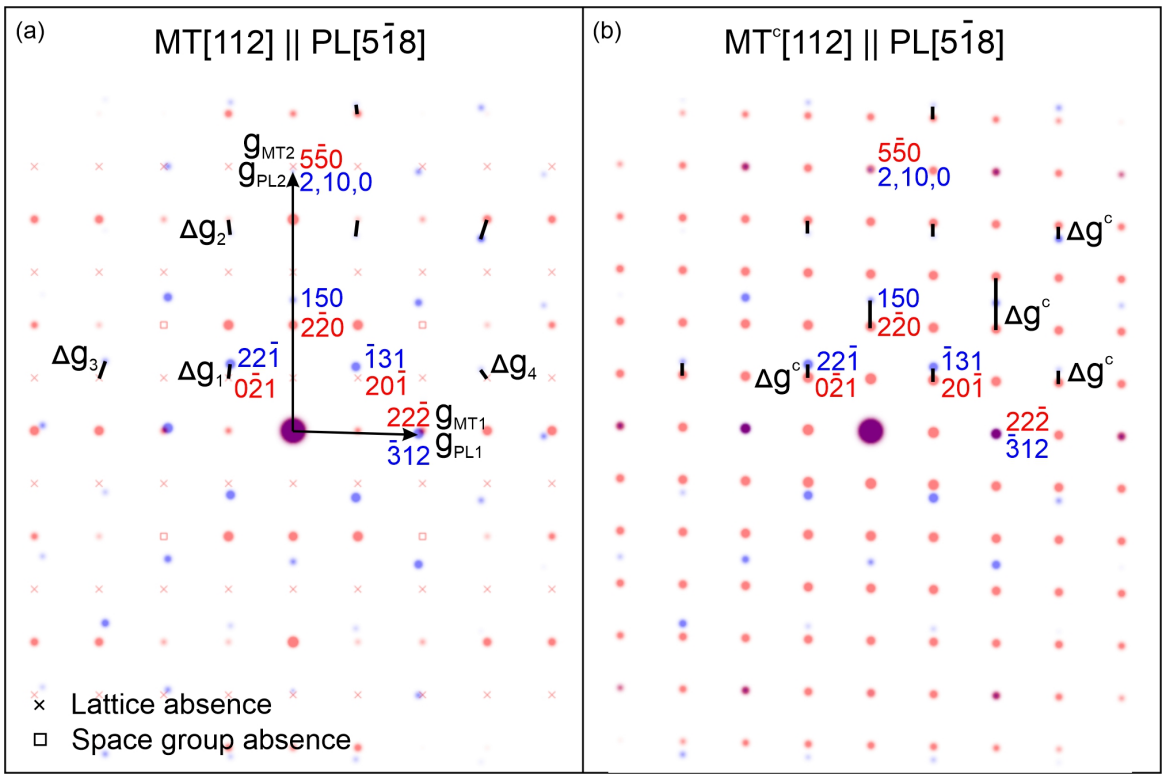

Figure 3.9: (a) Diffraction patterns of magnetite (red spots) and plagioclase (blue spots) superimposed according to the COR in Fig. 3.5f. Viewing direction is MT[112] || PL[5$\bar{1}$8]. Nearly coincident **g** vectors from magnetite and plagioclase are indicated by black arrows emanating from the origin. Representative $\Delta\mathbf{g}_i$ ($i = 1-4$) vectors with different directions and lengths are marked with black lines connecting plagioclase and magnetite diffraction spots. (b) Superposition of diffraction patterns of constrained magnetite (red spots) and plagioclase (blue spots) according to the COR in Fig. 3.5f. The $\Delta\mathbf{g}_i$ vectors now become $\Delta\mathbf{g}_i^c$ vectors. All $\Delta\mathbf{g}_i^c$ vectors are vertical and parallel to each other (black lines). The trace of the plate surface is perpendicular to all the $\Delta\mathbf{g}_i^c$ vectors and is thus horizontal. Viewing direction is MT^c[112] || PL[5$\bar{1}$8]. Low index lattice planes of magnetite (red) and plagioclase (blue) are indicated next to the corresponding diffraction spots. Symbols × and □ represent the forbidden diffraction spots, which are caused by lattice and space group, respectively.

The $\Delta\mathbf{g}$ vectors, $\Delta\mathbf{g}_i = \mathbf{g}_{\mathrm{MT}} - \mathbf{g}_{\mathrm{PL}} (i = 1-4)$, which all have different directions in Fig. 3.9a have become the $\Delta\mathbf{g}^c = \mathbf{g}^c_{\mathrm{MT}} - \mathbf{g}_{\mathrm{PL}}$ vectors in Fig. 3.9b, which are all parallel to each other and have orientations $\Delta\mathbf{g}^c \perp$ MT(1$\bar{1}$0) and $\Delta\mathbf{g}^c \perp$ PL(150). Thus, in the constrained situation, all lattice planes sharing the viewing direction MT[112] || PL[5$\bar{1}$8] as their common zone axis are perfectly coherent across a magnetite–plagioclase interface that is parallel to MT(1$\bar{1}$0) and PL(150). Such a situation has been referred to as an *exact phase boundary* by Robinson et al. (1971, 1977) and Fleet (1982) and corresponds to an O-line in O-lattice theory (Luo and Weatherly, 1987; Bollmann, 2012). In addition, a best fit direction lies in the MT(2$\bar{2}$0) || PL(150) lattice planes, which makes these lattice planes prone to serve as the habit plane for the growth of plate-shaped magnetite. The basal plane of the plate-shaped inclusion thus corresponds to an exact boundary for all lattice planes pertaining to this zone. This condition may, but need not necessarily produce a plate-shaped magnetite inclusion. Needle-shaped inclusions with this COR are also observed. For example, the cross-section of the PL($\bar{3}$12)n-MT micro-inclusion in main orientation containing interface segment MT(20$\bar{2}$) || PL(150) corresponds to the above-mentioned MT(2$\bar{2}$0) || PL(150) alignment.

The analysis of the $\Delta\mathbf{g}$ vectors connecting lattice planes in constrained magnetite with those in unconstrained plagioclase must be considered as a thought experiment. It is not clear, whether the lattice planes sharing the MT[112] || PL[$5\bar{1}8$] directions as their common zone axis were coherent across the magnetite–plagioclase interface at any time. As a matter of fact, such coherency would require that either one or both of the lattices were substantially deformed with associated elastic strain energy. The lattice misfit between magnetite and plagioclase in the actual configuration must be accommodated by atomic interfacial steps and dislocations (Ye and Zhang, 2002). Generally, in the actual configuration the interface consists of the habit plane as derived from the CCSL method, which decomposes into an arrangement of terraces and steps that accommodate the misfit (Howe and Spanos, 1999; Ye and Zhang, 2002; Shi et al., 2013). The exact nature of the dislocations at the magnetite–plagioclase interface remain unclear. Nevertheless, the analysis is considered instructive for interpreting the actually observed COR and lattice match, which only slightly deviate from the fully coherent interface between constrained magnetite and unconstrained plagioclase.

The plate-shaped magnetite micro-inclusions are often located in plagioclase domains that are devoid of needle-shaped inclusions (Fig. 3.1). It may thus be hypothesised that the plate-shaped magnetite micro-inclusions were formed by recrystallisation of several needle-shaped magnetite inclusions into the energetically more favourable plate morphology.

3.5 Summary and conclusions

The crystallographic basis of the SORs and CORs between needle-, lath- and plate-shaped magnetite micro-inclusions and plagioclase host was investigated using correlated optical and scanning transmission electron microscopy. The magnetite–plagioclase interfaces are crystalline, with no amorphous layer or gap between the two phases. The magnetite micro-inclusions of the plane normal type are elongated parallel to one of their MT⟨111⟩ directions, which, in turn, is perpendicular to one of seven specific plagioclase lattice planes including PL(112), PL($\bar{3}12$), PL(150), PL($1\bar{5}0$), PL(100), PL($\bar{3}\bar{1}2$) and PL($1\bar{1}2$) defining seven orientation classes. The inclusions elongation direction and shape orientations confer to the parallel alignment of the MT{222} lattice planes with either one of these specific lattice planes of plagioclase. This is ascribed to the good match between oxygen layers in the magnetite and plagioclase crystal structures across magnetite–plagioclase interfaces bounding the magnetite inclusions parallel to their elongation direction, which is ensured for these orientation relationships.

For each orientation class, specific orientation variants characterised by at least one additional parallel alignment of crystallographic planes or directions between magnetite and plagioclase are observed. When

the additional alignment is PL[14, -10, 7] || MT[100], the inclusion is classified as being in nucleation orientation, where FeO_6 octahedra of magnetite fit into channels parallel to PL[001] in the crystal structure of plagioclase in a favourable manner. The inclusions in nucleation orientation have regular, mostly MT{220} faceted cross-sections. The facets are mainly controlled by low index lattice planes of magnetite and by the commensurate impingement of low index magnetite and plagioclase lattice planes along the interface. Moreover, the inclusions in nucleation orientation typically show exact alignment of their elongation direction to the respective plane normal direction. If, in addition to the MT{111} || PL(*hkl*) alignment, one of the MT{220} lattice planes is parallel to another one of the specific plagioclase lattice planes, the inclusion is classified as being in main orientation. These inclusions show more complex cross-sections with typically only two facet orientations and otherwise curved, locally re-entrant magnetite–plagioclase interface segments. The facets of magnetite micro-inclusions in main orientation are mainly controlled by the parallel alignment of low index lattice planes of both, magnetite and plagioclase, and the inclusion elongation direction deviates by up to about 5° from the respective PL(*hkl*)-n direction.

The oxygen sub-lattices of magnetite and plagioclase are suggested to be responsible for the preferred orientation relationships as the observed CORs and SORs ensure continuity of the oxygen sub-lattices across the magnetite–plagioclase interfaces. In addition, the observed CORs and SORs minimises the rearrangement of oxygen atoms during growth of magnetite inside plagioclase.

The morphologies of the magnetite micro-inclusions indicate a potential transformation from nucleation to main orientations, an evolution that may be important in the context of paleomagnetic reconstructions relying on the natural remanent magnetisation of single grains of magnetite bearing plagioclase. Oriented magnetite micro-inclusions in plagioclase are common in mafic intrusive rocks from a variety of geological settings. Our findings from ocean floor gabbros are likely transferable to these other occurrences.

Appendix

Two pairs of diffraction spots, each comprising two closely spaced diffraction spots one pertaining to plagioclase and the other pertaining to magnetite, were selected, and a transformation was applied on magnetite to make the selected nearly coincident diffraction spots coincide. The transformation is represented by transformation matrix $\mathbf{A}_\mathrm{P}$ in direct space and by transformation matrix $\mathbf{A}_\mathrm{P}^*$ in reciprocal space. The transformation matrix is obtained in two steps: In the first step, the magnetite and plagioclase unit cells are expressed in terms of a common orthonormal coordinate system $Oxyz$ with unit vectors along the Ox, Oy and Oz-axes defining the base vectors **i**, **j** and **k**. The unit cell of a crystal is usually expressed in the crystal coordinate system defined by the lattice constants a, b, c, α, β, γ with the base vector **a**, **b** and **c**.

The orientation of the crystal coordinate system in the orthonormal coordinate system is chosen so that $\mathbf{a} \parallel Ox$ and $\mathbf{a} \times \mathbf{c} \parallel Oy$. The base vectors of the crystal coordinate system **a**, **b** and **c** expressed in orthonormal coordinates read

$$\begin{aligned} \mathbf{a} &= \mathbf{i}s_1^1 + \mathbf{j}s_1^2 + \mathbf{k}s_1^3 \\ \mathbf{b} &= \mathbf{i}s_2^1 + \mathbf{j}s_2^2 + \mathbf{k}s_2^3 \\ \mathbf{c} &= \mathbf{i}s_3^1 + \mathbf{j}s_3^2 + \mathbf{k}s_3^3. \end{aligned} \tag{3.2}$$

In matrix notation this is

$$\mathbf{u}^{\mathrm{T}} = \mathbf{u}_{(\mathrm{orth})}^{\mathrm{T}}\mathbf{S}, \tag{3.3}$$

where

$$\mathbf{S} = \begin{pmatrix} s_1^1 & s_2^1 & s_3^1 \\ s_1^2 & s_2^2 & s_3^2 \\ s_1^3 & s_2^3 & s_3^3 \end{pmatrix}, \tag{3.4}$$

u and $\mathbf{u}_{(\mathrm{orth})}$ represent the base vectors of the crystal coordinate system and of the orthonormal coordinate system, respectively, and $|^{\mathrm{T}}$ is the transpose operation.

The elements of the **S** matrix are obtained from the scalar products of the base vectors in crystal coordinate making use of the orthogonality of the base vectors in the orthonormal coordinate system (Bollmann, 2012), which yields

$$\mathbf{S} = \begin{pmatrix} a & b \cdot cos\gamma & c \cdot cos\beta \\ 0 & (b/sin\beta)(sin^2\beta - cos^2\alpha - cos^2\gamma + cos\alpha \cdot cos\beta \cdot cos\gamma)^{1/2} & 0 \\ 0 & (b/sin\beta)(cos\alpha - cos\beta \cdot cos\gamma) & c \cdot sin\beta \end{pmatrix}. \tag{3.5}$$

The column vectors of the **S** matrix are the unit vectors in the crystal coordinate system expressed as linear combinations of the base vectors of the orthonormal coordinate system.

The lattice constants of cubic magnetite $a_{\mathrm{MT}} = 8.397$ Å and of triclinic plagioclase $a_{\mathrm{PL}} = 8.1736$ Å, $b_{\mathrm{PL}} = 12.8736$ Å, $c_{\mathrm{PL}} = 7.1022$ Å, $\alpha_{\mathrm{PL}} = 93.462°$, $\beta_{\mathrm{PL}} = 116.054°$, $\gamma_{\mathrm{PL}} = 90.475°$, taken from Fleet (1981) and Wenk et al. (1980), respectively, were used to obtain $\mathbf{S}_{\mathrm{MT}}$ and $\mathbf{S}_{\mathrm{PL}}$ based on Eq. 4.4. Given a column vector **v** in the crystal coordinate system, the corresponding vector in the orthonormal coordinate system

$\mathbf{v}_{(\mathrm{orth})}$ can be expressed as $\mathbf{v}_{(\mathrm{orth})} = \mathbf{S}\mathbf{v}$.

In the next step, the transformation matrix $\mathbf{A}_\mathrm{P}^*$ is applied to magnetite to make the selected pairs of diffraction spots, which are represented by the reciprocal lattice vectors $\mathbf{g}_{\mathrm{PL}1}$, $\mathbf{g}_{\mathrm{PL}2}$, $\mathbf{g}_{\mathrm{PL}3}$ and $\mathbf{g}_{\mathrm{MT}1}$, $\mathbf{g}_{\mathrm{MT}2}$, $\mathbf{g}_{\mathrm{MT}3}$, respectively, coincide. The transformation matrix $\mathbf{A}_\mathrm{P}^*$ must suffice the condition

$$\mathbf{A}_\mathrm{P}^* \cdot (\mathbf{S}_\mathrm{MT}^* \cdot \mathbf{G}_\mathrm{MT}) = \mathbf{S}_\mathrm{PL}^* \cdot \mathbf{G}_\mathrm{PL} \tag{3.6}$$

where $\mathbf{A}_\mathrm{P}^*$ is the $\mathbf{A}_\mathrm{P}$ in reciprocal space $\mathbf{A}_\mathrm{P}^* = (\mathbf{A}_\mathrm{P}^\mathrm{T})^{-1}$, $\mathbf{S}_\mathrm{MT}^*$ and $\mathbf{S}_\mathrm{PL}^*$ are $\mathbf{S}_\mathrm{MT}$ and $\mathbf{S}_\mathrm{PL}$ expressed in reciprocal space. $\mathbf{G}_\mathrm{PL}$ is a 3×3 matrix $\mathbf{G}_\mathrm{PL} = (\mathbf{g}_{\mathrm{PL}1}, \mathbf{g}_{\mathrm{PL}2}, \mathbf{g}_{\mathrm{PL}3})$, where

$$\mathbf{g}_{\mathrm{PL}1} = \begin{pmatrix} -3 \\ 1 \\ 2 \end{pmatrix}, \quad \mathbf{g}_{\mathrm{PL}2} = \begin{pmatrix} 2 \\ 10 \\ 0 \end{pmatrix}, \quad \mathbf{g}_{\mathrm{PL}3} = \begin{pmatrix} 0.465 \\ -0.761 \\ 1 \end{pmatrix} /2. \tag{3.7}$$

The third vector $\mathbf{g}_{\mathrm{PL}3}$ is equivalent to PL$[5\bar{1}8]/5$ in reciprocal space. It is obtained by the following method: (i) PL$[5\bar{1}8]$ is transformed into a vector in reciprocal space preserving the same direction, i.e. PL$[5\bar{1}8]$ = PL(0.465, -0.761,1); (ii) the reciprocal vector PL(0.465, -0.761,1) is divided by 2 to adjust the length of PL$[5\bar{1}8]/5$.

$\mathbf{G}_\mathrm{MT}$ is a 3×3 matrix $\mathbf{G}_\mathrm{MT} = (\mathbf{g}_{\mathrm{MT}1}, \mathbf{g}_{\mathrm{MT}2}, \mathbf{g}_{\mathrm{MT}3})$, with

$$\mathbf{g}_{\mathrm{MT}1} = \begin{pmatrix} 2 \\ 2 \\ -2 \end{pmatrix}, \quad \mathbf{g}_{\mathrm{MT}2} = \begin{pmatrix} 5 \\ -5 \\ 0 \end{pmatrix}, \quad \mathbf{g}_{\mathrm{MT}3} = \begin{pmatrix} 1 \\ 1 \\ 2 \end{pmatrix} /3. \tag{3.8}$$

The third vector $\mathbf{g}_{\mathrm{MT}3}$ is equivalent to MT$[112]/2$ in reciprocal space.

In reciprocal space the constraint is obtained by rearranging Eq. 3.6, which yields

$$\mathbf{A}_\mathrm{P}^* = \mathbf{S}_\mathrm{PL}^* \cdot \mathbf{G}_\mathrm{PL} \cdot (\mathbf{S}_\mathrm{MT}^* \cdot \mathbf{G}_\mathrm{MT})^{-1}, \tag{3.9}$$

and finally $\mathbf{A}_\mathrm{P}$ is obtained from $\mathbf{A}_\mathrm{P} = ((\mathbf{A}_\mathrm{P}^*)^{-1})^\mathrm{T}$, which yields

$$\mathbf{A}_\mathrm{P} = \begin{pmatrix} -0.2339 & -0.6241 & 0.7733 \\ 0.7240 & -0.6319 & -0.3220 \\ 0.6814 & 0.4666 & 0.5428 \end{pmatrix} \tag{3.10}$$

The constrained MT unit cell MT^c can be expressed in orthonormal coordinate as

$$\mathbf{S}_\mathrm{MT}^\mathrm{c} = \mathbf{A}_\mathrm{P} \cdot \mathbf{S}_\mathrm{MT}, \tag{3.11}$$

which yields

$$\mathbf{S}_\mathrm{MT}^\mathrm{c} = \begin{pmatrix} -1.9635 & -5.2387 & 6.4911 \\ 6.0768 & -5.3046 & -2.7030 \\ 5.7195 & 3.9168 & 4.5561 \end{pmatrix} \tag{3.12}$$

The transformation applied to magnetite does not change the translation vectors of the unit cell, thus the constrained lattice constants, as well as the angles between each unit vector can be calculated from $\mathbf{S}_\mathrm{MT}^\mathrm{c}$. For instance, the constrained base vector $\mathbf{a}_\mathrm{MT}^\mathrm{c}$ can be expressed in orthonormal coordinate $\mathbf{a}_\mathrm{MT}^\mathrm{c}$=$\mathbf{S}_\mathrm{MT}^\mathrm{c}\cdot[100]'$, that is the first column in $\mathbf{S}_\mathrm{MT}^\mathrm{c}$. The value of the base vector $a_\mathrm{MT}^\mathrm{c} = 8.5730$ Å is the new lattice constant of the constrained magnetite. Similarly, b_MT^c and c_MT^c can be derived in the same manner. The angle between the base vectors $\mathbf{b}_\mathrm{MT}^\mathrm{c}$ and $\mathbf{c}_\mathrm{MT}^\mathrm{c}$ of the constrained magnetite thus define the angle $\alpha_\mathrm{MT}^\mathrm{c} = \measuredangle(\mathbf{b}_\mathrm{MT}^\mathrm{c}, \mathbf{c}_\mathrm{MT}^\mathrm{c})$, and is derived by the inverse tangent formula $\alpha_\mathrm{MT}^\mathrm{c} = \mathrm{atan2}(\| \mathbf{b}_\mathrm{MT}^\mathrm{c} \times \mathbf{c}_\mathrm{MT}^\mathrm{c} \|, \mathbf{b}_\mathrm{MT}^\mathrm{c} \cdot \mathbf{c}_\mathrm{MT}^\mathrm{c})$. $\beta_\mathrm{MT}^\mathrm{c}$ and $\gamma_\mathrm{MT}^\mathrm{c}$ can be obtained following the same procedure. The resultant lattice constants of constrained magnetite MT^c are listed in Table 3.4.

Acknowledgements

We thank Alexey Pertsev for providing the dredged samples. We thank two reviewers for their constructive critique, which helped to improve the presentation significantly. Editorial handling is gratefully acknowledged.

Funding

Funding by the Austrian Science Foundation (FWF), Grant No. I 3998N29, and by the Russian Foundation for Basic Research (RFBR), Grant No. 18-55-14003 are gratefully acknowledged. This project has received funding from the European Union's Horizon 2020 research and innovation programme under grant agreement No 823717 – ESTEEM3.

Author Contributions

GB: Study conception and design, sample preparation, data collection, results analysis and interpretation, first draft preparation; OA: Study conception and design, sample preparation; VR: STEM data collection; CL: STEM data collection; TJP: STEM data collection; GH: sample preparation; RA: Study conception and design, study supervision. All authors reviewed and commented on previous manuscript. Final manuscript is approved by all authors.

Bibliography

O. Ageeva, G. Habler, D. Topa, T. Waitz, C. Li, A. Pertsev, T. Griffiths, O. Zhilicheva, and R. Abart. Plagioclase hosted fe-ti-oxide micro-inclusions in an oceanic gabbro-plagiogranite association from the mid atlantic ridge at 13°34' n. *American Journal of Science*, 316(2):85–109, 2016. ISSN 0002-9599. doi: 10.2475/02.2016.01.

O. Ageeva, G. Habler, A. Pertsev, and R. Abart. Fe-Ti oxide micro-inclusions in clinopyroxene of oceanic gabbro: phase content, orientation relations and petrogenetic implication. *Lithos*, 290:104–115, 2017. doi: 10.1016/j.lithos.2017.08.007.

O. Ageeva, G. Bian, G. Habler, A. Pertsev, and R. Abart. Crystallographic and shape orientations of magnetite micro-inclusions in plagioclase. *Contributions to Mineralogy and Petrology*, 175(10):1–16, 2020. doi: 10.1007/s00410-020-01735-8.

O. Ageeva, G. Habler, S. A. Gilder, R. Schuster, A. Pertsev, O. Pilipenko, G. Bian, and R. Abart. Oriented magnetite inclusions in plagioclase: Implications for the anisotropy of magnetic remanence. *Geochemistry, Geophysics, Geosystems*, page e2021GC010272, 2022. doi: 10.1029/2021GC010272.

V. Beltenev, V. Ivanov, I. Rozhdestvenskaya, G. Cherkashov, T. Stepanova, V. Shilov, A. Pertsev, M. Davydov, I. Egorov, I. Melekestseva, et al. A new hydrothermal field at 13° 30 N on the Mid-Atlantic Ridge. *InterRidge News*, 16(9):10, 2007.

V. Beltenev, I. Ivanov, I. Rozhdestvenskaya, G. Cherkashev, T. Stepanova, V. Shilov, M. Davydov, A. Laiba, V. Kaylio, E. Narkevsky, et al. New data about hydrothermal fields on the mid-atlantic ridge between 11-14 N: 32nd cruise of r/v professor logatchev. *InterRidge News*, 18:13–17, 2009.

G. Bian, O. Ageeva, A. Rečnik, G. Habler, and R. Abart. Formation pathways of oriented magnetite micro-inclusions in plagioclase from oceanic gabbro. *Contributions to Mineralogy and Petrology*, 176(12):1–21, 2021. doi: 10.1007/s00410-021-01864-8.

W. Bollmann. *Crystal defects and crystalline interfaces*. Springer Science & Business Media, 2012.

E. G. Bosch and I. Lazić. Analysis of hr-stem theory for thin specimen. *Ultramicroscopy*, 156:59–72, 2015. ISSN 0304-3991. doi: https://doi.org/10.1016/j.ultramic.2015.02.004.

W. L. Brown, R. E. Openshaw, P. F. McMillan, and C. M. B. Henderson. A review of the expansion behavior of alkali feldspars: coupled variations in cell parameters and possible phase transitions. *American Mineralogist*, 69(11-12):1058–1071, 1984.

P. Champness. Nucleation and growth of iron oxides in olivines,(Mg, Fe) 2Sio4. *Mineralogical magazine*, 37(291):790–800, 1970. doi: 10.1180/minmag.1970.037.291.05.

J. W. Christian. *The theory of transformations in metals and alloys*. Newnes, 2002.

A. Cipriani, E. Bonatti, D. Brunelli, and M. Ligi. 26 million years of mantle upwelling below a segment of the mid atlantic ridge: The vema lithospheric section revisited. *Earth and Planetary Science Letters*, 285 (1-2):87–95, 2009. doi: 10.1016/j.epsl.2009.05.046.

U. Dahmen. Orientation relationships in precipitation systems. *Acta Metallurgica*, 30(1):63–73, 1982. doi: 10.1016/0001-6160(82)90045-1.

U. Dahmen, P. Ferguson, and K. Westmacott. Invariant line strain and needle-precipitate growth directions in Fe-Cu. *Acta Metallurgica*, 32(5):803–810, 1984. doi: 10.1016/0001-6160(84)90153-6.

D. J. Dunlop and Ö. Özdemir. *Rock magnetism: fundamentals and frontiers*. Number 3. Cambridge university press, 2001.

J. Escartin, C. Mevel, S. Petersen, D. Bonnemains, M. Cannat, M. Andreani, N. Augustin, A. Bezos, V. Chavagnac, Y. Choi, et al. Tectonic structure, evolution, and the nature of oceanic core complexes and their detachment fault zones (13° 20 n and 13° 30 n, Mid Atlantic Ridge). *Geochemistry, Geophysics, Geosystems*, 18(4):1451–1482, 2017. doi: 10.1002/2016GC006775.

J. M. Feinberg, H.-R. Wenk, P. R. Renne, and G. R. Scott. Epitaxial relationships of clinopyroxene-hosted magnetite determined using electron backscatter diffraction (ebsd) technique. *American Mineralogist*, 89(2-3):462–466, 2004. doi: 10.2138/am-2004-2-328.

M. Fleet. The structure of magnetite. *Acta Crystallographica Section B: Structural Crystallography and Crystal Chemistry*, 37(4):917–920, 1981. doi: 10.1107/S0567740881004597.

M. Fleet, G. A. Bilcox, and R. L. Barnett. Oriented magnetite inclusions in pyroxenes from the Grenville Province. *The Canadian Mineralogist*, 18(1):89–99, 1980.

M. E. Fleet. Orientation of phase and domain boundaries in crystalline solids. *American Mineralogist*, 67 (9-10):926–936, 1982.

W. Gao, C. L. Ciobanu, N. J. Cook, A. Slattery, F. Huang, and D. Wang. Nanoscale study of lamellar exsolutions in clinopyroxene from olivine gabbro: Recording crystallization sequences in iron-rich layered intrusions. *American Mineralogist: Journal of Earth and Planetary Materials*, 104(2):244–261, 2019. doi: 10.2138/am-2019-6764.

J. Howe and G. Spanos. Atomic structure of the austenite-cementite interface of proeutectoid cementite plates. *Philosophical Magazine A*, 79(1):9–30, 1999. doi: 10.1080/01418619908214271.

J. M. Howe. *Interfaces in materials: atomic structure, thermodynamics and kinetics of solid-vapor, solid-liquid and solid-solid interfaces*. Wiley-Interscience, 1997.

J. M. Howe, W. T. Reynolds, and V. K. Vasudevan. Static and in-situ high-resolution transmission electron microscopy investigations of the atomic structure and dynamics of massive transformation interfaces in a Ti-Al alloy. *Metallurgical and Materials Transactions A*, 33(8):2391–2411, 2002. doi: 10.1007/s11661-002-0362-4.

S.-L. Hwang, P. Shen, T.-F. Yui, and H.-T. Chu. On the coherency-controlled growth habit of precipitates in minerals. *Journal of Applied Crystallography*, 43(3):417–428, 2010. doi: 10.1107/S0021889810007454.

J. A. Karson, R. M. Lawrence, et al. Tectonic setting of serpentinite exposures on the western median valley wall of the MARK area in the vicinity of Site 920. In *PROCEEDINGS-OCEAN DRILLING PROGRAM SCIENTIFIC RESULTS*, pages 5–22. National Science Foundation, 1997.

I. Lazić, E. G. Bosch, and S. Lazar. Phase contrast stem for thin samples: Integrated differential phase contrast. *Ultramicroscopy*, 160:265–280, 2016. ISSN 0304-3991. doi: https://doi.org/10.1016/j.ultramic.2015.10.011.

D. Levy, R. Giustetto, and A. Hoser. Structure of magnetite (Fe3O4) above the Curie temperature: a cation ordering study. *Physics and Chemistry of Minerals*, 39(2):169–176, 2012. doi: 10.1007/s00269-011-0472-x.

C. Luo and G. Weatherly. The invariant line and precipitation in a Ni-45 wt% Cr alloy. *Acta metallurgica*, 35(8):1963–1972, 1987. doi: 10.1016/0001-6160(87)90025-3.

C. J. MacLeod, R. Searle, B. Murton, J. Casey, C. Mallows, S. Unsworth, K. Achenbach, and M. Harris. Life cycle of oceanic core complexes. *Earth and Planetary Science Letters*, 287(3-4):333–344, 2009. doi: 10.1016/j.epsl.2009.08.016.

E. S. Nikolaisen, R. J. Harrison, K. Fabian, and S. A. McEnroe. Hysteresis of natural magnetite ensembles: Micromagnetics of silicate-hosted magnetite inclusions based on focused-ion-beam nanotomography. *Geochemistry, Geophysics, Geosystems*, 21(11):e2020GC009389, 2020. doi: 10.1029/2020GC009389.

E. S. Nikolaisen, R. Harrison, K. Fabian, N. Church, S. A. McEnroe, B. E. Sørensen, and C. Tegner. Hysteresis parameters and magnetic anisotropy of silicate-hosted magnetite exsolutions. *Geophysical Journal International*, 229(3):1695–1717, 2022. doi: 10.1093/gji/ggac007.

H. Ondréas, M. Cannat, Y. Fouquet, and A. Normand. Geological context and vents morphology of the ultramafic-hosted Ashadze hydrothermal areas (Mid-Atlantic Ridge 13° N). *Geochemistry, Geophysics, Geosystems*, 13(11), 2012. doi: 10.1029/2012GC004433.

A. Pertsev, N. Bortnikov, E. Vlasov, V. Beltenev, I. Dobretsova, and O. Ageeva. Recent massive sulfide deposits of the semenov ore district, Mid-Atlantic Ridge, 13° 31 N: Associated rocks of the oceanic core complex and their hydrothermal alteration. *Geology of Ore Deposits*, 54(5):334–346, 2012. doi: 10.1134/S1075701512050030.

P. Robinson, H. W. Jaffe, M. Ross, and C. Klein Jr. Orientation of exsolution lamellae in clinopyroxenes and clinoamphiboles: consideration of optimal phase boundaries. *American Mineralogist: Journal of Earth and Planetary Materials*, 56(5-6):909–939, 1971.

P. Robinson, M. Ross, G. Nord, J. Smyth, and H. Jaffe. Exsolution lamellae in augite and pigeonite; fossil indicators of lattice parameters at high temperature and pressure. *American Mineralogist*, 62(9-10): 857–873, 1977.

Z.-Z. Shi, F.-Z. Dai, M. Zhang, X.-F. Gu, and W.-Z. Zhang. Secondary coincidence site lattice model for truncated triangular β-Mg2Sn precipitates in a Mg-Sn-based alloy. *Metallurgical and Materials Transactions A*, 44(6):2478–2486, 2013. doi: 10.1007/s11661-013-1633-y.

P. Sobolev. Orientation of acicular iron-ore mineral inclusions in plagioclase. *International Geology Review*, 32(6):616–628, 1990.

A. Sutton and R. Balluffi. *Interfaces in Crystalline Materials*. Clarendon Press, Oxford, 1995.

W. Tan, P. Liu, H. He, C. Y. Wang, and X. Liang. Mineralogy and Origin of Exsolution in Ti-rich Magnetite from Different Magmatic Fe-ti Oxide-bearing Intrusions. *The Canadian Mineralogist*, 54(3):539–553, 05 2016. ISSN 0008-4476. doi: 10.3749/canmin.1400069.

W. Tan, C. Y. Wang, S. M. Reddy, H. He, H. Xian, and C. Xing. Magnetite-rutile symplectite in ilmenite records magma hydration in layered intrusions. *American Mineralogist*, 107(3):395–404, 03 2022. ISSN 0003-004X. doi: 10.2138/am-2021-7777.

J. Tarduno, R. Cottrell, and A. Smirnov. The paleomagnetism of single silicate crystals: Recording geomagnetic field strength during mixed polarity intervals, superchrons, and inner core growth. *Reviews of Geophysics*, 44(1), 2006. doi: 10.1029/2005RG000189.

M. Tribaudino, R. Angel, F. Cámara, F. Nestola, D. Pasqual, and I. Margiolaki. Thermal expansion of plagioclase feldspars. *Contributions to Mineralogy and Petrology*, 160(6):899–908, 2010. doi: 10.1007/s00410-010-0513-3.

C. Wayman. The phenomenological theory of martensite crystallography: Interrelationships. *Metallurgical and Materials transactions A*, 25(9):1787–1795, 1994. doi: 10.1007/BF02649029.

G. Weatherly and R. Nicholson. An electron microscope investigation of the interfacial structure of semicoherent precipitates. *The Philosophical Magazine: A Journal of Theoretical Experimental and Applied Physics*, 17(148):801–831, 1968. doi: 10.1080/14786436808223031.

H. Wenk, W. Joswig, T. Tagai, M. Korekawa, and B. K. Smith. The average structure of An 62–66 labradorite. *American Mineralogist*, 65(1-2):81–95, 1980.

H.-R. Wenk, K. Chen, and R. Smith. Morphology and microstructure of magnetite and ilmenite inclusions in plagioclase from Adirondack anorthositic gneiss. *American Mineralogist*, 96(8-9):1316–1324, 08 2011. ISSN 0003-004X. doi: 10.2138/am.2011.3760.

F. Ye and W.-Z. Zhang. Coincidence structures of interfacial steps and secondary misfit dislocations in the habit plane between Widmanstätten cementite and austenite. *Acta materialia*, 50(11):2761–2777, 2002. doi: 10.1016/S1359-6454(02)00077-0.

E. Yücelen, I. Lazić, and E. Bosch. Phase contrast scanning transmission electron microscopy imaging of light and heavy atoms at the limit of contrast and resolution. *Scientific Report*, 8:2676, 2018. doi: https://doi.org/10.1038/s41598-018-20377-2.

R. Y. Zhang, J. F. Shu, H. K. Mao, and J. G. Liou. Magnetite lamellae in olivine and clinohumite from dabie uhp ultramafic rocks, central china. *American Mineralogist*, 84(4):564–569, 1999. doi: 10.2138/am-1999-0410.

W.-Z. Zhang. Reproducible orientation relationships developed from phase transformations—role of interfaces. *Crystals*, 10(11):1042, 2020. doi: 10.3390/cryst10111042.

W.-Z. Zhang and G. Purdy. O-lattice analyses of interfacial misfit. i. general considerations. *Philosophical Magazine A*, 68(2):279–290, 1993. doi: 10.1080/01418619308221205.

W.-Z. Zhang, F. Ye, C. Zhang, Y. Qi, and H.-S. Fang. Unified rationalization of the Pitsch and T–H orientation relationships between Widmanstätten cementite and austenite. *Acta materialia*, 48(9):2209–2219, 2000. doi: 10.1016/S1359-6454(00)00033-1.

Supplementary Information

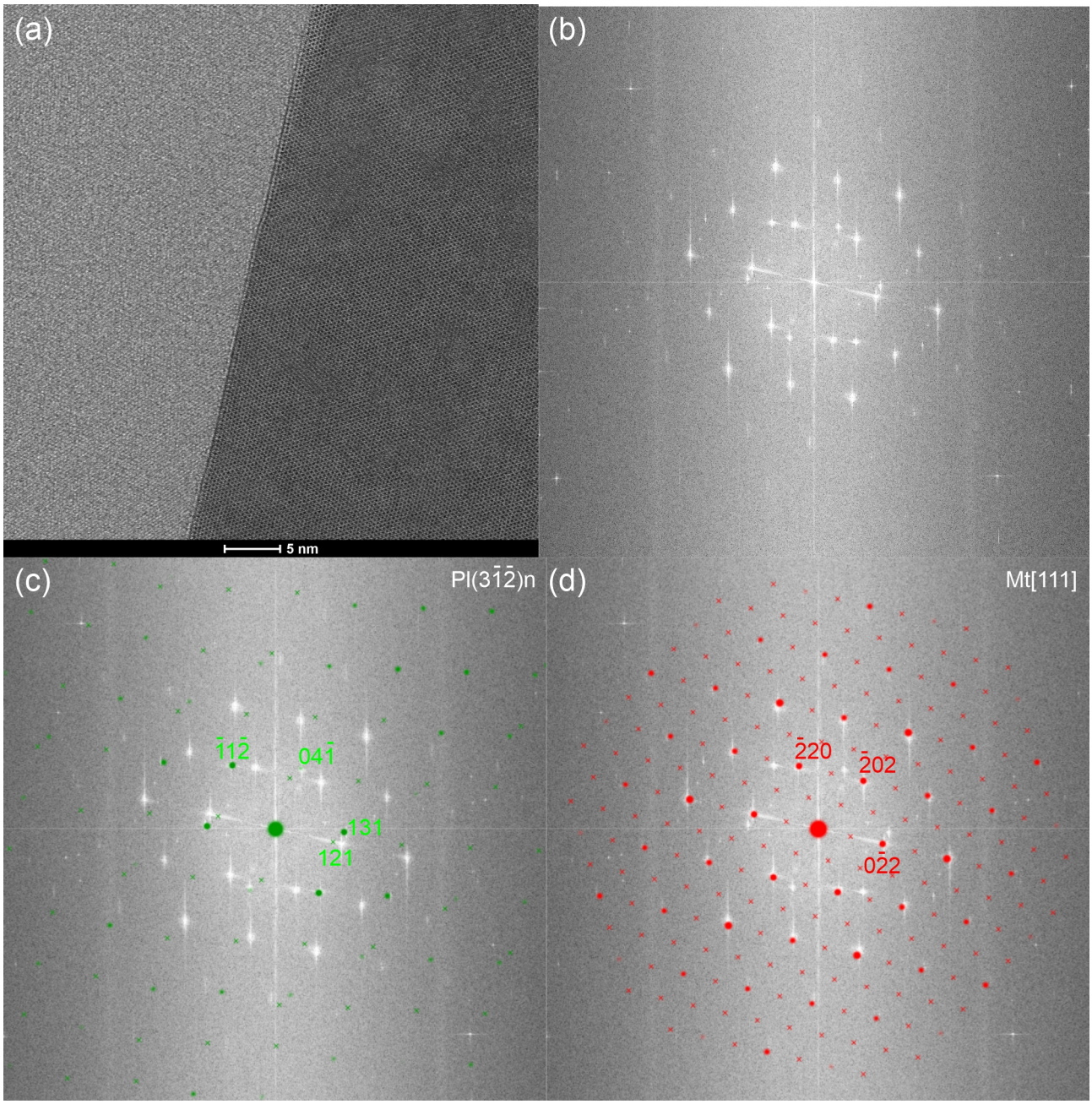

Figure S3.1: (a) Standard BF STEM imaging of magnetite-plagioclase interface facet F4 of a PL($\bar{3}12$)n-MT micro-inclusion in nucleation orientation. (b) Fast Fourier transformation on (a). (c) Simulated electron diffraction pattern of plagioclase superimposed on (b). The viewing direction is PL($\bar{3}12$)n. Indices correspond to the diffraction spots nearby, representing lattice planes in plagioclase in reciprocal space. (d) Simulated electron diffraction pattern of magnetite superimposed on (b). The viewing direction is MT[111]. Indices correspond to the diffraction spots nearby, representing lattice planes in magnetite in reciprocal space.

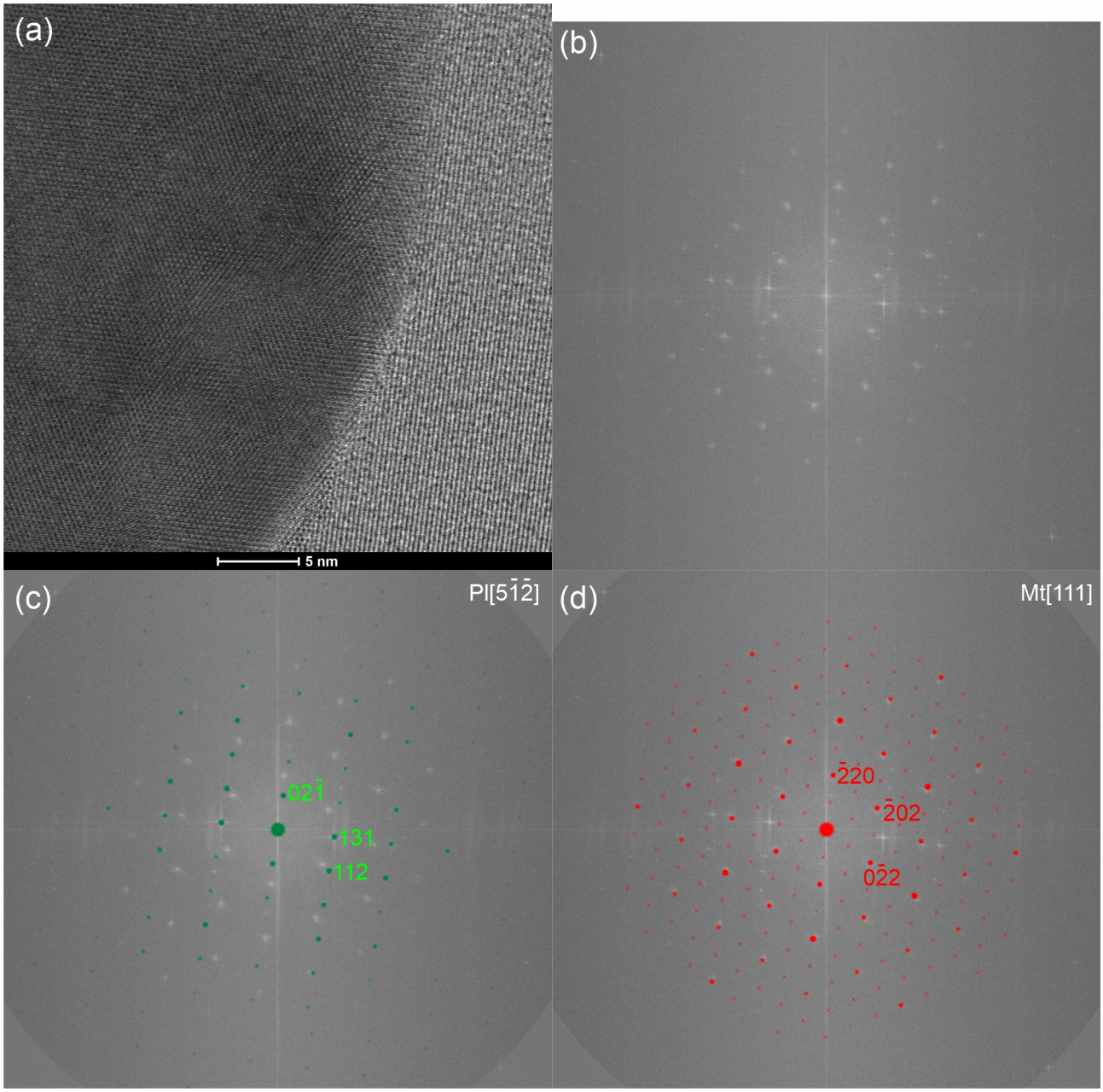

Figure S3.2: (a) Standard BF STEM imaging of magnetite-plagioclase interface of a PL($\bar{3}$12)n-MT micro-inclusion in main orientation. (b) Fast Fourier transformation on (a). (c) Simulated electron diffraction pattern of plagioclase superimposed on (b). The viewing direction is PL[5$\bar{1}\bar{2}$]. Indices correspond to the diffraction spots nearby, representing lattice planes in plagioclase in reciprocal space. (d) Simulated electron diffraction pattern of magnetite superimposed on (b). The viewing direction is MT[111]. Indices correspond to the diffraction spots nearby, representing lattice planes in magnetite in reciprocal space.

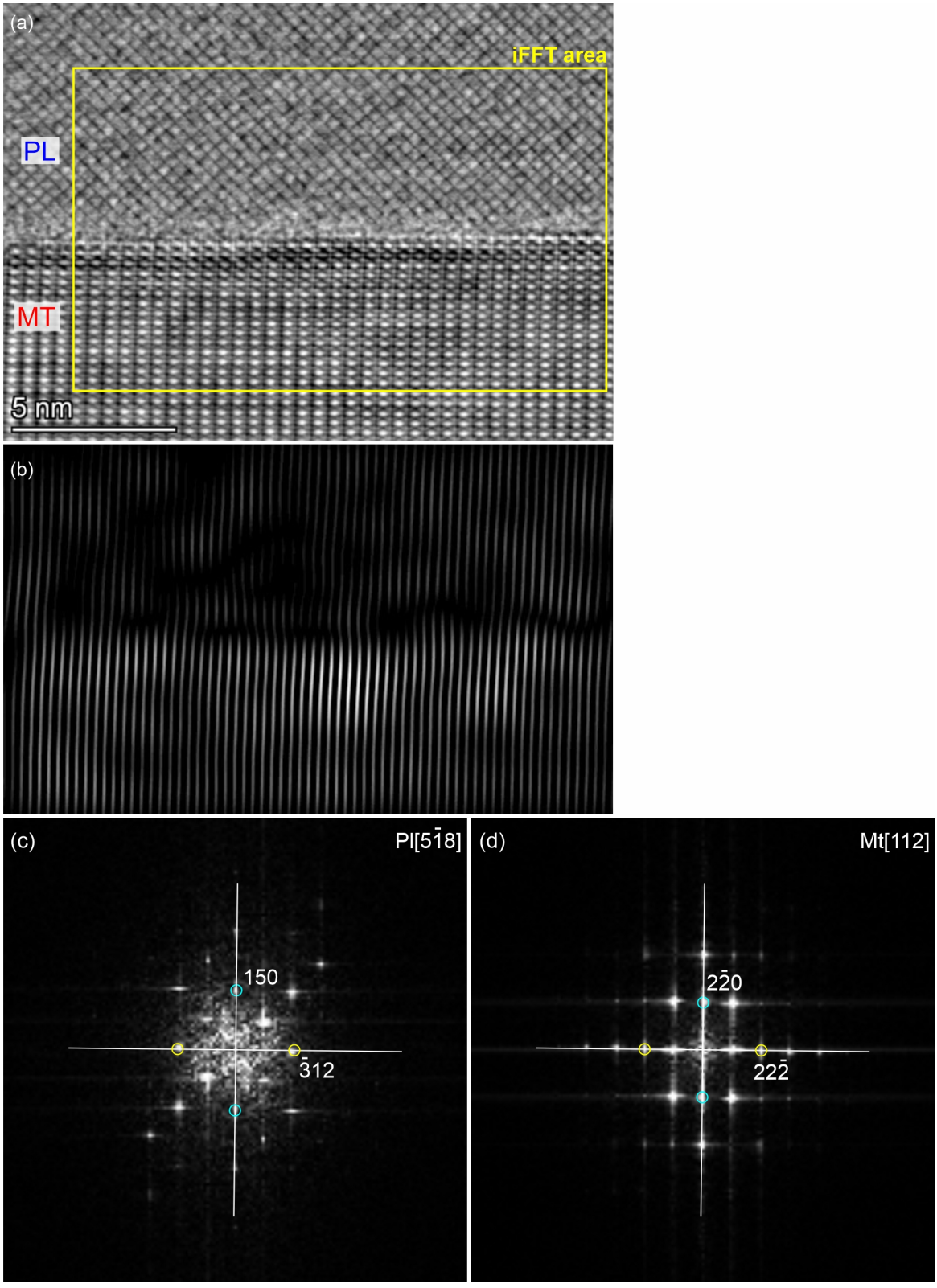

Figure S3.3: (a) iDPC-STEM imaging of the interface segment of a plate shaped PL($\bar{3}$12)n-MT micro-inclusion. (b) Inverse fast Fourier transformation of the area marked with the yellow rectangle in (a). MT(22$\bar{2}$) and PL($\bar{3}$12) lattice planes can been seen. (c) Fast Fourier transformation on plagioclase area in (a). Indices as well as circles indicate diffraction spots in plagioclase, which represent the lattice planes in plagioclase in reciprocal space. (d) Fast Fourier transformation on magnetite area in (a). Indices as well as circles indicate diffraction spots in magnetite, which represent the lattice planes in magnetite in reciprocal space.

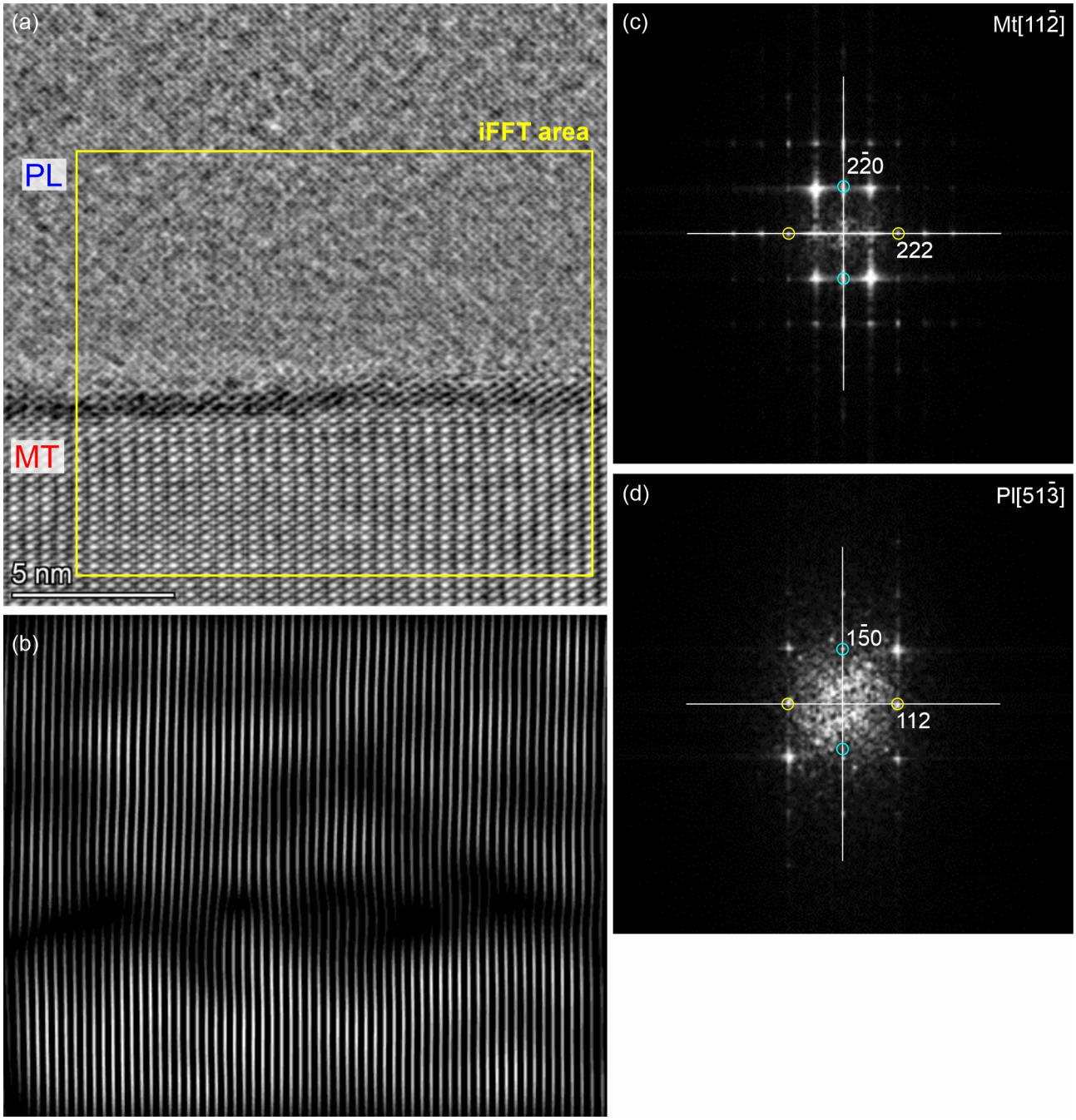

Figure S3.4: (a) iDPC-STEM imaging of the interface segment of a needle shaped PL(112)n-MT micro-inclusion. (b) Inverse fast Fourier transformation of the area marked with the yellow rectangle in (a). MT(222) and PL(112) lattice planes can been seen. (c) Fast Fourier transformation on magnetite area in (a). Indices as well as circles indicate diffraction spots in magnetite, which represent the lattice planes in magnetite in reciprocal space. (d) Fast Fourier transformation on plagioclase area in (a). Indices as well as circles indicate diffraction spots in plagioclase, which represent the lattice planes in plagioclase in reciprocal space.

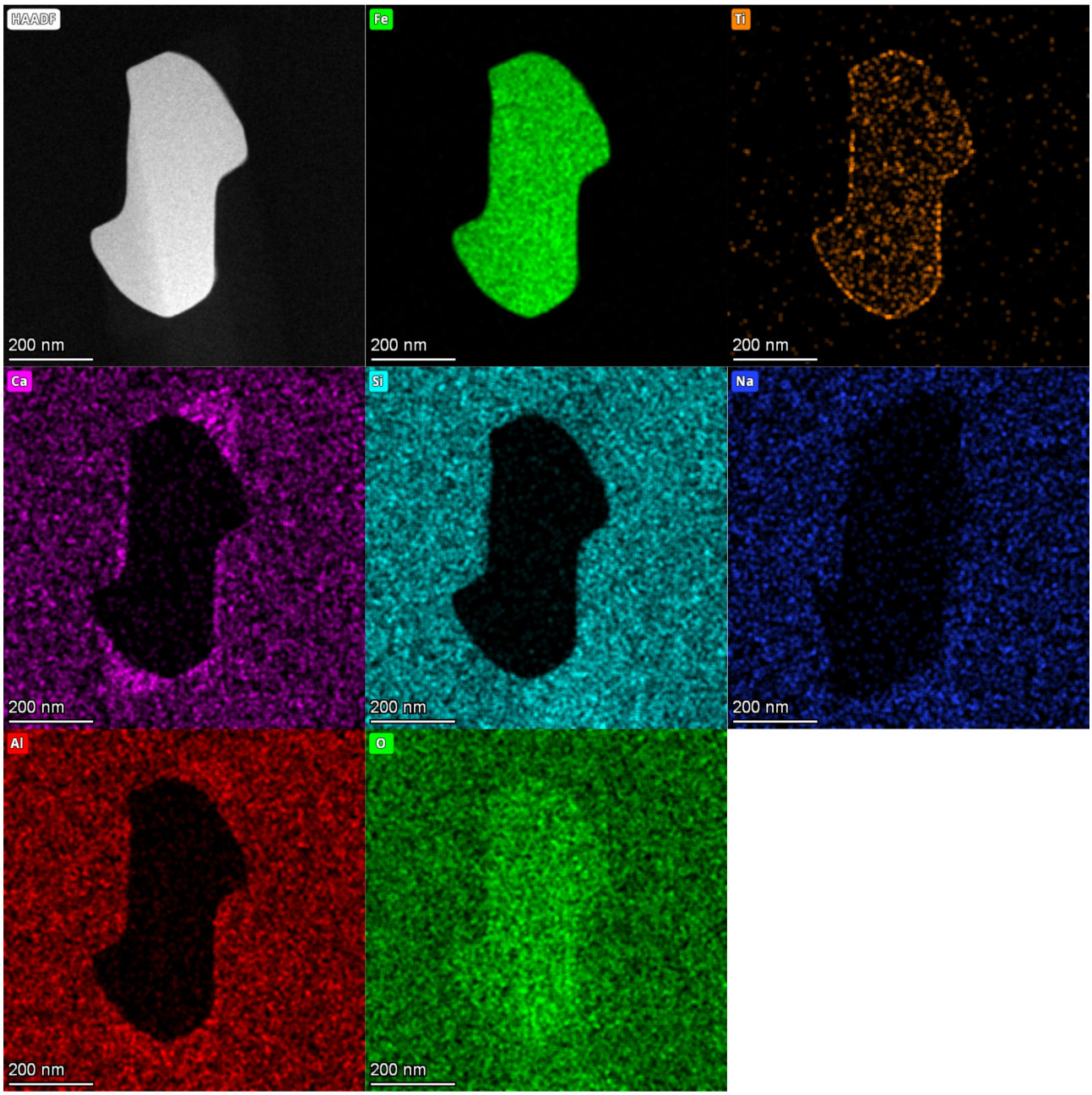

Figure S3.5: STEM-EDS element distribution maps of the cross section of PL(112)n-MT inclusion in main orientation. The contrast in the magnetite area shown in the HAADF image is due to the curtaining effect during FIB preparation, which also causes the Ca accumulation as shown in the Ca distribution map. Ti-rich rim around the inclusion is observed.

Chapter 4

Oriented secondary magnetite micro-inclusions in plagioclase from oceanic gabbro

Ge Bian[1,*], Olga Ageeva[1,2], Vladimir Roddatis[3], Gerlinde Habler[1], Anja Schreiber[3] Rainer Abart[1]
* Corresponding author

1. Department of Lithospheric Research, University of Vienna
2. Institute of Geology of Ore Deposit, Petrography, Mineralogy, and Geochemistry, Russian Academy of Sciences (IGEM, RAS)
3. Helmholtz Centre Potsdam, GFZ German Research Centre for Geosciences

Manuscript status:

Manuscript under review after revision

First submission: 07 September 2022 / Re-submission: 31 January 2023

Submitter's own contribution:

In this study, I have performed STEM specimens preparation using FIB technique, carried out STEM results analyses and interpretations, achieved crystallographic orientation analyses based on STEM results and prior EBSD results, and applied $\Delta\mathbf{g}$ method for magnetite-plagioclase interface structure and orientation reconstructions. In addition, I have prepared the first draft of this manuscript.

Abstract

Plagioclase hosted sub-micrometer to micrometer sized oriented needle and lath shaped magnetite micro-inclusions with their elongation direction aligned parallel to the plagioclase [001] direction were investigated using correlated optical, scanning electron and scanning transmission electron microscopy. The PL[001] magnetite micro-inclusions formed from older generations of differently oriented magnetite micro-inclusions by recrystallisation during hydrothermal alteration. Six orientation variants of PL[001] magnetite micro-inclusions occur, which share the same shape orientation but differ in their crystallographic orientation relationships to the plagioclase host. The magnetite-plagioclase interfaces are facetted. High resolution scanning transmission electron microscopy revealed that interface facets are aligned parallel to low index lattice planes corresponding to oxygen layers of either magnetite or plagioclase. In addition, linkage between prominent crystal structure elements of magnetite and plagioclase across the interfaces and accommodation mechanisms minimizing misfit between the two crystal structures were discerned. Combined evidence suggests that the shape and shape orientation as well as the crystallographic orientation relationships between the magnetite micro-inclusions and the plagioclase host are crystallographically controlled. The close crystal structure link between magnetite precipitates and plagioclase host ensures a low energy configuration driving recrystallization of older generations of differently orientated magnetite micro-inclusions into those that are aligned parallel to PL[001] and eases the underlying reaction kinetics. Due to their single to pseudo-single domain characteristics, the plagioclase hosted magnetite micro-inclusions are particularly robust carriers of natural remanent magnetization. Recrystallization of differently oriented pre-existing magnetite micro-inclusions into magnetite micro-inclusions with uniform shape orientation parallel to PL[001] has interesting consequences for the magnetic anisotropy of magnetite bearing plagioclase grains.

Keywords

Plagioclase hosted magnetite micro-inclusions · crystal and shape orientation relationships · interface facets · scanning transmission electron microscopy · crystallographic control

4.1 Introduction

Plagioclase (PL) from mafic plutonic rocks frequently contains needle-, lath- and plate shaped magnetite (MT) micro-inclusions (Wager and Mitchell, 1951; Davis, 1981; Feinberg et al., 2006b; Selkin et al., 2014;

Ageeva et al., 2016, 2020; Cheadle and Gee, 2017). The inclusions typically show systematic crystallographic orientation relationships (CORs) and shape orientation relationships (SORs) to the plagioclase host (Sobolev, 1990; Ageeva et al., 2020). For needle- and lath shaped magnetite micro-inclusions, two basic orientation types are discerned. The first type is represented by the so-called plane-normal type inclusions, which are elongated parallel to one of their MT⟨111⟩ directions, and are aligned parallel to the normal direction of specific plagioclase lattice planes. The second inclusion type is elongated along one of the MT⟨110⟩ directions, which is aligned parallel to the PL[001] direction. The magnetite inclusions of the plane-normal type probably formed by precipitation from Fe-bearing plagioclase during late magmatic stages (Bian et al., 2021). The MT{222} planes correspond to densely-packed oxygen layers in the crystal structure of magnetite, and they are aligned with plagioclase lattice planes corresponding to oxygen layers in the crystal structure of plagioclase, indicating that a good fit between the oxygen sublattices of the two phases represents the basis of the observed orientation relationships of the plane normal type inclusions (Ageeva et al., 2020). The PL[001] type micro-inclusions typically occur in the outermost regions of the plagioclase grains, and they are the dominant micro-inclusion type in samples that experienced hydrothermal overprint at sub-solidus conditions (Pertsev et al., 2015). The PL[001] type magnetite micro-inclusions are thus ascribed to hydrothermal processes (Ageeva et al., 2022). PL[001] type magnetite micro-inclusions have also been described from metamorphic rocks (Feinberg et al., 2004; Wenk et al., 2011).

Magnetite is the most important carrier of rock magnetism, and the systematic SORs of the magnetite micro-inclusions with the plagioclase host lead to magnetic anisotropy of magnetite bearing plagioclase. This is of interest in the context of paleomagnetic reconstructions, because due to their size, the magnetite micro-inclusions typically have single domain or pseudo-single domain magnetic characteristics, which makes them particularly robust carriers of remanent magnetization (Kent et al., 1978; Fleet et al., 1980; Davis, 1981; Dunlop and Özdemir, 2001; Renne et al., 2002; Feinberg et al., 2006a; Knafelc et al., 2019). The magnetic anisotropy arising from their anisotropic shape orientation distribution may, however, bias their magnetic record. In particular, the vector of natural remanent magnetization obtained from a magnetite bearing plagioclase grain may deviate from the direction of the magnetic field prevailing at the time, when the rock cooled through the Curie temperature (Usui et al., 2015; Nikolaisen et al., 2022), an effect that needs to be accounted for during paleomagnetic reconstructions. It was argued by Ageeva et al. (2022) that the orientation distribution of the needle and lath shaped magnetite micro-inclusions undergoes an evolution from an initial dominance of the plane-normal types, which prevail in pristine magmatic plagioclase, towards a dominance of the PL[001] type inclusions in hydrothermally overprinted feldspar. Such a shift in inclusion populations has important implications for the magnetic memory of magnetite bearing

plagioclase grains.

Oriented micro-inclusions of magnetite in clinopyroxene, of hematite in rutile (Hwang et al., 2010), and of rutile in garnet (Hwang et al., 2000, 2015, 2019; Proyer et al., 2013) have been studied using conventional transmission electron microscopy (TEM), and the crystallographic and shape orientation relationships between the inclusions and the host crystals have been rationalized based on TEM results. Through the advent of spherical aberration corrected scanning transmission electron microscopy (STEM) (Haider et al., 1998; Krivanek et al., 1999; Pennycook, 2017), atomic scale imaging of silicate minerals has become possible (Kogure and Okunishi, 2010), offering unprecedented insight into crystal structure and interfaces in crystalline materials (Li et al., 2016).

In this study, we made use of these developments and investigated PL[001] type magnetite micro-inclusions. The morphology, the spatial distribution, the CORs and SORs of PL[001]-MT type micro-inclusions with respect to the plagioclase host as well as the microscopic configurations of the magnetite-plagioclase interfaces were analyzed using correlated microscopy covering phenomena from the micrometer to the nanometer scale. More specifically, optical microscopy including universal stage, scanning electron microscopy (SEM) including electron backscatter diffraction (EBSD), and scanning transmission electron microscopy (STEM) were combined. Interface facet orientations were rationalized based on geometrical models of the microscopic configurations at magnetite-plagioclase interfaces, and the evolution from plane-normal type to the PL[001] type inclusions was addressed.

4.2 Materials and methods

4.2.1 Materials

Magnetite bearing plagioclase grains from oceanic gabbro samples 277-10s-d4, 277-10-d23, and 277-7-d12 were studied. The samples were dredged from the ocean floor during the 30'th cruise of the Research Vessel Professor Logachev (Beltenev et al., 2007, 2009). The dredge sites were located in an oceanic core complex along the Mid-Atlantic Ridge at 13°N (Karson et al., 1997; MacLeod et al., 2009). Detailed geological descriptions of the region can be found in MacLeod et al. (2009); Ondréas et al. (2012); Pertsev et al. (2012) and Escartin et al. (2017). The studied samples were taken from coarse-grained gabbro mainly comprised of plagioclase, clinopyroxene, orthopyroxene and amphibole. In petrographic thin section, oriented needle-, lath- and plate-shaped micro-inclusions of an opaque phase are observed in plagioclase.

4.2.2 Methods

Scanning electron microscopy

Secondary electron (SE) imaging and electron backscattered diffraction (EBSD) analyses of plagioclase hosting magnetite micro-inclusions were performed on an FEI Quanta 3D FEG-SEM, located at the Faculty of Earth Science, Geography and Astronomy, University of Vienna, Austria. The SEM is equipped with a Schottky type field-emission electron gun and an EDAX Pegasus Apex IV detector system comprising an EDAX Digiview V EBSD camera for crystallographic orientation determination. SE imaging was performed on chemo-mechanically polished carbon coated thin sections. During EBSD analysis and secondary electron imaging, the electron beam was set to an accelerating voltage of 15 kV and a probe current of ca. 4 nA in analytical mode. The stage was at 70° tilt, and the working distance was in the range of 14-14.5 mm. Details of the analytical parameters during EBSD analysis are described in Ageeva et al. (2022) Section 2.4. SE imaging was performed at 70° stage tilt and tilt-corrected. An about ± 1° error in the tilting angle may exist due to uneven surface of the thin section, which may introduce errors in the tilt correction and cause up to 1.3° error in the determination of the directions of interface traces.

Focused ion beam and Ar ion-milling

STEM specimens were prepared by Ga-FIB and Ar ion-milling. Specimen 277-10-d23 was extracted by focused ion beam (FIB) nanomachining using the FEI Quanta 3D FEG instrument described above. The ion column is equipped with a liquid Ga-ion source, a gas injection system for Pt- and C deposition, and an Omniprobe 100.7 micromanipulator for in situ lift-out. Based on combined EBSD crystal orientation data and optical microscopy, a site and orientation specific TEM foil of a PL[001]-MT needle cross section was prepared from a chemo-mechanically polished carbon-coated thin section. In a first step, a platinum layer was deposited at the extraction site to protect and support the TEM foil. The FIB section was oriented exactly perpendicular to the elongation direction of a PL[001]-MT inclusion. During FIB preparation, SE imaging was used for monitoring progress. The electron beam settings were at 15 kV accelerating voltage and c. 53 pA probe current. The setting for FIB induced SE imaging was 30 kV accelerating voltage and 10 pA probe current. For FIB micromachining an accelerating voltage of 30 kV was applied. During the extraction process, successively decreasing FIB probe current with 65 nA, 30 nA, 5 nA and 1 nA was used. Then, Pt-deposition at FIB settings of 30 kV and 0.1 nA was used to attach the TEM foil first to the tip of a tungsten micromanipulator needle and subsequently for mounting the foil to a Mo grid. The extracted TEM foil was about 20 × 20 μm in size and about 1.6 μm thick. Further thinning was done by subsequent Ar ion-milling.

A second TEM specimen was prepared from sample 277-7-d12 using a FEI Helios G4 UC Dual Beam (SEM-FIB). The instrument is located at Deutsches GeoForschungsZentrum (GFZ), Potsdam Imaging and Spectral Analysis (PISA) facility. To this end, a cylinder of 3.1 mm diameter and 2 mm height was extracted from a 2 mm thick rock chip. The cylinder was then polished to produce a 100 μm thick circular disc. The disc contains a single plagioclase grain with abundant magnetite micro-inclusions of different types. Final thinning of the disc was done using a Gatan DuoMill 600 instrument, operated at a voltage of 1 kV using argon ions (Ar^+) at an incident angle of 15° to remove residual amorphous material. In the TEM foil prepared from the rock chip, the identity of the investigated inclusions was not known a priori but had to be determined from the STEM experiments a posteriori.

Scanning transmission electron microscopy

A Thermo Fisher Scientific Themis Z 3.1transmission electron microscope was used for high-resolution imaging of the magnetite-plagioclase interfaces. The instrument is located at GFZ, PISA facility. The microscope is equipped with a Cs S-CORR probe corrector (spatial resolution at 300 kV $<$ 0.06 nm) and a SuperX detector for energy dispersive X-ray spectroscopy (EDS) to perform chemical analysis. High angle annular dark field (HAADF) and integrated differential phase contrast (iDPC) images were collected using STEM-HAADF and DF4 detectors using an accelerating voltage of 300 kV and a current of 10pA. The convergence semi-angle of the incident probe was set to 30 mrad.

The iDPC–STEM method enables direct imaging of the phase of the transmission function for non-magnetic samples (Lazić et al., 2016). For thin samples, this yields an image that is directly interpretable as the (projected) electrostatic potential (Yücelen et al., 2018). There are several advantages in using the iDPC-STEM, namely: (1) it is capable of imaging light and heavy elements simultaneously at sub-Å resolution with a low-dose incident beam; (2) HAADF and iDPC images can be collected simultaneously; (3) the signal to noise ratio (SNR) is superior to annular dark field (ADF) STEM imaging and also to other high-resolution phase contrast techniques (Yücelen et al., 2018). In our study we collected both HAADF and iDPC images for all analyzed magnetite needles and facets simultaneously. We also collected annular bright field ABF-STEM images at conditions usually used for visualizing oxygen atomic columns, see e.g. Jin et al. (2016). Fig. S4.1 in the supplementary material shows HAADF, ADF and iDPC-STEM images of plagioclase collected from the same area, and corresponding simulated images obtained from QSTEM software are inserted for comparison (Koch, 2002). Fig. S4.1 demonstrates that all images including iDPC indeed can be directly interpreted meaning that the bright or dark spots correspond to positions of atomic columns.

4.3 Results

4.3.1 Petrography

The investigated gabbro samples are mainly comprised of plagioclase, which is present at about 50% by volume, together with clinopyroxene, orthopyroxene and amphibole, each of which is present at about 10 to 15 vol%. Plagioclase has a grain size of about 1 to 3 mm and anorthite contents of 40 to 60 mol%, where the cores have usually higher anorthite contents than the rims. The lowest anorthite contents are observed along healed cracks, which probably were formed during hydrothermal stages. Plagioclase shows twinning after the Albite, the Pericline and the Carlsbad twin laws and contains abundant oriented micrometer and sub-micrometer sized needle- and lath-shaped inclusions of an opaque phase, which is mainly magnetite. In addition, plate shaped magnetite micro-inclusions are present. Typically, the needle and lath shaped magnetite micro-inclusions are absent in the immediate vicinity of the plate shaped inclusions. Finally, magnetite nano-inclusions with equant shapes are present, which are referred to as *dust-like inclusions*. Some of the magnetite micro-inclusions contain lamellar or irregularly shaped precipitates of ilmenite and/or ulvospinel.

For needle- and lath shaped magnetite micro-inclusions, seven SORs with respect to plagioclase are discerned that define the *plane-normal* type inclusions according to the terminology of Ageeva et al. (2020). These inclusions are elongated parallel to one of their MT⟨111⟩ directions, and they are aligned close to parallel to the normal direction of one of seven specific plagioclase lattice planes including PL(112)n, PL($1\bar{5}0$)n, PL($\bar{3}12$)n, PL(150)n, PL(100)n, PL($1\bar{1}2$)n, and PL($\bar{3}\bar{1}2$)n, where PL(*hkl*)n is the direction normal to the PL(*hkl*) lattice plane. One additional inclusion type is elongated along one of the MT⟨110⟩ directions, which is aligned parallel to the PL[001] direction. Henceforth, these inclusions are referred to as *PL[001] inclusions*.

Fig. 4.1a shows the distribution of the different inclusion types in a grain of magmatic plagioclase in plane polarized transmitted light. The plagioclase contains abundant oriented magnetite inclusions. Only in an irregularly *star shaped* domain the magnetite micro-inclusions are absent and the plagioclase appears bleached. In the central regions of the bleached domain, large equant grains of ilmenite are present, which appear to have collectively recrystallized from the pre-existing plane normal type magnetite micro-inclusions and will not be further addressed in this study. In the domains furthest away from the bleached inclusion-free area magnetite micro-inclusions of the plane normal type dominate corresponding to domains of pristine magmatic plagioclase (right hand side of Fig. 4.1a). At the transition between the pristine and the bleached domains, PL[001] inclusions dominate (dashed yellow lines in Fig. 4.1a). According to

Bian et al. (2021), the magnetite micro-inclusions of the plane-normal type probably formed by precipitation from Fe-bearing plagioclase, which had become supersaturated with respect to magnetite during late magmatic stages. The ilmenite plates in the central regions of the bleached domains and the PL[001] inclusions are clearly of secondary, likely of hydrothermal origin. A more localized situation is shown in Fig. 4.1b. There, several lath shaped PL[001]-MT type inclusions are aligned along a straight line interpreted as a healed crack. In this case, recrystallization of the plane normal type magnetite micro-inclusions into PL[001]-MT inclusion was confined to the healed crack itself, whereas plane-normal type magnetite micro-inclusions dominate around the healed crack. Another situation corroborating the secondary nature of the PL[001] inclusions is shown in Fig. 4.1c. There several PL[001] inclusions grew on a pre-existing plane-normal type inclusion.

4.3.2 CORs of PL[001]-MT micro-inclusions

PL[001]-MT micro-inclusions typically have prismatic shape. Combining crystal orientation data and universal stage measurements the elongation direction of type PL[001]-MT inclusions is found to be aligned with the PL[001] direction to within the accuracy of the universal stage optical measurements, which is about ± 3°. EBSD based crystal orientation analysis showed that the needle- and lath-shaped PL[001]-MT micro-inclusions are elongated parallel to one of their MT⟨110⟩ directions and that their COR to the plagioclase host is characterized by the parallel alignment of PL[001] || MT⟨110⟩ to within the accuracy of the orientation determination by Hough-transform based EBSD analysis, which is at $< 1°$ orientation deviation. Some of the dust-like inclusions show an approximate alignment of one of their MT⟨110⟩ directions with the PL[001] direction with an angular deviation of about 5° between the two directions. Nevertheless, these dust-like inclusions are classified as PL[001] type inclusions.

Given the parallel alignment of the PL[001] and one of the MT⟨110⟩ directions, additional crystallographic alignments between magnetite and plagioclase define three orientation variants of PL[001] type inclusions, which are referred to as orientation variants COR1A, COR1B and COR2, each of which has two subgroups due to the presence of two magnetite twins. Specific Miller indices are applied for describing these CORs, the conventions for assigning crystallographic directions are listed in Table 4.1. All three CORs have in common the parallel alignment of the crystallographic PL[001] and MT[110] directions to within ∼ 5°, as specified in Row1 of Table 4.1. The three orientation variants are discerned based on the additional parallel alignment of one of the MT{111} planes with specific lattice planes of plagioclase as indicated in Row3 of Table 4.1. COR1A with PL(150) || MT($1\bar{1}1$) and COR1B with PL($1\bar{5}0$) || MT($\bar{1}1\bar{1}$) are very closely related to one another, and typically form prismatic micro-inclusions. In contrast, COR2 with PL(120) ||

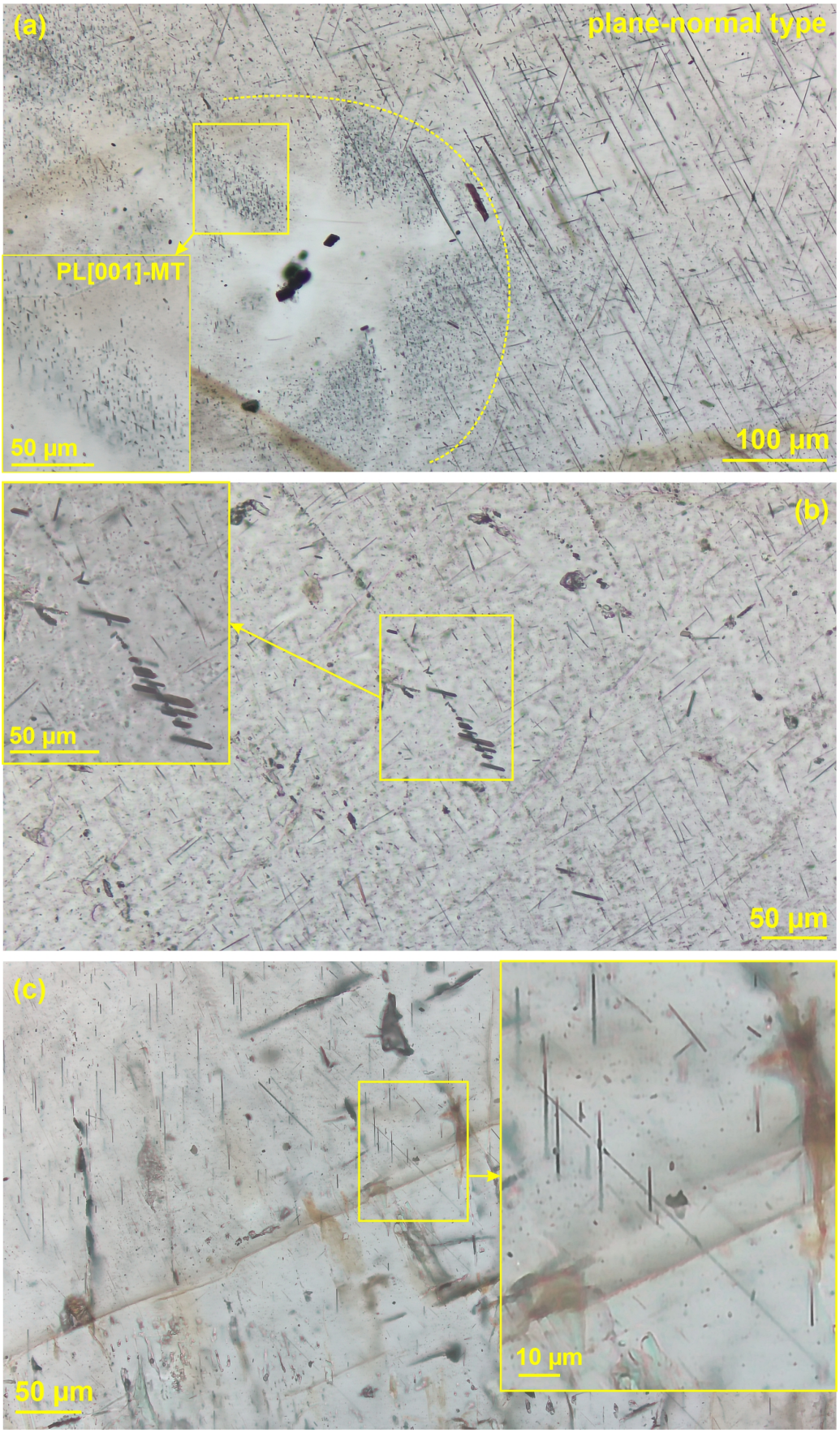

Figure 4.1: Plane polarized transmitted light optical images of plagioclase with abundant oriented magnetite micro-inclusions. (a) Irregularly shaped bleached domain with large isometric opaque Fe-Ti oxide (ilmenite) inclusions in the central regions surrounded by a halo (delimited by dashed yellow line) with dominantly fine-grained PL[001] type magnetite micro-inclusions and plane normal type inclusions outside the halo. A closeup of a domain with abundant PL[001] type inclusions (yellow rectangle) is shown in the insert on the lower left. (b) Array of lath shaped PL[001]-MT micro-inclusions along a thin healed crack, a closeup is shown in the insert. (c) PL[001]-MT micro-inclusions (vertical) growing on a pre-existing plane-normal type magnetite micro-inclusion, a closeup is shown in the insert.

MT($\bar{1}1\bar{1}$) is different and typically forms dust like inclusions. The two crystallographic alignments imply a third crystallographic alignment related to one of the MT⟨001⟩ directions, which is described in Row2 of Table 4.1. It must be noted, that the MT{111} planes are twin planes associated with the spinel twin law, a 180° rotation about the plane normal to the MT{111} twin plane. As a consequence, for the CORs defined by the entries in Row1-3 of Table 4.1 with respect to one twin variant of magnetite, another set of rational CORs exists with respect to the other twin variant of magnetite. Thus, for each of the three orientation variants, two subgroups exist, one with rational CORs with respect to magnetite twin 1 and another one with rational CORs with respect to magnetite twin 2. The second subgroup is defined by the alignment of PL[001] || MT[110] for COR1A and by PL[001] || MT[$\bar{1}\bar{1}$0] for COR1B and COR2, as listed in Row4 of Table 4.1, in addition to the alignments parallel to the twin plane as indicated in Row3 of Table 4.1. The third crystallographic alignment that follows naturally for the second subgroup is given in Row5 of Table 4.1. The CORs listed in Rows3-5 of Table 4.1 define the second subgroup with respect to magnetite twin 2 for each of the three COR variants. Thus, a total of six orientation variants exist for the PL[001] type inclusions, which are all characterized by rational CORs between the PL[001]-MT micro-inclusions and the plagioclase host.

The structural and orientation correspondences between magnetite and plagioclase with COR1A are illustrated in Fig. 4.2. Fig. 4.2a shows the plagioclase crystal structure with PL[-14,10,-7], PL(150) and PL(1$\bar{5}$0) indicated. A projection of the plagioclase unit cell along PL[001] is shown in Fig. 4.2b. Figs. 4.2c and 4.2d show the magnetite crystal structure according to COR1A with magnetite twin 1 and twin 2, respectively, and with MT[001], MT(1$\bar{1}$1) and MT($\bar{1}$10) indicated. The correspondence between plagioclase and magnetite lattice planes and lattice directions is highlighted by corresponding color codes. Fig. 4.2e shows a projection of the two magnetite twins in COR1A. The same illustrations as given for COR1A in Fig.4.2, are given for COR1B in Fig. 4.3. A simplified sketch of the orientation correspondence between the plagioclase and magnetite unit cells in COR1A and COR1B is shown in the supplementary material Fig. S4.2.

4.3.3 Interface orientations

In cross-section the prismatic PL[001]-MT type inclusions have convex polygonal shape comprised of pairs of parallel straight traces corresponding to different segments of a faceted inclusion-host interface. Secondary electron (SE) images of COR1A PL[001]-MT micro-inclusions pertaining to magnetite twin 2 are shown in Fig. 4.4 together with a stereographic projection illustrating the COR between the magnetite inclusions and the plagioclase host. All inclusions shown in Fig. 4.4 are hosted in a single crystal domain

Table 4.1: COR variants of PL[001]-MT micro-inclusions

	COR1A	COR1B	COR2	Row No.
Magnetite twin 1	PL[001] ‖ MT[$\bar{1}\bar{1}$0]	PL[001] ‖ MT[110]	PL[001] ∼‖ MT[110]	1
	PL[-14,10,-7] ‖ MT[001]	PL[14,10,7] ∼‖ MT[001]	PL[023] ‖ MT[010]	2
Magnetite twin plane	PL(150) ‖ MT(1$\bar{1}$1)	PL(1$\bar{5}$0) ‖ MT($\bar{1}$1$\bar{1}$)	PL(120) ‖ MT($\bar{1}$1$\bar{1}$)	3
Magnetite twin 2	PL[001] ‖ MT[110]	PL[001] ‖ MT[$\bar{1}\bar{1}$0]	PL[001] ∼‖ MT[$\bar{1}\bar{1}$0]	4
	PL(1$\bar{5}$0) ‖ MT($\bar{1}$10)	PL(150) ‖ MT(1$\bar{1}$0)	PL(1$\bar{2}$0) ‖ MT(1$\bar{1}\bar{3}$)	5
Inclusion shape	Mostly prismatic	Mostly prismatic	Mostly dust-like	6

of plagioclase with uniform crystallographic orientation. It is seen from the stereographic projection in Fig. 4.4a that one of the MT⟨110⟩ directions coincides with the PL[001] direction, which is inclined by about 30° to the viewing direction. Thus about 30° oblique cross-sections of the inclusions are observed at the sample surface. All inclusion cross-sections are bounded by a combination of straight interface segments and intermittent rounded outwards convex interface segments. Typically, three pairs of parallel interface trace segments produce hexagonal cross-sections. Given the acicular or prismatic shape of the magnetite inclusions, the straight interface segments are interpreted as the traces of prism planes, containing the MT⟨110⟩ direction that is parallel to the inclusion elongation direction as the common zone axis. The three differently oriented pairs of interface traces are denoted as Fi (i=1,2,4). Noting that the corresponding interface planes contain both, the MT⟨110⟩ direction that is parallel to the inclusion elongation direction and the respective interface trace on the sample surface, the three facets of the COR1A PL[001]-MT inclusions are identified as F1 ∼‖ PL(120), F2 ∼‖ PL(150), and F4 ∼‖ PL(1$\bar{5}$0). This assignment is subject to some uncertainty due to the limited resolution of SEM imaging at high probe current and angular resolution of the crystal orientation determination by EBSD. Nevertheless, the fact that different inclusions show similar facet orientations suggests crystallographic control of interface orientations.

4.3.4 Microscopic interface configurations

One about 15 μm long PL[001]-MT micro-inclusion was selected for analyzing the relationships between interface orientation, crystal structure and COR. Apart from PL[001] ‖ MT[110] the COR of the selected magnetite micro-inclusion with respect to the plagioclase host is characterized by PL(150) ‖ MT(2$\bar{2}$2) and PL(1$\bar{5}$0) ∼‖ MT($\bar{2}$20). Accordingly, the inclusion is classified as a COR1A variant pertaining to the magnetite twin 2 subgroup. A TEM foil containing a cross-section of the selected inclusion was extracted using FIB technique. The foil is oriented perpendicular to the inclusion elongation direction, so that the magnetite-plagioclase interfaces are edge on. Bright field (BF) and high-angle annular dark field (HAADF)

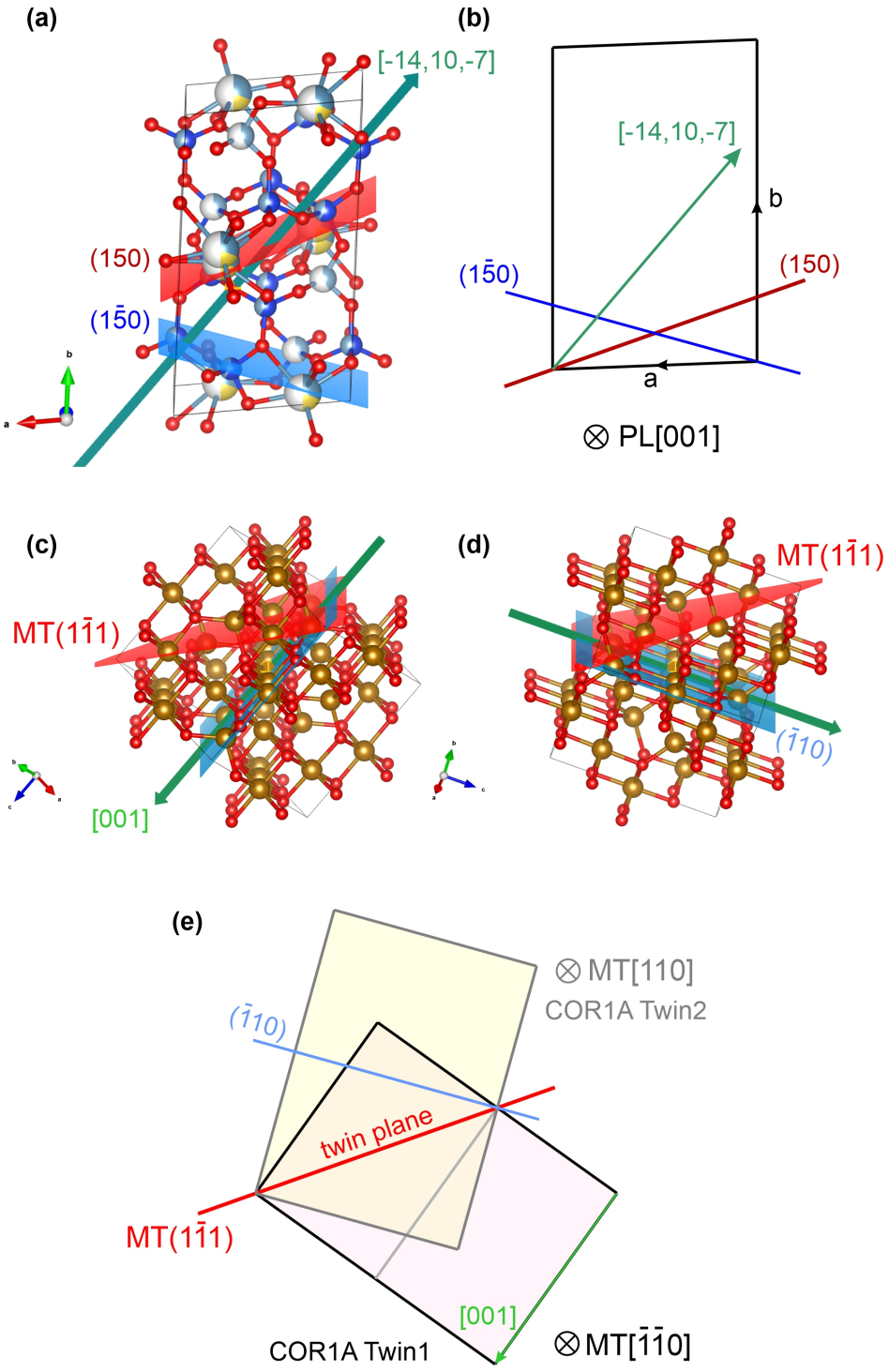

Figure 4.2: (a) Crystal structure model of plagioclase with PL[-14,10,-7], PL(150) and PL(1$\bar{5}$0) indicated. (b) 2D projection of the plagioclase unit cell viewing direction ‖ PL[001] with PL[-14,10,-7], PL(150) and PL(1$\bar{5}$0) indicated. (c) Crystal structure model of magnetite with MT[001], MT(1$\bar{1}$1) and MT($\bar{1}$10) indicated and with magnetite in the orientation of COR1A twin 1, i.e. PL[001] ‖ MT[$\bar{1}\bar{1}$0], PL[-14,10,-7] ‖ MT[001], and PL(150) ‖ MT(1$\bar{1}$1). (d) Crystal structure model of magnetite with MT[001], MT(1$\bar{1}$1) and MT($\bar{1}$10) indicated and with magnetite in the orientation of COR1A twin 2, i.e. PL[001] ‖ MT[110], PL(1$\bar{5}$0) ‖ MT($\bar{1}$10), and PL(150) ‖ MT(1$\bar{1}$1). (e) 2D projection of the magnetite unit cell COR1A twin 1 (viewing direction ‖ MT[$\bar{1}\bar{1}$0]) and twin 2 (viewing direction ‖ MT[110]) according to the orientation of plagioclase in (b) with twin plane MT(1$\bar{1}$1), along with MT[001], MT(1$\bar{1}$1) and MT($\bar{1}$10) indicated.

images of the selected inclusion cross-section are shown in Figs. 4.5a,b. The STEM images reveal an elongated, nearly symmetrical cross-section with long and short diameters of 80 and 200 nm, respectively. Chemical analysis (see supplementary material Fig. S4.3) confirms that the bright area in Fig. 4.5b is due to the presence of a Ti-rich phase, which supposedly is ulvöspinel as inferred from its cubic crystal symmetry. Interestingly, Ti is enriched along the magnetite-plagioclase interface (see supplementary material Fig. S4.3).

The inclusion cross-section is bounded by four major types of interface segments labelled Fi (i=1, 2, 3,

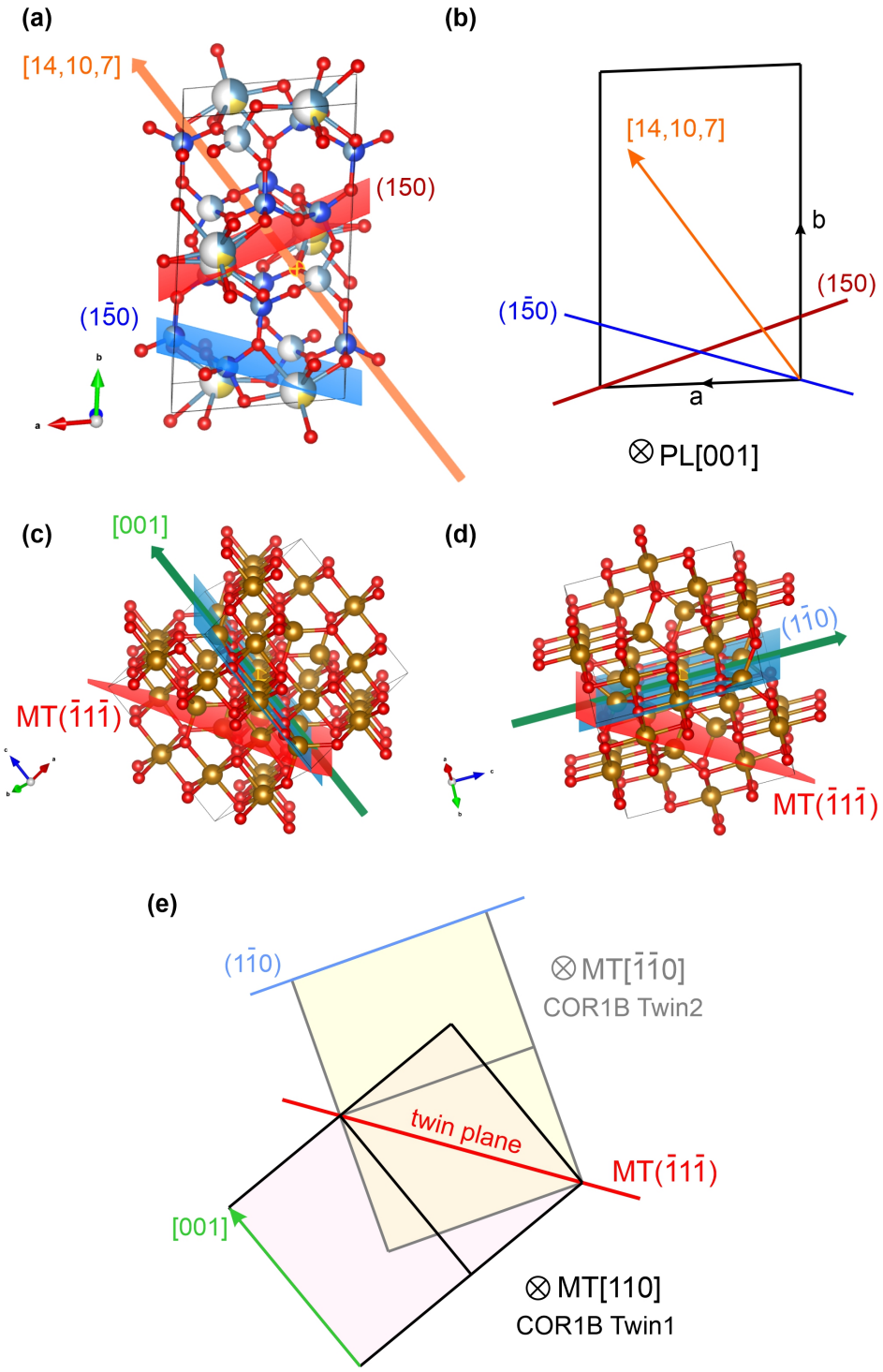

Figure 4.3: (a) Crystal structure model of plagioclase with PL[14,10,7], PL(150) and PL(1$\bar{5}$0) indicated. (b) 2D projection of the plagioclase unit cell viewing direction ∥ PL[001] with PL[14,10,7], PL(150) and PL(1$\bar{5}$0) indicated. (c) Crystal structure model of magnetite with MT[001], MT(1$\bar{1}$1$\bar{1}$) and MT(1$\bar{1}$0) indicated and with magnetite in the orientation of COR1B twin 1, i.e. PL[001] ∥ MT[110], PL[14,10,7] ∥ MT[001], and PL(1$\bar{5}$0) ∥ MT(1$\bar{1}$1$\bar{1}$). (d) Crystal structure of magnetite with MT[001], MT(1$\bar{1}$1$\bar{1}$) and MT(1$\bar{1}$0) indicated and with magnetite in the orientation of COR1B twin 2, i.e. PL[001] ∥ MT[110], PL(1$\bar{5}$0) ∥ MT(1$\bar{1}$1$\bar{1}$), and PL(150) ∥ MT(1$\bar{1}$0). (e) 2D projection of the magnetite unit cells in the orientation of COR1B twin 1 (viewing direction ∥ MT[110]) and twin 2 (viewing direction ∥ MT[1$\bar{1}$0]) according to the orientation of plagioclase in (b) with twin plane MT(1$\bar{1}$1$\bar{1}$), along with MT[001], MT(1$\bar{1}$1$\bar{1}$) and MT(1$\bar{1}$0) indicated.

4) and three less prominent interface segments (i=5, 6, 7), as indicated in Fig. 4.5b. Atomic scale observations at the different interface segments are shown in Figs. 4.5c-f, and the position of each acquisition is indicated by the yellow rectangles with alphabetic labels in Fig. 4.5a. Interface segments F1 and F2 correspond to those shown in Figs. 4.5d and 4.5f, respectively. Fig. 4.5c relates to interface segments F5 and F6. Fig. 4.5e shows the transition between interface segments F4 and F5. The orientations of the interface facets Fi in Fig. 4.5b as determined from the fast Fourier transformations (FFT) of the STEM images taken at the magnetite-plagioclase interface (supplementary material Fig. S4.4) are summarized in the second

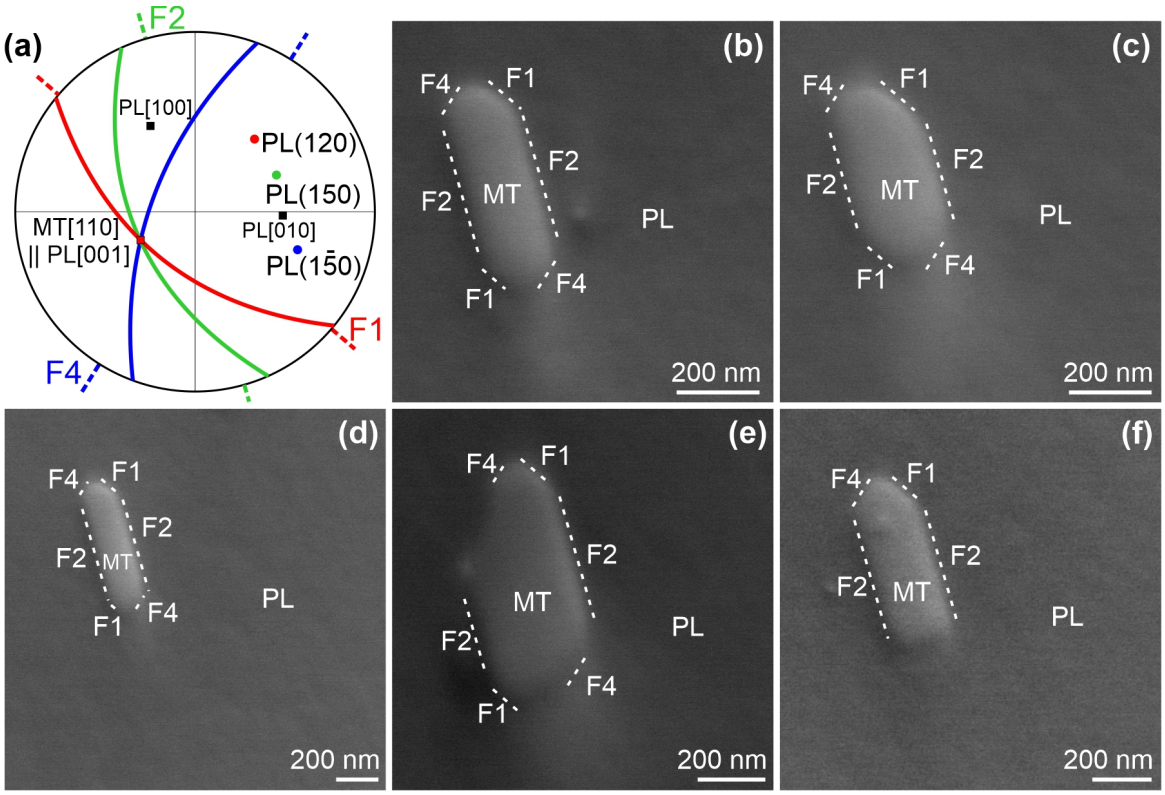

Figure 4.4: (a) Stereographic projection with viewing direction perpendicular to the specimen surface. The red, green and blue large circles represent plagioclase lattice planes, the associated poles are labelled with the respective Miller indices. The red, green and blue dashed straight lines indicate the traces of the facets observed in subfigures (b)-(f). (b-f) Secondary electron images of five PL[001]-MT micro-inclusions pertaining to the COR1A variant of spinel twin 2 in plagioclase, crystallographic orientations of plagioclase and magnetite as in (a). The inclusion's elongation direction is oblique to the specimen surface. The orientations of interface facet traces are highlighted with straight dashed lines and labelled as F*i* (i=1,2,4).

column of Table 4.2. Comparing the orientations of the interface facets with respect to plagioclase lattice planes obtained from STEM and SE images, the major interface segments F1, F2 and F4 in the STEM image (Fig. 4.5b) closely correspond to interface segments F1, F2 and F4 in the SE images (Fig. S4.4).

High-resolution iDPC-STEM images of the magnetite-plagioclase interface acquired at different interface segments are shown in Figs. 4.5c-f. Note that the iDPC-STEM images shown in Figs. 4.5c-f are somewhat rotated with respect to one another as can be seen from the traces of equivalent lattice planes in the different images. It can be seen in the iDPC-STEM images that the magnetite inclusion is in direct contact with the plagioclase host at each interface segment, and neither gaps nor amorphous layers are observed anywhere along the interface. The strong contrast at the interface is an artifact related to the "delocalization" effect, which is due to the large convergence angle of 30 mrad, which was chosen to achieve the highest possible spatial resolution. In this case, the electron rays of the beam are not perfectly parallel to the magnetite-plagioclase interface, which causes the pronounced contrasts along the phase boundaries (Borisevich et al., 2006).

Different orientation relationships between lattice fringes of the two phases and the interface trace

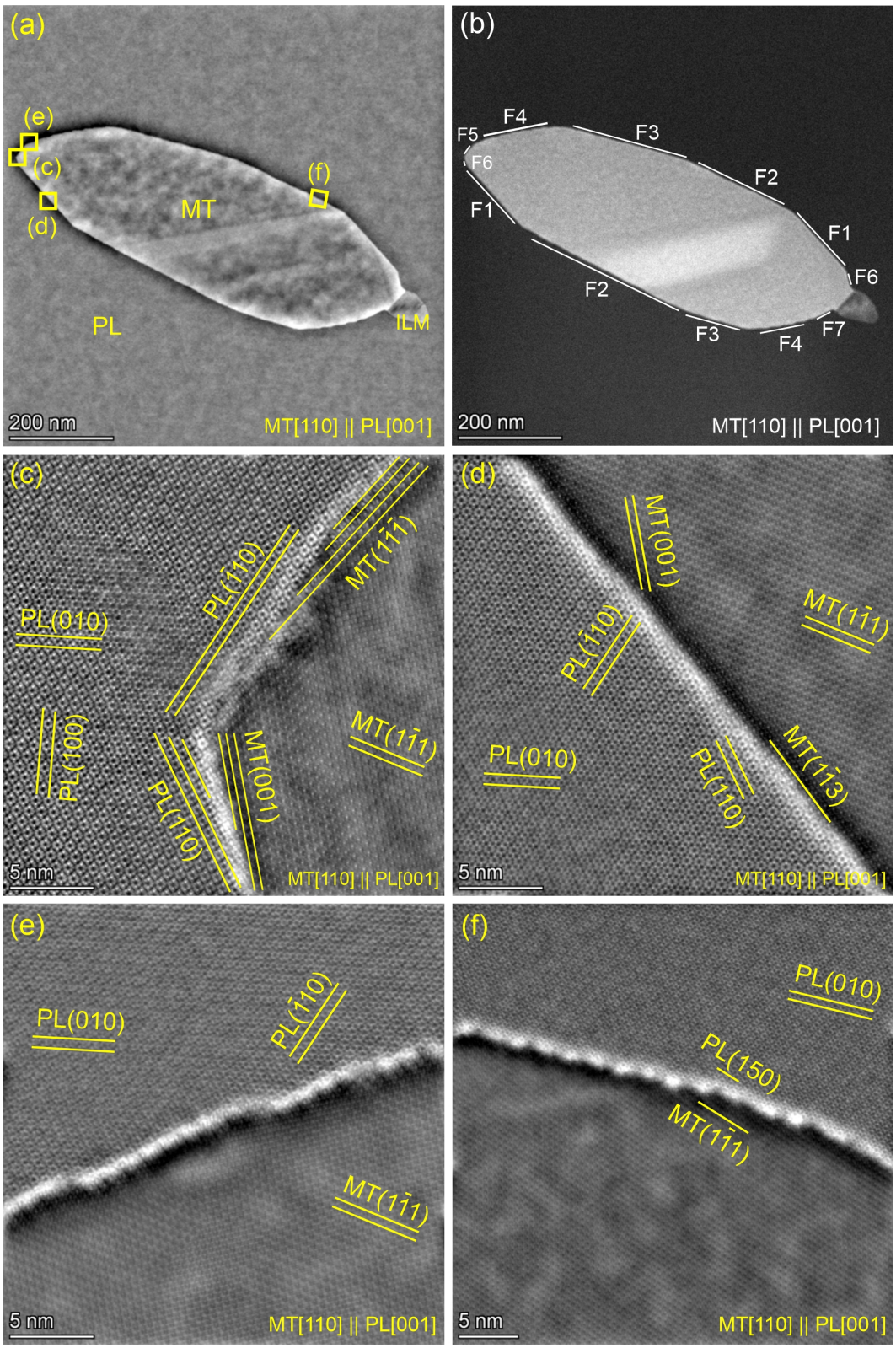

Figure 4.5: (a) Bright-field image showing the cross-section of a selected COR1A PL[001]-MT inclusion. The viewing direction is parallel to MT[110] || PL[001] in all subfigures. The positions, where the iDPC-STEM images shown in (c-f) were taken, are marked by yellow squares with corresponding alphabetical labels. (b) High-angle annular dark-field (HAADF) image of the inclusion shown in (a). The bright domain within magnetite is ulvospinel. The different facets of the magnetite-plagioclase interface are labelled as F*i* (*i*=1-7); (c-f) iDPC-STEM images of different magnetite-plagioclase interface segments. Characteristic lattice planes in magnetite and plagioclase are indicated. Slight rotations around the viewing direction exist among acquisitions, for reference some lattice plane traces are indicated.

Table 4.2: Faceted interface Fi ($i = 1-7$) configurations of a PL[001]-MT micro-inclusion. The first column represents each interface segments as indicated in Fig. 4.5b. The second column represents each facet's orientation with respect to magnetite (by $\Delta\mathbf{g}$ calculation) and plagioclase (by FFT estimation) lattice planes. The third column represents the definition of each facet related $\Delta\mathbf{g}$ defined by the $\mathbf{g}$ vectors of magnetite and plagioclase. The last column represents the orientation of each constrained MT^c-PL interface facet with respect to the lattice plane of the constrained magnetite unit cell (by $\Delta\mathbf{g}^c$ calculation).

	$\Delta\mathbf{g}_i$		$\Delta\mathbf{g}_i^c$
Fi	Orientation	Definition	Orientation
F1	MT(0.296 -0.296 0.908) $\sim\|\|$ PL(470)	$\mathbf{g}_{MT}(1\bar{1}\bar{1})-\mathbf{g}_{PL}(\bar{1}20)$	MT^c(0.193 -0.193 0.962)
F2	MT(-0.543 0.543 -0.641) $\sim\|\|$ PL(140)	$\mathbf{g}_{MT}(00\bar{1})-\mathbf{g}_{PL}(\bar{1}\bar{1}0)$	MT^c(-0.577 0.577 -0.577)
F3	MT(-0.611 0.611 -0.503) $\sim\|\|$ PL(180)	$\mathbf{g}_{MT}(1\bar{1}3)-\mathbf{g}_{PL}(220)$	MT^c(-0.577 0.577 -0.577)
F4	MT(0.698 -0.698 0.158) $\sim\|\|$ PL($\bar{1}$70)	$\mathbf{g}_{MT}(\bar{1}12)-\mathbf{g}_{PL}(2\bar{1}0)$	MT^c(0.688 -0.688 -0.230)
F5	MT(0.509 -0.509 -0.694) $\sim\|\|$ PL($\bar{6}$70)	$\mathbf{g}_{MT}(1\bar{1}1)-\mathbf{g}_{PL}(030)$	MT^c(0.503 -0.503 -0.703)
F6	MT(-0.076 0.076 -0.994) $\sim\|\|$ PL(210)	$\mathbf{g}_{MT}(2\bar{2}0)-\mathbf{g}_{PL}(\bar{1}40)$	MT^c(-0.192 0.192 -0.962)
F7	MT(0.689 -0.689 -0.226) $\sim\|\|$ PL($\bar{1}$30)	$\mathbf{g}_{MT}(\bar{1}10)-\mathbf{g}_{PL}(0\bar{1}0)$	MT^c(0.688 -0.688 -0.229)

are observed along the different interface segments. In Fig. 4.5c three interface segments are seen. The uppermost segment is parallel to the MT($1\bar{1}\bar{1}$) lattice fringes, and it is approximately parallel to PL($\bar{2}$30), but no lattice fringes corresponding to this lattice plane are visible in plagioclase. The second segment is parallel to the PL($\bar{1}$10) lattice fringes, and it is approximately parallel to MT($2\bar{2}\bar{3}$), but no lattice fringes corresponding to this lattice plane are visible in magnetite. The lowermost interface segment is approximately parallel to PL(210), but neither the MT(001) nor the PL(110) planes, the lattice fringes of which are visible, are parallel to this interface segment. In Fig. 4.5d, the interface is perfectly straight on the 10s of nm scale but neither the lattice fringes discernible in plagioclase nor those discernible in magnetite are parallel to the interface plane. The interfaces in Figs. 4.5e,f are curved on the 10s of nm scale and are stepped on the atomic scale. In Fig. 4.5e the terraces, the long sides of the steps, are parallel to the PL($\bar{1}$30) lattice fringes, but no lattice fringes parallel to the terraces are visible in magnetite. By contrast, in Fig. 4.5f the terraces are parallel to the MT($1\bar{1}1$) lattice fringes, but no lattice fringes parallel to the terraces are visible in plagioclase.

4.3.5 Interface configuration of a COR1B PL[001]-MT inclusion

High resolution iDPC-STEM images of different magnetite-plagioclase interface segments of a PL[001]-MT inclusion pertaining to the COR1B orientation variant are shown in Fig. 4.6. The COR of this magnetite inclusion to the plagioclase host is obtained from FFT analyses of an iDPC-STEM image (Supplementary material Fig. S4.5). The specimen was prepared without prior optical documentation and EBSD analysis

and so the morphology of the inclusion and its SOR with respect to the plagioclase host are not known. Based on the fact that the inclusion pertains to the COR1B variant, it may be supposed that it is a needle-shaped inclusion. The viewing direction is parallel to PL[001] in all subfigures. In this projection prominent channels running parallel to PL[001] in the crystal structure of plagioclase are edge on and appear as six membered rings of SiO_4 and AlO_4 tetrahedra (see crystal structure models in Fig. 4.6d,e). Small deviations between the MT[110] direction and the PL[001] direction can be discerned when plagioclase is in the PL[001] zone axis during the acquisition, and magnetite is slightly off the MT[110] zone axis. Nevertheless, continuous layers with intermediate grey contrast parallel to MT(001) alternating with arrays of isolated spots with relatively bright contrast can be discerned in magnetite. The continuous layers correspond to layers comprised of alternating tetrahedrally and octahedrally coordinated Fe-atoms parallel to MT(001), the isolated spots with bright contrast correspond to columns of octahedrally coordinated Fe-atoms extending parallel to MT[110] (Fig. 4.6).

The different segments of the magnetite-plagioclase interfaces shown in Figs. 4.6a,b,c are all wavy in appearance. In the high-resolution iDPC-STEM image of Fig. 4.6b it can be seen that at the magnetite-plagioclase interface the continuous layers parallel to MT(001) are connected to the six-membered rings representing the channels parallel to PL[001] in the plagioclase crystal structure. Apparently along the magnetite-plagioclase interface the spacing between the channels parallel PL[001] in plagioclase and the spacing between two continuous layers parallel to MT(001) in magnetite along the magnetite-plagioclase interface is different, and the MT(001) layers link up with the six-membered rings at different positions within the rings. In some places, the MT(001) layers are kinked in the immediate vicinity to the magnetite-plagioclase interface, so that they link up with the six membered rings (see bottom of Fig. 4.6b). In addition, at some interface segments, magnetite appears to undergo a structural transformation close to the magnetite-plagioclase interface. For example, at the interface segment shown in the upper part of Fig. 4.6c the bright spots representing the arrays of individual columns of octahedrally coordinated Fe atoms disappear in an about 1 nm wide zone along the interface, while the structure of the new phase clearly inherits elements from the previous magnetite structure.

Finally, two dimensional defects seem to have been introduced close to the magnetite-plagioclase interface, through which parts of the magnetite grain that are in direct contact with the plagioclase are displaced with respect to the remainder of the magnetite grain (Fig. 4.6a). A particularly instructive example is shown in Fig. 4.7, where stacking faults are present in the magnetite in the area highlighted by the green rectangle. A closeup of the domain is shown in Fig. 4.7b. Two stacking faults can be discerned. One is parallel to MT($\bar{1}1\bar{1}$) and the second is parallel to MT($\bar{1}11$) (see Fig. 4.7c). The two stacking faults cor-

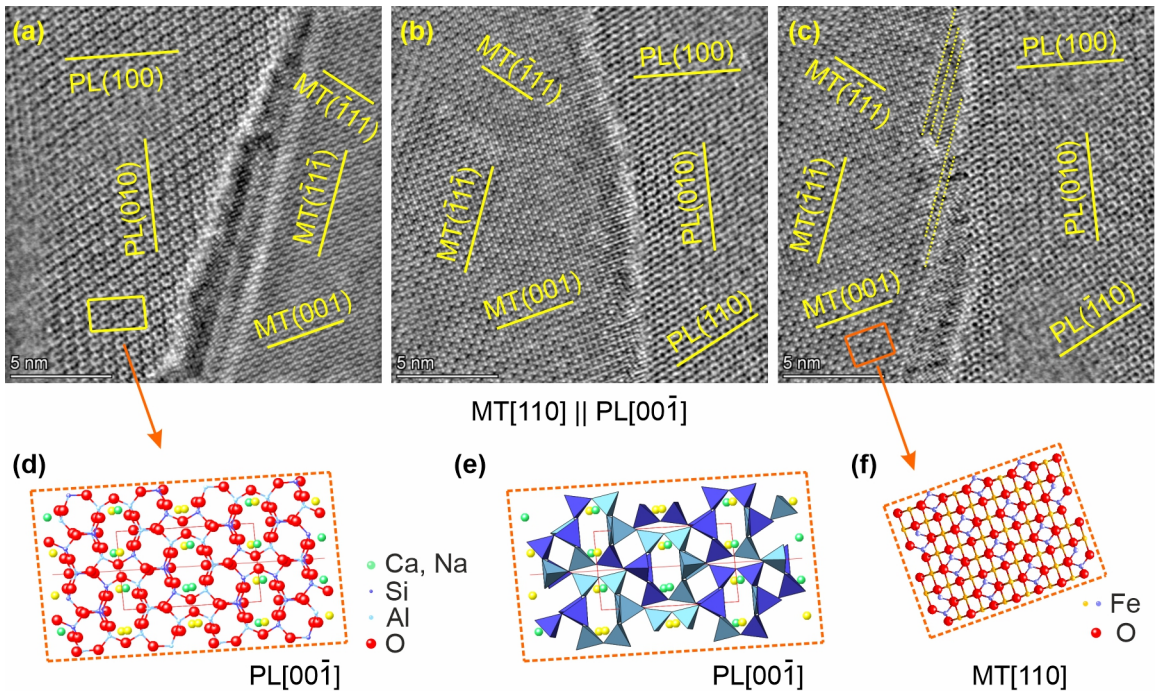

Figure 4.6: High resolution iDPC-STEM images of different magnetite-plagioclase interface segments of a COR1B PL[001] inclusion. The viewing direction is parallel to PL[001] in all subfigures, as MT[110] and PL[001] are not perfectly parallel in COR1B PL[001] inclusions, magnetite is slightly off the MT[110] zone axis. Some low-index lattice planes are indicated for both magnetite and plagioclase. Within the plagioclase domain, channels parallel to PL[001] appear as six membered rings. Crystal structure models of plagioclase and magnetite in appropriate orientations are shown for reference. Purple and yellow spheres in the stick and ball crystal structure models of magnetite represent tetrahedrally and octahedrally coordinated Fe cations, respectively. (a) Plagioclase (left) and magnetite (right) with stacking faults parallel to MT($\bar{1}1\bar{1}$) in magnetite close to the magnetite-plagioclase interface. (b) Magnetite (left) and plagioclase (right) with continuous layers parallel MT(001) apparently kinked in the immediate vicinity of the magnetite-plagioclase interface so that they meet up with the six membered rings representing the channels parallel to PL[001] in plagioclase. (c) Magnetite (left) and plagioclase (right) with domains along the magnetite-plagioclase interface, where the columns of octahedrally coordinated Fe atoms parallel MT(001) are missing – possibly constituting a new phase. (d) Ball-stick model of plagioclase crystal structure according to the yellow box in (a). (e) Polyhedral model of plagioclase crystal structure according to (d). (f) Ball-stick model of magnetite crystal structure according to the orange box in (c).

respond to Shockley partial dislocations. The stacking fault parallel to MT($\bar{1}1\bar{1}$) has a displacement vector **b**=1/6[1$\bar{1}\bar{2}$] and the stacking fault parallel to MT($\bar{1}11$) has a displacement vector **b**=1/6[$\bar{1}1\bar{2}$]. The magnetite domain bounded by the two stacking faults is thus shifted with respect to the bulk magnetite grain by 1/6[1$\bar{1}\bar{2}$]+ 1/6[$\bar{1}1\bar{2}$]=2/3[00$\bar{1}$]. A schematic sketch of this situation is shown in Fig. 4.7c. The black circles represent the oxygen atoms in the original magnetite crystal. The two small red arrows emanating from one oxygen atom indicate the 1/6[1$\bar{1}\bar{2}$] and 1/6[$\bar{1}1\bar{2}$] displacements associated with the two stacking faults. Cooperative application of these two displacements results in an overall 2/3[00$\bar{1}$] displacement, which is indicated by the heavy red arrow. Application of the overall displacement to the oxygen sub-lattice of the original magnetite grain produces the oxygen sub-lattice of the displaced magnetite domain, which is shown in blue.

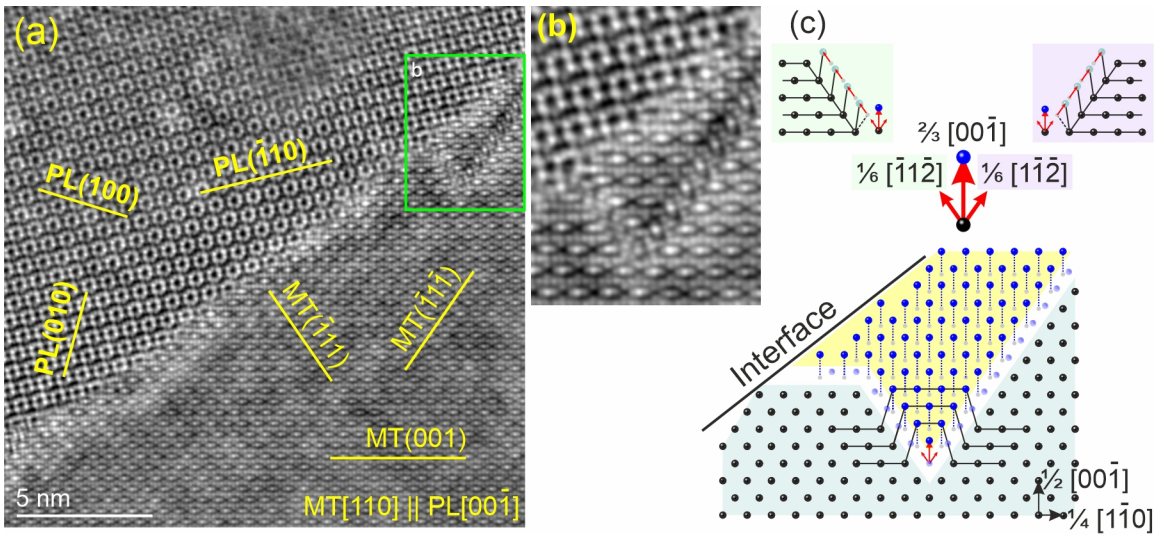

Figure 4.7: (a) Magnetite-plagioclase interface of the same COR1B type magnetite micro-inclusion as shown in Fig. 4.6 with stacking faults in magnetite highlighted with the green rectangle. (b) Closeup of the interface segment with associated stacking faults in the upper part of (a). The images have been rotated relative to Fig. 4.6 so that the MT(001) lattice planes are horizontal. (c) Sketch of the arrangement of oxygen atoms in the magnetite crystal structure as observed in (b).

4.4 Discussion

4.4.1 Genesis of PL[001]-MT inclusions

Based on the notion that the plane-normal type magnetite micro-inclusions occur in pristine plagioclase domains typically in the core regions of the grains, whereas the PL[001]-MT inclusions typically occur at the transition between pristine and hydrothermally altered domains, it is inferred that the PL[001]-MT inclusions formed later than the plane-normal type magnetite micro-inclusions. Indeed, petrographic evidence (Fig. 4.1) suggests that the PL[001]-MT inclusions formed by recrystallization from the pre-existing plane-normal type magnetite micro-inclusions. The spatial association with healed cracks and with the external portions of the plagioclase grains suggests that this recrystallization took place during hydrothermal overprint. Detailed descriptions of the hydrothermal history of the gabbroic rocks from comparable samples from the same dredge location can be found in Pertsev et al. (2015). The plane normal inclusions were inferred to have precipitated from Fe-bearing magmatic plagioclase during a late magmatic stage at temperatures in excess of about 600 °C (Bian et al., 2021). The PL[001] type inclusions formed at a later stage, probably at lower temperatures. This inference is corroborated by the fact that PL[001]-MT micro-inclusions typically contain precipitates of ulvospinel, which form by exsolution from Ti-bearing magnetite at temperatures $\leq$ 600 °C (Tan et al., 2016). In contrast, the magnetite micro-inclusions of the plane normal type contain lamellar precipitates of ilmenite that supposedly formed by high-temperature oxidation at $\geq$ 600 °C (Bian et al., 2021). Furthermore, in some places the secondary nature of the PL[001]-MT

micro-inclusions is evident from PL[001]-MT inclusions growing on pre-existing plane-normal magnetite inclusions (Fig. 4.1c).

4.4.2 Crystallographic basis for the SOR and CORs of PL[001]-MT inclusions

Out of the three COR variants of the PL[001]-MT micro-inclusions listed in Table 4.1 COR1A and COR1B are related by a 70° rotation about PL[001] || MT[110]. In variant COR2, the PL[001] and MT[110] directions are slightly misaligned, and bringing COR2 magnetite into COR1B orientation could be envisaged as a ∼5° rotation of the COR2 magnetite about MT($\bar{1}1\bar{1}$) || PL(120) that makes MT[110] parallel to PL[001] followed by a ∼120° rotation about MT[110] || PL[001], which makes the close-packed oxygen layers parallel to MT($\bar{1}1\bar{1}$) in magnetite parallel to the oxygen layers parallel to PL($1\bar{5}0$) in plagioclase, which corresponds to COR1B. A similar combination of rotations can be applied for relating the COR2 and COR1A variants.

Each COR variant has two subgroups that are related by the spinel twin law. As shown in Table 4.1 and Figs. 4.2-4.3, in magnetite twin 1, we have PL[-14,10,-7] || MT[001] for COR1A, and PL[14,10,7] ∼|| MT[001] for COR1B. These CORs have been classified as PL[001] type magnetite micro-inclusions in nucleation orientation by Ageeva et al. (2020). The plagioclase crystal structure contains channels parallel to PL[001], which appear as six membered rings of SiO_4 and AlO_4 tetrahedra in a projection parallel to PL[001] (see Fig. 4.6). The nucleation orientation is defined by the alignment of FeO_6 octahedra, which are basic building units of the magnetite crystal structure, so that they fit into these channels. The distance between two opposite apices of a FeO_6 octahedron is about 4.28 Å, and the line connecting opposing apices corresponds to one of the MT⟨100⟩ directions. There are several orientations in which the FeO_6 octahedra fit into the channels including orientations, where MT⟨100⟩ is parallel to PL[14,10,7], PL[-14,10,-7], PL[023], or PL[02$\bar{3}$]. We suppose that the good fit of FeO_6 octahedra in the channels of the plagioclase crystal structure ensures a low energy barrier for magnetite nucleation and thus the channels are preferred sites for nucleation of magnetite in plagioclase (Wenk et al., 2011; Ageeva et al., 2020).

If magnetite is present as magnetite twin 2, the COR1A and COR1B variants correspond to the PL[001] type magnetite micro-inclusions in main orientation (Ageeva et al., 2020), which ensures parallel alignment of important oxygen layers in plagioclase and in magnetite. “Important oxygen layers in plagioclase” we define as concentrations of oxygen atoms forming roughly planar, several atomic layers thick configurations parallel to certain plagioclase lattice planes. In magnetite, we consider the close packed oxygen layers, such as MT(222) lattice plane, as “important oxygen layers in magnetite”. In several places, the facets of the

magnetite-plagioclase interface are parallel to important oxygen layers in the magnetite and plagioclase crystal structures. For instance, in examples of COR1A magnetite twin 2 the magnetite-plagioclase interface follows PL($1\bar{5}0$) || MT($1\bar{1}0$) as shown in Fig. 4.2, and in examples of COR1B magnetite twin 2 the interface follows PL(150) || MT($1\bar{1}0$), as shown in Fig. 4.3. These interface facets contain the elongation direction of the inclusions and thus form prismatic facets. The parallel alignment of oxygen layers in magnetite and plagioclase probably represents a low energy configuration. In addition, it minimizes the distances over which oxygen atoms need to be shifted during the replacement of plagioclase by magnetite and thus lowers the energy barrier for magnetite growth within plagioclase host (Hwang et al., 2019).

In summary, all six COR variants of the PL[001] type magnetite micro-inclusions are related by crystallographic operations, which strongly suggests that the CORs of the PL[001] type magnetite inclusions to the plagioclase host are controlled by crystal structure fit between the two phases. In particular, the fit of the oxygen sub-lattices appears to be optimized across the magnetite-plagioclase interfaces. On the one hand, the good fit of the oxygen sub-lattices ensures low energy configurations and thus influences the CORs between the magnetite micro-inclusions and the plagioclase host. On the other hand, certain orientation variants, the two nucleation orientations, minimize the nucleation barrier and others minimize the extent over which oxygen ions must be displaced during the replacement of plagioclase by magnetite. The latter two phenomena ease magnetite nucleation and growth and thus influence the kinetics of magnetite precipitation in plagioclase host.

4.4.3 Crystallographic control on interface orientations of COR1A PL[001]-MT inclusions

Interface segments following certain directions that are similar for different magnetite inclusions in a single plagioclase domain and curved interface segments comprised of steps following lattice fringes in either plagioclase or magnetite indicate that interface orientations are crystallographically controlled. In microstructural equilibrium, interface orientations are selected so that the system attains a low energy configuration. Ultimately, interfacial energy in crystalline materials depends on the microscopic structure of the interface (Sutton and Balluffi, 1995; Zhang, 2020). In detail, quantification of interfacial energy is difficult and is beyond the scope of this work. We follow an alternative approach based on the notion that the degree of geometrical match between the lattices of magnetite and plagioclase along their interfaces provides a qualitative indication of interfacial energy. In the following, HR STEM images and corresponding simulated diffraction patterns are analyzed to shed light on the relationships between magnetite-plagioclase interface orientations and the degree of lattice match between the two phases.

In Fig. 4.8 simulated diffraction patterns of magnetite (red spots) and plagioclase (black spots) are superimposed according to the orientation relationship obtained from the STEM images shown in Fig. 4.5. The viewing direction is parallel to MT[110] || PL[001]. The diffraction spots define the reciprocal lattice vectors $\mathbf{g}_\kappa(hkl)$, where κ indicates the phase, plagioclase or magnetite, and (hkl) are the Miller indices of the lattice plane represented by the respective $\mathbf{g}$ vector. The difference vector between a magnetite and a plagioclase reciprocal lattice vector is denoted as $\Delta\mathbf{g} = \mathbf{g}_{\mathrm{MT}} - \mathbf{g}_{\mathrm{PL}}$ (Hirsch et al., 1977).

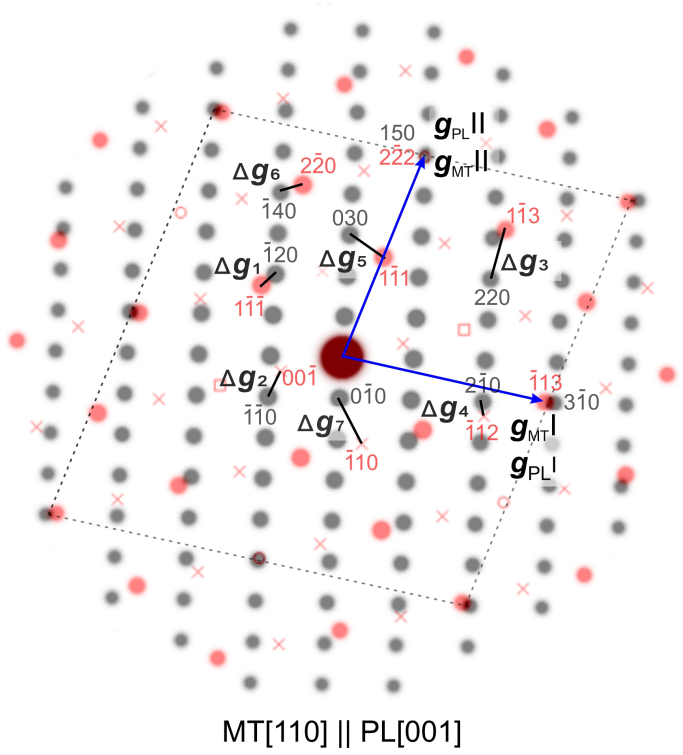

Figure 4.8: Simulated diffraction patterns of magnetite (red spots) and plagioclase (black spots) superimposed according to the orientation relationship obtained from the fast Fourier transformation (FFT) upon STEM images in Fig. 4.5d under viewing direction MT[110] || PL[001]. Near coincident diffraction spots $\mathbf{g}_{\mathrm{PLI}}$, $\mathbf{g}_{\mathrm{MTI}}$ and $\mathbf{g}_{\mathrm{PLII}}$, $\mathbf{g}_{\mathrm{MTII}}$ are indicated with arrows. $\Delta\mathbf{g}_i$ connecting diffraction spots of magnetite and plagioclase that are perpendicular to the corresponding facets Fi in Fig. 4.5b are indicated therein. The related diffraction spots of magnetite are indexed in red and of plagioclase are indexed in black.

It can be shown that the lattice planes represented by $\mathbf{g}_{\mathrm{MT}}(hkl)$ and $\mathbf{g}_{\mathrm{PL}}(hkl)$ meet in a coherent fashion at a plane that is oriented perpendicular to the corresponding $\Delta\mathbf{g}$ vector (Bäro and Gleiter, 1974; Luo and Weatherly, 1988). Such a plane is supposed to have lower interfacial energy as compared to other interface orientations. This would make such an interface prone to forming a facet of the magnetite-plagioclase interface (Zhang and Purdy, 1993; Zhang and Weatherly, 2005). The arrows in Fig. 4.8 mark two pairs of nearly coinciding diffraction spots $\mathbf{g}_{\mathrm{MTI}} = \mathrm{MT}(\bar{1}13)$, $\mathbf{g}_{\mathrm{PLI}} = \mathrm{PL}(3\bar{1}0)$, and $\mathbf{g}_{\mathrm{MTII}} = \mathrm{MT}(2\bar{2}2)$, $\mathbf{g}_{\mathrm{PLII}} = \mathrm{PL}(150)$. Together with their symmetrical equivalents they bound a parallelogram within the diffraction patterns shown in Fig. 4.8 containing the diffraction spots of low-index lattice planes from magnetite and plagioclase. Within this parallelogram seven $\Delta\mathbf{g}_i(i = 1-7)$ vectors can be identified that are perpendicular to the traces of the magnetite-plagioclase interfaces shown in Fig. 4.5b. The definitions of these $\Delta\mathbf{g}_i(i = 1-7)$ vectors are listed in the third column of Table 4.2. The orientations of interface segments Fi (i=1-7) can thus be determined from the related $\Delta\mathbf{g}_i$ vectors. The interface orientations expressed in terms of Miller indices referring to magnetite and to plagioclase are listed in the second column of Table 4.2.

Table 4.3: Lattice constants of plagioclase (PL) taken from Wenk et al. (1980), and of magnetite (MT) taken from Fleet (1981); in the last row the lattice constants of constrained magnetite, MT^c are given.

Phase	a / Å	b / Å	c / Å	α /°	β /°	γ /°
MT	8.3970	8.3970	8.3970	90	90	90
MT^c	8.3145	8.3156	8.0757	91.0735	88.9688	89.2397

Growth of magnetite within plagioclase implies motion of magnetite-plagioclase interfaces into the plagioclase. Across these interfaces the triclinic lattice of plagioclase is transformed to the cubic lattice of magnetite. In the following, we apply a constraint to one of the crystal lattices so that a more direct geometrical relationship between the two lattices is produced. We then check, whether in the constrained configuration geometrical models for describing the crystallographic relationships at the interface may be applied to explain interface orientations. For defining the transformation from the lattice of plagioclase to the lattice of magnetite, the metrics of the two lattices and their COR must be known. The lattice parameters of plagioclase and magnetite are taken from Wenk et al. (2011) and Fleet (1981), respectively, as listed in the first two rows of Table 4.3. The COR between plagioclase and magnetite of the inclusion under study is known from EBSD and HR STEM data. For obtaining the transformation matrix relating the two lattices three non-planar vectors are selected as a base within each of the lattices. One base vector is selected along the inclusion elongation direction, where MT[330] || PL[005] as $3 \cdot$ MT[110], $3 \times l_{\mathrm{MT}[110]} = 3 \times 11.871$ Å $= 35.613$ Å is nearly identical in length to $5 \cdot$ PL[001], $5 \times l_{\mathrm{PL}[001]} = 5 \times 7.1022$ Å $= 35.511$ Å. The other two base vectors are obtained by comparing the diffraction patterns of the two phases in Fig. 4.8. In the superimposed diffraction patterns, two pairs of nearly identical $\mathbf{g}_\kappa$ vectors are identified. The two pairs are formed by $\mathbf{g}_{\mathrm{PLI}} = \mathrm{PL}(3\bar{1}0)$ together with $\mathbf{g}_{\mathrm{MTI}} = \mathrm{MT}(\bar{1}13)$, and by $\mathbf{g}_{\mathrm{PLII}} = \mathrm{PL}(150)$ together with $\mathbf{g}_{\mathrm{MTII}} = \mathrm{MT}(2\bar{2}2)$ (see Fig. 4.8). These $\mathbf{g}_\kappa$ vectors are selected as the second and third base vectors for the plagioclase and magnetite lattices. Perfect coincidence of the selected $\mathbf{g}_{\mathrm{PLI}}$ and $\mathbf{g}_{\mathrm{MTI}}$ and of the $\mathbf{g}_{\mathrm{PLII}}$ and $\mathbf{g}_{\mathrm{MTII}}$ vectors can be obtained by applying a small strain to either one or to both lattices. Assuming the necessary strain is within the elastic limit, the exact strain could be calculated for both lattices, if the elastic constants are known. We take an alternative approach and test the two extreme scenarios, where only one lattice is strained while the other remains unstrained. The procedure for calculating the lattice of constrained magnetite to make it fit to the lattice of unstrained plagioclase is described in the appendix (Shi et al., 2013, 2021).

The lattice parameters of constrained magnetite, MT^c, are given in Table 4.3. It is seen that the lattice parameters of MTc only slightly differ from those of unconstrained magnetite. Fig. 4.9a shows the simulated diffraction patterns of plagioclase and constrained magnetite MT^c superimposed on one another

according to the observed COR over a large diffraction area. The red and black spots represent the diffraction pattern of constrained magnetite and of plagioclase, respectively. Figs. 4.9b-c show the simulated diffraction patterns of constrained magnetite MT^c and of plagioclase according to the COR over the central parallelogram area, respectively. Fig. 4.9d shows the superimposed diffraction patterns of Figs. 4.9b-c over a smaller diffraction area with the same color codes for constrained magnetite and plagioclase as in Fig. 4.9a. Through application of the constraint, several diffraction spots have become coincident, they are marked with circles. Moreover, several of the $\Delta\mathbf{g}$ vectors have become parallel. We refer to the $\mathbf{g}$ vectors of constrained magnetite as $\mathbf{g}^c_{\mathrm{MT}}$ vectors and to the $\Delta\mathbf{g}$ vectors defined by the difference between $\mathbf{g}^c_{\mathrm{MT}}$ and $\mathbf{g}_{\mathrm{PL}}$ as $\Delta\mathbf{g}^c$. The orientations of $\Delta\mathbf{g}^c_i$s with respect to the MT^c crystal coordinate system are given in the last column of Table 4.2. Within the quadrilateral domain defined by the coinciding diffraction spots (dashed line in Fig. 4.9d), three pairs of $\Delta\mathbf{g}_i$ vectors, which have been non parallel before application of the constraint, have become perfectly parallel $\Delta\mathbf{g}^c_i$ vectors in the constrained configuration: $\Delta\mathbf{g}^c_1 \parallel \Delta\mathbf{g}^c_6$, $\Delta\mathbf{g}^c_2 \parallel \Delta\mathbf{g}^c_3$, and $\Delta\mathbf{g}^c_4 \parallel \Delta\mathbf{g}^c_7$. While the superimposed magnetite and plagioclase diffraction patterns in the unconstrained configuration (Fig. 4.8) yield seven $\Delta\mathbf{g}_i$ vectors defined by low-index lattice planes of magnetite and plagioclase, each corresponding to a specific magnetite-plagioclase interface orientation, only four $\Delta\mathbf{g}^c_i$s remain after application of the constraint, indicating that only four interface orientations would be preferred in the constrained configuration. For three out of the four preferred interface orientations remaining in the constrained configuration two perfectly identical $\Delta\mathbf{g}^c_i$ vectors, each one defined by two different pairs of lattice planes in magnetite and plagioclase exist. This implies that each of these interface planes corresponds to an exact interface in the sense of Robinson et al. (1971), across which all lattice planes containing the viewing direction as the common zone axis are coherent. This configuration ensures perfect match between the magnetite and plagioclase lattice planes sharing this common zone axis, and these lattice planes are continuous across the interface (Hwang et al., 2010; Zhang and Yang, 2011).

Some of the lattice points of constrained magnetite and of plagioclase coincide constituting the *constrained coincidence site lattice* (CCSL). Figs. 4.9e-f represent the correspondence of the lattice points of constrained magnetite and plagioclase in real space. Both figures are oriented according to Fig. 4.9a. The viewing direction is parallel to the inclusion elongation direction PL[001] $\parallel$ MT^c[110]. For reference, a Cartesian coordinate system is introduced where the horizontal direction is taken as the X-axis, which corresponds to the [-0.162,0.162,0.973] direction of constrained magnetite and to the [0.891, 0.033, 0.453] direction of plagioclase. The vertical axis is taken as the Y-axis, which corresponds to the [0.69,-0.69,0.216] direction of constrained magnetite and to the [0.045,0.995,0.086] direction of plagioclase. In Fig. 4.9e, the CCSL points in different layers within the range of Z = [-0.1, 29.6] Å are indicated, where the differ-

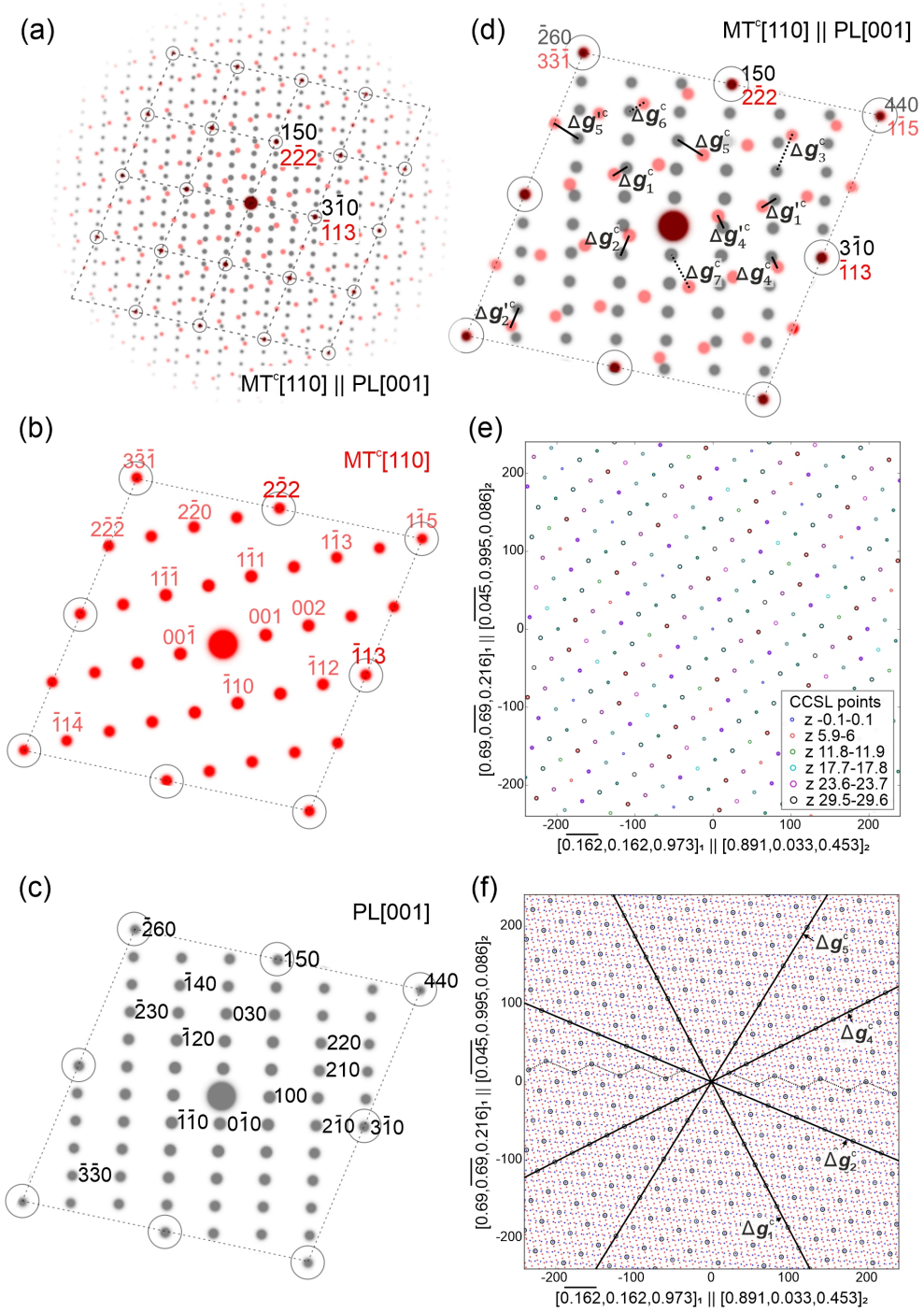

Figure 4.9: (a) Simulated diffraction patterns of constrained magnetite MT^c (red) and plagioclase (black) superimposed according to the observed orientation relationship. The coincident diffraction spots are referred to as CCSL points, which are highlighted with black circles, and the black dashed lines represent the CCSL in reciprocal space. (b) Simulated diffraction patterns of constrained magnetite according to the orientation in (a) over the central area with the Miller indices of the diffraction spots related to the $\Delta\mathbf{g}_i^c$s indicated. (c) Simulated diffraction spots of plagioclase according to the orientation in (a) over the central area with the Miller indices of the diffraction spots related to the $\Delta\mathbf{g}_i^c$s indicated. (d) Close up of the central CCSL marked in (a). Among the constrained $\Delta\mathbf{g}_i^c$s, $\Delta\mathbf{g}_3^c$, $\Delta\mathbf{g}_6^c$ and $\Delta\mathbf{g}_7^c$ have become parallel to $\Delta\mathbf{g}_2^c$, $\Delta\mathbf{g}_1^c$ and $\Delta\mathbf{g}_4^c$ (dashed lines). $\Delta\mathbf{g}_i'^c$s associated with different $\mathbf{g}_{\mathrm{MT}}^c$ and $\mathbf{g}_{\mathrm{PL}}$ that are found to be parallel to the aforementioned $\Delta\mathbf{g}_i^c$s are indicated. (e-f) CCSL points plotted in real space with orientations according to (a); the Z axis is parallel to the viewing direction. Axes labels indicate lattice directions of constrained magnetite (denoted as 1) and plagioclase (denoted as 2), the units on the axes are in Å. (e) CCSL points in real space at different positions along the Z axis in the range of $Z = [0.1, 29.6]$ Å, the different colors correspond to Z coordinate (see legend). (f) Relationships between interface facets' orientations and corresponding $\Delta\mathbf{g}_i^c$s, and the facets' intersections with the CCSL (black circles) within one repetition unit. Red and blue spots represent lattice points of constrained magnetite and plagioclase, respectively. Dashed lines represent a preferred terrace and ledge configuration observed at interface F2.

ent colors correspond to different positions along the Z axis (see legend). For clarity, the lattice points of constrained magnetite and plagioclase have been omitted. This pattern repeats along the Z direction after a distance of $MT^c[330] = PL[005]$. The facet orientations corresponding to the different $\Delta\mathbf{g}_i^c$s are shown in Fig. 4.9f. The red and blue spots in Fig. 4.9f represent lattice points of constrained magnetite and of plagioclase, respectively, in real space. The CCSL points are marked with black circles. Each facet is parallel to linear arrays of CCSL points, and the facet orientations are consistent with the observed facets of the selected PL[001]-MT micro-inclusion. The facet perpendicular to $\Delta\mathbf{g}_4^c$ has the highest density of CCSL points followed by the facet perpendicular to $\Delta\mathbf{g}_1^c$ and the facet perpendicular to $\Delta\mathbf{g}_2^c$. Finally, $\Delta\mathbf{g}_5^c$ has the lowest density of CCSL points in the 2D projection. Since the CCSL points in the range of $Z = [$-0.1, 29.6$]$ Å are distributed over different positions along the inclusion elongation direction, it is essential to also examine the CCSL points within each facet. The CCSL points in the different interface planes are shown in Fig. 4.10. In each plot the viewing direction is parallel to the corresponding $\Delta\mathbf{g}_i^c$ vector, the horizontal direction is the inclusion elongation direction, and the vertical direction is the in-plane direction in the respective interface facet that is perpendicular to the inclusion elongation direction. The two dashed vertical lines in each plot indicate the range of $Z = [$-0.1, 29.6$]$ Å. Red and blue spots are lattice points of constrained magnetite and of plagioclase, respectively. CCSL points are highlighted with circles. The absolute number of CCSL points within the range of $Z = [$-0.1, 29.6$]$ Å in each facet plane is indicated above each plot. From this number the areal density of CCSL points can be calculated for each facet plane. The relative proportions are similar to the density of the CCSL points on the interface traces in the 2D projection. The facet perpendicular to $\Delta\mathbf{g}_4^c$ has the highest areal density of CCSL points, followed by the facet perpendicular to $\Delta\mathbf{g}_1^c$ and the facet perpendicular to $\Delta\mathbf{g}_2^c$. The facet perpendicular to $\Delta\mathbf{g}_5^c$ has the lowest areal density of CCSL points.

Our observations corroborate the supposition that a high area density of CCSL points in the interface plane serves as a criterion for the selection of specific interface facets (Ye and Zhang, 2002). For example, for the commonly observed interface facet F1, which typically is sharp and straight on the atomic scale (Fig. 4.5d), the area density of CCSL points corresponding to $\Delta\mathbf{g}_1^c$ (Fig. 4.9d) is relatively high. The F1 interface segment is thus supposed to represent a low energy configuration. In contrast, for the least commonly observed interface segment F5, the area density of CCSL points is indeed substantially lower than for the other facets (Fig. 4.5b).

In the constrained situation $\Delta\mathbf{g}_1^c \parallel \Delta\mathbf{g}_6^c$, $\Delta\mathbf{g}_2^c \parallel \Delta\mathbf{g}_3^c$, and $\Delta\mathbf{g}_4^c \parallel \Delta\mathbf{g}_7^c$, the corresponding interface planes may account for an entire hexagonal needle cross-section bounded by three pairs of exact interfaces in the sense of Robinson et al. (1971). Upon relaxation of the constraint, a network of dislocations emerges that accommodates the resulting lattice misfit between magnetite and plagioclase (Ye and Zhang, 2002). In

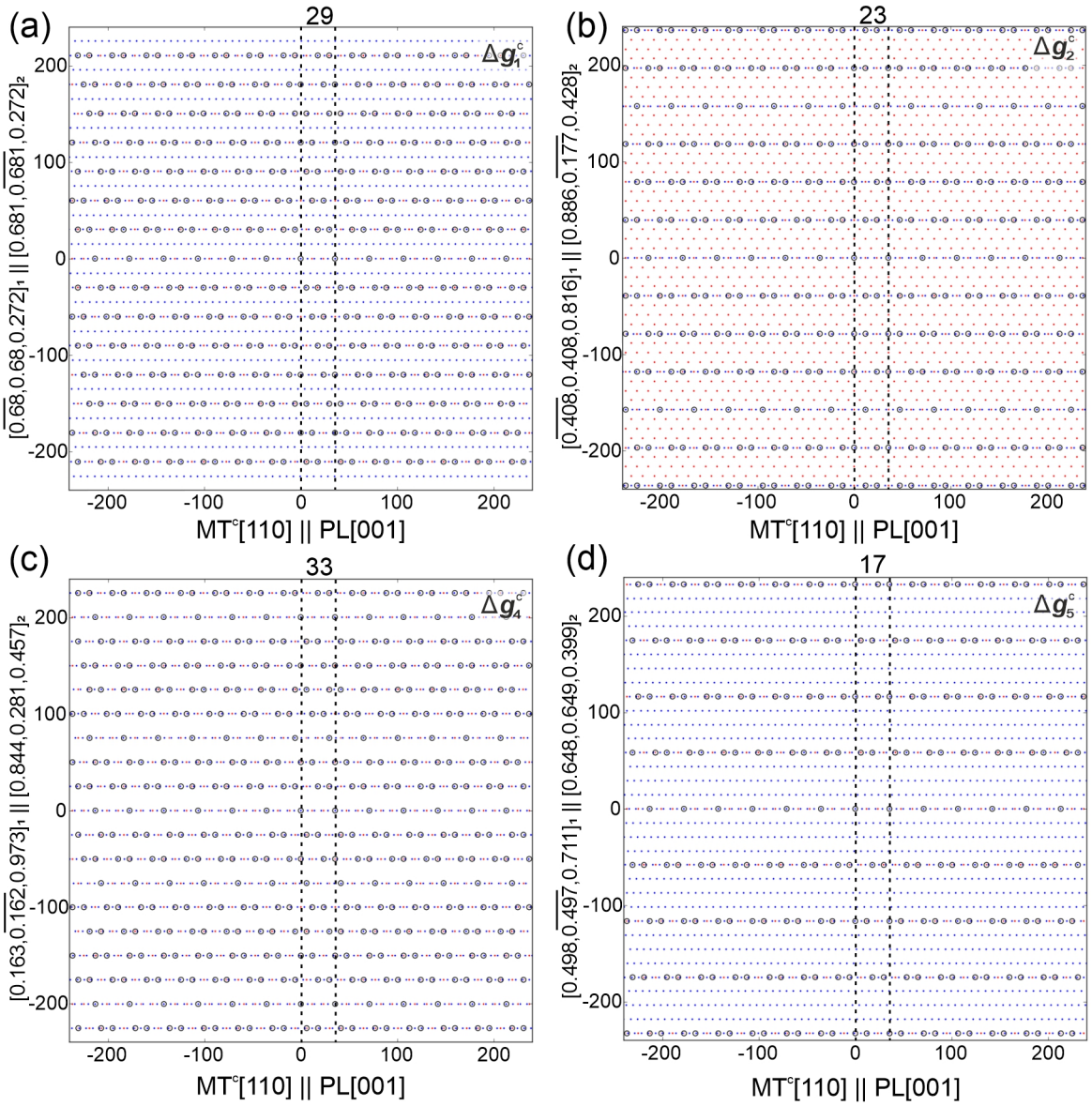

Figure 4.10: CCSL points (black circles) in the facet planes perpendicular to (a)$\Delta\mathbf{g}_1^c$, (b) $\Delta\mathbf{g}_2^c$, (c) $\Delta\mathbf{g}_4^c$ and (d) $\Delta\mathbf{g}_5^c$, as indicated at the top-right of each plot. The viewing direction is parallel to the respective $\Delta\mathbf{g}_i^c$ vector in each plot. The horizontal direction is the inclusion elongation direction. The red and blue spots represent lattice points of constrained magnetite and of plagioclase, respectively. The axes are labelled with the lattice directions of constrained magnetite (denoted as 1) and plagioclase (denoted as 2), the units are Å. The vertical dashed lines in each plot indicate the range of [0.1, 29.6] Åon the Z-axis, referred to as one repetition unit. The absolute numbers of the CCSL points within this range are indicated above each plot.

general, the observed interface facets show minute deviations from the facets obtained for the constrained situation. Typically, the facets corresponding to exact interfaces in the constrained situation decompose into ledge and terrace associations in the actual configuration, where the terraces follow the orientation of the exact interface from the constrained situation, and the ledges account for the lattice mismatch. Interface facets F2 and F4 (Figs. 4.5e-f) correspond to such configurations.

The iDPC-STEM image in Fig. 4.5f shows that the F2 interface facet decomposed into nm sized ledges and terraces. From the corresponding FFT result, the orientation of the terraces is parallel to the orientation of $\Delta\mathbf{g}_2^c$, i.e. MT($1\bar{1}1$) || PL(150). In Fig. 4.9d CCSL points in the vicinity of $\Delta\mathbf{g}_2^c$ are connected by a zig-zag line, corresponding to terraces parallel to MT($1\bar{1}1$) || PL(150) and ledges parallel to F4. The averaged orientation of the zig-zag line is nearly parallel to PL(010), which is identical to the orientation obtained from the FFT of Fig. 4.5f. The relative length of the ledge and terrace trace segments are consistent with the experimental results. Thus, we infer that the interface facet related to $\Delta\mathbf{g}_2^c$ transformed into a stepped structure containing ledge traces parallel to F4. We hypothesize that this transformation was driven by the tendency to increase the area density of CCSL points on the interface, which is higher for F4 interface planes than for the interface plane corresponding to $\Delta\mathbf{g}_2^c$.

We suggest that the seven segments that bound the cross-section of the inclusion are derived from the four interface facets in the constrained configuration. The lattice mismatch at the magnetite-plagioclase interfaces is assumed to be accommodated by a network of dislocations (Ye and Zhang, 2002). Even if the exact Burgers vectors of the dislocations remain unclear, the CCSL provides a reference for an idealized interface configuration and qualitatively explains the preference of certain facets.

4.4.4 Accommodation structures at interfaces of COR1B PL[001]-MT inclusions

The high-resolution iDPC-STEM images of the COR1B PL[001]-MT inclusion shown in Fig. 4.6 reveal the close linkage between continuous layers composed of alternating tetrahedrally and octahedrally coordinated Fe atoms parallel to MT(001) in magnetite to the columns parallel to the PL[001] in plagioclase across the magnetite-plagioclase interface. Apparently, along the magnetite-plagioclase interface the spacing between the channels parallel to PL[001] in plagioclase and the spacing between the continuous layers of Fe atoms parallel MT(001) in magnetite differ, and the misfit between the two structural elements in the crystal structures of magnetite and plagioclase leads to a variety of accommodation structures along the interface. The subtlest mode of accommodation is the kinking of the layers of Fe atoms parallel MT(001) in magnetite close to the magnetite-plagioclase interface such as is seen at the bottom of Fig. 4.6b. This

kinking may develop into a more severe mode of accommodation by the introduction of stacking faults as can be seen in Figs. 4.6a and 4.7. The two stacking faults seen in Fig. 4.7 are parallel to two different MT{111} lattice planes.

The cooperative displacement over $1/6[1\bar{1}\bar{2}]$ on the stacking fault parallel MT($\bar{1}1\bar{1}$) and over $1/6[\bar{1}1\bar{2}]$ on the stacking fault parallel MT($\bar{1}11$) leads to an overall displacement of the magnetite bounded by the two stacking faults and the magnetite-plagioclase interface over $2/3[00\bar{1}]$. Based on the notion that these stacking faults are only observed in the immediate vicinity of the magnetite-plagioclase interfaces, it is hypothesized that they are introduced to accommodate the misfit between the magnetite and the plagioclase lattices and to allow for better linkup between the MT(001) lattice planes and the six-membered rings representing the channels parallel to PL[001] in the plagioclase. It is not clear, whether the stacking faults were formed during precipitate growth, or were introduced after growth to release local stress that may have accumulated during precipitate growth. Occurrence of the stacking faults only in the immediate vicinity of the magnetite-plagioclase interface rather suggests formation after precipitate growth. The observed stacking faults correspond to the prominent MT{111}⟨112⟩ glide system in magnetite, which may have been activated to release local stress. It must be noted that the overall displacement neither is contained in the stacking fault parallel MT($\bar{1}1\bar{1}$) nor is it contained in the stacking fault parallel MT($\bar{1}11$). This implies that an extra layer of oxygen and iron extending parallel to MT($\bar{1}1\bar{1}$) and an extra layer of oxygen and iron extending parallel to MT($\bar{1}11$) need to be introduced along the two stacking faults. Displacement of the magnetite domain bounded by the two stacking faults thus requires material re-distribution within the magnetite.

Finally, in some places, accommodation of the lattice misfit appears to have produced fundamental changes of the crystal structure of magnetite so that a new phase has formed along an about 1 nm wide zone along the magnetite-plagioclase interface. There is no direct evidence, but circumstantial evidence suggests that this may also have involved diffusive material redistribution and stoichiometry change of the Fe-oxide phase.

4.5 Implications

Petrographic evidence suggests that the PL[001] magnetite micro-inclusions are of secondary nature in that they formed by recrystallization from older generations of so-called plane normal type magnetite micro-inclusions during hydrothermal processing of the rocks. The transformation of plane normal magnetite micro-inclusions to PL[001] micro-inclusions changes the magnetic anisotropy of magnetite bearing plagioclase, which needs to be considered during single grain magnetic measurements on plagioclase.

Six COR variants between PL[001] magnetite micro-inclusions and the plagioclase host exist that are related to one another by rational crystallographic operations indicating crystallographic control on the SOR and CORs of the PL[001] magnetite micro-inclusions with the plagioclase host. The microscopic interface configurations associated with the different orientation variants ensure low energy configurations in microstructural equilibrium and low energy barriers for nucleation and growth of magnetite precipitates in plagioclase.

The inclusions are faceted, where the interface facets are parallel to low index lattice planes in either magnetite or plagioclase or, the interfaces are stepped with the terraces of the steps parallel to low index lattice planes of either magnetite or plagioclase. In this context either a good fit between the oxygen lattices of the two phases or the parallel alignment of oxygen layers in magnetite and plagioclase appears to be the controlling factor. iDPC-STEM images also reveal linkup between important crystal structure units in plagioclase and in magnetite across the magnetite-plagioclase interfaces. In addition, they reveal accommodation features that shift marginal parts of magnetite grains relative to the bulk precipitate to arrive at a better fit between the two lattices. Locally magnetite seems to have lost its structure and potentially was transformed into another phase in the immediate vicinity of the magnetite-plagioclase interface. The geometry of the accommodation features makes it necessary to invoke re-distribution of Fe and O along the magnetite-plagioclase interface.

The orientation of the interface facets between plagioclase, which is a framework silicate, and magnetite an oxide with close-packed oxygen sublattice can be explained by the $\Delta\mathbf{g}$ method. The interface facets are oriented perpendicular to the $\Delta\mathbf{g}$ vectors that link the $\mathbf{g}$-vectors of low index lattice planes of magnetite and plagioclase in reciprocal space. The orientations of the interface facets only slightly deviate from the orientations of exact phase boundaries, which can be constructed, if one of the lattices is slightly deformed. By this operation a CCSL emerges, and exact magnetite-plagioclase phase boundaries parallel to low index lattice planes in the CCSL are obtained. Even if the constrained configuration probably never existed physically, the CCSL lattice and the $\Delta\mathbf{g}$ method applied to the constrained configuration are viable models that explain the selection of interface facets. In the actual configuration the deviation from exact phase boundaries is small and is accommodated by dislocations.

Appendix

We apply a transformation on the crystal lattice of magnetite (MT) to bring the selected nearly coincident diffraction spots of magnetite into coincidence with the corresponding diffraction spots of plagioclase. This transformation is expressed as a transformation matrix $\mathbf{A}^*_{\mathrm{II}}$, where |* refers to reciprocal space. In a first

step, the magnetite and plagioclase unit cells are expressed in terms of a common orthonormal coordinate system $Oxyz$ in units of Å with base vectors **i**, **j**, **k** along the Ox-, Oy-, and Oz-axes. In general, a crystal coordinate system is defined by the lattice constants $a, b, c, \alpha, \beta, \gamma$ with the base vectors **a**, **b**, **c**. The base vectors of the crystal coordinate system are oriented so that $\mathbf{a} \parallel Ox$ and $\mathbf{a} \times \mathbf{c} \parallel Oy$. The vectors **a**, **b** and **c** are now expressed in the orthogonal coordinates **i**, **j**, **k** by

$$\begin{aligned} \mathbf{a} &= \mathbf{i}s_1^1 + \mathbf{j}s_1^2 + \mathbf{k}s_1^3 \\ \mathbf{b} &= \mathbf{i}s_2^1 + \mathbf{j}s_2^2 + \mathbf{k}s_2^3 \\ \mathbf{c} &= \mathbf{i}s_3^1 + \mathbf{j}s_3^2 + \mathbf{k}s_3^3. \end{aligned} \tag{4.1}$$

In matrix notation this reads

$$\mathbf{u}^{\mathrm{T}} = \mathbf{u}_{(\mathrm{orth})}^{\mathrm{T}}\mathbf{S}, \tag{4.2}$$

where

$$\mathbf{S} = \begin{pmatrix} s_1^1 & s_2^1 & s_3^1 \\ s_1^2 & s_2^2 & s_3^2 \\ s_1^3 & s_2^3 & s_3^3 \end{pmatrix}, \tag{4.3}$$

and **u** are the base vectors of the crystal coordinates and $\mathbf{u}_{(\mathrm{orth})}$ are the base vectors of the orthogonal coordinate system. $|^{\mathrm{T}}$ is the transpose operation.

The coefficients of the **S** matrix are obtained from the scalar products of the base vectors in crystal coordinate making use of the orthogonality of the base vectors in the orthogonal coordinate system (Bollmann 1970)

$$\mathbf{S} = \begin{pmatrix} a & b \cdot cos\gamma & c \cdot cos\beta \\ 0 & (b/sin\beta)(sin^2\beta - cos^2\alpha - cos^2\gamma + cos\alpha \cdot cos\beta \cdot cos\gamma)^{1/2} & 0 \\ 0 & (b/sin\beta)(cos\alpha - cos\beta \cdot cos\gamma) & c \cdot sin\beta \end{pmatrix}, \tag{4.4}$$

where the column vectors of the **S** matrix are the unit vectors in the crystal coordinate system expressed as linear combinations of the base vectors of the orthonormal coordinate system.

The lattice constants of the cubic magnetite a_{MT}=8.397 Å, and of the triclinic plagioclase a_{PL}=8.1736

Å, b_{PL}=12.8736 Å, c_{PL}=7.1022 Å, α_{PL}=93.462°, β_{PL}=93.462° γ_{PL}=93.462°, taken from (Fleet, 1981) and (Wenk et al., 1980), respectively, were then introduced to Eq. 4.4 to obtain $\mathbf{S}_{PL}$ and $\mathbf{S}_{MT}$. Given a column vector $\mathbf{v}$ in the crystal coordinate system, the corresponding vector in the orthogonal coordinate $\mathbf{v}_{(orth)}$ can be expressed by $\mathbf{v}_{(orth)} = \mathbf{S}\mathbf{v}$.

In the next step, a transformation matrix $\mathbf{A_{II}}^*$ is applied to magnetite to make the selected pairs of diffraction spots, which are represented by the reciprocal lattice vectors $\mathbf{g}_{PL1}$, $\mathbf{g}_{PL2}$, $\mathbf{g}_{PL3}$ and $\mathbf{g}_{MT1}$, $\mathbf{g}_{MT2}$, $\mathbf{g}_{MT3}$, respectively, coincident.

The transformation matrix $\mathbf{A_{II}}^*$ must satisfy the condition

$$\mathbf{A}^*_{II} \cdot (\mathbf{S}^*_{MT} \cdot \mathbf{G}_{MT}) = \mathbf{S}^*_{PL} \cdot \mathbf{G}_{PL} \tag{4.5}$$

where $\mathbf{S}^*$ represents $\mathbf{S}$ in reciprocal space with $\mathbf{S}^* = (\mathbf{S}^T)^{-1}$. $\mathbf{G}_{PL}$ is a 3×3 matrix consisting of three non-coplanar plagioclase lattice vectors in reciprocal space $\mathbf{G}_{PL} = (\mathbf{g}_{PLI}, \mathbf{g}_{PLII}, \mathbf{g}_{PLIII})$, where

$$\mathbf{g}_{PLI} = \begin{pmatrix} 3 \\ \bar{1} \\ 0 \end{pmatrix}, \quad \mathbf{g}_{PLII} = \begin{pmatrix} 1 \\ 5 \\ 0 \end{pmatrix}, \quad \mathbf{g}_{PLIII} = \begin{pmatrix} -0.1010 \\ -0.0218 \\ 0.2000 \end{pmatrix}. \tag{4.6}$$

It must be noted that vector $\mathbf{g}_{PL3}$ is equivalent to PL[005] expressed in reciprocal space by the following procedure: (i) PL[001] is transformed into a vector in reciprocal space preserving the same direction and the same length, i.e. PL[001] = PL(-0.505, -0.109, 1.0). (ii) The reciprocal vector PL(-0.505, -0.109, 1.0) is divided by 5 to adjust its length to PL[005]. Similarly, $\mathbf{G}_{MT}$ is a 3×3 matrix consisting of three magnetite lattice vectors in reciprocal space. It is expressed as $\mathbf{G}_{MT} = (\mathbf{g}_{MTI}, \mathbf{g}_{MTII}, \mathbf{g}_{MTIII})$, where

$$\mathbf{g}_{MTI} = \begin{pmatrix} \bar{1} \\ 1 \\ 3 \end{pmatrix}, \quad \mathbf{g}_{MTII} = \begin{pmatrix} 2 \\ \bar{2} \\ 2 \end{pmatrix}, \quad \mathbf{g}_{MTIII} = \begin{pmatrix} 0.1667 \\ 0.1667 \\ 0 \end{pmatrix}. \tag{4.7}$$

The third vector $\mathbf{g}_{MT3}$ corresponds to MT[330] expressed in reciprocal space by the same procedure as described for $\mathbf{g}_{PL3}$. The transformation matrix $\mathbf{A_{II}}^*$ is then obtained from

$$\mathbf{A}^*_{II} = \mathbf{S}^*_{PL} \cdot \mathbf{g}_{PL} \cdot (\mathbf{S}^*_{MT} \cdot \mathbf{g}_{MT})^{-1} \tag{4.8}$$

and finally, the transformation matrix $\mathbf{A}_{\mathrm{II}}$ in real space is calculated as $\mathbf{A}_{\mathrm{II}} = ((\mathbf{A}^{*}_{\mathrm{II}})^{-1})^{\mathrm{T}}$

$$\mathbf{A}_{\mathrm{II}} = \begin{pmatrix} -0.4804 & -0.1390 & 0.8252 \\ 0.6693 & -0.6693 & 0.2869 \\ 0.5499 & 0.7170 & 0.4029 \end{pmatrix} \tag{4.9}$$

The matrix $\mathbf{S}^{\mathrm{c}}_{\mathrm{MT}}$ of the constrained magnetite is obtained from

$$\mathbf{S}^{\mathrm{c}}_{\mathrm{MT}} = \mathbf{A}_{\mathrm{II}} \cdot \mathbf{S}_{\mathrm{MT}}, \tag{4.10}$$

which yields

$$\mathbf{S}^{\mathrm{c}}_{\mathrm{MT}} = \begin{pmatrix} -4.0321 & -1.1669 & 6.9269 \\ 5.6185 & -5.6185 & 2.4079 \\ 4.6158 & 6.0184 & 3.3819 \end{pmatrix} \tag{4.11}$$

The transformation applied to magnetite does not change the translation vectors of the unit cell, thus the constrained magnetite lattice constants, as well as the angles between each unit vector can be calculated from $\mathbf{S}^{\mathrm{c}}_{\mathrm{MT}}$. For instance, the constrained base vector $\mathbf{a}^{\mathrm{c}}_{\mathrm{MT}}$ can be expressed in orthonormal coordinate $\mathbf{a}^{\mathrm{c}}_{\mathrm{MT}} = \mathbf{S}^{\mathrm{c}}_{\mathrm{MT}} \cdot [100]'$, that is the first column in $\mathbf{S}^{\mathrm{c}}_{\mathrm{MT}}$. The value of the base vector $a^{\mathrm{c}}_{\mathrm{MT}} = 8.3145$ is the new lattice constant of the constrained magnetite. $b^{\mathrm{c}}_{\mathrm{MT}}$ and $c^{\mathrm{c}}_{\mathrm{MT}}$ can be derived in the same manner. The angle between the base vectors $\mathbf{b}^{\mathrm{c}}_{\mathrm{MT}}$ and $\mathbf{c}^{\mathrm{c}}_{\mathrm{MT}}$ of the constrained magnetite thus define the angle $\alpha^{\mathrm{c}}_{\mathrm{MT}} = \measuredangle(\mathbf{b}^{\mathrm{c}}_{\mathrm{MT}}, \mathbf{c}^{\mathrm{c}}_{\mathrm{MT}})$, and is derived by the inverse tangent formula $\alpha^{\mathrm{c}}_{\mathrm{MT}} = \mathrm{atan2}(||\mathbf{b}^{\mathrm{c}}_{\mathrm{MT}} \times \mathbf{c}^{\mathrm{c}}_{\mathrm{MT}}||, \mathbf{b}^{\mathrm{c}}_{\mathrm{MT}} \cdot \mathbf{c}^{\mathrm{c}}_{\mathrm{MT}})$. $\beta^{\mathrm{c}}_{\mathrm{MT}}$ and $\gamma^{\mathrm{c}}_{\mathrm{MT}}$ are obtained following the same procedure. The resultant constrained magnetite lattice constants are shown in Table 4.3. The unit cell of constrained magnetite differs only slightly from the unconstrained magnetite unit cell.

Acknowledgements

Funding by the Austrian Science Foundation (FWF), Grant No. I 3998N29, and by the Russian Foundation for Basic Research (RFBR), Grant No. 18-55-14003 is gratefully acknowledged. We thank Alexey Pertsev

for providing the dredged sample. FIB sample preparation was done in the Laboratory for scanning electron microscopy and focused ion beam applications, Faculty of Geosciences, Geography and Astronomy at the University of Vienna (Austria). Authors thank the European Regional Development Fund and the State of Brandenburg for the Themis Z TEM (part of the Potsdam Imaging and Spectral Analysis Facility (PISA)). We thank the constructive suggestions provided by two reviewers. Editorial handling is gratefully acknowledged.

Author Contributions

GB: Study conception and design, sample preparation, data collection, results analysis and interpretation, first draft preparation; OA: Study conception and design, sample preparation; VR: STEM data collection; GH: sample preparation; RA: Study conception and design, study supervision. All authors reviewed and commented on previous manuscript. Final manuscript is approved by all authors.

Bibliography

O. Ageeva, G. Habler, D. Topa, T. Waitz, C. Li, A. Pertsev, T. Griffiths, O. Zhilicheva, and R. Abart. Plagioclase hosted fe-ti-oxide micro-inclusions in an oceanic gabbro-plagiogranite association from the mid atlantic ridge at 13°34' n. *American Journal of Science*, 316(2):85–109, 2016. ISSN 0002-9599. doi: 10.2475/02.2016.01.

O. Ageeva, G. Bian, G. Habler, A. Pertsev, and R. Abart. Crystallographic and shape orientations of magnetite micro-inclusions in plagioclase. *Contributions to Mineralogy and Petrology*, 175(10):1–16, 2020. doi: 10.1007/s00410-020-01735-8.

O. Ageeva, G. Habler, S. A. Gilder, R. Schuster, A. Pertsev, O. Pilipenko, G. Bian, and R. Abart. Oriented magnetite inclusions in plagioclase: Implications for the anisotropy of magnetic remanence. *Geochemistry, Geophysics, Geosystems*, page e2021GC010272, 2022. doi: 10.1029/2021GC010272.

G. Bäro and H. Gleiter. On the structure and migration of incoherent interphase boundaries between fcc and bcc crystals. *Acta Metallurgica*, 22(2):141–143, 1974. doi: 10.1016/0001-6160(74)90003-0.

V. Beltenev, V. Ivanov, I. Rozhdestvenskaya, G. Cherkashov, T. Stepanova, V. Shilov, A. Pertsev, M. Davydov, I. Egorov, I. Melekestseva, et al. A new hydrothermal field at 13° 30 N on the Mid-Atlantic Ridge. *InterRidge News*, 16(9):10, 2007.

V. Beltenev, I. Ivanov, I. Rozhdestvenskaya, G. Cherkashev, T. Stepanova, V. Shilov, M. Davydov, A. Laiba, V. Kaylio, E. Narkevsky, et al. New data about hydrothermal fields on the mid-atlantic ridge between 11-14 N: 32nd cruise of r/v professor logatchev. *InterRidge News*, 18:13–17, 2009.

G. Bian, O. Ageeva, A. Rečnik, G. Habler, and R. Abart. Formation pathways of oriented magnetite microinclusions in plagioclase from oceanic gabbro. *Contributions to Mineralogy and Petrology*, 176(12):1–21, 2021. doi: 10.1007/s00410-021-01864-8.

A. Y. Borisevich, A. R. Lupini, and S. J. Pennycook. Depth sectioning with the aberration-corrected scanning transmission electron microscope. *Proceedings of the National Academy of Sciences*, 103(9):3044–3048, 2006. doi: 10.1073/pnas.0507105103.

M. J. Cheadle and J. S. Gee. Quantitative textural insights into the formation of gabbro in mafic intrusions. *Elements: An International Magazine of Mineralogy, Geochemistry, and Petrology*, 13(6):409–414, 2017. doi: 10.2138/gselements.13.6.409.

K. E. Davis. Magnetite rods in plagioclase as the primary carrier of stable nrm in ocean floor gabbros. *Earth and Planetary Science Letters*, 55(1):190–198, 1981.

D. J. Dunlop and Ö. Özdemir. *Rock magnetism: fundamentals and frontiers*. Number 3. Cambridge university press, 2001.

J. Escartin, C. Mevel, S. Petersen, D. Bonnemains, M. Cannat, M. Andreani, N. Augustin, A. Bezos, V. Chavagnac, Y. Choi, et al. Tectonic structure, evolution, and the nature of oceanic core complexes and their detachment fault zones (13° 20 n and 13° 30 n, Mid Atlantic Ridge). *Geochemistry, Geophysics, Geosystems*, 18(4):1451–1482, 2017. doi: 10.1002/2016GC006775.

J. M. Feinberg, H.-R. Wenk, P. R. Renne, and G. R. Scott. Epitaxial relationships of clinopyroxene-hosted magnetite determined using electron backscatter diffraction (ebsd) technique. *American Mineralogist*, 89(2-3):462–466, 2004. doi: 10.2138/am-2004-2-328.

J. M. Feinberg, R. J. Harrison, T. Kasama, R. E. Dunin-Borkowski, G. R. Scott, and P. R. Renne. Effects of internal mineral structures on the magnetic remanence of silicate-hosted titanomagnetite inclusions: An electron holography study. *Journal of Geophysical Research: Solid Earth*, 111(B12), 2006a. doi: 10.1029/2006JB004498.

J. M. Feinberg, H.-R. Wenk, G. R. Scott, and P. R. Renne. Preferred orientation and anisotropy of seismic and magnetic properties in gabbronorites from the bushveld layered intrusion. *Tectonophysics*, 420(3-4): 345–356, 2006b. doi: 10.1016/j.tecto.2006.03.017.

M. Fleet. The structure of magnetite. *Acta Crystallographica Section B: Structural Crystallography and Crystal Chemistry*, 37(4):917–920, 1981. doi: 10.1107/S0567740881004597.

M. Fleet, G. A. Bilcox, and R. L. Barnett. Oriented magnetite inclusions in pyroxenes from the Grenville Province. *The Canadian Mineralogist*, 18(1):89–99, 1980.

M. Haider, H. Rose, S. Uhlemann, E. Schwan, B. Kabius, and K. Urban. A spherical-aberration-corrected 200kv transmission electron microscope. *Ultramicroscopy*, 75(1):53–60, 1998. ISSN 0304-3991. doi: https://doi.org/10.1016/S0304-3991(98)00048-5. URL `https://www.sciencedirect.com/science/article/pii/S0304399198000485`.

P. Hirsch, A. Howie, R. Nicholson, D. Pashley, and M. Whelan. Electron microscopy of thin crystals, 1977.

S.-L. Hwang, P. Shen, H.-T. Chu, and T.-F. Yui. Nanometer-size α-pbo2-type tio2 in garnet: A thermobarometer for ultrahigh-pressure metamorphism. *Science*, 288(5464):321–324, 2000. doi: 10.1126/science.288.5464.321.

S.-L. Hwang, P. Shen, T.-F. Yui, and H.-T. Chu. On the coherency-controlled growth habit of precipitates in minerals. *Journal of Applied Crystallography*, 43(3):417–428, 2010. doi: 10.1107/S0021889810007454.

S.-L. Hwang, P. Shen, H.-T. Chu, T.-F. Yui, and Y. Iizuka. Origin of rutile needles in star garnet and implications for interpretation of inclusion textures in ultrahigh-pressure metamorphic rocks. *Journal of Metamorphic Geology*, 33(3):249–272, 2015. doi: 10.1111/jmg.12119.

S.-L. Hwang, P. Shen, H.-T. Chu, T.-F. Yui, Y. Iizuka, and H.-P. Schertl. Rutile inclusions in garnet from a dissolution-reprecipitation mechanism. *Journal of Metamorphic Geology*, 37(8):1079–1098, 2019. doi: 10.1111/jmg.12502.

L. Jin, C.-L. Jia, I. Lindfors-Vrejoiu, X. Zhong, H. Du, and R. E. Dunin-Borkowski. Direct demonstration of a magnetic dead layer resulting from a-site cation inhomogeneity in a (la, sr) mno3 epitaxial film system. *Advanced materials interfaces*, 3(18):1600414, 2016. doi: 10.1002/admi.201600414.

J. A. Karson, R. M. Lawrence, et al. Tectonic setting of serpentinite exposures on the western median valley wall of the MARK area in the vicinity of Site 920. In *PROCEEDINGS-OCEAN DRILLING PROGRAM SCIENTIFIC RESULTS*, pages 5–22. National Science Foundation, 1997.

D. V. Kent, B. Honnorez, N. D. Opdyke, and P. J. Fox. Magnetic properties of dredged oceanic gabbros and the source of marine magnetic anomalies. *Geophysical Journal International*, 55(3):513–537, 1978. doi: 10.1111/j.1365-246X.1978.tb05925.x.

J. Knafelc, J. Filiberto, E. C. Ferré, J. A. Conder, L. Costello, J. R. Crandall, M. D. Dyar, S. A. Friedman, D. R. Hummer, and S. P. Schwenzer. The effect of oxidation on the mineralogy and magnetic properties of olivine. *American Mineralogist: Journal of Earth and Planetary Materials*, 104(5):694–702, 2019. doi: 10.2138/am-2019-6829.

C. T. Koch. *Determination of core structure periodicity and point defect density along dislocations*. Arizona State University, 2002.

T. Kogure and E. Okunishi. Cs-corrected haadf–stem imaging of silicate minerals. *Journal of Electron Microscopy*, 59(4):263–271, 2010. doi: 10.1093/jmicro/dfq003.

O. Krivanek, N. Dellby, and A. Lupini. Towards sub-Å electron beams. *Ultramicroscopy*, 78(1):1–11, 1999. ISSN 0304-3991. doi: https://doi.org/10.1016/S0304-3991(99)00013-3.

I. Lazić, E. G. Bosch, and S. Lazar. Phase contrast stem for thin samples: Integrated differential phase contrast. *Ultramicroscopy*, 160:265–280, 2016. ISSN 0304-3991. doi: https://doi.org/10.1016/j.ultramic.2015.10.011.

C. Li, T. Griffiths, T. Pennycook, C. Mangler, P. Jeřábek, J. Meyer, G. Habler, and R. Abart. The structure of a propagating mgal2o4/mgo interface: linked atomic-and μm-scale mechanisms of interface motion. *Philosophical Magazine*, 96(23):2488–2503, 2016. doi: 10.1080/14786435.2016.1205233.

C. Luo and G. Weatherly. The interphase boundary structure of precipitates in a ni-cr alloy. *Philosophical Magazine A*, 58(3):445–462, 1988. doi: 10.1080/01418618808210423.

C. J. MacLeod, R. Searle, B. Murton, J. Casey, C. Mallows, S. Unsworth, K. Achenbach, and M. Harris. Life cycle of oceanic core complexes. *Earth and Planetary Science Letters*, 287(3-4):333–344, 2009. doi: 10.1016/j.epsl.2009.08.016.

E. S. Nikolaisen, R. Harrison, K. Fabian, N. Church, S. A. McEnroe, B. E. Sørensen, and C. Tegner. Hysteresis parameters and magnetic anisotropy of silicate-hosted magnetite exsolutions. *Geophysical Journal International*, 229(3):1695–1717, 2022. doi: 10.1093/gji/ggac007.

H. Ondréas, M. Cannat, Y. Fouquet, and A. Normand. Geological context and vents morphology of the ultramafic-hosted Ashadze hydrothermal areas (Mid-Atlantic Ridge 13° N). *Geochemistry, Geophysics, Geosystems*, 13(11), 2012. doi: 10.1029/2012GC004433.

S. J. Pennycook. The impact of stem aberration correction on materials science. *Ultramicroscopy*, 180:22–33, 2017. ISSN 0304-3991. doi: https://doi.org/10.1016/j.ultramic.2017.03.020. URL `https://www.sciencedirect.com/science/article/pii/S0304399117301213`. Ondrej Krivanek: A research life in EELS and aberration corrected STEM.

A. Pertsev, N. Bortnikov, E. Vlasov, V. Beltenev, I. Dobretsova, and O. Ageeva. Recent massive sulfide deposits of the semenov ore district, Mid-Atlantic Ridge, 13° 31 N: Associated rocks of the oceanic core complex and their hydrothermal alteration. *Geology of Ore Deposits*, 54(5):334–346, 2012. doi: 10.1134/S1075701512050030.

A. N. Pertsev, L. Y. Aranovich, V. Y. Prokofiev, N. S. Bortnikov, A. Cipriani, S. S. Simakin, and S. E. Borisovskiy. Signatures of residual melts, magmatic and seawater-derived fluids in oceanic lower-crust gabbro from the vema lithospheric section, central atlantic. *Journal of Petrology*, 56(6):1069–1088, 2015. doi: 10.1093/petrology/egv028.

A. Proyer, G. Habler, R. Abart, R. Wirth, K. Krenn, and G. Hoinkes. Tio 2 exsolution from garnet by open-system precipitation: evidence from crystallographic and shape preferred orientation of rutile inclusions. *Contributions to Mineralogy and Petrology*, 166:211–234, 2013. doi: 10.1007/s00410-013-0872-7.

P. R. Renne, G. R. Scott, J. M. Glen, and J. M. Feinberg. Oriented inclusions of magnetite in clinopyroxene: Source of stable remanent magnetization in gabbros of the Messum Complex, Namibia. *Geochemistry, Geophysics, Geosystems*, 3(12):1–11, 2002. doi: 10.1029/2002GC000319.

P. Robinson, H. W. Jaffe, M. Ross, and C. Klein Jr. Orientation of exsolution lamellae in clinopyroxenes and clinoamphiboles: consideration of optimal phase boundaries. *American Mineralogist: Journal of Earth and Planetary Materials*, 56(5-6):909–939, 1971.

P. A. Selkin, J. S. Gee, and W. P. Meurer. Magnetic anisotropy as a tracer of crystal accumulation and transport, middle banded series, stillwater complex, montana. *Tectonophysics*, 629:123–137, 2014. doi: /10.1016/j.tecto.2014.03.028.

Z.-Z. Shi, F.-Z. Dai, M. Zhang, X.-F. Gu, and W.-Z. Zhang. Secondary coincidence site lattice model for truncated triangular β-Mg2Sn precipitates in a Mg-Sn-based alloy. *Metallurgical and Materials Transactions A*, 44(6):2478–2486, 2013. doi: 10.1007/s11661-013-1633-y.

Z.-Z. Shi, H.-T. Chen, K. Zhang, F.-Z. Dai, and X.-F. Liu. Crystallography of precipitates in Mg alloys. *Journal of Magnesium and Alloys*, 9(2):416–431, 2021. doi: 10.1016/j.jma.2020.06.013.

P. Sobolev. Orientation of acicular iron-ore mineral inclusions in plagioclase. *International Geology Review*, 32(6):616–628, 1990.

A. Sutton and R. Balluffi. *Interfaces in Crystalline Materials*. Clarendon Press, Oxford, 1995.

W. Tan, P. Liu, H. He, C. Y. Wang, and X. Liang. Mineralogy and Origin of Exsolution in Ti-rich Magnetite from Different Magmatic Fe-ti Oxide-bearing Intrusions. *The Canadian Mineralogist*, 54(3):539–553, 05 2016. ISSN 0008-4476. doi: 10.3749/canmin.1400069.

Y. Usui, T. Shibuya, Y. Sawaki, and T. Komiya. Rock magnetism of tiny exsolved magnetite in plagioclase from a paleoarchean granitoid in the pilbara craton. *Geochemistry, Geophysics, Geosystems*, 16(1):112–125, 2015. doi: https://doi.org/10.1002/2014GC005508.

L. R. Wager and R. Mitchell. The distribution of trace elements during strong fractionation of basic magma—a further study of the skaergaard intrusion, east greenland. *Geochimica et Cosmochimica Acta*, 1(3):129–208, 1951. doi: 10.1016/0016-7037(51)90016-6.

H. Wenk, W. Joswig, T. Tagai, M. Korekawa, and B. K. Smith. The average structure of An 62–66 labradorite. *American Mineralogist*, 65(1-2):81–95, 1980.

H.-R. Wenk, K. Chen, and R. Smith. Morphology and microstructure of magnetite and ilmenite inclusions in plagioclase from Adirondack anorthositic gneiss. *American Mineralogist*, 96(8-9):1316–1324, 08 2011. ISSN 0003-004X. doi: 10.2138/am.2011.3760.

F. Ye and W.-Z. Zhang. Coincidence structures of interfacial steps and secondary misfit dislocations in the habit plane between Widmanstätten cementite and austenite. *Acta materialia*, 50(11):2761–2777, 2002. doi: 10.1016/S1359-6454(02)00077-0.

E. Yücelen, I. Lazić, and E. Bosch. Phase contrast scanning transmission electron microscopy imaging of light and heavy atoms at the limit of contrast and resolution. *Scientific Report*, 8:2676, 2018. doi: https://doi.org/10.1038/s41598-018-20377-2.

W.-Z. Zhang. Reproducible orientation relationships developed from phase transformations—role of interfaces. *Crystals*, 10(11):1042, 2020. doi: 10.3390/cryst10111042.

W.-Z. Zhang and G. Purdy. O-lattice analyses of interfacial misfit. i. general considerations. *Philosophical Magazine A*, 68(2):279–290, 1993. doi: 10.1080/01418619308221205.

W.-Z. Zhang and G. Weatherly. On the crystallography of precipitation. *Progress in materials science*, 50(2): 181–292, 2005. doi: 10.1016/j.pmatsci.2004.04.002.

W.-Z. Zhang and X.-P. Yang. Identification of singular interfaces with δgs and its basis of the o-lattice. *Journal of materials science*, 46(12):4135–4156, 2011. doi: 10.1007/s10853-011-5431-x.

Supplementary Information

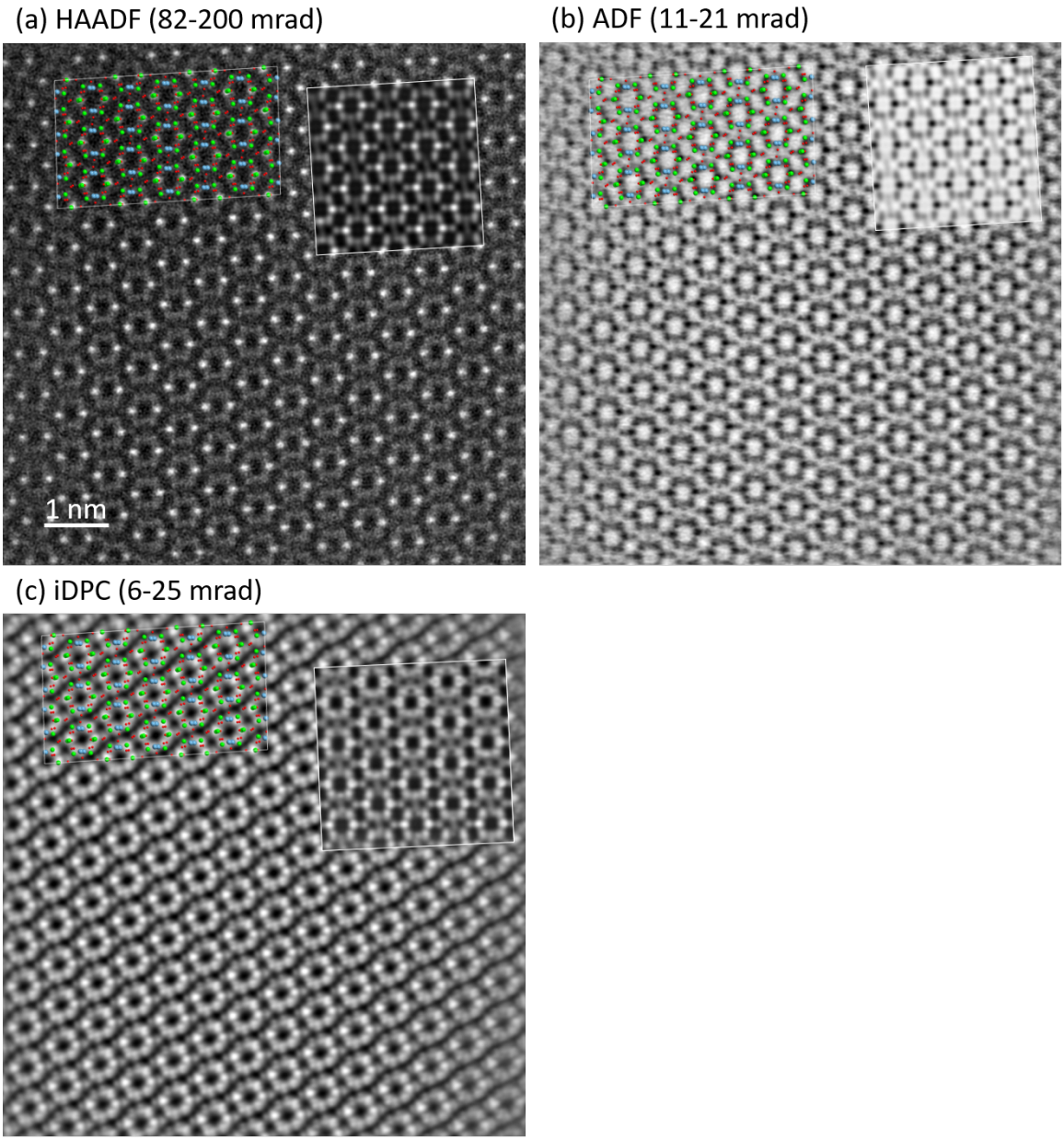

Figure S4.1: (a) High angle annular dark field (HAADF), (b) annular dark field (ADF) with collection angles 11-21 mrad, (c) integrated differential phase contrast (iDPC) with collection angles 6-25 mrad scanning electron transmission electron microscopy (STEM) of plagioclase along PL[001]. The crystal structure of plagioclase is superimposed on top of each acquisition according to the atomic column correspondence. The corresponding simulated images are shown as insets in the top right corner.

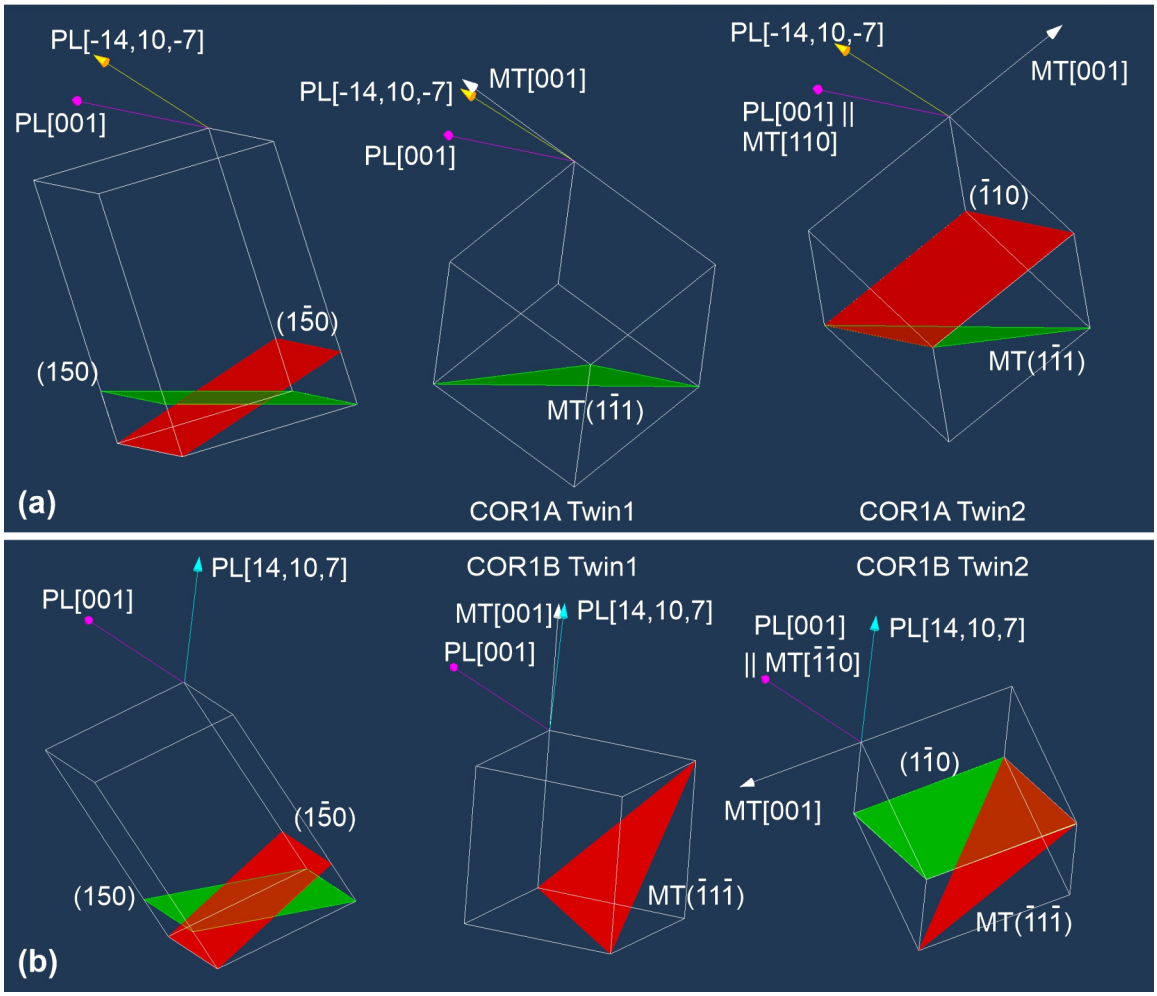

Figure S4.2: (a) COR1A between plagioclase and magnetite unit cells. PL[001], PL[-14,10,-7], PL(150) and PL(1$\bar{5}$0) are shown in the plagioclase unit cell. Magnetite unit cell COR1A twin 1 shows correspondence between PL[001] || MT[$\bar{1}\bar{1}$0], PL(150) || MT(1$\bar{1}$1) and PL[-14,10,-7] || MT[001] with a small deviation. Magnetite unit cell COR1A twin 2 shows correspondence between PL[001] || MT[110], PL(150) || MT(1$\bar{1}$1) and PL(1$\bar{5}$0) || MT($\bar{1}$10). (b) COR1B between plagioclase and magnetite unit cells. PL[001], PL[14,10,7], PL(150) and PL(1$\bar{5}$0) are shown in the plagioclase unit cell. Magnetite unit cell COR1B twin 1 shows correspondence between PL[001] || [110], PL(1$\bar{5}$0) || MT($\bar{1}$1$\bar{1}$) and PL[14,10,7] || MT[001] with a small deviation. Magnetite unit cell COR1B twin 2 shows correspondence between PL[001] || MT[$\bar{1}\bar{1}$0], PL(1$\bar{5}$0) || MT($\bar{1}$1$\bar{1}$) and PL(150) || MT(1$\bar{1}$0).

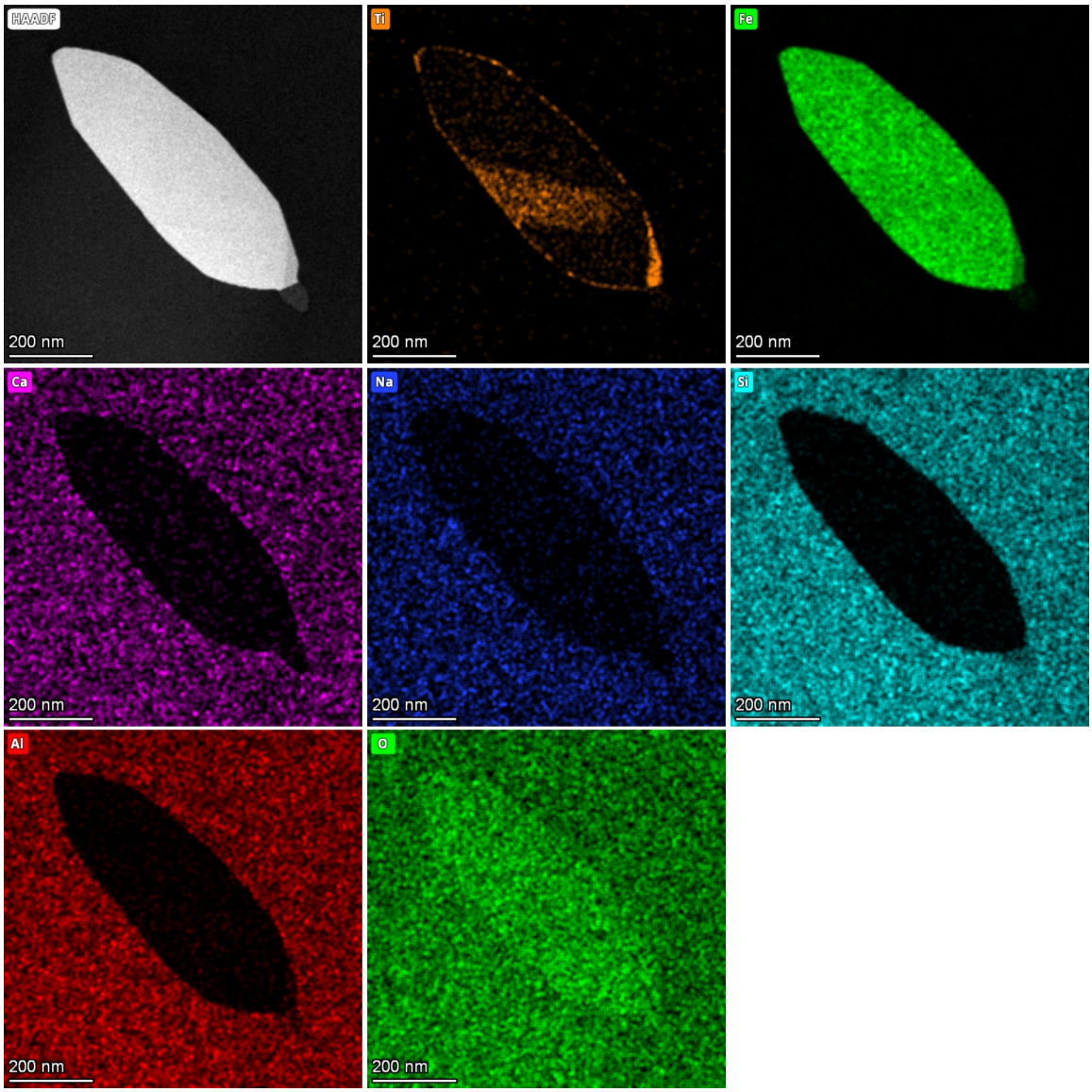

Figure S4.3: STEM-EDS elemental distribution maps of the cross-section of a COR1A PL[001]-MT micro-inclusion in main orientation. The inclusion is magnetite containing a Ti-rich phase in the central area. The second phase is most likely ulvospinel according to the cubic symmetry. A Ti-rich rim is observed along the magnetite-plagioclase interface.

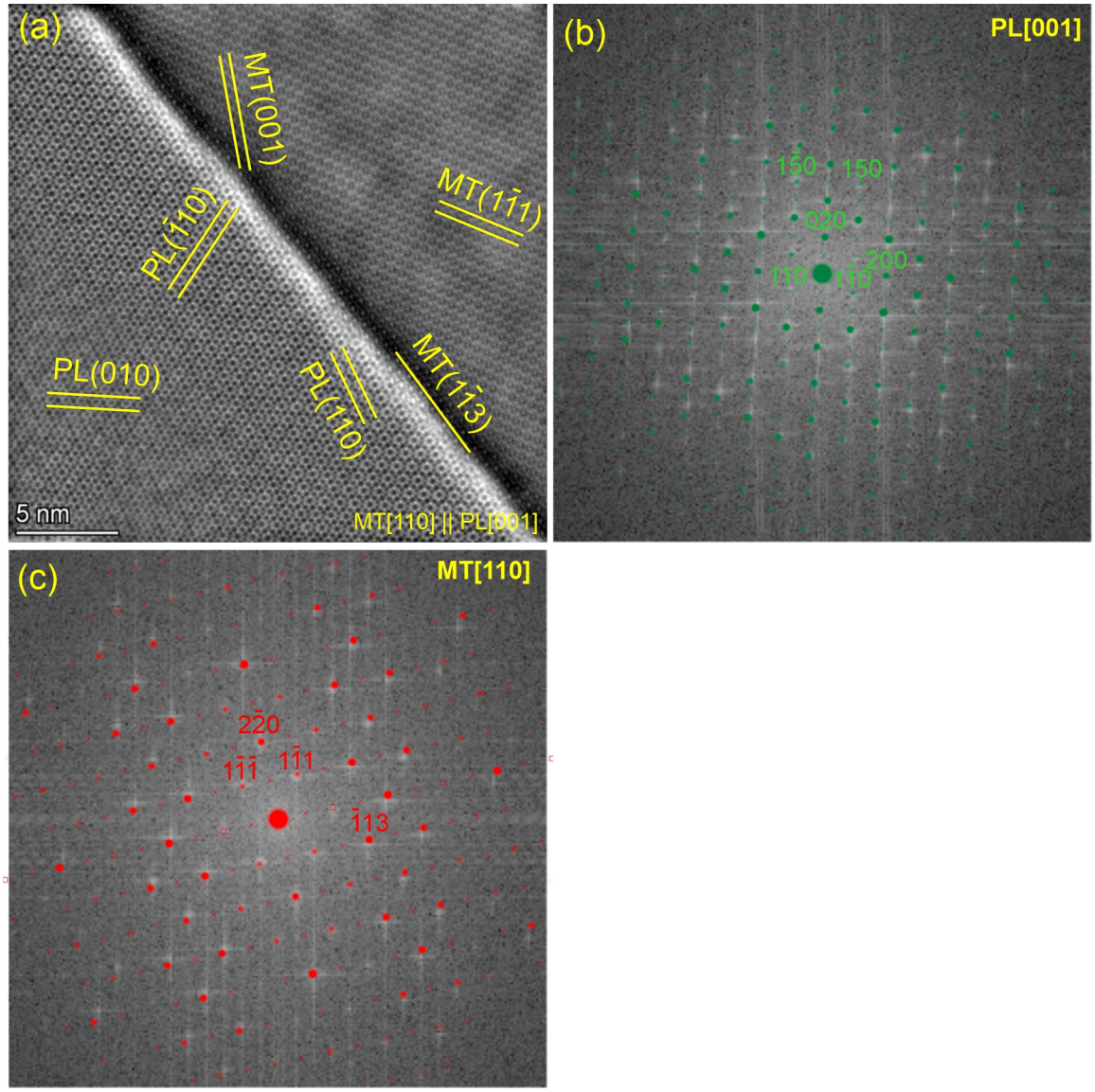

Figure S4.4: (a) iDPC-STEM image of an interface segment of the magnetite-plagioclase interface of a COR1A PL[001]-MT micro-inclusion in main orientation. Viewing direction is MT[110] || PL[001]. Lattice fringes in magnetite and in plagioclase are highlighted and indexed. (b) Fast Fourier transformation (FFT) of the plagioclase area in (a). The simulated diffraction pattern of plagioclase (green dots) according to the orientation in (a) is superimposed. Representative diffraction spots representing the lattice planes in plagioclase in reciprocal space are indexed with green Miller indices nearby. (c) FFT of the magnetite area in (a). Simulated diffraction pattern of magnetite (red dots) according to the orientation in (a) is superimposed. Representative diffraction spots representing the lattice planes in magnetite in reciprocal space are indexed with red Miller indices nearby.

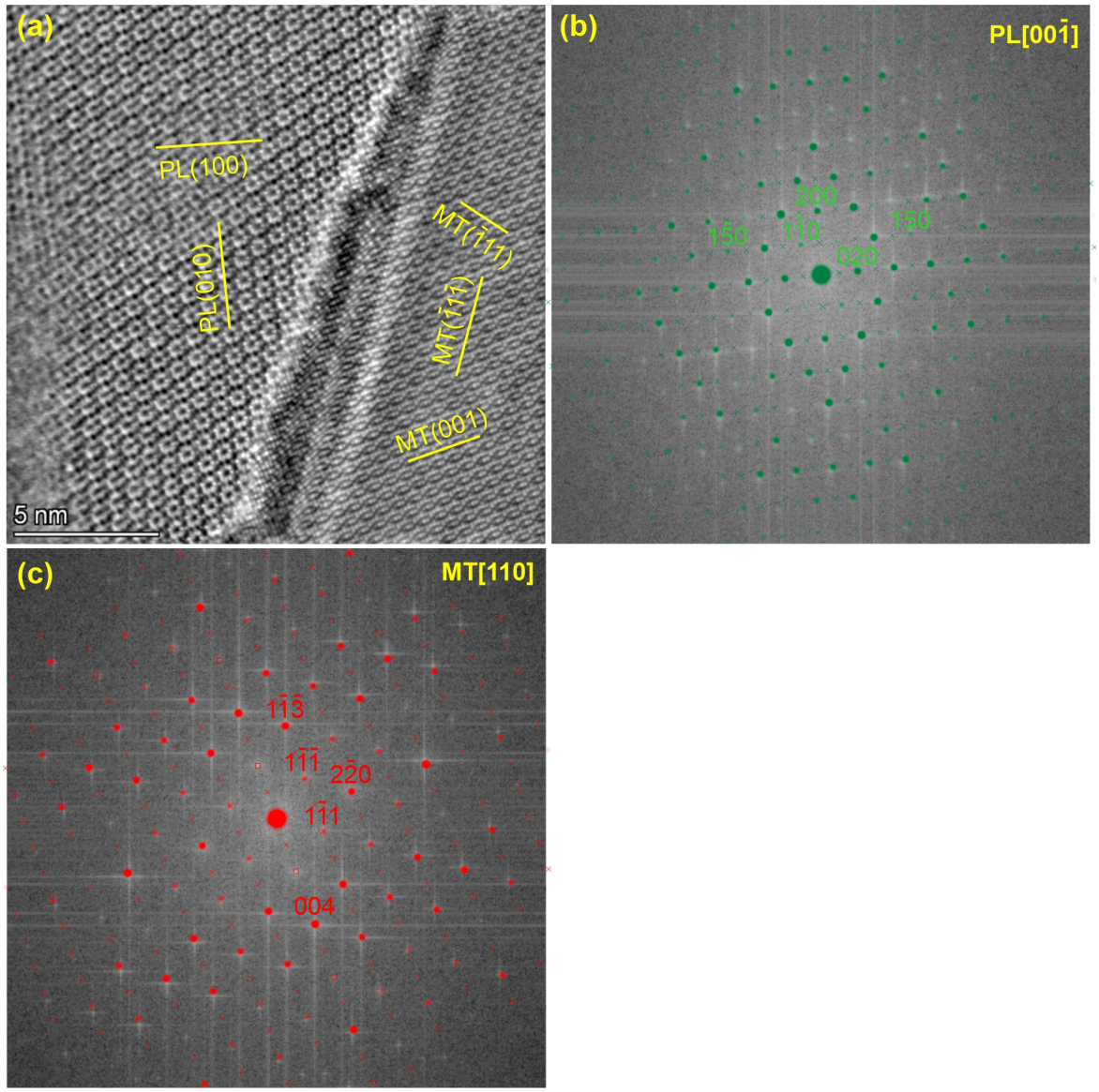

Figure S4.5: (a) iDPC-STEM of an interface segment of the magnetite-plagioclase interface of a COR1B PL[001]-MT micro-inclusion in main orientation. Viewing direction is MT[110] ‖ PL[00$\bar{1}$]. Lattice fringes in magnetite and in plagioclase are highlighted and indexed. (b) Fast Fourier transformation (FFT) of the plagioclase area in (a). Simulated diffraction pattern of plagioclase (green dots) according to the orientation in (a) is superimposed. Representative diffraction spots representing the lattice planes in plagioclase in reciprocal space are indexed with green Miller indices nearby, (c) FFT of the magnetite area in (a). Simulated diffraction pattern of magnetite (red dots) according to the orientation in (a) is superimposed. Representative diffraction spots representing the lattice planes in magnetite in reciprocal space are indexed with red Miller indices nearby.

Chapter 5

Concluding Discussion

5.1 Plane normal type magnetite micro-inclusions

5.1.1 Definition

Oriented needle-, lath- and plate shaped magnetite (MT) micro-inclusions in rock-forming plagioclase (PL) from oceanic gabbro dredged at the mid-Atlantic ridge at 13° 01–02' N, 44° 52' W were investigated. The magnetite micro-inclusions in the plagioclase host crystals have been classified into eight shape orientation relationships (SORs). Two fundamental types of the magnetite micro-inclusions are classified according to the shape and crystallographic correspondences between magnetite and plagioclase: the plane normal type and the PL[001] type. The needle shaped magnetite micro-inclusions of the plane normal type are elongated parallel to one of their MT⟨111⟩ directions, which, in turn, is perpendicular to one of seven specific plagioclase lattice planes including PL(112), PL($\bar{3}$12), PL(150), PL(1$\bar{5}$0), PL(100), PL(1$\bar{1}$2) and PL($\bar{3}\bar{1}$2) defining seven orientation classes. The inclusions elongation direction and shape orientations confer to the parallel alignment of the MT{222} lattice planes with either one of these specific lattice planes of plagioclase. Therefore, for each SOR class the inclusions are named after PL(*hkl*)n-MT, where PL(*hkl*) denotes the specific lattice planes of plagioclase and "n" refers to the plane normal direction. The inclusions of plane normal type are usually distributed in the central and pristine zones of plagioclase grains. The magnetite grains may be accompanied by subordinate ortho and/or clinopyroxene giving rise to composite inclusions. Within the magnetite micro-inclusions, ilmenite (ILM) lamellae that oriented along MT{111} ‖ ILM(0001) are often observed.

5.1.2 Origin

The formation of plane normal type magnetite micro-inclusions is probably due to the exsolution from a Fe-bearing plagioclase. The systematic shape and crystallographic orientation relationships (CORs) between

magnetite and plagioclase exclude the possibility that magnetite grains crystallised from parental magma and were oriented by physical contact with growth facets of plagioclase and subsequently overgrown by plagioclase, a process known as synneusis. Based on mass balance considerations, exsolution from Fe-bearing plagioclase requires partial reduction of the ferric iron originally contained in the plagioclase and necessitates extraction of oxygen from the plagioclase. The reducing environment probably prevailed during interaction with reducing fluids from the serpentinization of associated ultramafic rocks. Reducing fluids drove the out-diffusion of oxygen from the plagioclase grains. The shape and crystallographic orientation relationships between the magnetite micro-inclusions and the plagioclase host follow the plagioclase lattice orientations in different plagioclase twin domains indicating that the inclusions were formed synchronous to or after twinning. This evidence rules out the hypothesis that magnetite grains nucleated and grew on the surface of growing plagioclase grains and were engulfed by rapidly growing plagioclase grains. The presence of up to about 15 vol% of oriented, relatively coarse ilmenite lamellae within the plane normal type magnetite micro-inclusions indicates oxidation-exsolution or direct exsolution from Ti-rich magnetite at temperatures $\geq$ 600 °C (Tan et al., 2016). This is above the Curie temperature of magnetite implying that the magnetic signatures of the magnetite-bearing plagioclase grains represent thermoremanent magnetization.

5.1.3 SORs and CORs

The crystallographic basis of the shape and crystallographic orientation relationships between needle-, lath- and plate shaped magnetite micro-inclusions and the plagioclase host was investigated using correlated optical and scanning transmission electron microscopy. The elongation directions of needle- and lath shaped magnetite micro-inclusions are ascribed to the good match between oxygen layers in the magnetite and plagioclase crystal structures across magnetite-plagioclase interfaces bounding the magnetite inclusions (Ageeva et al., 2020). In the magnetite crystal structure, MT{222} lattice planes are close packed oxygen planes. In plagioclase crystal structure, the aforementioned seven specific lattice planes are parallel to the oxygen layers, where concentrations of oxygen atoms in the plagioclase crystal structure form roughly planar, several atomic layer thick configurations. For a needle shaped PL(112)n-MT micro-inclusion, the elongation direction is parallel to one of the MT$\langle 111 \rangle$ || PL(112)n, which also indicates the parallel alignment between one of the MT{222} || PL(112) lattice planes. Moreover, the *d*-spacings of MT{222} and of PL(112) are comparable. The lattice misfit between the two lattice planes is 1.6%, which indicates that a misfit dislocation is required at every 63rd MT{222} lattice plane. The presence of the misfit dislocation has been validated by inverse fast Fourier transformation (iFFT) on the magnetite-plagioclase interface

scanning transmission electron microscopy (STEM) images along the inclusion elongation direction, as shown in Chapter 3 Fig. 3.6.

For each SOR class, specific COR variants characterised by at least one additional parallel alignment of crystallographic planes or directions between magnetite and plagioclase are observed. When the additional alignment is PL[14,10,7] or PL[14,-10,7] || one of the MT⟨100⟩, the inclusion is classified as being in nucleation orientation, where FeO_6 octahedra of magnetite fit into channels parallel to PL[001] in the crystal structure of plagioclase in a favourable manner. The inclusions in nucleation orientation typically show exact alignment of their elongation direction to the respective plane-normal direction. If, in addition to the MT{111} || PL(*hkl*) alignment, one of the MT{220} lattice planes is parallel to another one of the specific plagioclase lattice planes, the inclusion is classified as being in main orientation. The elongation direction of the plane normal magnetite micro–inclusion in main orientation deviates by up to about 5° from the respective PL(*hkl*)-n direction.

5.1.4 Interface configurations

The magnetite-plagioclase interfaces of the selected magnetite micro-inclusions including inclusions in nucleation and in main orientations were investigated using state-of-the-art STEM. The STEM specimens were prepared using FIB technique to ensure each specimen containing magnetite-plagioclase interfaces along or perpendicular to the elongation direction of the respective inclusion.

The magnetite-plagioclase interfaces are crystalline, with no amorphous layer or gap between the two phases, as shown in Chapter 3 Figs. 3.3-3.7. The cross section of a PL($\bar{3}$12)n-MT inclusion in nucleation orientation has a regular, outward convex shape (Chapter 3 Fig. 3.2). The magnetite-plagioclase interfaces are faceted and differently oriented interface segments have similar proportions. Combining crystallographic analyses based on FFT results obtained from STEM images, the interface facets are mostly parallel to MT{220} lattice planes. According to lattice fringes observed in the STEM images, the magnetite-plagioclase interface facets are mainly controlled by low index lattice planes of magnetite and by the commensurate impingement of low index magnetite and plagioclase lattice planes along the interface (Chapter 3 Fig. 3.3) (Howe et al., 2002).

The cross section of a needle shaped PL($\bar{3}$12)n-MT inclusion in main orientation is close to a rectangular shape with small fractions of re-entrant, while the cross section of a needle shaped PL(112)n-MT inclusion in main orientation has a nearly centro-symmetrical shape and is bounded by a number of differently oriented straight or slightly curved interface segments, which are connected by both outwards convex and outwards concave segments (Chapter 3 Fig. 3.2). Those inclusions that are in main orientations show more

complex cross sections with typically only two facet orientations and otherwise curved, locally re-entrant magnetite-plagioclase interface segments. The facets of magnetite micro-inclusions in main orientation are mainly controlled by the parallel alignment of low index lattice planes of both, magnetite and plagioclase (Chapter 3 Fig. 3.4).

Along the elongation direction of the needle shaped PL(112)n-MT inclusion in main orientation, the preferred growth direction has been attributed to the oxygen layers alignment across the magnetite-plagioclase interface (Ageeva et al., 2020). Moreover, the STEM images presented in Chapter 3 Fig. 3.6 show that the magnetite-plagioclase interface appears parallel to one of the MT{220} || PL($1\bar{5}0$), which is the definition of this SOR class inclusions in main orientation. Thus, the second crystallographic correspondence that defines the inclusion in main orientation also served as a faceted interface that bounded the inclusion to the observed shape. It is worth noting that PL($1\bar{5}0$) is an oxygen layer in the plagioclase crystal structure. A more pronounced effect of this mechanism was observed in a plate shaped PL($\bar{3}12$)n-MT inclusion. From STEM images shown in Chapter 3 Fig. 3.5, the basal plane of the plate shaped inclusion is parallel to one of MT{220} || PL(150), which is the second alignment defining the inclusion in main orientation. PL(150) is also an oxygen layer in plagioclase crystal structure. Hence, the oxygen sub-lattices of magnetite and plagioclase are suggested to be responsible for the preferred orientation relationships as the observed CORs and SORs ensure continuity of the oxygen sub-lattices across the magnetite-plagioclase interfaces. In addition, the observed CORs and SORs minimise the need for rearrangement of oxygen atoms during growth of magnetite inside plagioclase (Hwang et al., 2010).

The morphologies of the magnetite micro-inclusions indicate a potential transformation from nucleation to main orientations in that the inclusions in nucleation orientations usually have regular geometries and the interface facets are dominated by magnetite while the inclusions in main orientations usually have irregular shapes and the interface facets show signs of accommodations between the two phases. This possible transformation is probably driven by the accommodations of magnetite following the oxygen sub-lattice in plagioclase. As a result, the elongation directions of the inclusions in main orientations slightly deviated from the respective PL(*hkl*)n directions. In addition, the polycrystalline ilmenite in the inclusions in main orientation (Chapter 3 Fig. 3.6) may also result from recrystallization of the inclusion from nucleation to main orientations.

5.1.5 Roles in paleomagnetic reconstructions

Due to their small sizes and high aspect ratio, as well as the fact that they were protected by silicate hosts from external alterations, plane normal type magnetite micro-inclusions are ideal recorders of paleomag-

netic signals. The current study confirmed that the inclusions formed at a temperature at least > 600 °C, which is above the Curie temperature of magnetite. Thus, the magnetic records obtained from the plane normal type magnetite micro-inclusions are thermal remanent magnetization, which are regarded as the primary paleomagnetic signals and can be applied for paleomagnetic reconstructions (Ageeva et al., 2022). The evolution of inclusions from nucleation to main orientation may be important in the context of paleomagnetic reconstructions relying on the natural remanent magnetization of single grains of magnetite bearing plagioclase. Oriented magnetite micro-inclusions in plagioclase are common in mafic intrusive rocks from a variety of geological settings. Our findings on the systematics of the magnetite micro-inclusions from ocean floor gabbros are likely transferable to these other occurrences.

5.2 PL[001] type magnetite micro-inclusions

5.2.1 Definition

Magnetite micro-inclusions of the PL[001] type are needle- and lath shaped and have their elongation directions parallel to one of the MT⟨110⟩ directions, which is aligned with the PL[001] direction. PL[001] type inclusions are usually distributed in the rim and altered zones of plagioclase grains. For instance, they are often associated with healed cracks in plagioclase grains (Chapter 4, Fig. 4.1). Moreover, the PL[001] type magnetite micro-inclusions are often accompanied with ulvospinel exsolutions that are oriented along MT{100}.

5.2.2 Origin

Petrographic evidence suggests that the PL[001] magnetite micro-inclusions are of secondary nature and formed later than plane normal type inclusions. PL[001] type micro-inclusions typically occur at the rim zone or the transition zone between pristine and hydrothermally altered zones in plagioclase grain, while the plane normal type inclusions usually are concentrated in the central and pristine zones. The PL[001] type inclusions may be the products of recrystallizations of the plane normal type inclusions. The association of PL[001] type inclusions with healed cracks and rim zones in plagioclase suggests that the recrystallization of the magnetite micro-inclusions occurred during hydrothermal overprint. Moreover, optical microscopy (Chapter 4, Fig. 4.1) revealed that groups of PL[001] magnetite micro-inclusions derived from recrystallization of pre-existing plane normal type inclusions. The temperature when PL[001] type inclusions formed is probably lower than 600 °C in that they formed at a later stage. The ulvospinel exsolutions contained in PL[001] magnetite micro-inclusions further corroborate this hypothesis, as this reaction

happens at temperature < 600 °C.

5.2.3 SOR and CORs

The elongation direction of needle- and lath shaped PL[001] type inclusions is strongly parallel to PL[001] and one of MT[110] directions, which is attributed to the accommodation of the FeO_6 octahedra of the magnetite crystal structure in channels in the plagioclase crystal structure parallel to the PL[001] (Wenk et al., 2011).

Similar to plane normal type inclusions, the PL[001] type inclusions are also found in nucleation and in main orientations. If one of the MT⟨001⟩ directions is parallel to PL[14,10,7], PL[14,-10,7], PL[023] or PL[$0\bar{2}3$], the inclusion is in nucleation orientation. If one of the MT{222} lattice planes is parallel to PL($1\bar{5}0$) or PL(150), the inclusion is in main orientation. The CORs of inclusions in nucleation and in main orientations are related to magnetite spinel twinning (Chapter 4 Table 4.1). In total, six COR variants between PL[001] magnetite micro-inclusions and the plagioclase host have been observed and are related to one another by rational crystallographic operations indicating crystallographic control on the SOR and CORs of the PL[001] magnetite micro-inclusions with the plagioclase host.

5.2.4 Interface configurations

A selected PL[001] type inclusion in main orientation was prepared for STEM study using FIB and the specimen contained the cross section of the inclusion. STEM images show that the inclusions are faceted, where the interface facets are parallel to low index lattice planes in either magnetite or plagioclase, or the interfaces are stepped with the terraces of the steps parallel to low index lattice planes of either magnetite or plagioclase. In this context either a good fit between the oxygen lattices of the two phases or the parallel alignment of oxygen layers in magnetite and plagioclase appears to be the controlling factor (Hwang et al., 2010). IDPC-STEM images also reveal linkup structures between important crystal structure units in plagioclase and in magnetite across the magnetite-plagioclase interfaces. In addition, they reveal accommodation features that shift marginal parts of magnetite grains relative to the bulk precipitate to arrive at a better fit between the two lattices (Chapter 4, Fig. 4.6-4.7). Locally magnetite seems to have lost its structure and potentially was transformed into another phase in the immediate vicinity of the magnetite-plagioclase interface (Chapter 4, Fig. 4.7). The geometry of the accommodation features makes it necessary to invoke re-distribution of Fe and O along the magnetite-plagioclase interface.

The orientation of the interface facets between framework silicate plagioclase and close-packed oxide magnetite can be explained by the $\Delta\mathbf{g}$ method (Hwang et al., 2010). The interface facets are oriented

perpendicular to the $\Delta\mathbf{g}$ vectors that link the $\mathbf{g}$-vectors of low index lattice planes of magnetite and plagioclase in reciprocal space. The orientations of the interface facets only slightly deviate from the orientations of exact phase boundaries, which can be constructed, if one of the lattices is slightly deformed. By this operation a CCSL emerges (Ye and Zhang, 2002; Shi et al., 2013), and exact magnetite-plagioclase phase boundaries parallel to low index lattice planes in the CCSL are obtained. Even if the constrained configuration probably never existed physically, the CCSL lattice and the $\Delta\mathbf{g}$ method applied to the constrained configuration are viable models that explain the selection of interface facets. In the actual configuration the deviation from the exact phase boundaries is small and is accommodated by dislocations.

Overall, the microscopic interface configurations associated with the different orientation and structure variants ensure low energy configurations in microstructural equilibrium and low energy barriers for nucleation and growth of magnetite precipitates in plagioclase (Sutton and Balluffi, 1995).

5.2.5 Roles in paleomagnetic reconstructions

The orientation distribution of different populations of needle shaped magnetite micro-inclusions with different SORs imparts a magnetic anisotropy to the plagioclase host grains, which will contribute to an overall anisotropic susceptibility of remanence of a plagioclase single grain. The transformation of plane normal to PL[001] type magnetite micro-inclusions changes the overall distributions of the needle- and lath shaped magnetite micro-inclusions, and as a result also changes the magnetic anisotropy of magnetite bearing plagioclase. Moreover, the PL[001] type inclusions are expected to be formed at a later stage below 600 °C. The magnetic signals may not be primary TRM. Thus, special attention is needed during the interpretation of single grain magnetic measurements on plagioclase when PL[001] type inclusions are dominant.

Bibliography

O. Ageeva, G. Bian, G. Habler, A. Pertsev, and R. Abart. Crystallographic and shape orientations of magnetite micro-inclusions in plagioclase. *Contributions to Mineralogy and Petrology*, 175(10):1–16, 2020. doi: 10.1007/s00410-020-01735-8.

O. Ageeva, G. Habler, S. A. Gilder, R. Schuster, A. Pertsev, O. Pilipenko, G. Bian, and R. Abart. Oriented magnetite inclusions in plagioclase: Implications for the anisotropy of magnetic remanence. *Geochemistry, Geophysics, Geosystems*, page e2021GC010272, 2022. doi: 10.1029/2021GC010272.

J. M. Howe, W. T. Reynolds, and V. K. Vasudevan. Static and in-situ high-resolution transmission electron microscopy investigations of the atomic structure and dynamics of massive transformation interfaces in a Ti-Al alloy. *Metallurgical and Materials Transactions A*, 33(8):2391–2411, 2002. doi: 10.1007/s11661-002-0362-4.

S.-L. Hwang, P. Shen, T.-F. Yui, and H.-T. Chu. On the coherency-controlled growth habit of precipitates in minerals. *Journal of Applied Crystallography*, 43(3):417–428, 2010. doi: 10.1107/S0021889810007454.

Z.-Z. Shi, F.-Z. Dai, M. Zhang, X.-F. Gu, and W.-Z. Zhang. Secondary coincidence site lattice model for truncated triangular β-Mg2Sn precipitates in a Mg-Sn-based alloy. *Metallurgical and Materials Transactions A*, 44(6):2478–2486, 2013. doi: 10.1007/s11661-013-1633-y.

A. Sutton and R. Balluffi. *Interfaces in Crystalline Materials*. Clarendon Press, Oxford, 1995.

W. Tan, P. Liu, H. He, C. Y. Wang, and X. Liang. Mineralogy and Origin of Exsolution in Ti-rich Magnetite from Different Magmatic Fe-ti Oxide-bearing Intrusions. *The Canadian Mineralogist*, 54(3):539–553, 05 2016. ISSN 0008-4476. doi: 10.3749/canmin.1400069.

H.-R. Wenk, K. Chen, and R. Smith. Morphology and microstructure of magnetite and ilmenite inclusions in plagioclase from Adirondack anorthositic gneiss. *American Mineralogist*, 96(8-9):1316–1324, 08 2011. ISSN 0003-004X. doi: 10.2138/am.2011.3760.

F. Ye and W.-Z. Zhang. Coincidence structures of interfacial steps and secondary misfit dislocations in the habit plane between Widmanstätten cementite and austenite. *Acta materialia*, 50(11):2761–2777, 2002. doi: 10.1016/S1359-6454(02)00077-0.

Appendix A

Distributions of the magnetite micro-inclusions in plagioclase

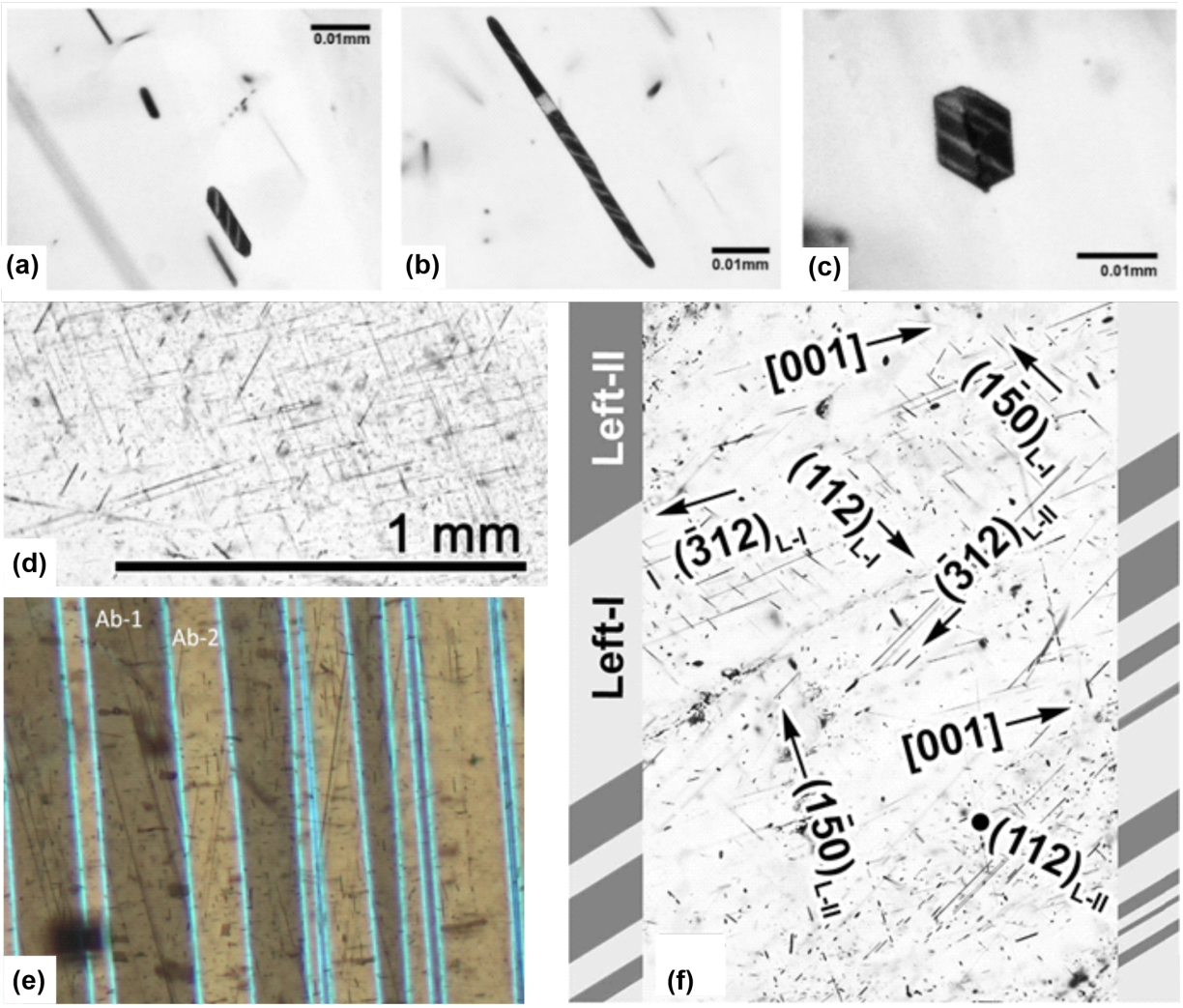

Figure A.1: Optical images of plagioclase-host magnetite inclusions; (a)-(c) Morphologies of magnetite inclusions; (d) Overview of image; (e) Albite twinned plagioclase with magnetite micro-inclusions; (f) SORs of magnetite inclusions in different plagioclase twin domains.

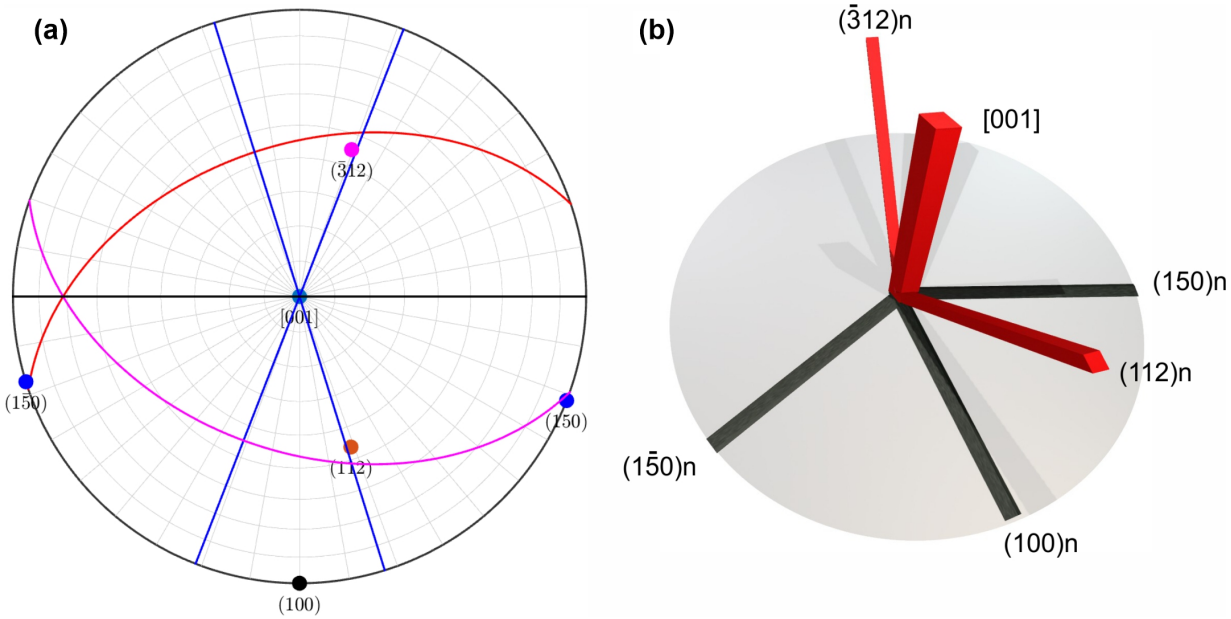

Figure A.2: (a) Poles of needle elongation direction of six orientation classes of plagioclase-host magnetite inclusions in stereographic projection; (b) schematic illustration of corresponding magnetite needles.

Appendix B

(S)TEM specimens preparation

B.1 No. 277-10-d21

This specimen contains cross sections of needle-shaped PL($\bar{3}$12)n-MT inclusion in main and nucleation orientation, and was studied in Chapter 3.

B.1.1 Foil description

Notation

277-10 is the serial number of the thin section, d21 denotes domain 21.

Preparation

FEI Quanta 3D FEG-SEM with focused ion beam (FIB) application

Dimension

The foil area is about 15×15 μm. The area of the thinned window is about 4×6 μm, the thickness is about 45-55 nm, as shown in Figure B.1a. The foil is seriously bent, as shown in Figure B.1b. For clarification, in the text the upper side of the foil means the side near Pt-layer, the front side of the foil means the viewing direction is in front of the grid with the letters appear properly, and the back side of the foil means the viewing direction is perpendicular to the grid with the letters appear mirrored.

Location of the Foil on the Mo grid

The foil is mounted on the central pin of the Mo grid, and it is facing towards pin C, as shown in Figure B.2a. This TEM foil is stored in the centre of the blue rubber pad for transportation.

B.1.2 Micro-inclusion description

In the thin area this foil contains two magnetite (MT) micro-inclusions in cross section. From the SE image in Figure B.1a the two micro-inclusions show differently shaped cross sections. The matrix surrounding the two micro-inclusions is plagioclase (PL), which is known to be beam-sensitive.

The foil is prepared to show the two micro-inclusions in cross section. The viewing direction is along the PL(-312)-normal and one of the MT⟨111⟩ directions. The viewing direction also corresponds to the elongation direction of the micro-inclusions. The micro-inclusion located in the upper part of the foil (near the Pt layer) corresponds to the so called “main orientation” in the sense of Ageeva et al. (2020), and the lower one corresponds to the so called “nucleation orientation”. Both micro-inclusions are elongated along the same crystallographic directions of PL and MT, but their lattices are rotated with respect to one-another

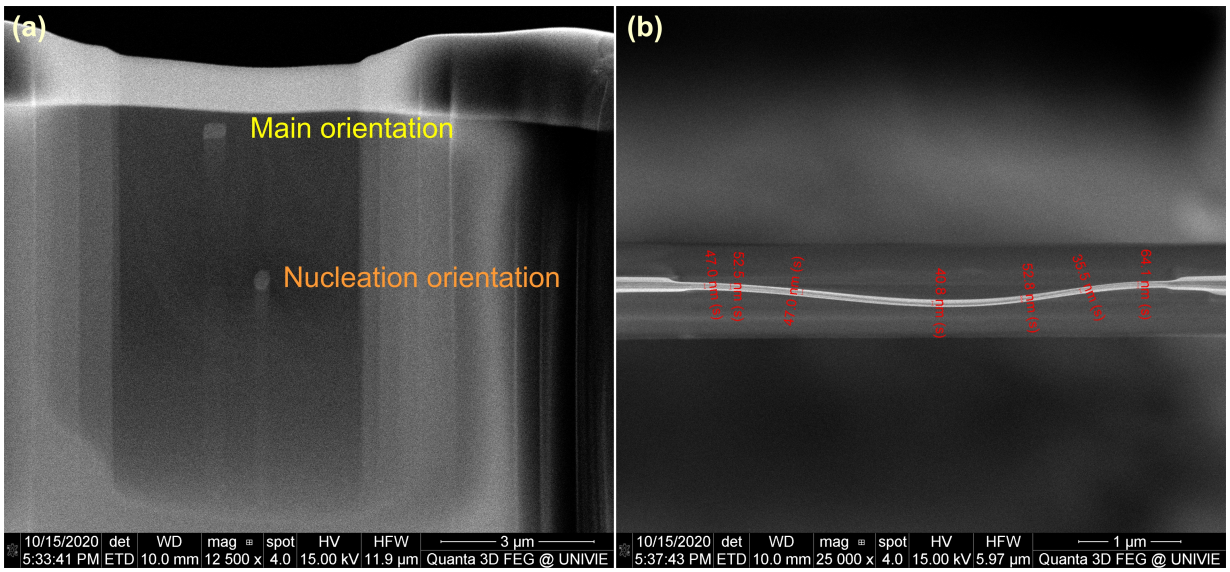

Figure B.1: FIB foil containing needle-shaped PL($\bar{3}$12)n-MT inclusion in main and nucleation orientation (studied in Chapter 3). (a) Back side of the TEM foil with pin B on the right side (not shown). The micro-inclusion with main orientation is seen in the upper part of the foil and has a rectangular shape; while the micro-inclusion with nucleation orientation is seen in the lower part of the foil and has a near hexagonal shape. (b) TEM foil view from the upper side of the foil with pin B on the right side (not shown). The bending of the foil can be seen. The thickness of the thin area is approximately 45-55 nm.

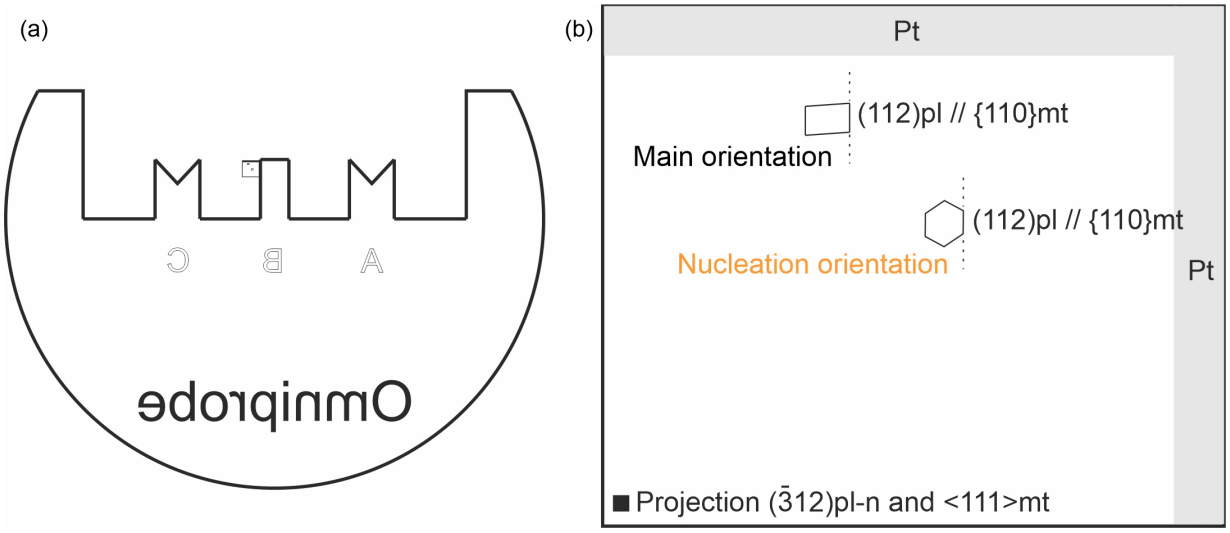

Figure B.2: Sketch of the FIB foil containing needle-shaped PL($\bar{3}$12)n-MT inclusion in main and nucleation orientation (studied in Chapter 3). (a) Sketch of the location of the foil on the Mo grid; (b) sketch of the foil and the micro-inclusions information viewed from the back side of the Mo grid (compare Fig. B.1a). Here (*hkl*)pl-n represents the normal of the plagioclase plane (*hkl*).

around the needle elongation direction and they have different facets. All facets are edge on in the TEM foil.

From the SE image shown in Figure B.1a, the micro-inclusion with main orientation shows a rectangular cross section, while the micro-inclusion with nucleation orientation shows a near hexagonal cross section. Combining the EBSD data shown in Figure B.3b and c and the simulation of the diffraction patterns using CrystalMaker (Figure B.4), we infer that for both micro-inclusions some sections of the MT-PL interfaces correspond to the one of the MT{110} and PL(112) lattice planes (see Figure B.2b). Both lattice planes are expected to be perpendicular to the plane of the foil, and are perpendicular to the horizontal direction in the foil.

For both, the micro-inclusions with main orientation and nucleation orientation, there are other interface segments that still need to be defined. We would like to obtain structural information from these facets

using STEM. We are interested in unravelling to what extent these interfaces are coherent and what kind of misfits or steps are present at the interfaces for the two phases with different orientation relationships.

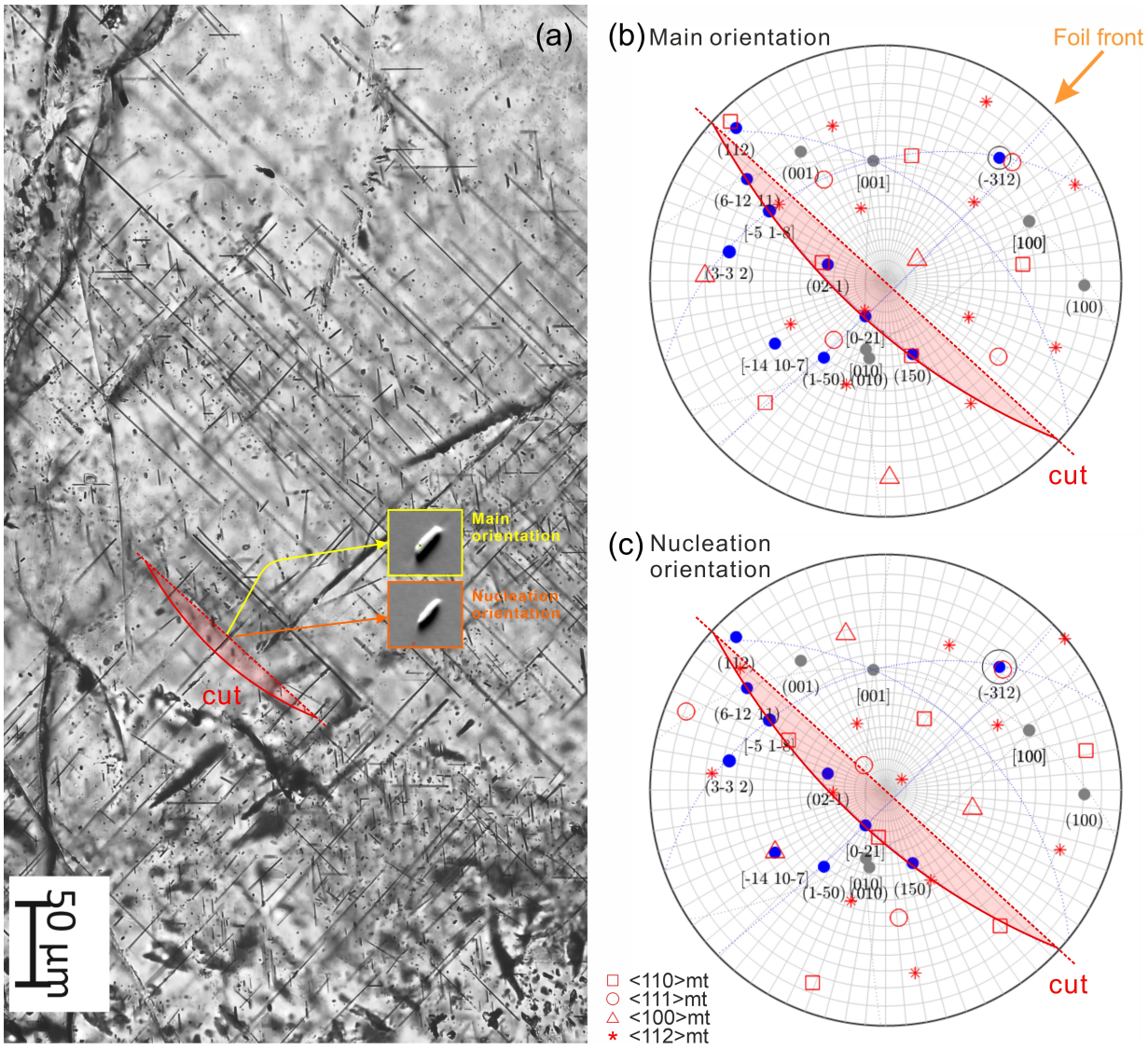

Figure B.3: (a) Transmitted light optical image of domain 21 in thin section 277-10. (b), (c) Stereographic projections (upper hemisphere) showing the poles of important lattice planes for the main orientation and for the nucleation orientation of the micro-inclusions, respectively. The red symbols indicate the poles of MT crystallographic directions, while the blue dots correspond to important planes and directions of PL, and the grey dots are the lattice plane and directions of the PL unit cell. For the micro-inclusion in main orientation the pole of PL(-312) nearly coincides with MT⟨111⟩ with a deviation of about 4°. For the nucleation orientation the pole of PL(-312) is almost coincident with MT⟨111⟩. Regarding facets: The pole of PL(112) coincides with MT⟨011⟩ in main orientation. Further orientation relationships need to be specified with higher resolution images and SAED data (studied in Chapter 3).

B.1.3 Task list

1. SAED for magnetite-plagioclase around the cross sections for both micro-inclusions. The foil is prepared to be under the projection PL(-312)-normal and MT[111]. However, the foil is bent so tilt under the TEM may be required.
   When PL and MT can't be aligned simultaneously in the suggested zone axes, separate SAED of different areas may be required; if the diffraction pattern of PL is hard to see under this projection, finding a nearby PL projection is also plausible.

2. Bright field and dark field images of the morphology of the two micro-inclusions and the host plagioclase, and the interfaces between the two phases around the cross sections.

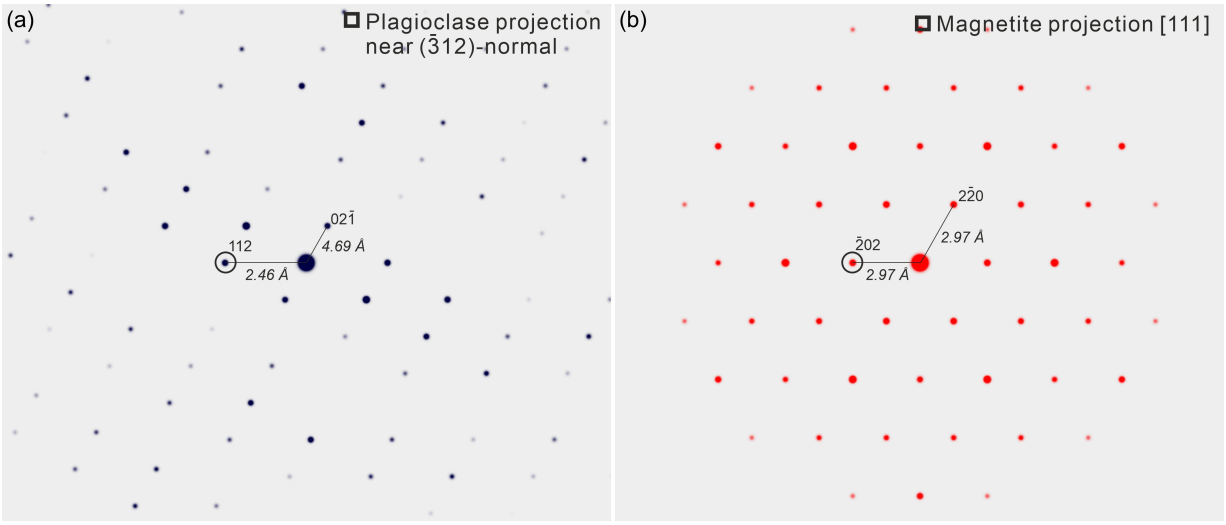

Figure B.4: Simulated diffraction patterns of main orientation with the viewing direction perpendicular to the foil, which is (a) nearly parallel to the PL(-312)-normal and to the (b) MT[111] direction. The expected facet between PL and MT lattice planes is indicated by solid circles, which is PL(112) and MT(-202), as the vertical boundary of the cross sections shown in Figure 1a. The d-spacing of each lattice plane in the real space is indicated.

3. Scanning TEM (STEM) with high-angle annular dark-field (HAADF) and annular bright-field (ABF) detectors for obtaining direct structure and composition information of the host-inclusion interfaces at the atomic scale.

4. Ptychography with in focus STEM probe and a convergent-beam electron diffraction (CBED) direct detection camera with simultaneous Z-contrast imaging as the most advanced method for the atomic scale characterization of the host-inclusion interfaces.

B.1.4 Expected results

1. In the SAED around nucleation orientation micro-inclusion, the diffraction pattern of MT shows a hexagonal shape, as shown in Figure B.4b, which corresponds to the hexagonal shape in the SE image in Figure B.1a. While the main orientation micro-inclusion has a rectangular shape.

2. In the SAED PL(112) and MT(-202) are near parallel, and PL(02-1) is near 120° to PL(112), MT(2-20) is at exact 120° to MT(-202), as shown in Figure B.4. However, this doesn't correspond to the shape shown in the SE image in Figure B.1a. We will need direct interface structure to decide the facets.

3. Direct interface structures at atomic scale between MT-PL around the transverse cross section of two micro-inclusions with main orientation and nucleation orientation, respectively.

B.2 No. 277-10-d8

This specimen contains cross section of a plate-shaped PL($\bar{3}$12)n-MT inclusion in main orientation, and was studied in Chapter 3.

B.2.1 Specimen description

The TEM foil is mounted on the Cu grid pin B for transport. As shown in Fig. B.5a, the foil can be seen on the upper left of pin B. Fig. B.5b shows the view from the bottom side (viewing direction upwards) of Fig. B.5a, and the magnetite needle is seen in the upper right of the foil, also there might be ilmenite inside the inclusion.

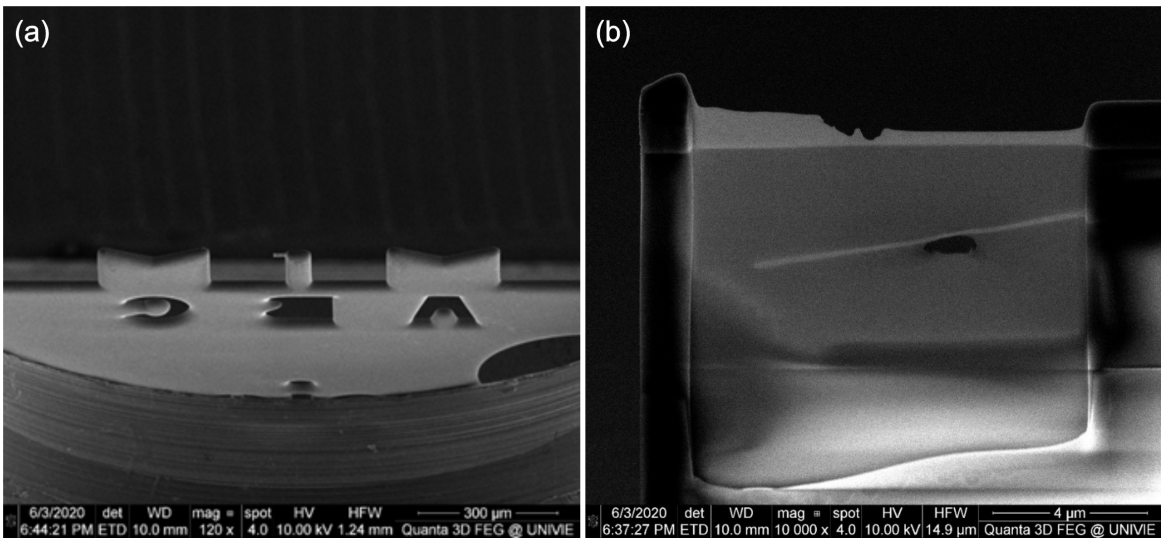

Figure B.5: (a) TEM foil of domain 8 can be seen on the upper left of pin B. (b) Front side of the TEM foil with pin B on the right side (not shown). The magnetite needle is seen in the upper right of the foil. There is a hole near the needle which might be suitable for HRTEM. The foil is viewed from the bottom side (viewing direction upwards) in (a). (The thin portion of the foil is away from the pin B so the thin portion may be fragile while transfer.)

B.2.2 Envisaged procedure

We would put the sample into the holder as shown in the Fig. B.6(a), which ensures that the needle elongation direction is parallel to the TEM x-direction. The needle elongation direction is almost parallel to the foil and is parallel to magnetite [11-1]. The arrow at the end of the needle in Fig. B.6(b) is parallel to [11-1] of magnetite. Meanwhile, the magnetite [112] direction is almost perpendicular to the foil.

From EBSD data we know that plagioclase [-5 1 -8] is parallel to magnetite [112], we also know that slight deviations are likely so that [-5 1 -8] of plagioclase is inclined by 0.3° along the horizontal direction to the left, and by 1.4° along the vertical direction down. These angles may be reference for finding the desired zone axis (which is [-5 1 -8] in this foil) of plagioclase.

SAED results by simulation using Crystalmaker are shown in Fig. B.7. The results show that magnetite (11-1) is parallel to plagioclase (-312), and the *d*-spacing ratio of these two crystal planes is 2:1; furthermore, magnetite (-220) is nearly parallel to plagioclase (150). Be aware the foil is bent and a rotation of only 0.5° away from the zone axes will lose the diffraction pattern.

B.2.3 Task list

1. Bright field and dark field images of the morphology of the inclusion (with ilmenite lamellae if they exist in the inclusion) and the host plagioclase, and the interfaces between the different phases

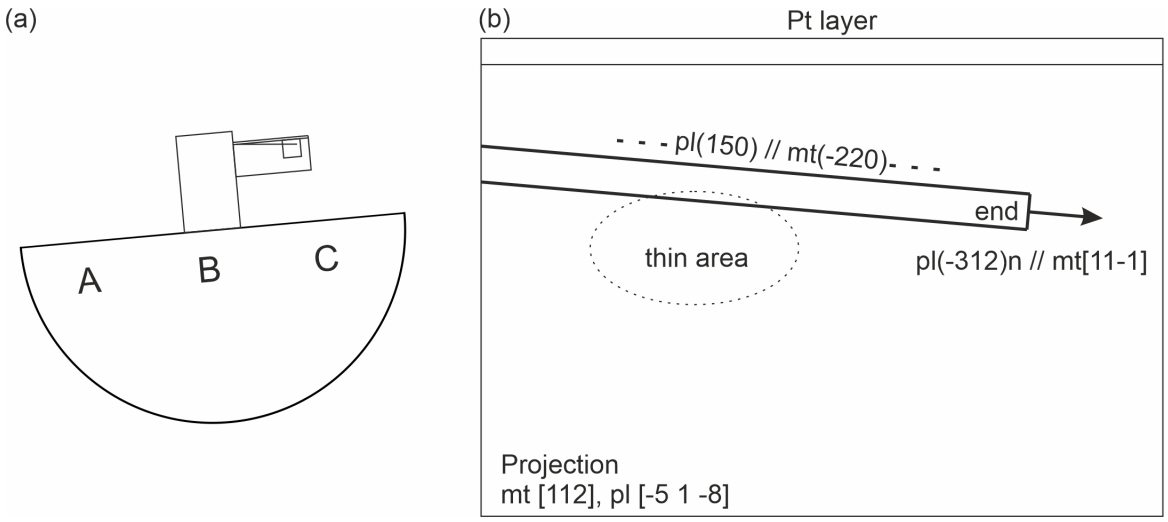

Figure B.6: (a) Sketch for the ideal position of the foil in the TEM sample holder and (b) sketch of the foil and the inclusion information. Here pl(*hkl*)n represents the normal of plagioclase plane (*hkl*).

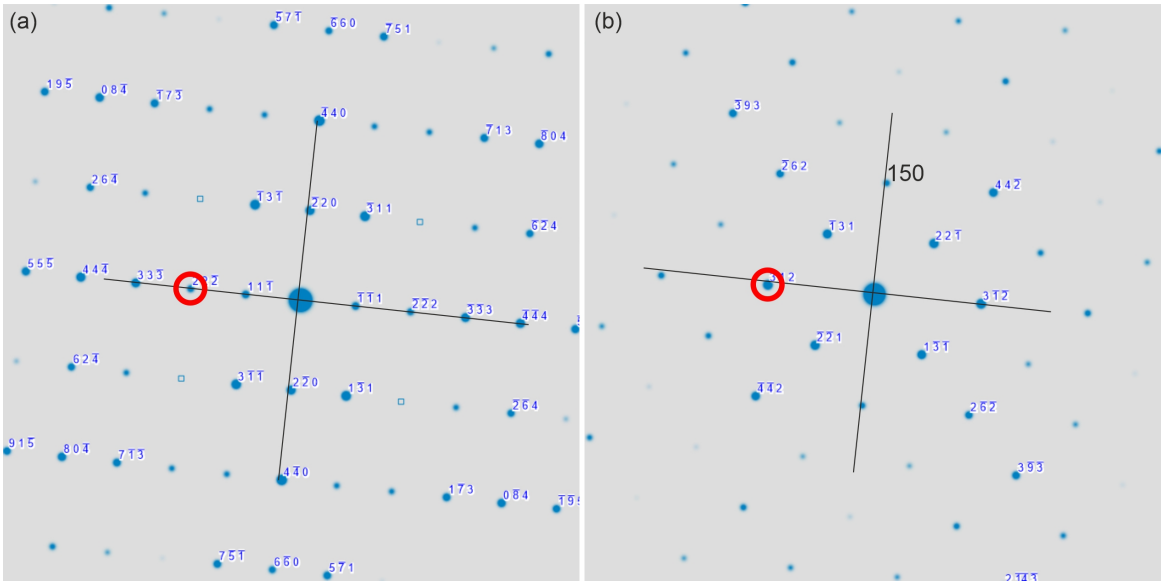

Figure B.7: Simulated electron diffraction pattern of (a) magnetite zone axis [112] and (b) plagioclase zone axis [-5 1 -8]. The black crosses in the image indicate the alignment of these two directions of the crystal planes and the red circles indicate the *d*-spacing correspondence for the plagioclase (-312) plane and magnetite {111} plane.

2. SAED for magnetite-plagioclase, magnetite-ilmenite, and ilmenite-plagioclase areas. If the different phases cannot be aligned in zone axes together, separate SAED of different areas are also interesting

3. HRTEM for detailed structure of magnetite-plagioclase interface; in this foil the plagioclase (150) facet is parallel to magnetite (-220) which should both be edge on if magnetite [112] and plagioclase [-5 1 -8] are in the viewing direction

B.3 No. 277-10-d23

This specimen contains a needle-shaped PL(112)n-MT inclusion along its elongation direction, and was studied in Chapter 3.

B.3.1 Foil descriptions

The TEM foil is mounted on the Cu grid pin B for transport. As shown in Fig. B.8a, the foil can be seen on the upper left of pin B. Fig. B.8b shows the view from the bottom side (viewing direction upwards) of Fig. B.8a, and the magnetite needle is seen in the upper right of the foil, slightly dark domains in the needle are probably ilmenite lamellae.

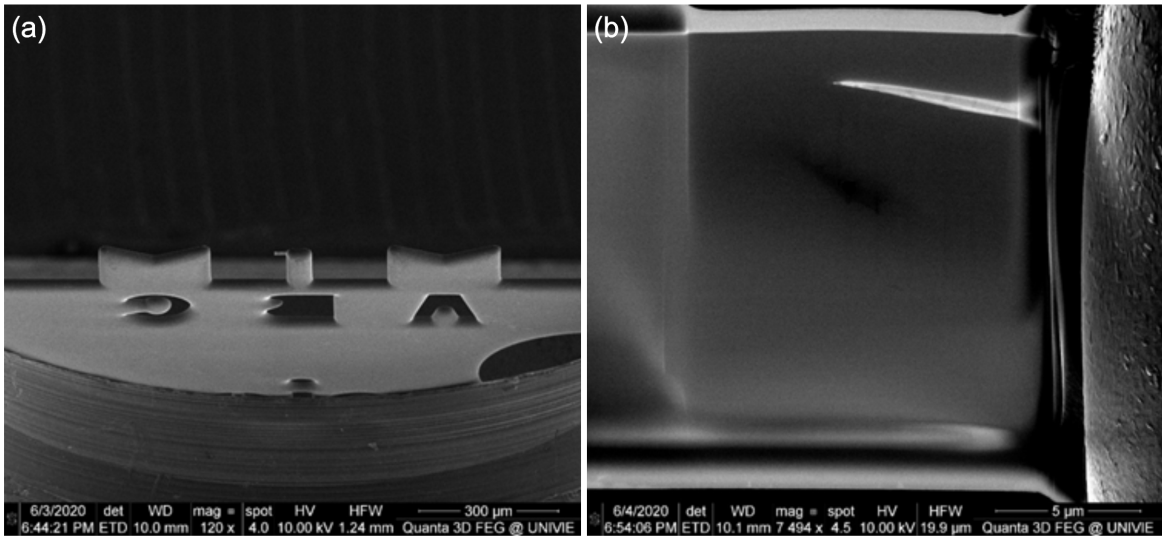

Figure B.8: (a) TEM foil of domain 23 can be seen on the upper left of pin B. (b) Plane view of the TEM foil with pin B on the right side. The magnetite needle is seen in the upper right of the foil, slightly dark domains in the needle are probably ilmenite lamellae. The foil is viewed from the bottom side (viewing direction upwards) in (a).

B.3.2 Envisaged procedure

We would put the sample into the holder as shown in the Fig. B.10, which ensures the trace of the needle elongation direction is parallel to the TEM x-direction. The needle elongation direction is inclined by 8.45° with respect to the plane of the foil. The needle is elongated parallel to magnetite [11-1]. The arrow at the end of the needle in Fig. B.10 is parallel to [11-1] of magnetite and points into the foil with an inclination angle of 8.45°. As a consequence, the magnetite [112] direction deviates by 8.45° from the direction perpendicular to the plane of the foil. Tilting along the trace of the needle elongation direction by 8.45° should bring the magnetite [112] into viewing direction.

From EBSD data we know that plagioclase [-5 -1 3] is parallel to magnetite [112], we also know that slight deviations of this alignment are likely and [-5 -1 3] of plagioclase is inclined by 3° along the horizontal direction to the right, and 0.2° along the vertical direction up with respect to [112] of magnetite. These angles may be reference for finding the desired zone axis (which is [-5 -1 3] in this foil) of plagioclase.

SAED results by simulation using Crystalmaker are shown in Fig. B.11. The results show that magnetite (11-1) is parallel to plagioclase (112), and the *d*-spacing ratio of the two crystal planes is 2:1; furthermore, magnetite (-220) is nearly parallel to plagioclase (1-50). Be aware that the foil is bent and by a deviation of only 0.5° from the zone axes the diffraction pattern will be lost.

B.3.3 Task list

1. Bright field and dark field images of the morphology of the inclusion (with ilmenite lamellae) and the host plagioclase, and the interfaces between the different phases

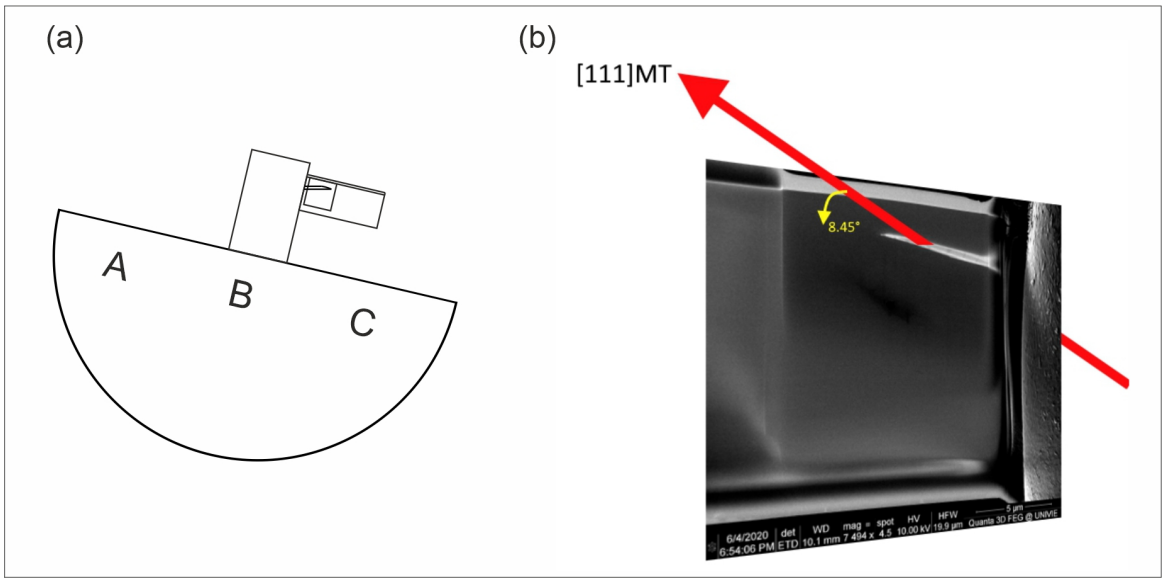

Figure B.9: (a) Sketch of the ideal position of the foil in the TEM sample holder and (b) the inclusion elongation direction in the foil based on Fig. B.8b.

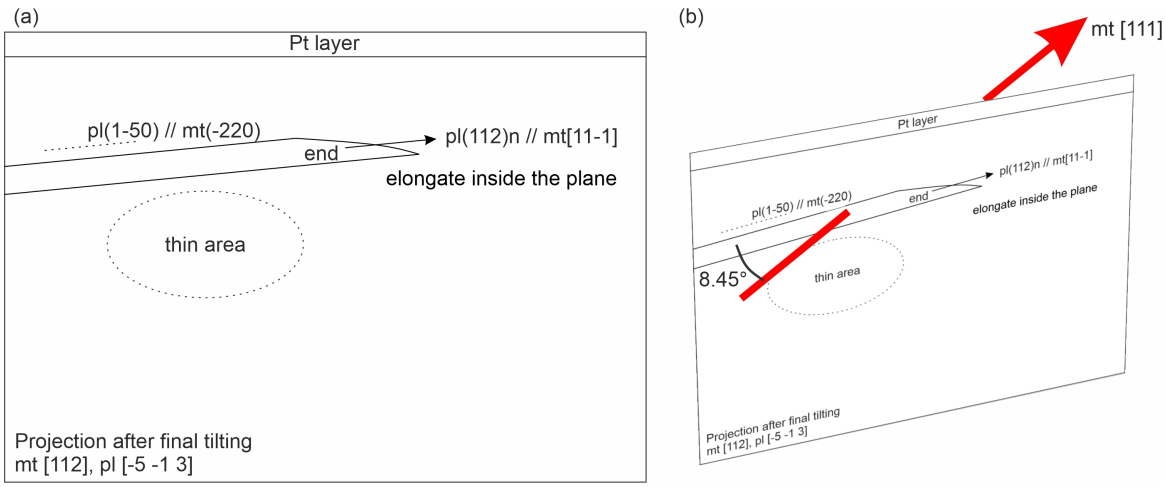

Figure B.10: (a) Sketch of the foil and the inclusion and (b) the elongation direction of the inclusion based on (a). Here pl(*hkl*)n represents the normal of plagioclase plane (*hkl*).

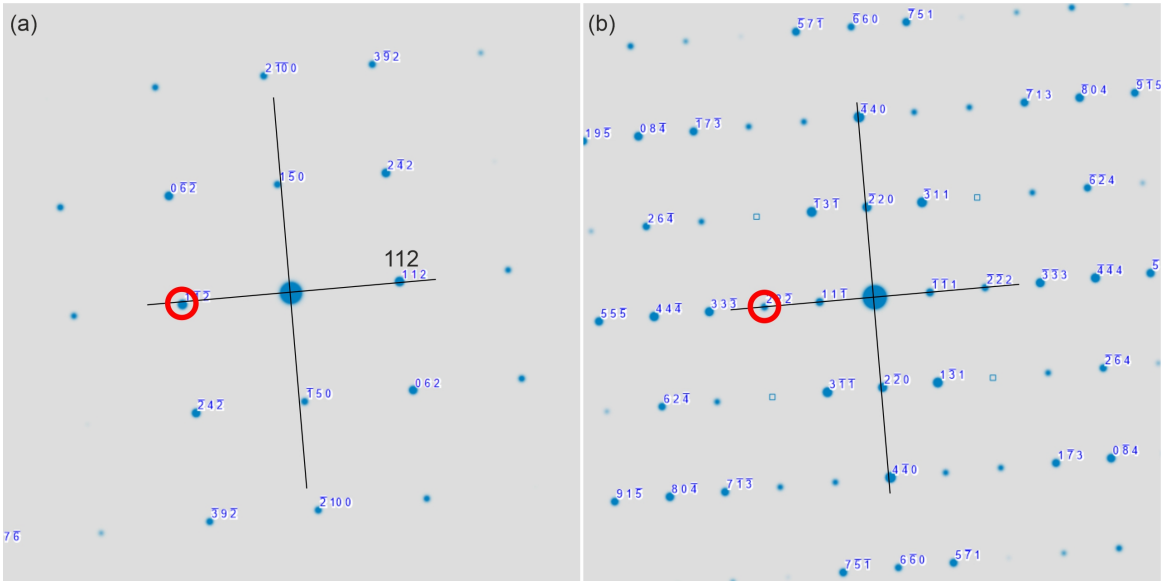

Figure B.11: Simulated electron diffraction pattern of (a) plagioclase zone axis [-5 -1 3] and (b) magnetite zone axis [112]. The black crosses in the image indicate the alignment of these two directions of the crystal planes and the red circles indicate the *d*-spacing correspondence for the plagioclase (112) plane and magnetite {111} plane.

2. SAED for magnetite-plagioclase, magnetite-ilmenite, and ilmenite-plagioclase areas. If the different phases cannot be aligned in zone axes together, separate SAED of different areas are also interesting

3. Detailed structure of magnetite-plagioclase interface; in this foil the plagioclase (1-50) facet is parallel to magnetite (-220). The interface should be edge on if magnetite [112] and plagioclase [-5 -1 3] are in viewing directions

B.4 No. 277-10-d23-cs

This specimen contains cross section of a needle-shaped PL(112)n-MT inclusion in main orientation, and was studied in Chapter 3.

B.4.1 Specimen description

The sample is located at the Position I of the sample holder. The TEM foil is mounted on the Mo grid on the central pin for transport. The surface of the foil is expected to have redepositions due to the rough cutting. The thickness of the foil is about 2 μm.

The foil contains a PL(112)n-MT inclusion. From the prior EBSD result, this type of inclusions has the following COR: MT[111] || PL(112)-normal and MT(2-20) || PL(1-50). The extraction intended to have the cross-section of the PL(112)n-MT inclusion in the foil. Fig. B.12 shows the inclusion intersecting the surface of the petrographic thin section before the FIB extraction. The elongation direction of this inclusion deviates by 7-8° from the surface of the petrographic thin section. The red sector at the upper-right corner of the figure indicates that the FIB extraction is perpendicular to the inclusion elongation direction so that the cross-section of the inclusion lies in the FIB foil. We don't have secondary electron images of the foil, so we couldn't tell the exact position of the needle in the foil but we are sure that it is in the foil.

The expected zone axes of the two phases in the foil are PL(112)-normal and MT[111]. There should not be much tilt of the sample to reach this projection when finding the zone axes. Perhaps MT could be a guide to find the MT[111] and the PL(112)-normal can be reached simultaneously. Under the above-mentioned zone axes, the expected electron diffraction is shown in Fig. B.12. The shape of the inclusion cross-section is of great interest, as well as the detailed structures of the facets that formed the cross-section of the inclusion. Particularly, the straight and sharp interface facets between MT and PL.

As shown in Fig. B.12, the black duplet lines have the same dimension and are located at the same position between the two subfigures. Therefore, the intersects of the diffraction spots with the black duplet lines, for example, PL(1-50) and MT(2-20), could tell that PL(1-50) is parallel to MT(2-20) and these two lattice planes have comparable *d*-spacings. Similarly, PL(-3-12) is close parallel to MT(-2-24) but they don't have similar *d*-spacings. From this method, the inclusion cross-section can be anticipated to be bounded by at least two sets of facets, i.e. PL(1-50) || MT(2-20) and PL(-3-12) || MT(-2-24).

B.4.2 Task list

1. Bright field and dark field images of the morphology of the inclusion and the host plagioclase, and the interfaces between different phases
2. SAED for magnetite-plagioclase area
3. Detailed structure of magnetite-plagioclase interface. In this foil the inclusion may have different facets and should be edge on if magnetite [111] and plagioclase (112)-normal are in the viewing directions. The facets could be PL(1-50) || MT(2-20) and PL(-3-12) || MT(-2-24)

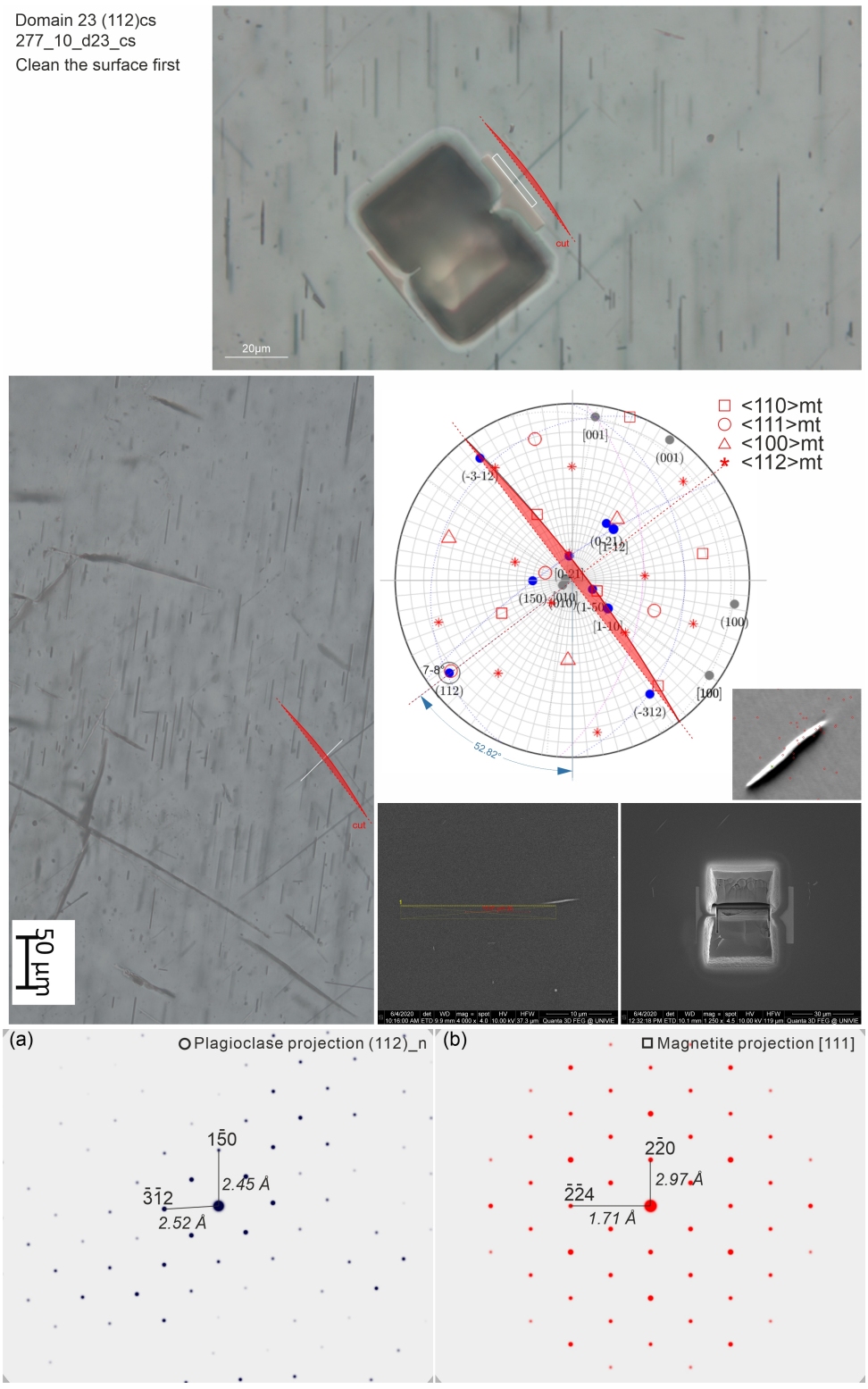

Figure B.12: Top: Optical image of the thin section. Red line indicates the targeted FIB extract site. Middle: Stereographic projection (upper hemisphere) showing the poles of important lattice planes for the PL(112)n-MT in main orientation. The red symbols indicate the poles of MT crystallographic directions, while the blue dots correspond to important planes and directions of PL, and the grey dots are the lattice plane and directions of the PL unit cell. Pole of PL(112) nearly coincides with MT⟨111⟩ with a deviation of about 1°. Bottom: Simulated electron diffraction pattern of (a) plagioclase zone axis (112)-normal and (b) magnetite zone axis [111]. The black duplet lines in the two images have the same dimensions and locate at the same position with respect to each image. The intersect of the black lines and the diffraction spots may indicate the potential alignment of the lattice planes between MT and PL. In the suggested viewing direction, two sets of facets of the inclusion cross-section are anticipated, i.e. PL(1-50) ‖ MT(2-20) and PL(-3-12) || MT(-2-24).

B.5 No. 277-10-d23-e

This specimen contains the cross section of a needle-shaped PL[001]n-MT inclusion, and was studied in Chapter 4.

B.5.1 Foil description

The sample is located at the Position II of the sample holder. The TEM foil is mounted on a Mo grid on the central pin for transport. The surface of the foil is expected to have redepositions due to the rough cutting. The thickness of the foil is about 1.6 μm.

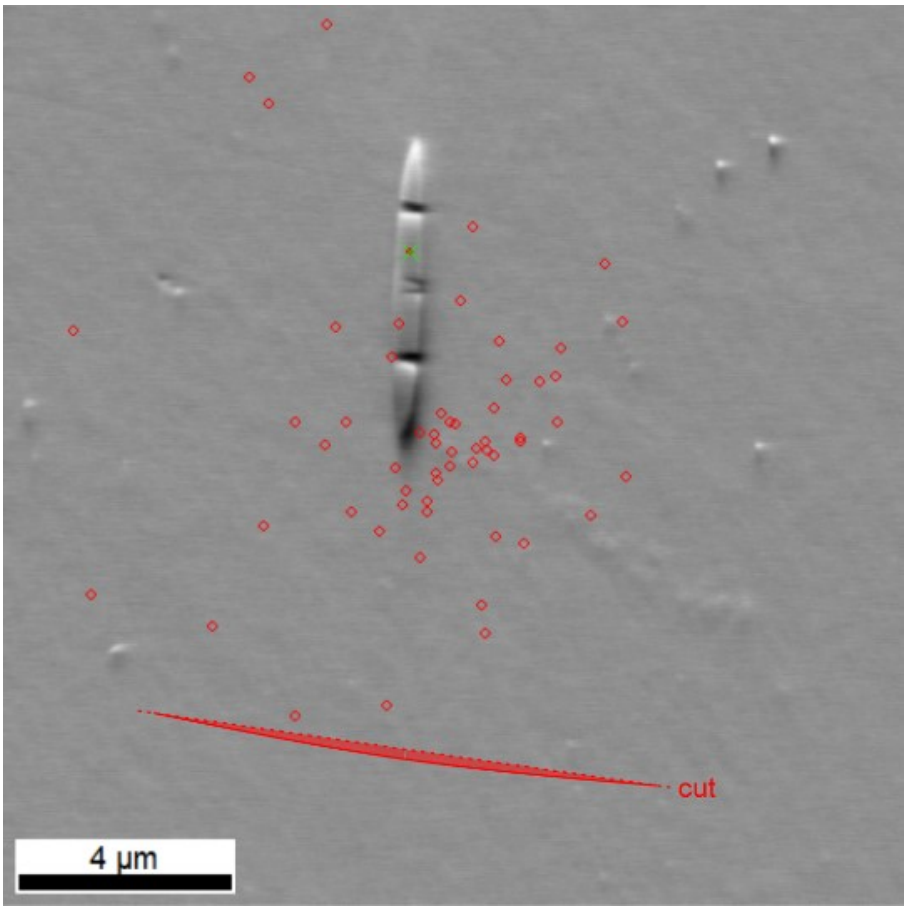

Figure B.13: PL[001]-MT inclusion observed on the surface of the petrographic thin section that is supposed to be lying in Sample 277-10-d23-e with its cross-section. The dark lines inside of the inclusion are expected to be ilmenite exsolutions. The red sector at the bottom indicates the FIB extraction is perpendicular to the elongation direction of the inclusion.

This foil contains a PL[001]-MT inclusion. From the previous EBSD result, this type of inclusions has the following COR: MT[1-10] || PL[001] and MT(222) || PL(1-50). The extraction intended to have the cross-section of the PL[001]-MT inclusion in the foil. Fig. B.13 shows the inclusion intersecting the surface of the petrographic thin section before the FIB extraction. The elongation direction of this inclusion is 4-5° deviating from parallel to the surface of the petrographic thin section. The red sector at the bottom of the figure indicates that the FIB extraction is perpendicular to the inclusion elongation direction so that the cross-section of the inclusion lies in the FIB foil. We don't have secondary electron images of the foil, so we couldn't tell the exact position of the needle in the foil but we are sure that it is in the foil.

The expected zone axes of the two phases in the foil are PL[001] and MT[1-10]. There should not be much tilt of the sample necessary to reach this projection when finding the zone axes. Under the above-mentioned zone axes, the expected electron diffraction is shown in Fig. B.14. The shape of the inclusion cross-section is of great interest, as well as the detailed structures of the facets that formed the cross-section of the inclusion. Particularly, the straight and sharp interface facets between MT and PL.

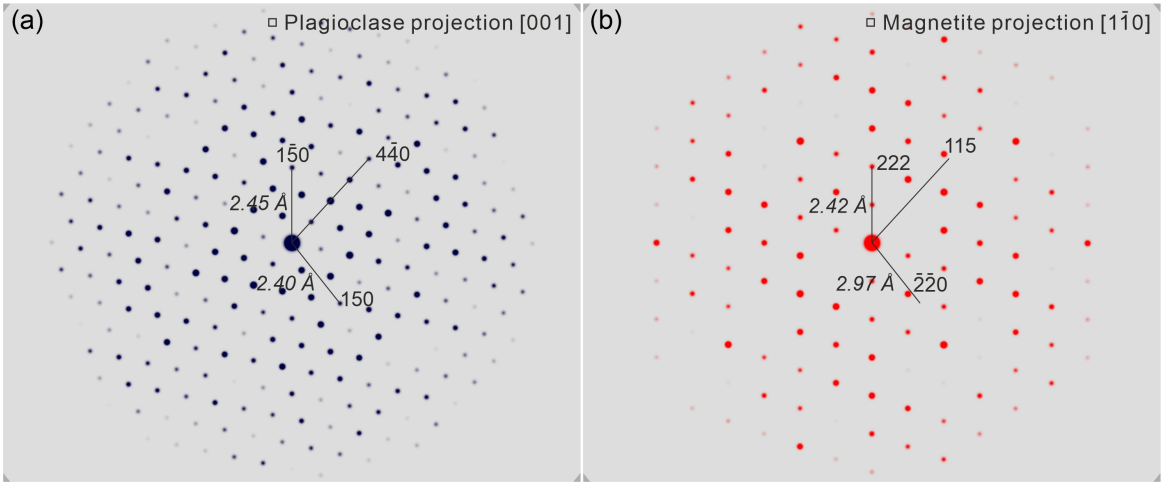

Figure B.14: Simulated electron diffraction pattern of (a) plagioclase zone axis [001] and (b) magnetite zone axis [1-10]. The black triplet lines in the two images have the same dimensions and locate at the same position with respect to each image. The intersect of the black lines and the diffraction spots may indicate the potential alignment of the lattice planes between MT and PL. In the suggested viewing direction, three sets of facets of the inclusion cross-section are anticipated, i.e. PL(1-50) || MT(222) and PL(4-40) || MT(115) and PL(150) || MT(-2-20).

As shown in Fig. B.14, the black triplet lines have the same dimension and are located at the same positions between the two subfigures. Therefore, the intersects of the diffraction spots with the black triplet lines, for example, PL(1-50) and MT(222), could tell that PL(1-50) is parallel to MT(222) and these two lattice planes have nearly identical *d*-spacings. At the same time, PL(4-40) is close parallel to MT(115), and PL(150) is close parallel to MT(-2-20). Moreover, PL(4-40) and MT(115), PL(150) and MT(-2-20) also share comparable *d*-spacings. From this method, the inclusion cross-section can be anticipated to be bounded by at least three sets of facets, i.e. PL(1-50) || MT(222) and PL(4-40) || MT(115) and PL(150) || MT(-2-20).

B.5.2 Task list

1. Bright field and dark field images of the morphology of the inclusion and the host plagioclase, and the interfaces between different phases

2. SAED for magnetite-plagioclase area

3. Detailed structure of magnetite-plagioclase interface. In this foil the inclusion may have different facets and should be edge on if magnetite [1-10] and plagioclase [001] are in the viewing directions. The facets could be PL(1-50) || MT(222) ans PL(4-40) || MT(115) and PL(150) || MT(-2-20)

Appendix C

Modified optimal phase boundary model

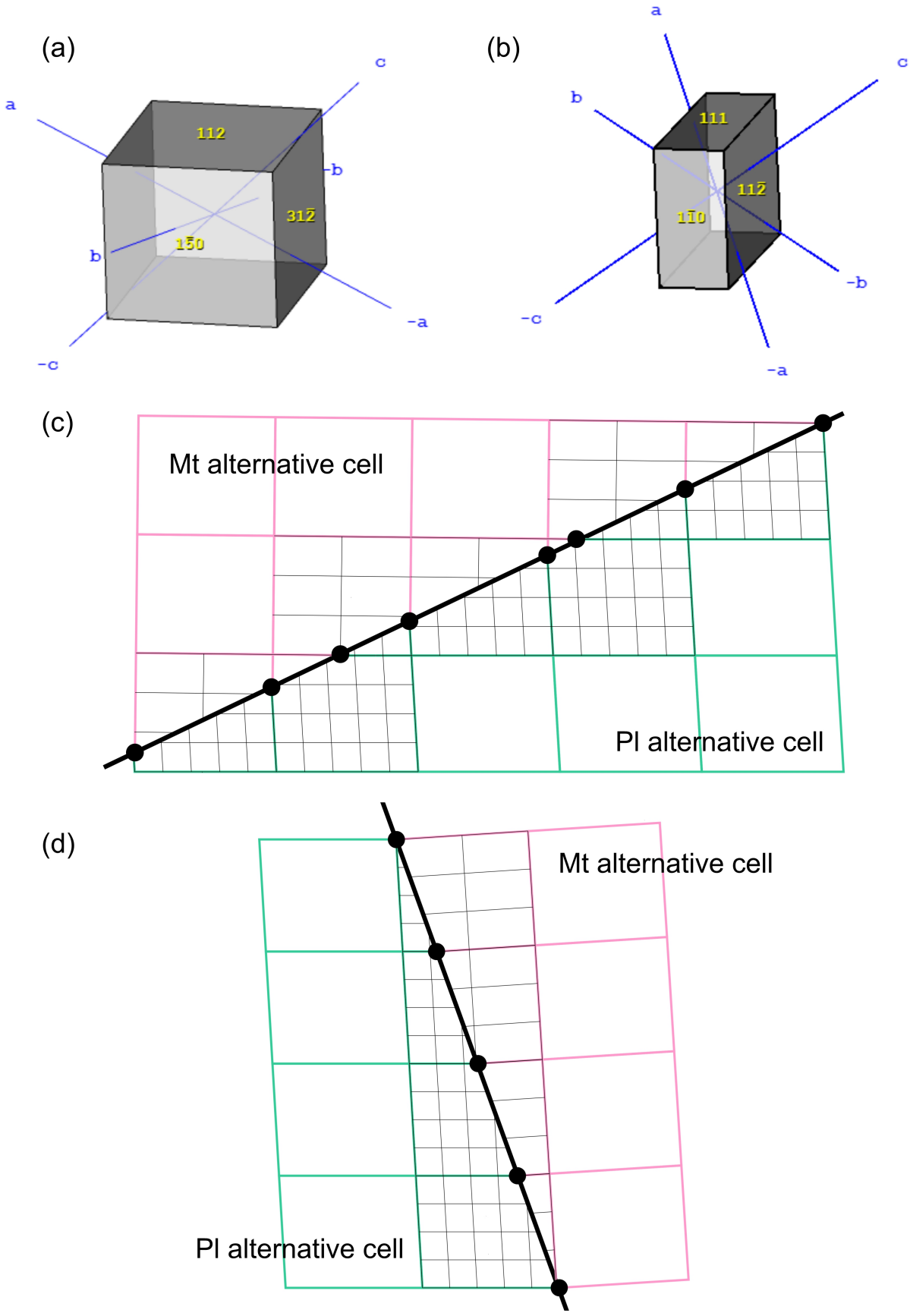

Figure C.1: (a) and (b): schematic sketches of mutually perpendicular lattice planes in (a) plagioclase and (b) magnetite. (c) and (d): two solutions of the optimal phase boundary (heavy black lines, black dots indicate locations of perfect match between the two lattices) for a Pl(112)-needle in general orientation viewed parallel to Mt[111]; based on the perfect d-spacing match between Pl(112) and Mt{111} (viewing direction) the problem is reduced to 2D; to obtain solutions by OPB theory, the Pl unit cell was multiplied by 2×3 and the Mt unit cell by 5×4.